Monographs in Electrochemistry
Series Editor: F. Scholz

Györö G. Láng
Cesar A. Barbero

Laser Techniques for the Study of Electrode Processes

Springer

Laser Techniques for the Study of Electrode Processes

Monographs in Electrochemistry

Surprisingly, a large number of important topics in electrochemistry is not covered by up-to-date monographs and series on the market, some topics are even not covered at all. The series Monographs in Electrochemistry fills this gap by publishing indepth monographs written by experienced and distinguished electrochemists, covering both theory and applications. The focus is set on existing as well as emerging methods for researchers, engineers, and practitioners active in the many and often interdisciplinary fields, where electrochemistry plays a key role. These fields will range – among others – from analytical and environmental sciences to sensors, materials sciences and biochemical research.

Information about published and forthcoming volumes is available at
http://www.springer.com/series/7386

Series Editor: Fritz Scholz, University of Greifswald, Germany

Győző G. Láng • Cesar A. Barbero

Laser Techniques for the Study of Electrode Processes

Springer

Gyözö G. Láng
Eötvös Loránd University
Inst. Chemistry
Pázmány Péter S. 1/A
Budapest
Hungary

Cesar A. Barbero
Universidad Nacional de Rio Cuarto
Chemistry Department
Rio Cuarto Córdoba
Argentina

ISSN 1865-1836 e-ISSN 1865-1844
ISBN 978-3-642-27650-7 e-ISBN 978-3-642-27651-4
DOI 10.1007/978-3-642-27651-4
Springer Heidelberg Dordrecht London New York

Library of Congress Control Number: 2012935872

Printed on acid-free paper

Springer is part of Springer Science+Business Media (www.springer.com)

Preface

For the study of electrode processes, the application of lasers has proved to be very successful. Györző Láng (Budapest, Hungary) and Cesar Barbero (Rio Cuarto, Argentina) have undertaken the task to present the use of lasers (1) for studies of interfacial stress changes of solid electrodes and (2) for the study of changes of the refractive index of solutions near electrode surfaces. The first part of the monograph contains a very sound discussion of the thermodynamics of electrode surfaces, as it can be hardly found elsewhere. The entire monograph excels in a clear presentation of the theoretical background, the experimental setups, and well-chosen illustrative examples. This book will be an indispensable reading for postgraduate students and scientists wishing to use these laser techniques in electrochemical investigations. The two authors have decisively contributed to the development of the presented techniques, and their in-depth knowledge guarantees that the reader gets an authoritative and reliable source which will be valid for many years to come.

Greifswald, Germany Fritz Scholz

Introduction

In 2010, the scientific community celebrated the 50th anniversary of the creation of laser.

Without a doubt, the invention of the laser was one of the groundbreaking scientific achievements of the twentieth century leading to creation of new communication instruments, optical devices, space exploration, computer production, and mastery of nuclear energy. Lasers are oscillators that operate at optical frequencies and produce intense beams of light which are monochromatic, coherent, and highly collimated. The frequencies of operation lie within a spectral region that extends from the very far infrared to the vacuum ultraviolet or soft X-ray region.

In common with electronic circuit oscillators, a laser is constructed from an amplifier with an appropriate amount of positive feedback ("light oscillation by stimulated-emission of radiation"). The acronym LASER, which stands for "light amplification by stimulated emission of radiation," is in reality, therefore, a slight misnomer. (The more truthful acronym "LOSER" was long ago deemed inappropriate.)

Lasers can be classified into four basic categories: gas discharge lasers, semiconductor diode lasers, optically pumped lasers, and "other" lasers. The last category includes chemical lasers, combustion lasers, Röntgen lasers, gas-dynamics lasers, and "others" developed primarily for military and scientific applications.

Some of the properties of laser light are unique, while others are similar to conventional sources (e.g., lamps) but with an increased photon flux. The wavelength (or color) of laser light is extremely pure (monochromatic) when compared to other light sources, and all of the photons that make up the laser beam have a fixed phase relationship with respect to one another. This means that laser light have a high degree of spatial and temporal coherence, unattainable using other technologies. Temporal coherence implies that the interference of laser beams is possible even when the optical path is changed by centimeter to meters. In that way, interferometers can be easily built using laser light. Temporal coherence is related with the high monochromaticity of laser light. Spatial coherence typically is expressed through the output being a narrow beam which is diffraction limited. The light from lasers typically has very low divergence. It can travel over long distances or can be focused to very tiny spots, achieving a very high irradiance. While high power can be attainable with other sources, it is more practical to use lasers to achieve high irradiance with small total power.

When we use the term “light,” we are referring to a type of electromagnetic wave ranging from 1 nm to 1,000 μm in wavelength. The visible spectrum is the portion of the electromagnetic spectrum that is visible to (can be detected by) the human eye. It ranges from approximately 400–700 nm. The electromagnetic spectrum between the wavelengths 0.7 and 1,000 μm is known as the infrared radiation. Conventionally, the 0.7–10 μm band is called the near infrared region (NIR), and beyond that is the far infrared band (FIR). The ultraviolet region (UV) ranges from 200 to 400 nm; below 200 nm is the deep ultraviolet.

Most lasers operate at discrete frequencies. Although some types of lasers operate at several different wavelengths simultaneously, the limited number of laser wavelengths may be a disadvantage in certain applications. These difficulties can be overcome by using a dye laser or an optical parametric oscillator (OPO) whose wavelength of operation can be altered in a controlled manner. Alexandrite, chromium LiSAF, chromium LiCaF, and titanium sapphire lasers can be tuned continuously over specific spectral regions. Of course, multiline emission can be both a benefit and a detriment, depending on the application.

Laser technology touches almost every aspect of everyone’s life. In fact, much of modern technology depends on the capabilities that lasers have made possible. Since the operation of the first laser in 1960, literally hundreds of different laser varieties have been developed, and the light that they produce is being used in thousands of applications ranging from precision measurement to materials processing, from telecommunications to data storage, from supermarket bar codes to eye operations. Laser applications include laser surgery, metal and nonmetal cutting, electronic components welding, radar detection, fiber optics, making holograms, laser printing, and others. Lasers are indispensable in many fields such as in science, medical therapy, aerospace, maritime, telecommunication, and entertainment, and last but not least, the development of lasers has opened up new areas of research in physics and chemistry.

Lasers have also found applications in many areas of electrochemistry such as electrochemical deposition, etching, synthesis, polymerization, investigation of electrochemical processes, and photoelectrochemical conversion and storage. In fact, many of today’s laser applications are considered novel or recent, but this is not always the case. For instance, the term “laser interferometer” refers to an interferometer using a laser light source. Obviously, this does not necessarily mean that these devices cannot be used with conventional light sources, but in most cases, the laser light improves significantly the performance of the system. As a result of the use of lasers, some classical optical techniques have been substantially modified; others are entirely new. Electrochemists are particularly interested in these techniques because optical methods are usually nondestructive, contactless, and implementable in situ. Optical measurements yield data that are independent of other electrochemical techniques and can often be performed simultaneously with the latter.

Two relevant areas of electrochemical research are reviewed in the present volume: Part I of the book (Chaps. 1–8, written by G.G. Láng) is dedicated to the determination of interfacial stress changes in electrochemical systems, while Part II (Chaps. 9–14, written by C.A. Barbero) focuses on the use of laser light to measure changes of refractive index in the electrochemical solutions which are related with photothermal effects and/or concentration gradients.

The first chapter deals with the definitions of some general and specific terms concerning the electrochemistry of solid/liquid interfaces.

Several aspects of the thermodynamic theory and their physical interpretation are discussed in Chaps. 2 and 3. There is no doubt that despite the advent of surface-sensitive techniques, thermodynamic measurements remain a valuable tool for the investigation of surfaces and interfaces, and the understanding of the thermodynamics of solid/liquid interfaces is of importance to all surface scientists and electrochemists. It is not surprising, therefore, that during the past decades, several attempts have been made to derive thermodynamic equations for the solid/liquid interface, and several methods were suggested for the measurement of changes in the interfacial stress of "solid electrodes" as a function of various physicochemical parameters, e.g., the electrode potential. Difficulties of existing theories are critically reviewed in Chap. 3.

Methods for the experimental determination of (interfacial) stress changes in electrochemical systems are discussed in the next three chapters (Chaps. 4, 5, and 6). The essential components of two frequently used methods—the "bending beam method" and "Kösters interferometry"—are lasers. In essence, the main difference between the two above techniques is the detection system: position sensing with photodiodes ("position sensitive detectors," PSD) in case of the bending beam method and automated detection of light intensity changes in case of the laser interferometer. These issues are addressed in more detail in Chaps. 5 and 6.

In Chap. 7, selected results of bending beam (bending plate) experiments with optical detection are presented as illustrative examples. In order to demonstrate the capabilities and limitations of stress measurements in electrochemical systems, relevant results obtained using two different experimental techniques (the bending beam method and Kösters laser interferometry) are discussed.

Chapter 8 gives a brief overview of the mathematical background, some important mathematical concepts, and various functional relationships underlying the thermodynamic theory of interfaces.

The second part of the book from Chap. 9 onward deals with the use of laser light to measure changes of refractive index in the electrochemical solutions which are related with photothermal effects and/or concentration gradients.

In Chap. 9, an introduction to the refractive index detection with laser light is made with a brief account of the development of the techniques discussed in Part II of the book: Probe Beam Deflection (PBD) and Photothermal Deflection Spectroscopy (PDS).

Chapter 10 gives a brief overview of the mathematical background of PBD techniques, along with a discussion of the experimental details.

In Chap. 11, the application of PBD to electrochemical systems involving surface confined species are critically reviewed and discussed. Such systems involve electroactive thin films, redox monolayers and multilayers, and porous electrodes. The data gathered has applications in batteries, supercapacitors, fuel cells, sensors, etc. It is shown that such kind of electrochemical system is the main field of application of PBD technique.

On the other hand, in Chap. 12, the application of PBD techniques to the study of concentration gradients due to redox changes in solution species is reviewed. There are fewer studies of such systems due to the inherent difficulty to analyze the PBD data.

In Chap. 13, the theory of PDS is discussed, and the application of PDS to electrochemical systems is reviewed.

Finally, in Chap. 14, the application of different techniques able to monitor the fluxes of mobile species to electrochemical systems is reviewed and the results compared to the application of PBD to similar systems.

Contents

Part I Experimental Determination of Interfacial Stress Changes in Electrochemical Systems

Part II Probe Beam Deflection (PBD)

Part I

Experimental Determination of Interfacial Stress Changes in Electrochemical Systems

Chapter 1
Introduction and Basic Concepts

1.1 Issues Related to Electrified Interfaces and Electrocapillarity: Some Introductory Remarks

The properties of the electronic conductor–ionic conductor interface (e.g., the interface between a metal and an electrolyte solution) directly influence the electrochemical processes occurring in an electrochemical system. It is not surprising, therefore, that the interest in the structure and properties of charged solid–liquid interfaces has increased steadily throughout the past 50 years and stimulated interesting discussions and debates in the electrochemical community. The understanding of fundamental aspects of interfacial electrochemistry is also important for other fields of research, such as materials science, nanoscience, biology, medical science, and sensor and battery research, as well as for technologies based on electrochemical techniques.

The solid–liquid interface plays a fundamental role in a number of physical and chemical phenomena as chemisorption, catalysis, metal deposition, and in biologically important processes. Since the early days of modern surface science, one of the main goals of electrochemical research has been to find correlations between the structures formed by surface atoms and adsorbates and the macroscopic kinetic rates of electrochemical reactions. The formation of interfaces between conducting phases is known to be accompanied by a spatial separation of charge such that electric potential differences may appear. The whole array of charged species, neutral molecules, or oriented dipoles existing at a metal–solution interface is called the electrochemical (or electrical) double layer. For such systems, the important thermodynamic quantity is the intensive parameter conjugate to surface area, often called the “surface tension,” “interfacial tension,” “surface stress,” or “interface stress.” Electrocapillarity is the study of the interfacial tension (stress) as a function of the electrode potential. Precise quantitative measurements of interfacial tensions have been obtained for liquid–liquid interfaces as reported, for example, refs. [1–6]. The interpretation of electrocapillary data obtained with liquid metals in contact with electrolyte solutions is greatly facilitated by the

G.G. Láng and C.A. Barbero, *Laser Techniques for the Study of Electrode Processes*, Monographs in Electrochemistry, DOI 10.1007/978-3-642-27651-4_1,

characteristic of ideal polarizability. For perfectly (ideally) polarizable electrodes, the relationship between the interfacial tension, the electrode potential, and the surface charge density can be described by the Lippmann equation [7].

On the other hand, a study of the interfacial stress of "solid electrodes" is complicated by many factors, and with the exception of a few special situations, the absolute interfacial tension at the solid–liquid interface is inaccessible by experimental methods. In addition, a solid does not generally exhibit an "equilibrium" surface. According to [8], "their surface will be largely a frozen-in record of an arbitrary past history." Although a change in a thermodynamic parameter may not result in full equilibrium, the system can escape from the constraint by optimization of, for example, "the distribution of imperfections, surface waves and humps" [9] in the rational time scale, or more generally, it will approach relative minima of the Gibbs energy of the interface. Despite the above problems, during the past decades, several attempts have been made to derive thermodynamic equations for the solid–liquid interface, and several methods were suggested for measurements of *changes* in the "specific surface energy," "interfacial tension," "surface stress," or "interfacial stress" of solid electrodes.

In the next two chapters, several aspects of the thermodynamic theory of solid–liquid interfaces are reviewed, and their physical interpretation is discussed. Techniques and equipment for the precise measurement of the deformation of thin plates, strips, or cantilevers are presented in Chaps. 4–6. Chapter 7 briefly reviews a few of the relevant experimental results obtained using the "bending beam" method and Kösters laser interferometry. Some of the mathematical concepts used in Part I of the book are summarized in Chap. 8.

The author thanks the Alexander von Humboldt Stiftung, the Japan Society for the Promotion of Science, and the Hungarian Scientific Research Fund (Grants OTKA-K-37588 and OTKA-K-67994/OMFB-01078/2007) for support of research related to the subject of Part I of this book.

1.2 Selected Concepts and Definitions in Electrochemistry and Surface Science

Careful description of its objects and clear-cut terms should be the basis of any "true" science, and the need for precise language and terminology cannot be overestimated. Misinterpretations and misunderstandings in science are often caused by ignoring or marginalizing the importance of clear concepts and definitions. A fundamental problem is that conceptual definitions often are not specified in precise terms. In some cases, definitions are not explicitly provided or are overly generic. Unfortunately, there are also similar problems with some terms and definitions used in interfacial electrochemistry. As it has been pointed out recently in [10], "interfacial electrochemistry is not the only field of science in which tacit assumptions are made, some that can readily be justified and some that are dubious or totally wrong." A second problem is that constitutive definitions (used in theories) do not always match operational definitions. For instance, if one searches for the term "electrode," a number of divergent and confusing definitions can be found in the electrochemical literature. Apparently, this is also the case for many other terms.

The situation has improved recently with the appearance of the Electrochemical Dictionary [11], a reference manual where the reader can quickly find brief explanations of scientific terms used in the electrochemical literature.

There are, however, some features which require further consideration. Since the next chapters deal with interfacial electrochemistry, it is necessary to clarify the definitions of some of the most commonly used terms related to electrified interfaces. Therefore, in the next section, definitions of some general and specific terms concerning the electrochemistry of solid–liquid interfaces will be discussed.

1.2.1 What Is an "Electrode" and What Is a "Solid Electrode"?

There exist several different definitions of the term "electrode" in the electrochemical literature. A selection of definitions is presented below:

(i) [12, p. 202]

> There are currently two usages for the term electrode, namely either (i) the electron conductor connected to the external leads or (ii) the → half cell between one electron conductor and at least one ionic conductor. The latter version has usually been favored in electrochemistry [13, p. 73]. The half cell, i.e., the electrode may have a rather complicated structure. . .A satisfactory definition, which includes the factors and problems mentioned above, may be as follows. The electrode consists of two or more electrically conducting phases switched in series between which charge carriers (ions or electrons) can be exchanged, one of the terminal phases being an electron conductor and the other an electrolyte.

(ii) [14, p.273]:

> In electrochemistry an electrode is an electronic conductor in contact with an ionic conductor. The electronic conductor can be a metal, or a semiconductor, or a mixed electronic and ionic conductor. The ionic conductor is usually an electrolyte solution; however, solid electrolytes and ionic melts can be used as well. The term 'electrode' is also used in a technical sense, meaning the electronic conductor only. . . In the simplest case the electrode is a metallic conductor immersed in an electrolyte solution.

(iii) [15, p.22]:

> In heterogeneous systems, the electrode is a typical basic unit. The electrode is an electrochemical system in which at least two phases are in contact and one of them being first-order conductor, the other a second-order conductor (usually this is an electrolyte solution).

(iv) [16, p. 2]:

> In electrochemical systems, we are concerned with the processes and factors that affect the transport of charge across the interface between chemical phases, for example, between an electronic conductor (an electrode) and an ionic conductor (an electrolyte).

The most important conclusion emerging from the above is that there are really two quite different things covered by the term "electrode": an electronic conductor phase (alone) and the entire assembly of an electronic conductor in intimate contact with an ionic conductor. This may lead to confusions and misconceptions, as will be pointed out later.

Some additional points should be noted here:

1. In the same book from which quotation (iv) was taken, the term is also used in another sense [16, p. 3]: "…one standardizes the other half of the cell by using an electrode (called a reference electrode) made up of phases having essentially constant composition. The internationally accepted primary reference is the standard hydrogen electrode (SHE), or normal hydrogen electrode (NHE), which has all components at unit activity...."
2. The statement in point (i) above (see [12]) that "The latter version has usually been favored in electrochemistry" is probably true for classical electrochemistry. However, unfortunately, the importance of the fundamental aspects of electrochemistry may have declined in the past two or three decades [10], and there is a risk today that electrochemistry may lose its status as a fundamental science and merely become a branch of materials science [17]. As a consequence, the term "electrode" is increasingly used to designate an electronic conductor (a metal rod, wire, plate, etc.), even in the "electrochemical" literature.
3. The term "half-cell" is often used instead of "electrode." It may nevertheless seem strange to talk about an electrochemical cell consisting of three or four "half-cells."
4. The definition proposed in [12] is also not without problems. For instance, it does not exclude the possibility of the presence of several (more than one) electrified interfaces (i.e., electrodes) between electronically and ionically conducting phases in the system (which is in fact defined as a chain of conducting phases).
5. The electrode is sometimes defined as follows: "it is a material system in which the electrode reaction takes place at an interface" [15, p. 27]. Obviously, this definition does not apply to the "ideal polarized" [18] ("ideally polarizable" or "perfectly polarizable" [19, 20]) electrode (discussed later).

By taking into account the above considerations, the following relatively simple definition may be relevant:

> An electrode is a heterogeneous electrochemical system including one interface (or several interfaces which are not connected in series) at which the type of electrical conduction changes from electronic to ionic or to mixed (or vice versa).

Although widely used, the term “solid electrode” remains unclear and confusing for those that are unfamiliar with electrochemical definitions. According to the above, the definition of a “solid electrode” can be given as follows:

> An electrode that contains an electronically conducting solid phase in contact with an ionically conducting liquid phase.

Conceptually, the most important conclusion of the above discussion is that a “solid electrode” is a multicomponent, multiphase electrochemical system, containing at least one solid phase. This means that it cannot be treated as a pure solid.

On the other hand, it is well known that thermodynamics usually deal not with matter at all, but with models of matter. This is also true for the thermodynamics of solids. The manifestation of properties of real solids is multiple and depends on the time of observation. This subject has been discussed in detail, e.g., in the excellent review by Rusanov [21]. According to the author of [21], “The question can arise: is it possible to find a perfect model and to use only this model in all cases? The answer will be negative. … If we are curious, for instance about whether a real solid, with numerous structural defects, is capable of distributing pressure uniformly and isotropically, the result will be different depending on the period of time given for observation: the very short time typical for a laboratory experiment, or eternity.”

A possible, thermodynamically correct alternative choice is the model of a “completely elastic body” with the following properties:

1. There is at least a single “immobile” component in the system, the particles of which are firmly fixed (by a passive resistance) at their sites in a crystalline lattice, which makes their diffusion impossible. The introduction of “internal constraints” that operate selectively is a tool for creating a theory of a, strictly speaking, nonequilibrium system using the language of equilibrium thermodynamics.
2. The mechanism of equalizing chemical potentials does not operate in this model with respect to the immobile component, and a chemical potential gradient can appear even for an “equilibrium state.”
3. The model may include any number of mobile components which are distributed with uniform chemical potentials at equilibrium.

1.2.2 Surface, Interface, and Interphase

In physical chemistry, the term “surface” usually means the termination of a solid or liquid phase bordering to vacuum [22]. This condition is often emphasized by using the term “free surface.” In some cases, the term “surface” is used in the macroscopic sense and means the outermost face of a solid, which can be produced and maintained under normal external conditions by conventional methods like cutting, polishing, and etching. This approach implies that the surface is in contact with the ambient atmosphere [23]. The term “surface of a metal” usually means the top layer of atoms or ions. Surfaces can be divided into ideal and real [24]. Ideal surfaces exhibit no surface lattice defects; real surfaces may have all types of defects (vacancies, impurities, grain boundaries, dislocations, etc.). In the microscopic sense, the term surface is used very often for an atomically clean and atomically smooth crystal plane.

In electrochemistry, however, the plane that ideally marks the boundary between two phases is called the “interface,” and “surface” means practically always the *interface* between two phases, i.e., two solid phases, two liquid phases, or a solid phase and a liquid phase. On the other hand, if attention is actually focused on only one of the two phases, this plane is often called the “surface” of the phase. This approach, however, may lead to confusion.

The region between two phases where the properties vary (usually in the direction perpendicular to the surface) between those of the bulk is the interfacial region. It can also be regarded as a distinct, although not autonomous, phase and be called the *interphase* [25]. While the “interface” is two-dimensional, the “interphase” is assumed to be three-dimensional, which possesses volume.

Charged components may or may not cross the interface between two phases. The terms “ideally polarizable interface” and “ideally polarizable interphase” are used when no charged component is common to both phases adjoining the (electrified) interphase, i.e., the interface is impermeable to electric charge. Heterogeneous electrochemical systems that possess this property are called “ideally polarizable” or “ideal polarized” electrodes. The concept of ideal polarizability implies the total absence of charge transfer between the two adjacent phases. The term “perfectly polarizable electrode” is often used when the state of the electrode is uniquely defined by the amount of charge consumed. This concept is somewhat broader than that of ideal polarizability [26].

1.2.3 Elastic and Plastic Surface Strains

If the area of the interface between two liquid phases is changed, there is no barrier to prevent molecules (or atoms) from entering or leaving the interfacial region. Although these processes are supposed to have a certain inertia, a new state of equilibrium can be reached, in which each surface molecule covers the same area as in the original undistorted state. This means that the number of molecules (or atoms) in the interface region has changed, but the area per molecule (or atom) at the surface has not. The surface strain, i.e., the change in surface area per unit area, is said to be “plastic” in this case.

In case of a metal far from its melting point, a distortion of the surface can be thought of as resulting in a change of area which cannot be accommodated by migration of atoms to and from the surface. The presence of long-range order (e.g., in an ideal solid) can be interpreted as a consequence of internal constraints. While the distortion persists the number of atoms in the surface region remains

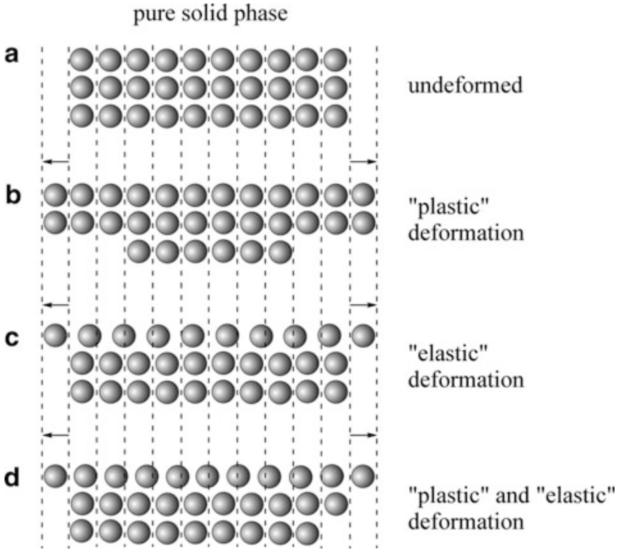

Fig. 1.1 Plastic and elastic deformations of a pure solid phase

constant, but the area occupied by each atom differs from that in the undistorted case. Such a surface strain is said to be "elastic" [27]. For the case of a crystalline solid plastic and elastic, deformations can be illustrated by the schematic pictures shown in Fig. 1.1. In the case schematized in Fig. 1.1d, the "total" strain may be imagined to be divided into two contributions, the "plastic" strain and the "elastic" strain.

When dealing with solid–liquid interfaces, the situation is much more complicated (see Fig. 1.2). If such an interface is strained, the total number of atoms of the solid at the interface (n_s) may or may not change. In the first case, n_s changes, but the area per atom at the surface does not change. On the contrary, the surface density of molecules coming from the liquid phase may not necessarily change (Fig. 1.2b). In the second case, the number of atoms of the solid in the surface region remains constant, but the area occupied by each atom differs from that in the undeformed state. This type of deformation is very often called "elastic" deformation, and the strain is called elastic strain [28]. On the other hand, atoms or molecules can be exchanged between the interfacial region and interior of the fluid in order to maintain the same area density. This means that while n_s remains constant during the deformation, this is not necessarily true for molecules in the surface region in the liquid (Fig. 1.2c).

In consequence, it is not easy to construct a consistent model to account for all these features or to imagine situations in which all deformations are purely "plastic" or "elastic." In addition, in a "general system," each of the phases can be multicomponent.

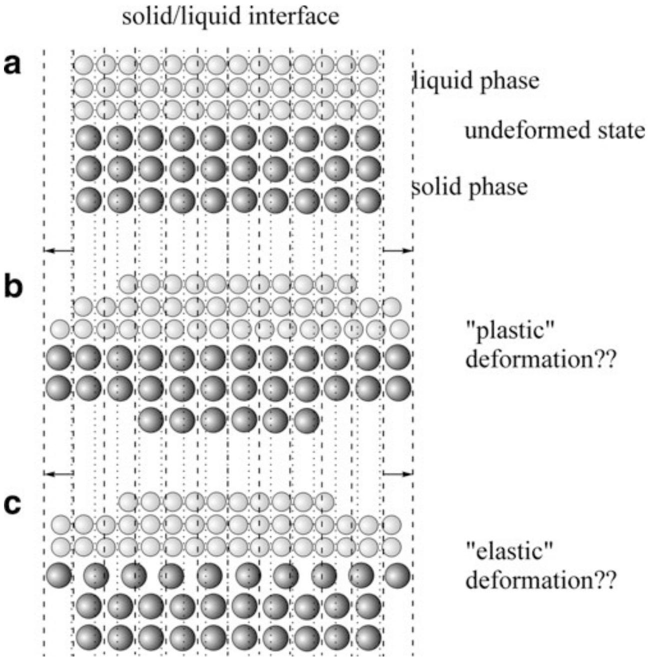

Fig. 1.2 Schematic representation of the deformation of the solid/liquid interface

Electrochemical systems containing charged species and electrified solid–liquid interfaces ("solid electrodes") are even more complex. In such cases, the assumption that deformation can be separated into two (purely "plastic" and purely "elastic") contributions is highly questionable. Nevertheless, the adaptation of an approach developed for one-component systems provides a perfect opportunity for confusing the concepts of continuum elasticity theory and equilibrium thermodynamics.

As a matter of fact, in electrochemical-mechanical experiments involving solid electrodes, the deformations are typically very small, and the applied stress level is assumed to be such that the surface strain of the solid remains within the elastic limit.

1.2.4 "Surface Stress" or "Interfacial Stress"?

Detailed knowledge of the structure and thermodynamic properties of solid–liquid interfaces contributes to a better understanding of interfacial phenomena. In spite of the introduction of a range of powerful surface analytical techniques, thermodynamic measurements remain a valuable tool for the investigation of surfaces and interfaces. Unfortunately, for solid electrodes, the thermodynamic interpretation of the results from various methods in terms of physicochemical properties of the system is not without problems. An important point in the application of thermodynamic principles to interfaces is the experimental determination of the intensive thermodynamic parameter conjugate to the surface area.

In the relevant IUPAC recommendations [26], the terms "superficial work," "surface stress," and "generalized surface parameter" are proposed to replace the terms "surface tension," "surface (free) energy," and "specific surface work (energy)." However, as it has been correctly pointed out by Ibach [29], the *energy of the solid–liquid interface* changes when the surface area changes. This means that even those modifications of the interfacial region which are microscopically associated with the liquid side of the interface will contribute to the deformation (e.g., to the bending of a sample). This is obviously true in spite of the often-heard argument that the species in the liquid phase cannot exert a lateral force on the solid because of the vanishing shear modulus in the liquid.

When applying, e.g., the bending beam method (see Chaps. 4–6) in experiments with solid electrodes, the question arises as to what is really measured when the electrode potential is varied. Taking into account the considerations outlined above, it is clear that the experimentally determinable quantity is the *change* of the intensive parameter conjugate to the interface area. This quantity is intimately related to the properties of the solid-liquid *interface* and not just to the properties of the *surface* of the solid phase; therefore, it seems reasonable to refer to it as the "interface stress change" or "interfacial stress change." Consequently, the intensive parameter conjugate to the area of the interface is identified as the interfacial (or interface) stress. Nevertheless, the term "interfacial tension" may also be used, if there is no danger of confusion.

References

1. Grahame DC (1947) Chem Rev 41:441–501
2. Parsons R (1954) Equilibrium properties of electrified interfaces. In: Bockris JO'M, Conway BE (eds) Modern aspects of electrochemistry, vol 1. Academic Press, New York
3. Delahay P (1965) Double layer and electrode kinetics. Interscience, New York
4. Aveyard R, Haydon D (1973) An introduction to the principles of surface chemistry. Cambridge University Press, Cambridge
5. Bockris JO'M, Conway BE, Yeager E (eds) (1980) Comprehensive treatise of electrochemistry, vol 1. Plenum Press, New York
6. Girault H, Schiffrin D (1989) Electrochemistry of liquid-liquid interfaces. In: Bard AJ (ed) Electroanalytical chemistry, vol 15. Marcel Dekker, New York
7. Lippmann G (1875) Ann Chim Phys 5:494–549
8. Adamson AW, Ling I (1964) Adv Chem Ser 43:57–73
9. Herring C (1951) Phys Rev 82:87–93
10. Gileadi EJ (2011) Solid State Electrochem 15:1359–1371
11. Bard AJ, Inzelt G, Scholz F (eds) (2008) Electrochemical dictionary. Springer, Berlin
12. Inzelt G (2008) Electrode. In: Bard AJ, Inzelt G, Scholz F (eds) Electrochemical dictionary. Springer, Heidelberg

13. Cohen ER, Cvitas T, Frey JG et al (eds) (2007) IUPAC quantities, units and symbols in physical chemistry, 3rd edn. Cambridge, RSC Publishing
14. Komorsky-Lovric S (2010) Working electrodes. In: Scholz F (ed) Electroanalytical methods, 2nd edn. Springer, Heidelberg
15. Kiss L (1988) Kinetics of Electrochemical metal dissolution, Studies in physical and theoretical chemistry 47. Elsevier, Amsterdam
16. Bard AJ, Faulkner L (2001) Electrochemical methods: fundamentals and applications, 2nd edn. Wiley, New York
17. Damaskin BB, Petrii OA (2011) J Solid State Electrochem 15:1317–1334
18. Graham DC (1947) Chem Rev 41:441–501
19. Koenig FO (1934) J Phys Chem 38:111–128
20. Koenig FO (1934) J Phys Chem 38:339–363
21. Rusanov AI (1996) Surf Sci Rep 23:173–247
22. Scholz F (2008) Surface. In: Bard AJ, Inzelt G, Scholz F (eds) Electrochemical dictionary. Springer, Heidelberg
23. Herman MA, Richter W, Sitter H (2004) Epitaxy, physical principles and technical implementation. Springer, Berlin
24. Paunovic M, Schlesinger M (2006) Fundamentals of electrochemical deposition. Wiley, New York
25. Trasatti S, Parsons R (1986) Pure Appl Chem 58:437–454
26. Bagotsky VS (2006) Fundamentals of electrochemistry. Wiley, Hoboken, NJ
27. Linford RG (1978) Chem Rev 78:81–95
28. Cammarata RC (1997) Mater Sci Eng A237:180–184
29. Ibach H (1997) Surf Sci Rep 29:193–263

Chapter 2
Elements of the Thermodynamic Theory of Electrified Interfaces

2.1 Introduction

Despite the advent of surface-sensitive techniques, thermodynamic measurements remain a valuable tool for the investigation of surfaces and interfaces. Electrodes are, in fact, capillary systems because the interactions between the different phases take place via the surface region. Thus, the understanding of the thermodynamics of electrified interfaces is of importance to all surface scientists and electrochemists. The topic may also be of some interest to the general reader because thermodynamics relates quantities that can be measured directly to quantities that are needed for the purposes of understanding or calculations.

The aim of this chapter is to present a simple and concise treatment of electrified interfaces within the framework of classical thermodynamics. More detailed discussions can be found in several excellent reviews and research papers [1–15].

2.2 Basic Concepts and Notions

The plane ideally marking the boundary between two phases is called the interface. Although interfaces are always dealt with from a thermodynamic point of view, if attention is actually focused on only one of the two phases, the plane ideally marking the boundary between the phase and the environment is called the surface of the phase.

The region between two phases where the properties vary between those in the bulk is the "interfacial or interface region." It is sometimes regarded as a distinct—though not autonomous—phase and is called the interphase.

A surface does not exist in isolation. It is the interface region in a two-phase system and valid thermodynamic conclusions can only be drawn by considering the system, namely, the interface and the two bordering regions, as a whole. Provided that the radius of curvature is large, the interface/interphase may be regarded as

G.G. Láng and C.A. Barbero, *Laser Techniques for the Study of Electrode Processes*, Monographs in Electrochemistry, DOI 10.1007/978-3-642-27651-4_2,

plane and its energy then differs from that of a bulk phase by a term expressing the contribution of changes of energy due to a change of the area of contact. Edge effects can be eliminated by considering a section of an interface in a larger system. There is no clear boundary between the interfacial region and the bulk of the phases so that the thickness of the interphase depends on the model chosen to describe this region.

With few exceptions, solid surfaces are not flat. The geometric area, as represented by the product of the length and breadth of a rectangle enclosing part of a surface, is not the same as the actual surface area which takes into account the areas of the hills and valleys within the rectangle. If the surface is very rough, with very pronounced and irregular asperities, the geometric area is considerably smaller than the actual area. (Such a surface is unlikely to be in a state of equilibrium and caution should be exercised when considering systems containing such surfaces.) The properties of a portion of surface are dependent on orientation, and if there are many portions of different orientation, correct summation over the whole surface may be a difficult task. Consideration will be restricted here to systems in which the difference between geometric and actual areas is not of overriding importance. (This complication is not always dealt with in standard texts because they tend to concentrate on the surface thermodynamics of liquid systems which usually possess smooth surfaces.)

Usually, the thickness of the interface or local values of physical quantities (parameters) cannot be measured. That is the reason why integrated quantities (which are accessible experimentally, or can be calculated from experimental data) are used for the thermodynamic characterization of interfaces.

Generally, these quantities are given by the expression

$$\Psi^{\sigma} = \int_{\alpha\alpha}^{\beta\beta} \Xi(\xi)\mathrm{d}\xi, \tag{2.1}$$

where Ξ is the local value of any physical quantity in the interfacial region, ξ is the coordinate perpendicular to the plane of the interface, Ψ^{σ} is the integrated quantity, and $\alpha\alpha$ and $\beta\beta$ are the two adjacent phases.

2.3 Gibbs and Guggenheim Model of the Interface

Many properties of a system, for example, concentration of a particular species, vary as a function of the distance perpendicular to the surface, as shown in Fig. 2.1a.

There are two approaches to describing the thermodynamic properties of interfaces.

The first, the classical Gibbs approach, is based on a model in which a real interface layer is replaced by a dividing surface [16]. Gibbs found it mathematically convenient to consider an idealized system depicted in Fig. 2.1b, with properties identical with those of the whole real system. The "surface of discontinuity" or "dividing surface" in the idealized system is a two-dimensional region whose position is determined by the requirements that the property under consideration should maintain a uniform value in each bulk phase right up to the dividing surface. This corresponds to equating the two shaded areas in Fig. 2.1b. A disadvantage of

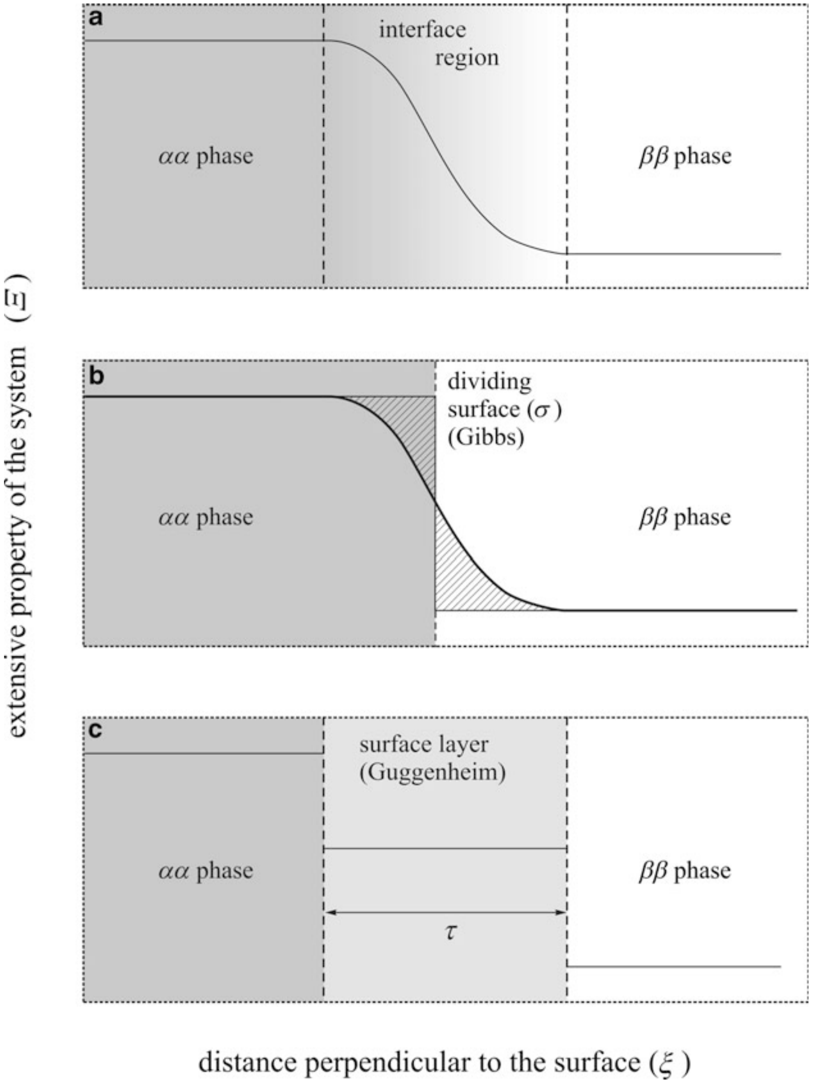

Fig. 2.1 (**a**) The real interface. (**b**) The Gibbs model of the interface. (**c**) The Guggenheim model of the interface ("interphase")

this approach is that the position of the dividing surface alters according to the property considered. This is of particular importance when considering adsorption.

An alternative approach is that of Guggenheim in which the surface is considered as a region possessing thickness (and volume), the boundaries of which lie at the positions where the actual bulk phase properties cease to be uniform (Fig. 2.1c).

In this approach, two dividing surfaces, one at each boundary, are employed. A disadvantage is that terms dependent on surface volume are present in the equations, but it is difficult to assign values to these terms.

Given a system, subsystems consisting of a segment of the interface and finite volumes of the adjacent phases can be selected. In principle, these subsystems should not be geometrically regular in shape; however, the rectangular parallelepiped-shaped domain is usually the most expedient selection. In two dimensions, the macroscopic subsystem selected for investigation is represented by the WXYZ rectangle (Fig. 2.2). It may be expedient to be more explicit and to define a surface or interfacial layer of finite thickness (τ) bounded by two appropriately chosen surfaces parallel to the phase boundary, one in each of the adjacent homogeneous bulk phases. A layer of this kind is sometimes called a Guggenheim layer. (For very highly curved surfaces (radii of curvature of the same magnitude as τ), the notion of a surface layer may lose its usefulness.)

Let the area of the surface or interface in the system, defined according to the above concepts, be denoted by A and the internal energy by U. The V volume of the system is the sum of the volumes of the two phases $\alpha\alpha$ and $\beta\beta$, and the volume of the inhomogeneous region:

$$V = V^{\alpha\alpha} + V^{\beta\beta} + V^{\text{inh}}. \tag{2.2}$$

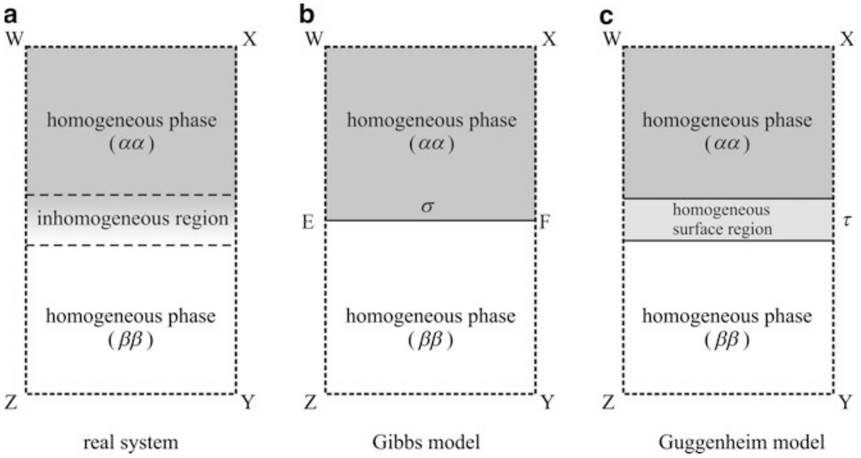

Fig. 2.2 The macroscopic subsystem selected for investigation, the Gibbs model, and the Guggenheim model

The internal energy can be given as follows:

$$U = U^{\alpha\alpha} + U^{\beta\beta} + U^{\text{inh}}. \tag{2.3}$$

Of course, this division is completely arbitrary since the values on the right-hand sides of Eqs. (2.2) and (2.3) depend on the (arbitrary) choice of the dividing surface(s). In the Guggenheim model, the V^{σ} volume of the interfacial layer is

$$V^{\sigma} = \tau A. \tag{2.4}$$

The Gibbs dividing surface (or Gibbs surface) is a geometrical surface chosen parallel to the interface and used to define the volumes of the bulk phases. That is,

$$V = V^{\alpha\alpha} + V^{\beta\beta}. \tag{2.5}$$

This means that the volume of the s surface phase is $V^{\sigma} \equiv 0$.

2.4 Adsorption

A quantitative measure of adsorption may be, and usually is, based on the following general definition: Adsorption of one or more of the components, at one or more of the phase boundaries of a multicomponent, multiphase system, is said to occur if the concentrations in the interfacial layers are different from those in the adjoining bulk phases. Consequently, the overall stoichiometry of the system deviates from that corresponding to a reference system of homogeneous bulk phases whose volumes and/or amounts are defined by suitably chosen dividing surfaces or by a suitable algebraic method.

In the Gibbs method, to treat the thermodynamics of surfaces, the interface is regarded as a mathematical dividing surface. Thus, the Gibbs interface is a two-dimensional homogeneous phase without thickness. In Guggenheim's approach, the interface is considered to be a surface phase with finite thickness and volume treated in a way analogous to bulk phases, except that the thermodynamic equations contain terms related to the contributions of changes of energy due to changes of area and electrical state of the interface.

The two apparently different approaches can be essentially characterized by the following procedure:

- There is an idealized surface or surface phase separating two homogeneous bulk phases $\alpha\alpha$ and $\beta\beta$ (see Fig. 2.3). The bulk phases are in equilibrium with the surface phase.
- Two separated reference systems α and β thought to be noninteracting homogeneous bulk phases have to be chosen—the conditions of temperature, pressure, composition, etc., being identical to those in the adsorption equilibrium. Both reference systems consist of suitably defined amounts of the components. Each of the chosen reference amounts is characterized by its respective molar or specific properties.

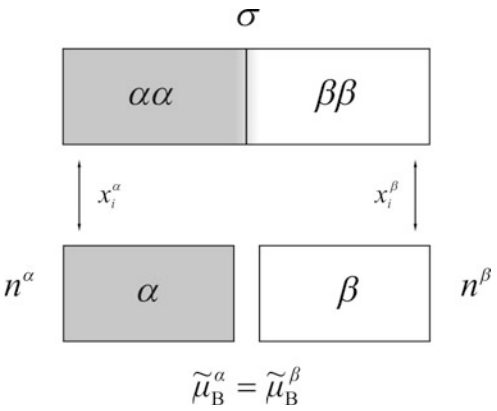

Fig. 2.3 The real system (an idealized surface or surface phase is separating two homogeneous bulk phases $\alpha\alpha$ and $\beta\beta$) and the reference systems α and β

– Any extensive property of the reference systems is simply the sum of the contributions from the reference amounts, without any contributions from interactions with the interfacial layer in the real system.

The surface excess quantities are then the respective differences between the real system and the chosen reference system.

If a Gibbs dividing surface is used for the definition of surface excesses, the reference amounts in the two reference phases are thought to be contained in and making up the volume of the actual real system but can equally well be thought to be quite independent and spatially apart one from the other. Evidently, the volume of the chosen reference amounts is not necessarily equal to the volume of the real system. It is even not necessary that the corresponding phases are effectively present in their chosen reference states within the real system. In principle, this is why the Gibbs and the Guggenheim approaches can be considered as equivalent.

However, there is a very important restriction in the Guggenheim approach replacing the condition of equivalent volumes in the Gibbs method: The reference systems must be chosen in such a manner that the remaining "surface phase" has a constant thickness. Thus, this restriction essentially affects the choice of the geometrical shape of the reference systems. However, since the reference systems are homogeneous bulk phases, their thermodynamic properties are independent of the shape. For this reason, a set of appropriate reference systems can be always selected without loss of generality. This consideration determines implicitly the selection of thermodynamic systems "with cylindrical shape" [17], with a "parallelepiped" [18], simply as a "section" of the interface cut out by perpendicular planes [19–21], etc.

The surface excess amount or Gibbs adsorption of component i is n_i^σ, which may be positive or negative, is defined as the excess of the amount of this component actually present in the system over that present in a reference system of the same volume as the real system and in which the bulk concentrations in the two phases remain uniform up to the Gibbs dividing surface:

$$n_i^\sigma = n_i - n_i^\alpha - n_i^\beta = n_i - n^\alpha x_i^\alpha - n^\beta x_i^\beta = n_i - n^\alpha x_i^{\alpha\alpha} - n^\beta x_i^{\beta\beta}, \tag{2.6}$$

where n_i is the total amount of component i in the “real” system, x_i^α and x_i^β are the mole fractions in phases $\alpha(\alpha\alpha)$ and $\beta(\beta\beta)$, respectively. n^α and n^β are the total amounts of the components (“total number of moles”) in the reference systems. It is clear from Eq. (2.6) that the surface excess amount is well defined only when n^α and n^β are fixed. It can be also seen that with different n^α and n^β values, we have different values of n_i^α.

According to the above considerations, the surface excess X^σ of any extensive property X is calculated as

$$X^\sigma = X - X^\alpha - X^\beta, \tag{2.7}$$

where X denotes the value of the property for the whole system and X^a, X^b the values for the reference systems. The internal energy U is an extensive property.

The relation that gives the internal energy as a function of the extensive parameters is a fundamental relation. If the fundamental relation of a particular system is known, all conceivable thermodynamic information about this system can be ascertained [22].

The internal energies of the reference phases are given by

$$U^\alpha = U^\alpha\left(S^\alpha, V^\alpha, n_1^\alpha \ldots n_m^\alpha\right) \tag{2.8}$$

and

$$U^\beta = U^\beta\left(S^\beta, V^\beta, n_1^\beta \ldots n_m^\beta\right). \tag{2.9}$$

The internal energy (U) of the system depends on the entropy (S), volume (V), the amounts $n_1 \ldots n_m$ of the components $1 \ldots m$, and the surface area (A), respectively:

$$U = U(S, V, A, n_1 \ldots n_m). \tag{2.10}$$

Thus, the excess of the internal energy is given by

$$U^\sigma = U - U^\alpha - U^\beta \tag{2.11}$$

and the excess of the entropy is

$$S^\sigma = S - S^\alpha - S^\beta. \tag{2.12}$$

Evidently, the excess internal energy function

$$U^\sigma = U^\sigma\left(S^\sigma, V^\sigma, A, n_1^\sigma \ldots n_m^\sigma\right), \tag{2.13}$$

is a homogeneous function of degree one with respect to all variables, if $V^\sigma \equiv 0$ (Gibbs model), or $V^\sigma = A\tau$ (Guggenheim model), since in these cases

$$U^\sigma\left(kS^\sigma, kV^\sigma, kA, kn_i^\sigma \ldots kn_m^\sigma\right) = kU^\sigma\left(S^\sigma, V^\sigma, A, n_i^\sigma \ldots n_m^\sigma\right) \tag{2.14}$$

for all $k > 0$ real numbers (see Chap. 8). In the frames of the Gibbs model,

$$U^\sigma = U^\sigma\left(S^\sigma, A, n_1^\sigma \ldots n_m^\sigma\right) \tag{2.15}$$

and

$$U^\sigma\left(kS^\sigma, kA, kn_i^\sigma \ldots kn_m^\sigma\right) = kU^\sigma\left(S^\sigma, A, n_i^\sigma \ldots n_m^\sigma\right), \tag{2.16}$$

according to Euler's theorem (Chap. 8):

$$U^\sigma = T^\sigma S^\sigma + \gamma A + \sum_i \mu_i^\sigma n_i^\sigma, \tag{2.17}$$

where γ is the intensive (interfacial) parameter conjugate to the extensive parameter A.

It should be noted that one of the most important questions in interfacial thermodynamics is related to the existence of a fundamental relation (fundamental function) of the form given in Eq. (2.13) or Eq. (2.15). If such a function exists, then every thermodynamic attribute is completely and precisely determined.

Due to the thermodynamic equilibrium,

$$T^\sigma = T^\alpha = T^\beta = T^{\alpha\alpha} = T^{\beta\beta} = T,$$

$$\mu_i^\sigma = \mu_i^\alpha = \mu_i^\beta = \mu_i^{\alpha\alpha} = \mu_i^{\beta\beta} = \mu_i$$

and so on.

Consequently, there is no need to add superscripts to T, $\mu_1 \ldots \mu_m$, because these must have values uniform throughout α, β, $\alpha\alpha$, $\beta\beta$, and σ in order that there may be thermal, hydrostatic, and physicochemical equilibrium.

In the reference phases, the following relationships are valid:

$$U^\alpha = TS^\alpha - pV^\alpha + \sum_i \mu_i n_i^\alpha \tag{2.18}$$

and

$$U^\beta = TS^\beta - pV^\beta + \sum_i \mu_i n_i^\beta. \tag{2.19}$$

According to Eqs. (2.15) and (2.17), the intensive parameter (γ) is defined by

$$\gamma = \left(\frac{\partial U^\sigma}{\partial A}\right)_{S^\sigma, n_1^\sigma \ldots n_m^\sigma}. \tag{2.20}$$

This expression is mathematically correct; however, it is not really useful for practical purposes. Equation (2.15) expresses the dependence of the energy U on the basis of independent variables S^σ, A, $n_1^\sigma \dots n_m^\sigma$. This set of independent variables is not by any means the most convenient. It is usually preferable to use T as an independent variable instead of S. If the experiment is such that the external conditions are constant temperature and constant pressure, the most convenient potential function to use is the Gibbs free energy function, G, obtained from U by two Legendre transformations (see Chap. 8). According to this,

$$G^\alpha = U^\alpha + pV^\alpha - TS^\alpha, \tag{2.21}$$

$$G^\beta = U^\beta + pV^\beta - TS^\beta. \tag{2.22}$$

Consequently,

$$G^\alpha = \sum_i \mu_i n_i^\alpha, \tag{2.23}$$

$$G^\beta = \sum_i \mu_i n_i^\beta \tag{2.24}$$

and the excess Gibbs free energy is given as

$$G^\sigma = \gamma A + \sum_i \mu_i n_i^\sigma. \tag{2.25}$$

By using the G function, γ is defined by

$$\gamma = \left(\frac{\partial G^\sigma}{\partial A}\right)_{T, n_1^\sigma \dots n_m^\sigma}. \tag{2.26}$$

Unfortunately, this new definition of γ is still not appropriate for experimental studies or to confirm experimental results since

$$G^\sigma\left(T, A, n_1^\sigma \dots n_m^\sigma\right),$$

remains ill defined and arbitrary (because $n_1^\sigma \dots n_m^\sigma$ clearly depend on the selection of the reference systems). The Gibbs free energy function for the whole system can be expressed as follows:

$$G = \gamma A + \sum_i \mu_i n_i^\alpha + \sum_i \mu_i n_i^\beta + \sum_i \mu_i n_i^\sigma = \gamma A + \sum_i \mu_i \left(n_i^\alpha + n_i^\beta + n_i^\sigma\right). \tag{2.27}$$

This means that γ can also be defined in terms of the Gibbs free energy function of the whole system as

$$\gamma = \left(\frac{\partial G}{\partial A}\right)_{T,p,n_1\ldots n_m}, \tag{2.28}$$

or in terms of the Helmholtz (free) energy function, as

$$\gamma = \left(\frac{\partial F}{\partial A}\right)_{T,V,n_1\ldots n_m}. \tag{2.28A}$$

(The Helmholtz energy or "free energy" function is defined as the Legendre transform of the internal energy function, $F = U - TS$.)

It should be noted that since no volume term appears in Eq. (2.15), there is no distinction between the surface Helmholtz and Gibbs free energies.

According to the foregoing considerations, G^σ is a partly homogeneous function of degree one in the variables A and $n_1^\sigma \ldots n_m^\sigma$ (see Chap. 8). The expression for the total differential of G^σ is

$$\mathrm{d}G^\sigma = \left(\frac{\partial G^\sigma}{\partial T}\right)_{A,n_1^\sigma\ldots n_m^\sigma}\mathrm{d}T + \left(\frac{\partial G^\sigma}{\partial A}\right)_{T,n_1^\sigma\ldots n_m^\sigma}\mathrm{d}A + \sum_i \left(\frac{\partial G^\sigma}{\partial A}\right)_{T,A,n_{j\neq i}^\sigma}\mathrm{d}n_i^\sigma. \tag{2.29}$$

Taking into account that

$$\left(\frac{\partial G^\sigma}{\partial T}\right)_{A,n_1^\sigma\ldots n_m^\sigma} = -S^\sigma,\ \left(\frac{\partial G^\sigma}{\partial A}\right)_{T,n_1^\sigma\ldots n_m^\sigma} = \gamma,\ \text{and}\quad \left(\frac{\partial G^\sigma}{\partial A}\right)_{T,A,n_{j\neq i}^\sigma} = \mu_i,$$

Eq. (2.29) can be written as follows:

$$\mathrm{d}G^\sigma = -S^\sigma\mathrm{d}T + \gamma\mathrm{d}A + \sum_i \mu_i\mathrm{d}n_i^\sigma. \tag{2.30}$$

In order to get an expression for $\mathrm{d}G^\sigma$ from Eq. (2.25) comparable with Eqs. (2.29) and (2.30), we must differentiate G^σ "generally," that is, with respect to the same variables as in Eq. (2.25), expressed explicitly or implicitly. These are T, A, and $n_1^\sigma \ldots n_m^\sigma$. This gives

$$\mathrm{d}G^\sigma = \gamma\mathrm{d}A + A\mathrm{d}\gamma + \sum_i \mu_i\mathrm{d}n_i^\sigma + \sum_i n_i^\sigma\mathrm{d}\mu_i. \tag{2.31}$$

There are thus two (general) expressions for $\mathrm{d}G^\sigma$ [Eqs. (2.30) and (2.31)], both of which are correct. This can only be the case if

$$S^\sigma \mathrm{d}T + A\mathrm{d}\gamma + \sum_i n_i^\sigma \mathrm{d}\mu_i = 0, \qquad (2.32)$$

which is the so-called Gibbs–Duhem equation for interfaces. (A more detailed derivation of the Gibbs–Duhem equation for "partly homogeneous functions" can be found in Chap. 8.)

It should be noted that as it has been shown earlier, the existence of a relationship among the various intensive parameters is a consequence of the linear homogeneous property of the fundamental relation. This means that Eq. (2.31) is a pure mathematical consequence of the homogeneity condition.

At constant temperature,

$$-A\mathrm{d}\gamma = \sum_i n_i^\sigma \mathrm{d}\mu_i. \qquad (2.33)$$

Dividing both sides of the equation by A yields

$$-\mathrm{d}\gamma = \sum_i \frac{n_i^\sigma}{A} \mathrm{d}\mu_i = \sum_i \mathit{\Gamma}_i \mathrm{d}\mu_i, \qquad (2.34)$$

where $\mathit{\Gamma}_i$ is the surface excess concentration of species i. This expression is commonly called the Gibbs adsorption equation.

In the case of liquid/liquid interfaces, the interfacial intensive parameter can be identified with the interfacial tension. It is sometimes called specific surface energy [19, 23].

Two important points should be noted here:

1. In the case of charged species (ionic components) "electrochemical potentials" ($\tilde{\mu}_i$) may be used instead of "chemical potentials" in the corresponding equations.
2. It follows from the definition equation [Eq. (2.6)] that the $\mathit{\Gamma}_i$ values are uncertain since they depend on the arbitrary selection of n^α and n^β.

However, when examining the thermodynamic properties of interfaces, it is important to find measurable quantities that do not depend on the size of the reference phases. For this purpose, the following procedure can be used:

At constant temperature and pressure, the Gibbs–Duhem relationships for the two reference bulk phases are:

$$\sum_i x_i^\alpha \mathrm{d}\mu_i = 0 \qquad (2.35)$$

and

$$\sum_i x_i^\beta \mathrm{d}\mu_i = 0. \qquad (2.36)$$

Using Eqs. (2.35) and (2.36), it is possible to express $\mathrm{d}\mu_1$ and $\mathrm{d}\mu_2$ (i.e., the differential changes of the chemical potentials of two selected components) as a function of the other $\mathrm{d}\mu_i$ values and the mole fractions at constant temperature and pressure

$$\mathrm{d}\mu_1 = -\frac{x_2^\alpha}{x_1^\alpha}\mathrm{d}\mu_2 - \sum_{i\neq 1,2}\frac{x_i^\alpha}{x_1^\alpha}\mathrm{d}\mu_i \tag{2.37}$$

and

$$\mathrm{d}\mu_2 = -\frac{x_1^\beta}{x_2^\beta}\mathrm{d}\mu_1 - \sum_{i\neq 1,2}\frac{x_i^\beta}{x_2^\beta}\mathrm{d}\mu_i. \tag{2.38}$$

Solving the set of equations (2.37) and (2.38) for $\mathrm{d}\mu_1$ and $\mathrm{d}\mu_2$ and substituting the results into Eqs. (2.33) and (2.34), we obtain

$$-\,\mathrm{d}\gamma = \frac{1}{A}\sum_{i\neq 1,2}\left(n_i^\sigma + \frac{x_2^\alpha x_i^\beta - x_2^\beta x_i^\alpha}{x_1^\alpha x_2^\beta - x_2^\alpha x_1^\beta}n_1^\sigma + \frac{x_1^\beta x_i^\alpha - x_1^\alpha x_i^\beta}{x_1^\alpha x_2^\beta - x_2^\alpha x_1^\beta}n_2^\sigma\right)\mathrm{d}\mu_i, \tag{2.39}$$

or

$$-\,\mathrm{d}\gamma = \sum_{i\neq 1,2}\left(\Gamma_i + \frac{x_2^\alpha x_i^\beta - x_2^\beta x_i^\alpha}{x_1^\alpha x_2^\beta - x_2^\alpha x_1^\beta}\Gamma_1 + \frac{x_1^\beta x_i^\alpha - x_1^\alpha x_i^\beta}{x_1^\alpha x_2^\beta - x_2^\alpha x_1^\beta}\Gamma_2\right)\mathrm{d}\mu_i. \tag{2.40}$$

Since

$$\Gamma_i = \frac{1}{A}\left(n_i - n^\alpha x_i^\alpha - n^\beta x_i^\beta\right), \tag{2.41}$$

we get

$$-\,\mathrm{d}\gamma = \frac{1}{A}\sum_{i\neq 1,2}\left(n_i + n_1\frac{x_2^\alpha x_i^\beta - x_2^\beta x_i^\alpha}{x_1^\alpha x_2^\beta - x_2^\alpha x_1^\beta} + n_2\frac{x_1^\beta x_i^\alpha - x_1^\alpha x_i^\beta}{x_1^\alpha x_2^\beta - x_2^\alpha x_1^\beta}\right)\mathrm{d}\mu_i, \tag{2.42}$$

Equation (2.42) can be written in the simpler form:

$$-\,\mathrm{d}\gamma = \sum_{i\neq 1,2}\Gamma'_i\mathrm{d}\mu_i, \tag{2.43}$$

where Γ_i' denotes the (relative) surface excess of component i with respect to the two selected components. It is clear that the (relative) surface excesses does not depend any more on the selection of the reference systems (i.e., on the selection of n^α and n^β).

2.5 The Electrocapillary Equation and the Lippmann Equation

In the case of electrodes and electrolyte solutions, the expressions derived above should be modified.

The term "electrode" is used here to denote heterogeneous electrochemical systems, in which at least two phases are connected and one of them is an electronic conductor or a semiconductor, while the other is an ionic conductor, usually an electrolyte solution (see Chap. 1).

In case of an electronic conductor (metal)/electrolyte solution interface, we should take into account that the solvent of the electrolyte solution is not a component of the electronic conductor or semiconductor phase. The same may be true for other components. Let α denote an ionic conductor phase (e.g., an aqueous electrolyte solution), and let β denote the electronic conductor (or semiconductor) phase. In the aqueous electrolyte solution, component 1 (the solvent) is water (or another component which is absent from the electronic conductor/semiconductor phase). We denote the mole fraction of this component by x_v^α.

In this case

$$x_1^\alpha = x_v^\alpha$$

and

$$x_1^\beta = x_v^\beta = 0.$$

Similarly, we can select a component (constituent) of the metal phase (component 2), which is absent from the electrolyte solution, that is,

$$x_2^\beta = x_{\mathrm{M}}^\beta$$

and

$$x_2^\alpha = x_{\mathrm{M}}^\alpha = 0.$$

We can consider that in the metal phase, there is a formal electrochemical (dissociation) equilibrium between atoms of metal M_i and the corresponding cations $\mathrm{M}_i^{z_i}$ of ionic charge z_i and the electrons (i.e., we can consider these species as constituents of the metal phase). The condition of electroneutrality can be temporally relaxed, so all the extensive variables appearing in Eq. (2.43) may be treated as independent. The electron is the only component besides metal ions in a pure metal phase. Of course, in case of alloys, we have several components.

Taking into account the above considerations, Eq. (2.43) can be written as

$$-\,\mathrm{d}\gamma = \sum_{i \neq 1,2} \left(\Gamma_i - \Gamma_v \frac{x_i^{\alpha}}{x_v^{\alpha}} - \Gamma_M \frac{x_i^{\beta}}{x_{\mathrm{M}}^{\beta}} \right) \mathrm{d}\tilde{\mu}_i. \tag{2.44}$$

In case of ideally polarizable electrodes,

$$-\,\mathrm{d}\gamma = \sum \left(\Gamma_j - \Gamma_v \frac{x_j}{x_v} \right) \mathrm{d}\tilde{\mu}_j + \sum \left(\Gamma_k - \Gamma_M \frac{x_k}{x_M} \right) \mathrm{d}\tilde{\mu}_k, \tag{2.45}$$

where index j denotes components in the electrolyte solution and index k refers to components of the metal phase.

Electrocapillary measurements, like any other electrochemical measurements, require the use of a complete cell, that is, one with two electrodes. One electrode is the ideal polarized electrode; the other electrode is a reversible charge-transfer electrode. However, it is important to realize from the outset that this second electrode is not an ordinary “constant-potential” reference electrode like the saturated calomel electrode (SCE). Rather, it is simply some electrode dipping into the solution S, which is reversible (in the Nernstian sense) to one of the ions of that solution. This second electrode of the electrocapillary cell is called the indicator electrode and denoted by the symbol IN.

The particular ion of the solution to which electrode IN is reversible will be called the indicator ion.

A solution S containing c cationic species and a anionic species could be prepared in many different ways. However, for the purpose of the thermodynamic treatment, the most general electrocapillary equation can be derived if we assume that the ions of the solution are furnished by neutral binary salts. Of the $c \times a$ different binary salts that could be chosen, we shall select $c + a - 1$ binary salts in the following way: If the indicator electrode IN is reversible to cation j', we arbitrarily select an anion, say k'. If the indicator electrode is reversible to anion k', we arbitrarily select a cation, say j'. In either case, we have selected a binary salt containing ions j' and k'. We call this salt the indicator salt. The electrolyte solution is then considered to have been made up by dissolving $c + a - 2$ additional binary salts of which $c - 1$ have anion k' in common with the indicator salt; the remaining $a - 1$ salts have cation j' in common with the indicator salt.

Thus, the Gibbs adsorption equation for an ideally polarizable electrode and for the cation-reversible indicator electrode at constant temperature T and pressure p can be given in the following form [3, 24]:

$$\begin{aligned} \mathrm{d}\gamma = & -q_{\mathrm{M}}\mathrm{d}E_{+} - \sum_{i \neq i'} \Gamma_{ii'}\mathrm{d}\mu_i - \sum_{j \neq j'} \frac{\Gamma_{jh'}}{\nu^{+}_{jk'}}\mathrm{d}\mu_{jk'} - \sum_{k \neq k'} \frac{\Gamma_{kh'}}{\nu^{-}_{j'k}}\mathrm{d}\mu_{j'k} \\ & - \sum_{h \neq h'} \Gamma_{hh'}\mathrm{d}\mu_h - \left[\left(\frac{\Gamma_{k'h'}}{\nu^{-}_{j'k'}} \right) - \left(\frac{1}{|z_{k'}|\nu^{-}_{j'k'}} \right) \sum_{j \neq j'} \Gamma_{jh'} z_j \right] \mathrm{d}\mu_{j'k'}, \end{aligned} \tag{2.46}$$

where q_{M} is the charge density on the metal side of the interface, subscript i indicates the components (metals) in the metallic phase (a single phase alloy), subscript h designates the neutral molecular species in the solution, γ is the interfacial intensive parameter, the z's are the ionic charges, the Γ and μ values are the surface excesses and chemical potentials of the various components, respectively, and the ν's indicate the number of moles of cations (or anions) per formula weight of the salt.

This equation or more generally, the equation

$$\begin{aligned} \mathrm{d}\gamma = & -s^{\sigma}\mathrm{d}T - q_{\mathrm{M}}\mathrm{d}E_{+} - \sum_{i \neq i'} \Gamma_{ii'}\mathrm{d}\mu_i - \sum_{j \neq j'} \frac{\Gamma_{jh'}}{\nu^{+}_{jk'}}\mathrm{d}\mu_{jk'} - \sum_{k \neq k'} \frac{\Gamma_{kh'}}{\nu^{-}_{j'k}}\mathrm{d}\mu_{j'k} \\ & - \sum_{h \neq h'} \Gamma_{hh'}\mathrm{d}\mu_h - \left[\left(\frac{\Gamma_{k'h'}}{\nu^{-}_{j'k'}} \right) - \left(\frac{1}{|z_{k'}|\nu^{-}_{j'k'}} \right) \sum_{j \neq j'} \Gamma_{jh'} z_j \right] \mathrm{d}\mu_{j'k'}, \end{aligned} \tag{2.47}$$

is called the "electrocapillary equation." Equation (2.46) can be written in a somewhat simpler form [25]; however, all these results show that even in the case of a very simple system, the Gibbs adsorption equation could take various forms depending on the choice of independent components, the indicator electrolyte, and the indicator ion, and it cannot be given in a simple generalized form as done, e.g., in [26].

From Eq. (2.46),

$$-\left(\frac{\partial \gamma}{\partial E} \right)_{p,T,\mu_j,\mu_k} = q_{\mathrm{M}}, \tag{2.48}$$

where

$$q_{\mathrm{M}} = F \sum_j z_j \Gamma_j = -F \sum_k z_k \Gamma_k. \tag{2.49}$$

Equation (2.48) is usually called the Lippmann equation. The Lippmann equation and the electrocapillary equation are strictly valid for liquid/liquid interfaces.

However, at least in principle, they do not apply to “solid electrodes” under elastic strain.

An illustrative example will serve to highlight the differences between the two cases.

2.5.1 Example for the Application of the Electrocapillary Equation

The phase α is supposed to be an electrolyte with cations K^+ and anions A^- in a not-dissociated solvent L. The phase p is a pure liquid metal thought to dissociate into metal ions M^+ and electrons e^-. The amounts of a component i in the two bulk phases and in the interphase are n^α, n^β, and n_i^σ, respectively. The total differential of the internal energy of the plane interface is

$$\mathrm{d}U^\sigma = T\mathrm{d}S^\sigma + \gamma\mathrm{d}A + \sum_i \tilde{\mu}_i^\sigma \mathrm{d}n_i^\sigma, \tag{2.50}$$

with the intensive interfacial parameter γ. The Gibbs–Duhem equation can be written as

$$S^\sigma\mathrm{d}T + A\mathrm{d}\gamma + \sum_i n_i^\sigma \mathrm{d}\tilde{\mu}_i^\sigma = 0. \tag{2.51}$$

Electroneutrality in the whole system corresponds to

$$n_{\mathrm{K}^+} - n_{\mathrm{A}^-} + n_{\mathrm{M}^+} - n_{e^-} = 0 \tag{2.51}$$

and electroneutrality in the bulk phases to

$$x_{\mathrm{K}^+}^\alpha = x_{\mathrm{A}^-}^\alpha, \tag{2.52}$$

$$x_{\mathrm{M}^+}^\beta = x_{e^-}^\beta. \tag{2.53}$$

The following material balances yield the excess amounts in the interface:

$$n_{\mathrm{K}^+}^\sigma = n_{\mathrm{K}^+} - x_{\mathrm{K}^+}^\alpha n_{\mathrm{K}^+}^\alpha, \tag{2.54}$$

$$n_{\mathrm{A}^-}^\sigma = n_{\mathrm{A}^-} - x_{\mathrm{A}^-}^\alpha n_{\mathrm{A}^-}^\alpha, \tag{2.55}$$

$$n_{\mathrm{M}^+}^\sigma = n_{\mathrm{M}^+} - x_{\mathrm{M}^+}^\beta n_{\mathrm{M}^+}^\beta, \tag{2.56}$$

$$n_{e^-}^\sigma = n_{e^-} - x_{e^-}^\beta n_{e^-}^\beta, \tag{2.57}$$

$$n_{\mathrm{L}}^{\sigma} = n_{\mathrm{L}} - x_{\mathrm{L}}^{\alpha} n_{\mathrm{L}}^{\alpha}. \tag{2.58}$$

The Gibbs adsorption equation at constant T is

$$A\mathrm{d}\gamma + n_{\mathrm{K}^+}^{\sigma}\mathrm{d}\tilde{\mu}_{\mathrm{K}^+}^{\sigma} + n_{\mathrm{A}^-}^{\sigma}\mathrm{d}\tilde{\mu}_{\mathrm{A}^-}^{\sigma} + n_{\mathrm{L}}^{\sigma}\mathrm{d}\mu_{\mathrm{L}}^{\sigma} + n_{\mathrm{M}^+}^{\sigma}\mathrm{d}\tilde{\mu}_{\mathrm{M}^+}^{\sigma} + n_{e^-}^{\sigma}\mathrm{d}\tilde{\mu}_{e^-}^{\sigma} = 0. \tag{2.59}$$

In chemical equilibrium, the electrochemical potentials

$$\tilde{\mu}_{\iota}^{\chi} = \mu_{\iota}^{\chi} + zF\varphi^{\chi}.$$

of the particles with the charges $z = \pm 1$ are all the same in all phases (F is the Faraday constant, the superscript indicates the corresponding phase):

$$\tilde{\mu}_{\mathrm{K}^+} = \tilde{\mu}_{\mathrm{K}^+}^{\sigma} = \tilde{\mu}_{\mathrm{K}^+}^{\alpha} = \mu_{\mathrm{K}^+}^{\alpha} + F\varphi^{\alpha}, \tag{2.60}$$

$$\tilde{\mu}_{\mathrm{A}^-} = \tilde{\mu}_{\mathrm{A}^-}^{\sigma} = \tilde{\mu}_{\mathrm{A}^-}^{\alpha} = \mu_{\mathrm{A}^-}^{\alpha} - F\varphi^{\alpha}, \tag{2.61}$$

$$\mu_{\mathrm{L}} = \mu_{\mathrm{L}}^{\sigma} = \mu_{\mathrm{L}}^{\alpha}, \tag{2.62}$$

$$\tilde{\mu}_{\mathrm{M}^+} = \tilde{\mu}_{\mathrm{M}^+}^{\sigma} = \tilde{\mu}_{\mathrm{M}^+}^{\beta} = \mu_{\mathrm{M}^+}^{\beta} + F\varphi^{\beta}, \tag{2.63}$$

$$\tilde{\mu}_{\mathrm{e}^-} = \tilde{\mu}_{\mathrm{e}^-}^{\sigma} = \tilde{\mu}_{\mathrm{e}^-}^{\beta} = \mu_{\mathrm{e}^-}^{\beta} - F\varphi^{\beta}, \tag{2.64}$$

$$\tilde{\mu}_{\mathrm{K}^+} + \tilde{\mu}_{\mathrm{A}^-} = \mu_{\mathrm{K}^+} + \mu_{\mathrm{A}^-} = \mu_{\mathrm{KA}} = \mu_{\mathrm{KA}}^{\sigma}, \tag{2.65}$$

The Gibbs–Duhem equations for the bulk phases at constant T and p are

$$n_{\mathrm{K}^+}^{\alpha}\mathrm{d}\tilde{\mu}_{\mathrm{K}^+}^{\alpha} + n_{\mathrm{A}^-}^{\alpha}\mathrm{d}\tilde{\mu}_{\mathrm{A}^-}^{\alpha} + n_{\mathrm{L}}^{\alpha}\mathrm{d}\mu_{\mathrm{L}}^{\alpha} = 0, \tag{2.66}$$

$$n_{\mathrm{M}^+}^{\beta}\mathrm{d}\tilde{\mu}_{\mathrm{M}^+}^{\beta} + n_{\mathrm{e}^-}^{\beta}\mathrm{d}\tilde{\mu}_{\mathrm{e}^-}^{\beta} = 0. \tag{2.67}$$

From Eqs. (2.51) to (2.67), one obtains

$$-\mathrm{d}\gamma = \frac{1}{A}\left[\left(n_{\mathrm{K}^+} - \frac{x_{\mathrm{K}^+}^{\alpha}}{x_{\mathrm{L}}^{\alpha}} n_{\mathrm{L}}\right)\mathrm{d}\mu_{\mathrm{KA}} + (n_{\mathrm{K}^+} - n_{\mathrm{A}^-})\mathrm{d}\tilde{\mu}_{\mathrm{e}^-}^{\beta} + F\mathrm{d}\left(\varphi^{\alpha} - \varphi^{\beta}\right)\right]. \tag{2.68}$$

The change in the potential difference between the two phases can only be measured in an electrochemical cell containing a reference electrode. If the reference electrode is reversible with respect to the anion A^-, the change in the (measurable) electrode potential can be expressed as

$$\mathrm{d}E = \frac{1}{F}\left(\mathrm{d}\mu_{\mathrm{A}^-}^{\alpha} - \mathrm{d}\mu_{\mathrm{e}^-}^{\beta}\right) - \mathrm{d}\left(\varphi^{\alpha} - \varphi^{\beta}\right). \tag{2.69}$$

With Eqs. (2.68) and (2.69), we obtain

$$-\mathrm{d}\gamma = \frac{1}{A}\left[\left(n_{\mathrm{K}^+} - \frac{x^{\alpha}_{\mathrm{K}^+}}{x^{\alpha}_{\mathrm{L}}} n_{\mathrm{L}}\right)\mathrm{d}\mu_{\mathrm{KA}} + F(n_{\mathrm{A}^-} - n_{\mathrm{K}+})\mathrm{d}E\right] = \Gamma'_{\mathrm{K}^+}\mathrm{d}\mu_{\mathrm{KA}} + q_{\mathrm{M}}\mathrm{d}E, \tag{2.70}$$

with the relative surface excess of the cation on the solution side and the surface charge q_{M} on the metal side. The classical Lippmann equation follows from Eq. (2.70):

$$-\left(\frac{\partial\gamma}{\partial E}\right)_{T,p,\mu_{\mathrm{KA}}} = q_{\mathrm{M}}. \tag{2.71}$$

2.5.2 The Ideally Polarizable Electrode when There Is no Complete Equilibrium Established Between the Bulk of a Solid and the Interface

The charging of an interface/interphase results in a certain movement of the atoms in the interfacial region and an exchange of material between the interfacial region and the bulk. In case of a plane interface, equilibrium is attained if the temperature, pressure, and the chemical potentials of all components are equal in the whole system. The transport of material is relatively fast in a liquid. However, in a real solid, the movement of material is usually very slow. Adsorption may change the specific surface energy of different crystal faces in a different way requiring adjustment of the equilibrium shape with a corresponding stress distribution. The nonequilibrium stresses change the chemical potential of the metal [7, 27].

In an ideal solid phase which is free of vacancies and interstitials, there is no transport of the "immobile" components or constituents (atoms or ions), but electrons may be mobile. Nevertheless, the interfacial region can be in equilibrium with the adjacent fluid phase [17, 23]. However, the chemical potentials of the immobile components (or constituents) in the interfacial region can differ from those in the bulk solid, i.e., although mechanical equilibrium is maintained, chemical equilibrium cannot be established between the bulk and the interfacial region.

This means that Eq. (2.63) is not valid, and

$$\tilde{\mu}^{\sigma}_{\mathrm{M}^+} \neq \tilde{\mu}^{\beta}_{\mathrm{M}^+}. \tag{2.72}$$

Instead of Eq. (2.70), one obtains

$$\begin{aligned}-\mathrm{d}\gamma^{\mathrm{s}} =& \frac{1}{A}\left[\left(n_{\mathrm{K}^+} - \frac{x^{\alpha}_{\mathrm{K}^+}}{x^{\alpha}_{\mathrm{L}}} n_{\mathrm{L}}\right)\mathrm{d}\mu_{\mathrm{KA}} + \left(n_{\mathrm{M}^+} - x^{\beta}_{\mathrm{M}^+} n^{\beta}_{\mathrm{M}^+}\right)\left(\mathrm{d}\tilde{\mu}^{\sigma}_{\mathrm{M}^+} + \mathrm{d}\tilde{\mu}_{\mathrm{e}^-}\right)\right] \\ &+ \frac{1}{A}F(n_{\mathrm{A}^-} - n_{\mathrm{K}+})\mathrm{d}E = \mathit{\Gamma}'_{\mathrm{K}^+}\mathrm{d}\mu_{\mathrm{KA}} + \mathit{\Gamma}_{\mathrm{M}^+}\left(\mathrm{d}\tilde{\mu}^{\sigma}_{\mathrm{M}^+} + \mathrm{d}\tilde{\mu}_{\mathrm{e}^-}\right) + q_{\mathrm{M}}\mathrm{d}E.\end{aligned} \tag{2.73}$$

Experimentally, one may obtain the path-dependent "specific surface energy" or "interfacial stress" γ^{s}. The chemical and the mechanical contributions to the irreversible part of the excess Gibbs free energy of the surface occur in combinations given by the equilibrium reference state and the adsorption equilibrium toward the fluid phase. According to the local equilibrium in the interfacial region,

$$\mathrm{d}\tilde{\mu}^{\sigma}_{\mathrm{M}^+} + \mathrm{d}\tilde{\mu}_{\mathrm{e}^-} = \tilde{\mu}^{\sigma}_{\mathrm{M}}, \tag{2.74}$$

thus,

$$-\,\mathrm{d}\gamma^{\mathrm{s}} = \mathit{\Gamma}'_{\mathrm{K}^+}\mathrm{d}\mu_{\mathrm{KA}} + \mathit{\Gamma}_{\mathrm{M}^+}\mathrm{d}\tilde{\mu}^{\sigma}_{\mathrm{M}} + q_{\mathrm{M}}\mathrm{d}E \tag{2.75}$$

and instead of Eq. (2.71), we get

$$-\left(\frac{\partial\gamma^{\mathrm{s}}}{\partial E}\right)_{T,p,\mu_{\mathrm{KA}}} = q_{\mathrm{M}} + \mathit{\Gamma}_{\mathrm{M}^+}\left(\frac{\partial\tilde{\mu}^{\sigma}_{\mathrm{M}}}{\partial E}\right)_{T,p,\mu_{\mathrm{KA}}} = q_{\mathrm{M}} + q^{\mathrm{s}}. \tag{2.76}$$

Thus, for a solid electrode, there is an additional contribution to the equilibrium superficial charge. This quantity is connected with the deviation from the equilibrium between the interfacial region and the bulk of the solid; however, its value depends on the selection of the reference system. On the other hand, in case of a real solid containing a high concentration of point defects, the additional charge and the corresponding nonequilibrium specific surface energy (interfacial stress) may be time dependent on a long time scale.

2.5.3 Additional Remarks

Concerning the variables of the fundamental relation (function), the question may arise whether the area of the interface (A) is an appropriate state variable or not. There are two limiting cases (models) for which the answer seems obvious (we limit ourselves to isotropic conditions for simplicity): (1) All constituents are mobile in the adjacent phases. (2) The solid phase is ideally elastic.

In the first case, there is no thermodynamic difference between a liquid/liquid and a solid/liquid interface. On the other hand, the area of the interface and the other thermodynamic variables unequivocally determine the surface state of an isotropic ideally elastic solid. However, in conventional measurements of interfacial stress changes of solid electrodes, the deformation practically always remains within the elastic limit. Consequently, *A* can reasonably be considered as an independent thermodynamic variable.

References

1. Koenig FO (1934) J Phys Chem 38:111–128
2. Koenig FO (1934) J Phys Chem 38:339–363
3. Guggenheim EA, Adam NK (1933) Proc Roy Soc London 139:218–236
4. Grahame DC, Whitney RB (1942) J Am Chem Soc 64:1548–1552
5. Graham DC (1947) Chem Rev 41:441–501
6. Mohilner DM (1962) J Phys Chem 66:724–726
7. Defay R, Prigigine I, Bellemans A, Everett DH (1966) Surface tension and adsorption. Longmans, Bristol
8. Soffer A (1972) J Electroanal Chem 40:153–165
9. Mohilner DM (1966) The electrical double layer. In: Bard AJ (ed) Electroanalytical chemistry, vol 1. Marcel-Dekker, New York
10. Parsons R (1984) Thermodynamic methods for the study of interfacial regions in electrochemical systems. In: Bockris JO'M, Conway BE, Yeager E (eds) Comprehensive treatise of electrochemistry, Vol. 1, The double layer. Plenum, New York
11. Girault HHJ, Schiffrin DJ (1989) Electrochemistry of liquid\liquid interfaces. In: Bard AJ (ed) Electroanalytical chemistry, vol 15. Marcel Dekker, New York
12. Hansen RS (1962) J Phys Chem 66:410–415
13. Goodrich FC (1968) Trans Farad Soc 64:3403–3415
14. Everett DH (1987) Pure Appl Chem 59:45–52
15. Damaskin BB, Petrii OA (2011) J Solid State Electrochem 15:1317–1334
16. Gibbs JW (1873–1897, reprinted in 1961) The scientific papers of J. Willard Gibbs. Dover, New York
17. Eriksson JC (1969) Surf Sci 14:221–246
18. Eriksson JC (1965) Ark Kemi 25:331–341
19. Linford RG (1978) Chem Rev 78(1978):81–95
20. Randles JEB, Behr B (1972) J Electroanal Chem 35:389–404
21. Guggenheim EA (1940) Trans Farad Soc 36:397–412
22. Callen H (1985) Thermodynamics and an introduction to thermostatistics, 2nd edn. Wiley, New York
23. Láng G, Heusler KE (1994) J Electroanal Chem 377:1–7
24. Láng G, Seo M, Horányi G (2000) ACH-Models Chem 137:121–132
25. Plieth EJ (1970) J Electroanal Chem 27:468–471
26. Trasatti S, Parsons R (1986) Pure Appl Chem 58:437–454
27. Schmalzried H, Navrotsky A (1975) Festkörperthermodynamik. Verlag Chemie, Weinheim

Chapter 3
Some Problems Related to the Surface Thermodynamics of “Solid Electrodes”

3.1 The “Generalized Lippmann Equation”

In contrast to the expressions presented in Chap. 2, a “generalized” Lippmann equation held to be valid generally for solid electrodes was published in an IUPAC recommendation [1]:

$$(\partial\gamma^{\pi}/\partial E)_{T,p,\mu_i,\ldots} = -q_{\mathrm{M}} - (\gamma^{\pi} - \sigma)(\partial\varepsilon_{\mathrm{e}}/\partial E)_{T,p,\mu_i,\ldots}. \tag{3.1}$$

In Eq. (3.1), γ^{π} is the “superficial work”; σ is the surface stress; q_{M}, the charge density on the metal side of the electrode; p, the pressure; T, the temperature; μ_i, the chemical potential of the component i; ε_{e}, the elastic strain; and E, the electrode potential. According to [1], in the more general case (i.e., if one of the phases is an anisotropic solid), σ is a tensor. Although the mathematical derivation (and hence the validity) of the “generalized” or “modified” Lippmann equation and its corollaries has been repeatedly questioned [2–5], many authors consider it to be the most general equation for electrified solid–liquid interfaces (or for solid electrodes) [6–16], etc. Equation (3.1) follows from a (modified) “Gibbs adsorption equation”:

$$0 = s^{\pi}\mathrm{d}T + \sum_i \Gamma_i^{\pi}\mathrm{d}\mu_i + q_{\mathrm{M}}\mathrm{d}E + \mathrm{d}\gamma^{\pi} + (\gamma^{\pi} - \sigma)\mathrm{d}\varepsilon_{\mathrm{e}} \tag{3.2}$$

obtained from theoretical considerations [17–24]. However, the theoretical result for the electrified solid–liquid interface (e.g., the generalized Lippmann equation) has not yet been confirmed by experimental evidence. This provides a further basis for reasonable doubts concerning its applicability.

A brief review of the derivation of the “generalized Lippmann equation” (for isotropic interfaces) is given in the next sections.

G.G. Láng and C.A. Barbero, *Laser Techniques for the Study of Electrode Processes*,
Monographs in Electrochemistry, DOI 10.1007/978-3-642-27651-4_3,

3.1.1 On the Derivation of the Generalized Lippmann Equation

In the review article [19], which formed the basis of the IUPAC recommendation [1], the author apparently did not question that U^σ is a homogeneous function of the first degree, but he simply adopted the rather confusing statement [22, 23] in that U^σ is a homogeneous function only, if the relationship is written in the integral form.

The total differential of the excess (surface) internal energy

$$U^\sigma = U^\sigma\left(S^\sigma, Q^\sigma, n_1^\sigma, \ldots, n_m^\sigma, A\right) = TS^\sigma + \sum_i \mu_i n_i^\sigma + EQ^\sigma + \gamma^\pi A \tag{3.3}$$

was given as

$$\mathrm{d}U^\sigma = T\mathrm{d}S^\sigma + \sum_i \mu_i \mathrm{d}n_i^\sigma + E\mathrm{d}Q^\sigma + \gamma^\mathrm{s}\mathrm{d}A \tag{3.4}$$

with the “surface intensive parameter” γ^s. The charge of the whole system (Q) and the excess charge (Q^σ) have been considered as independent variables. The other variables in Eqs. (3.3) and (3.4) are the excess entropy S^σ, the area of the interface A, and the excess amounts $n_1^\sigma \ldots n_m^\sigma$, respectively.

A “surface Gibbs−Duhem relation” was obtained from differentiation of Eq. (3.3) and subtraction of Eq. (3.4) in the form:

$$0 = S^\sigma \mathrm{d}T + \sum_i n_i^\sigma \mathrm{d}\mu_i + Q^\sigma \mathrm{d}E + \gamma^\pi \mathrm{d}A + A\mathrm{d}\gamma^\pi - \gamma^\mathrm{s}\mathrm{d}A. \tag{3.5}$$

It should be noted here that Eq. (3.5) which is called the “Gibbs−Duhem equation” in [19] cannot, in fact, bear this name, since it contains differentials of the extensive parameter A. This is inconsistent with classical thermodynamics stating that the Gibbs−Duhem equation presents the relationship between the intensive parameters in the differential form [25] (see also Chap. 8). The presence of an extensive variable in a “Gibbs−Duhem relation” is of itself an indication of conceptual and mathematical inconsistencies in the derivation of the final expression.

After division by A,

$$0 = s^\sigma \mathrm{d}T + \sum_i \Gamma_i^\sigma \mathrm{d}\mu_i + q^\sigma \mathrm{d}E + \gamma^\pi \frac{\mathrm{d}A}{A} + \mathrm{d}\gamma^\pi - \gamma^\mathrm{s} \frac{\mathrm{d}A}{A} \tag{3.6}$$

and

$$\mathrm{d}A/A = \mathrm{d}\varepsilon_\mathrm{tot} \tag{3.7}$$

(where $\mathrm{d}\varepsilon_\mathrm{tot}$ is the total area strain) yielded

$$0 = s^{\sigma}\mathrm{d}T + \sum_i \Gamma_i^{\sigma}\mathrm{d}\mu_i + q^{\sigma}\mathrm{d}E + \gamma^{\pi}\frac{\mathrm{d}A}{A} + \mathrm{d}\gamma^{\pi} - \gamma^{\mathrm{s}}\frac{\mathrm{d}A}{A} \tag{3.8}$$

or

$$0 = s^{\sigma}\mathrm{d}T + \sum_i \Gamma_i\mathrm{d}\mu_i + q^{\sigma}\mathrm{d}E + \gamma^{\pi}\mathrm{d}\varepsilon_{\mathrm{tot}} + \mathrm{d}\gamma^{\pi} - \gamma^{\mathrm{s}}\mathrm{d}\varepsilon_{\mathrm{tot}}, \tag{3.9}$$

where the superficial charge has been defined by

$$q^{\sigma} = \frac{Q - Q^{\alpha} - Q^{\beta}}{A}. \tag{3.10}$$

The total strain has been divided into two contributions, the “plastic strain” $\mathrm{d}\varepsilon_{\mathrm{p}}$ and elastic strain $\mathrm{d}\varepsilon_{\mathrm{e}}$ so that

$$\mathrm{d}\varepsilon_{\mathrm{tot}} = \mathrm{d}\varepsilon_{\mathrm{p}} + \mathrm{d}\varepsilon_{\mathrm{e}}. \tag{3.11}$$

The generalized surface intensive parameter γ^{s} has been formally defined in terms of the “superficial work”, γ^{π}, and the surface stress, σ, by the equation

$$\gamma^{\mathrm{s}} = \frac{\mathrm{d}\varepsilon_{\mathrm{p}}}{\mathrm{d}\varepsilon_{\mathrm{tot}}}\gamma^{\pi} + \frac{\mathrm{d}\varepsilon_{\mathrm{e}}}{\mathrm{d}\varepsilon_{\mathrm{tot}}}\sigma, \tag{3.12}$$

where $\mathrm{d}\varepsilon_{\mathrm{p}}$ and $\mathrm{d}\varepsilon_{\mathrm{e}}$ are the “plastic” and “elastic” contributions to the total strain $\mathrm{d}\varepsilon_{\mathrm{tot}}$.

Equations (3.9), (3.11), and (3.12) were used to obtain Eq. (3.13):

$$0 = s^{\sigma}\mathrm{d}T + \sum_i \Gamma_i\mathrm{d}\mu_i + q^{\sigma}\mathrm{d}E + \mathrm{d}\gamma^{\pi} + (\gamma^{\pi} - \sigma)\mathrm{d}\varepsilon_{\mathrm{e}} \tag{3.13}$$

or

$$-\mathrm{d}\gamma^{\pi} = s^{\sigma}\mathrm{d}T + \sum_i \Gamma_i\mathrm{d}\mu_i + q^{\sigma}\mathrm{d}E + (\gamma^{\pi} - \sigma)\mathrm{d}\varepsilon_{\mathrm{e}}. \tag{3.14}$$

According to the author of [19] Eq. (3.13) “*is a most versatile form of the Gibbs–Duhem equation for a surface, from which three major thermodynamic equations, namely the Shuttleworth equation, the Gibbs adsorption equation and the Lippmann equation may be immediately obtained.*

The most conventional form of the Lippmann equation involves the quantity

$$(\partial\gamma^{\pi}/\partial E)_{T,\mu_i,\varepsilon_{\mathrm{e}}},$$

which is related to q^σ *by*

$$(\partial\gamma^\pi/\partial E)_{T,\mu_i} = -q^\sigma - (\gamma^\pi - \sigma)(\partial\varepsilon_\mathrm{e}/\partial E)_{T,\mu_i}. \tag{3.15}$$

The magnitude of the second term is highly uncertain, in view of the difficulty of obtaining unambiguous values of σ *and also* $(\partial\varepsilon_\mathrm{e}/\partial \mathrm{E})_{T,\mu_i}$.”

In order to examine the validity of the above statements, we will concentrate on the mathematical details of the derivation of Eq. 3.13. Special attention will be given to the mathematical consequences of the homogeneous property of the fundamental equation.

It is clear from Eq. 3.3 that the function

$$U^\sigma\left(S^\sigma, Q^\sigma, n_1^\sigma, \ldots, n_m^\sigma, A\right) = TS^\sigma + EQ^\sigma + \sum_i \mu_i n_i^\sigma + \gamma^\pi A$$

is a homogeneous function of the first degree with respect to the extensive variables since for any real number $k > 0$

$$U^\sigma\left(kS^\sigma, kQ^\sigma, kn_1^\sigma, \ldots, kn_m^\sigma, kA\right) = kU^\sigma\left(S^\sigma, Q^\sigma, n_1^\sigma, \ldots, n_m^\sigma, A\right). \tag{3.16}$$

According to Euler’s theorem (see Chap. 8),

$$\begin{aligned} U^\sigma = {} & \left(\frac{\partial U^\sigma}{\partial S^\sigma}\right)_{n^\sigma_{1,\ldots,m}, Q^\sigma, A} S^\sigma + \sum_i^m \left(\frac{\partial U^\sigma}{\partial n_i^\sigma}\right)_{S^\sigma, n^\sigma_{1,\ldots,i\neq j,\ldots m}, Q^\sigma, A} n_i^\sigma \\ & + \left(\frac{\partial U^\sigma}{\partial Q^\sigma}\right)_{S^\sigma, n^\sigma_{1,\ldots,m}, A} Q^\sigma + \left(\frac{\partial U^\sigma}{\partial A}\right)_{S^\sigma, n^\sigma_{1,\ldots,m}, Q^\sigma} A. \end{aligned} \tag{3.17}$$

The total differential of the fundamental equation is

$$\begin{aligned} \mathrm{d}U^\sigma = {} & \left(\frac{\partial U^\sigma}{\partial S^\sigma}\right)_{n^\sigma_{1,\ldots,m}, Q^\sigma, A} \mathrm{d}S^\sigma + \sum_i^m \left(\frac{\partial U^\sigma}{\partial n_i^\sigma}\right)_{S^\sigma, n^\sigma_{1,\ldots,i\neq j,\ldots m}, Q^\sigma, A} \mathrm{d}n_i^\sigma \\ & + \left(\frac{\partial U^\sigma}{\partial Q^\sigma}\right)_{S^\sigma, n^\sigma_{1,\ldots,m}, A} \mathrm{d}Q^\sigma + \left(\frac{\partial U^\sigma}{\partial A}\right)_{S^\sigma, n^\sigma_{1,\ldots,m}, Q^\sigma} \mathrm{d}A. \end{aligned} \tag{3.18}$$

In Eqs. (3.17) and (3.18), the partial derivatives are the same being homogeneous zero-degree functions of the extensive variables. It follows that the surface intensive parameter conjugate to the extensive variable A is

$$\gamma = \left(\frac{\partial U^\sigma}{\partial A}\right)_{S^\sigma, n^\sigma_{1,\ldots,m}, Q^\sigma}. \tag{3.19}$$

By replacing the partial derivatives with the corresponding symbols one obtains

$$U^\sigma = TS^\sigma + EQ^\sigma + \sum_i \mu_i n_i^\sigma + \gamma A \tag{3.20}$$

and

$$\mathrm{d}U^\sigma = T\mathrm{d}S^\sigma + \sum_i^m \mu_i \mathrm{d}n_i^\sigma + E\mathrm{d}Q^\sigma + \gamma \mathrm{d}A. \tag{3.21}$$

The Gibbs–Duhem relation is a mathematical consequence following directly from Eqs. (3.20) and (3.21) (see Chap. 8):

$$0 = S^\sigma \mathrm{d}T + \sum_i^m n_i^\sigma \mathrm{d}\mu_i + Q^\sigma \mathrm{d}E + A\,\mathrm{d}\gamma. \tag{3.22}$$

Since Eq. (3.4) corresponds to Eq. (3.21) and Eq. (3.3) to Eq. (3.20), one is forced to conclude that introducing two different parameters for the same variable (i.e., for the intensive parameter conjugate to A) into Eq. (3.3) and Eq. (3.4) is misleading, if not erroneous. Consequently, if $\gamma^\pi \neq \gamma^\mathrm{s}$, Eqs. (3.3) and (3.4) define different variables in the U^σ function, and Eqs. (3.5), (3.6), and (3.13)–(3.15) cannot be valid.

Most probably, the first cautious critical remarks concerning the dual approach to the specific surface energy of solid electrodes were formulated in [2]. A theoretical analysis of the fundamental relations describing the thermodynamic properties of the electrified solid–liquid interface has been published in [3]. In [8] counterarguments were brought up supporting that the surface excess of the internal energy of solid–liquid interface cannot be regarded as a homogeneous function of the first degree with respect to all extensive variables, when the surface is subjected to elastic deformation. The equation derived in [8] is analogous with equation (3.15), but it was recognized that it "*is definitely roughly approximate. In practice, however, its application to metal/electrolyte interphases is usually justified.*"

Such statements are particularly surprising since, as it has been rightly pointed out in [4], thermodynamic equations cannot be "roughly approximate," and there is no any experimental evidence for the "generalized Lippmann equation." Contrary to this view, it has been claimed [6] that the validity of the generalized Lippmann equation can be verified experimentally. Unfortunately, it remains the secret of the authors what sorts of *experiments* are appropriate to overcome *mathematical* inconsistencies in the derivation of an equation.

3.1.2 On the Derivation of the Shuttleworth Equation

According to the above considerations, the thermodynamic theory of solid–liquid interfaces cannot be accepted as proven. The situation is even more complicated if the interface is electrically charged. A recent theoretical debate on the derivation of the so-called Shuttleworth equation provides a good example of these problems.

One of the most important equations of surface science was derived by Shuttleworth in 1950 [26] for "*a large one-component crystal in equilibrium with its vapor*" *and especially* "*for an isotropic substance, or for a crystal face with a three- (or greater) fold axis of symmetry*":

$$\gamma = F + A(\mathrm{d}F/\mathrm{d}A), \tag{3.23}$$

where γ is the surface tension, A is the surface area, and F is the surface Helmholtz free energy. According to the author in this case, "*all normal components of the surface stress equal the surface tension.*" A tensorial form of the Shuttleworth equation was proposed in [27]. In [19], Eq. (3.13) was used for the derivation of a modified version of Shuttleworth's equation:

$$\sigma = \gamma^{\pi} + \left(\frac{\partial \gamma^{\pi}}{\partial \varepsilon_{\mathrm{e}}}\right)_{T,\mu_i,E}. \tag{3.24}$$

Equation (3.24) looks very like as the original Shuttleworth equation having formally the same structure and terms, but instead of the native term of the total strain, it contains the term of elastic strain.

Recently, a new approach to the thermodynamics of surface tension of solids has been introduced by Bottomley et al. [28]. The authors considered three different derivations of the Shuttleworth equation and demonstrated their incompatibility with Hermann's mathematical structure of thermodynamics [29]. Hermann's analysis implies that the conjugate to each state variable is unique, which is easy to check for well-known thermodynamic potentials and fundamental equations. In conclusion, the authors stated [28]: "*if Hermann's mathematical structure of thermodynamics is true, and if Shuttleworth's equation is a thermodynamic equation, then Shuttleworth's equation is false.*"

Discussion was continued for years, but the opponents found no compromise. For more details, we refer to the original literature [30–43].

References

1. Trasatti S, Parsons R (1986) Pure Appl Chem 58:437–454
2. Láng G, Heusler KE (1994) J Electroanal Chem 377:1–7
3. Láng G, Heusler KE (1999) J Electroanal Chem 472:168–173
4. Marichev VA (2006) Surf Sci 600:4527–4536
5. Marichev VA (2010) Adv Colloid Interface Sci 157:34–60
6. Go J-Y, Pyun S-I (2004) J Kor Electrochem Soc 7:211–219
7. Guidelli R (1998) J Electroanal Chem 453:69–77
8. Guidelli R (1999) J Electroanal Chem 472:174–177
9. Lipkowski J, Schmickler W, Kolb DM, Parsons R (1998) J Electroanal Chem 452:193–197

10. Schmickler W, Leiva E (1998) J Electroanal Chem 453:61–67
11. Valincius G (1999) J Electroanal Chem 478:40–49
12. Haiss W (2001) Rep Prog Phys 64:591–648
13. Tian F, Pei JH, Hedden DL, Brown GM, Thundat T (2004) Ultramicroscopy 100:217–223
14. Tabard-Cossa V, Godin M, Burgess IJ, Monga T, Lenox RB, Grütter P (2007) Anal Chem 79:8136–8143
15. Kramer D (2007) Phys Chem Chem Phys 10:168–177
16. Garcia-Araez N (2011) J Phys Chem C 115:501–510
17. Eriksson JC (1969) Surf Sci 14:221–246
18. Linford RG (1973) J Electroanal Chem 43:155–157
19. Linford RG (1978) Chem Rev 78:81–95
20. Couchman PR, Jesser WA, Kuhlmann-Wilsdorf D (1972) Surf Sci 33:429–436
21. Couchman PR, Jesser WA (1973) Surf Sci 34:212–224
22. Couchman PR, Everett DH, Jesser WA (1975) J Colloid Interface Sci 52:410–411
23. Couchman PR, Everett DH (1976) J Electroanal Chem 67:382–386
24. Couchman PR, Davidson CR (1977) J Electroanal Chem 85:407–409
25. Gutman EM (1995) J Phys Condens Matter 7:L663–L667
26. Shuttleworth R (1950) Proc Phys Soc A 63:444–457
27. Herring C (1953) The use of classical macroscopic concepts in surface energy problem. In: Gomer R, Smith CS (eds) Structure and properties of solid surfaces. The University of Chicago Press, Chicago
28. Bottomley DJ, Makkonen L, Kolari K (2009) Surf Sci 603:97–101
29. Hermann R (1973) Geometry, physics and systems. Marcel Dekker, New York
30. Bottomley DJ, Makkonen L, Kolari K (2009) Surf Sci 603:2347
31. Bottomley DJ, Makkonen L, Kolari K (2009) Surf Sci 603:2350–2351
32. Bottomley DJ, Makkonen L, Kolari K (2009) Surf Sci 603:2356–2357
33. Eriksson JC, Rusanov AI (2009) Surf Sci 603:2348–2349
34. Marichev VA (2009) Surf Sci 603:2345–2346
35. Ibach H (2009) Surf Sci 603:2352–2355
36. Rusanov AI, Shchekin AK, Tatyanenko DV (2009) J Chem Phys 131:161104
37. Marichev VA (2009) Colloids Surf A Physicochem Eng Asp 345:1–12
38. Bottomley DJ, Makkonen L, Kolari K (2010) Surf Sci 604:2066–2068
39. Eriksson JC, Rusanov AI (2010) Surf Sci 603:1062–1063
40. Eriksson JC, Rusanov AI (2010) Surf Sci 604:2069–2071
41. Marichev VA (2010) Prot Met 46:383–402
42. Marichev VA (2011) Prot Met 47:25–30
43. Marichev VA (2011) Colloids Surf A Physicochem Eng Asp 389:63–68

Chapter 4
Experimental Methods for the Measurement of Surface Stress Changes

4.1 Introduction

As it has been pointed out in the previous chapters, the thermodynamic theory of the electrified solid/liquid interface and the thermodynamic interpretation of the results from various methods in terms of physicochemical properties of the system are not without problems [1–21].

In principle, the results of the theoretical work can be checked experimentally; however, the study of the specific surface energies of electrified solid/liquid interfaces is complicated by many factors. The value of the "absolute surface tension" of some relatively simple covalently bonded, ionic, rare-gas, and metallic crystals could be estimated theoretically [22], and the surface tensions of some solid surfaces have been determined experimentally in some special cases [22, 23]. For the calculation of the surface stress, σ, Vermaak and coworkers [24–26] measured the radial strain in small (solid) spheres of Au, Ag, and Pt by electron diffraction and determined an average surface stress using the following equation:

$$\sigma = -\frac{3}{2}E\varepsilon r,$$

where E is the bulk modulus, ε is the radial strain, and r is the radius of the sphere, respectively. Their results are listed in Table 4.1 in order to allow easy comparison with other results in the literature.

However, the methods used in these experiments are designed for the solid/gas interface and are mostly inappropriate for use in the presence of an electrolyte solution; consequently, they cannot be applied to study the surface energetics of solid electrodes. Theoretical calculations of surface stresses generally involve calculating the surface free energy and its derivative with respect to elastic strain. Both first principles and semiempirical atomic potential calculations involving computer simulations have been attempted; however, only first-principle approaches yield accurate values for surface stress [27]. Tabulated values of the

G.G. Láng and C.A. Barbero, *Laser Techniques for the Study of Electrode Processes*,
Monographs in Electrochemistry, DOI 10.1007/978-3-642-27651-4_4,

Table 4.1 Experimental surface stress data from [24–26]

Materials	Surface stress, σ (J m^{-2})	Temperature, T (°C)
Au	1.18 + 0.20	50
Ag	1.42 + 0.30	55
Pt	2.57 + 0.40	65

surface stress and surface energy for a variety of metals, ionic solids, and semiconductors can be found in reviews [27, 28].

It is not surprising, therefore, that during the past decades, several methods were suggested for the measurements of *changes* of the interfacial stress ("interfacial tension," "surface stress," "specific surface energy," etc.) of solid electrodes (e.g., [29–70]).

According to the classification proposed by Morcos [71], attempts to determine the interface stress of solid electrodes fall into two main categories: measurement of the potential dependence of contact angle established by liquid phase on the solid surface [72–74] and the measurement of the variation in interface stress experienced by the solid as a function of potential. Changes in the interface stress may either be measured "directly" [39, 57], with a piezoelectric element, or be obtained indirectly [36, 75–78], by measuring the potential dependence of the strain (i.e., the deformation of the electrode) and then calculating the variation in stress from the appropriate form of Hooke's law.

It should be emphasized again that the above methods only yield changes of the interfacial stress as a function of various physicochemical parameters, e.g., as a function of electrode potential, and in principle, if there are both "plastic" and "elastic" contributions to the total strain, the changes of the "generalized surface parameter" [79] (i.e., the interfacial intensive parameter conjugate to the surface are) can be determined.

Unfortunately, most of the proposed methods have drawbacks, i.e., they are technically demanding, they cannot be used to monitor changes of the interfacial stress, they are semiempirical and depend on doubtful assumptions, etc.

In this chapter, the different techniques used for the determination of changes of interface stress of electrodes (the piezoelectric method (e.g., [39, 53, 75]), the extensometer method (e.g., [80, 81]) and its variants, and the electrochemical "bending beam" method (e.g., [30–38, 75, 78, 82–85])) as well as the kind and quality of information that can be achieved using these methods are discussed. Special attention has been paid to problems related to the use of the "bending beam" ("bending cantilever," "laser beam deflection," "wafer curvature") and "bending plate/disc" methods.

In bending beam measurements, a thin metal strip or a thin strip of glass or other substrate (on which the metal film is deposited) is rigidly clamped at one end in a fixed mount to form a cantilever. The deflection of the free end, as the strip becomes bent, is then measured by some means.

It should be noted that in most of the literature reviewed here, the intensive parameter conjugate to the surface area is usually called "surface tension" or "surface stress" and is denoted generally by γ_s or σ_s, respectively. In order to be consistent with the original literature, wherever and whenever possible, we will keep the “original” notation throughout the next chapters.

4.2 The Piezoelectric Method

According to our knowledge, Gokhshtein [39–52] was the first to measure changes $\partial\gamma_s/\partial E$ of γ_s with the electrode potential E at platinum electrodes in sulfuric acid using the “piezoelectric method.” This method, originally developed by Gokhshtein and further improved by other scientists [53–70], especially by Seo et al. [57–68], is a powerful in situ method for the rapid determination of surface energy changes.

The method is “direct” in the sense that it is the variation in the electrode deformation that is “registered” directly by a piezoelectric element. A metal plate is rigidly connected, in a special manner, to a highly sensitive piezoelectric element (Fig. 4.1).

The applied potential consists of a mean (DC) component upon which is superimposed on a high-frequency component. Usually, a sinusoidal signal is superimposed on a linear potential sweep. Electrode potential oscillation with the amplitude ΔE results in oscillation with an amplitude $\Delta\gamma_s$ in the surface stress, generating mechanical oscillation in the entire electrode–piezoelement unit.

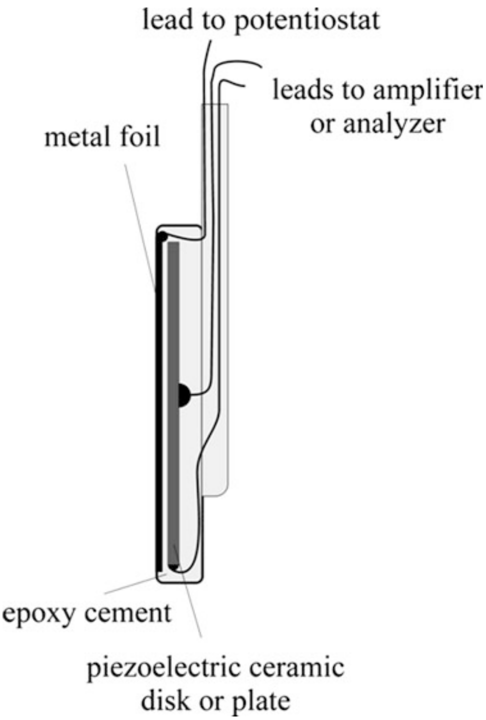

Fig. 4.1 Schematic illustration of a device for the “piezoelectric method”

The piezoelectric element converts the mechanical oscillations to alternating electric signals, which can be detected by using a lock-in amplifier, an oscilloscope, or a frequency response analyzer. In fact, this is some kind of electromechanical immittance measurement. The geometry of the electrode and its oscillation is of no fundamental importance. The metal in contact with the electrolyte solution may be made in the form of a tight filament which can make lengthwise oscillations, a straight rectangular rod which can make bending oscillations, etc. (Fig. 4.2). The alternating surface stress sets in motion not only the electrode, but the whole electrode and piezoelement system since the inertia forces are essential.

The oscillations of surface stress can also be excited by the application of high-frequency current. In this case, the amplitude of the surface charge density is kept constant by specifying the amplitude of the alternating current. According to [50], under such conditions, $\Delta\gamma_s$ will be proportional to the derivative $\partial\gamma_s/\partial E$, which is called the "$\varphi$-estance." If the electric variable is the potential, and the measurement is carried out with a constant amplitude ΔE, the amplitude of the piezoelectric voltage $|A|$ is proportional to the derivative of the surface stress with respect to the electrode potential $\partial\gamma_s/\partial E$, and the phase angle ($\varphi$) contains information about the change in the sign of $\partial\gamma_s/\partial E$. The $\partial\gamma_s/\partial q$ value is related to $\partial\gamma_s/\partial E$ (designated by Gokhshtein as q-estance and φ-estance, respectively [39, 49]) by

$$\frac{\partial\gamma_s}{\partial q} = \frac{\partial\gamma_s}{\partial E}\frac{\partial E}{\partial q} = \frac{1}{C}\frac{\partial\gamma_s}{\partial E},$$

where C is the electrode capacitance.

If the contribution of components resulting from the measuring instruments and the mechanical properties of the system to φ is kept constant, the electrode potential corresponding to the change of the sign of $\partial\gamma_s/\partial E$ can be evaluated from the relative change of φ [57]. According to [57], the relation between $\Delta\gamma_s$ and $\partial\gamma_s/\partial E$ can be given as

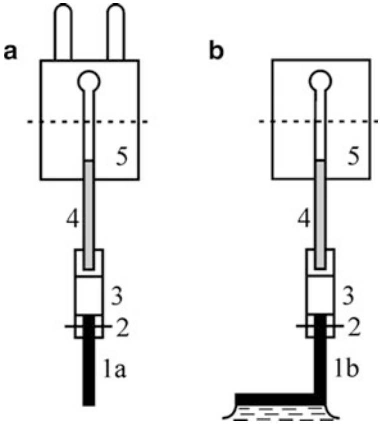

Fig. 4.2 Piezoelement units designed by Gokhshtein: (**a**) with plunger and (**b**) with foot. (1a, 1b) metal plate, rod, or filament; (2) holder; (3) rib; (4) piezoelement; and (5) plug

$$\Delta\gamma_s = \int \frac{d\gamma_s}{dE} dE \propto \int |A| dE.$$

By applying this method, $\partial\gamma_s/\partial E$ is measured at high frequencies, and the quantitative determination of $\Delta\gamma_s$ requires a difficult calibration procedure (the transfer function characteristic for the mechanical coupling is rather complicated [39]). However, the potentials of extrema of the surface stress vs. potential function can be obtained directly. The relation between the piezoelectric signals ($|A|$ and φ) and the $\Delta\gamma_s$ vs. E curve is shown schematically in Fig. 4.3.

A series of piezoelectric surface stress change measurements has been performed to date in order to understand electrode processes such as electrosorption and initial oxidation. This technique was capable of detecting sensitively the shift in potential of zero charge (pzc) due to the adsorption of ions and the sign reversal of surface charge due to the formation and reduction of surface oxide phases. For example, in case of platinum in sulfuric acid solutions, Gokhshtein observed two extrema in the hydrogen adsorption region [39]. Similar results were obtained by Seo et al. [57], applying the same experimental technique to platinum in 0.5 M acid sulfate solutions. On the other hand, Malpas et al. [53] observed only one extremum at $E \approx 0.05$ V for platinum in 0.1 M sulfuric acid. The electrode potential of the

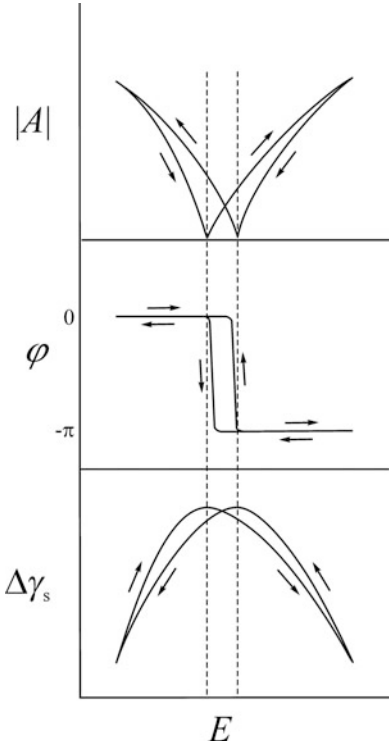

Fig. 4.3 Measured and computed quantities in a typical piezoelectric experiment: The amplitude of the piezoelectrical signal $|A|$, the phase angle φ, and the change of surface stress $\Delta\gamma_s$, as a function of the electrode potential E. Numerical integration of the experimentally determined $|A|$ curve with respect to the electrode potential yields a quantity proportional to $\Delta\gamma_s$

maximum was found to shift with pH to more negative values according to $\partial E_m/\partial \text{pH}$ −40 mV [57].

Obviously, because of the dynamic features of the method, the recorded variation in surface stress does not always correspond to equilibrium conditions. For perfectly polarizable electrodes, e.g., Au in contact with aqueous sodium sulfate solution in a certain electrode potential range, equilibrium may be reached during the measurement because the time for charging/discharging of the electrochemical double layer is shorter than the period of oscillation of the interfacial tension. In case of platinum, the period of oscillation is shorter than the time necessary for adsorption of hydrogen or oxygen to reach equilibrium; thus, the results depend on the frequency of oscillation as well as on the rate on the scan rate of the linear sweep.

An important advantage of the piezoelectric method is the selective separation of surface energy contributions from other side effects, such as changes in bulk stress due to diffusion or Joule heating of the electrolyte solution [39].

4.3 The Extensometer Method and Related Techniques

An extensometer instrument that directly measures change in the length of a very thin metal ribbon or wire has been proposed in [80]. In this instrument, the ribbon in contact with an electrolyte solution served as a working electrode in an electrochemical cell. The ribbon was kept under an approximately constant force (a mechanically applied tensile stress) throughout the experiment by mounting it axially inside a glass tube.

The schematic design of the extensometer is shown in Fig. 4.4.

As depicted in Fig. 4.4, the upper end of the ribbon or wire is attached to a spring. The spring constant of the spring should be small compared with the stiffness of the ribbon. The lower end of the ribbon is attached to the glass tube through a Teflon plug. An aluminum bobbin mounted on the quartz spindle forms two capacitors with fixed plates mounted in the head. Small changes in the two capacitances due to length changes of the ribbon are measured with an electronic capacitance sensor. The output voltage $V(\Delta L)$ and the change in the length of the ribbon are described by the relationship:

$$V(\Delta L) = K_1\left[\left(\frac{1}{C_1}\right) - \left(\frac{1}{C_2}\right)\right] = K_2\Delta L,$$

where C_1 and C_2 are the two capacitances and K_1 and K_2 are proportionality constants.

In a series of experiments, Beck et al. [80, 81, 86–88] attempted to determine variations in surface stress as a function of potential by using this method. According to the authors' opinion, the change in the surface stress with potential

Fig. 4.4 Schematic design of extensometer

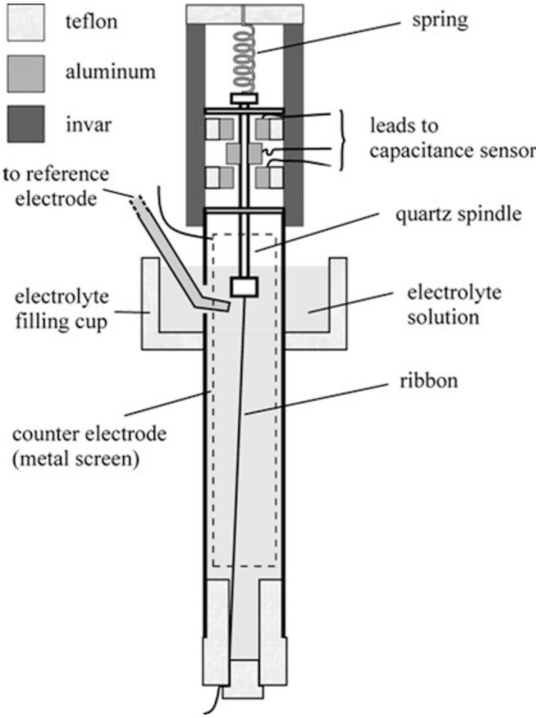

causes a change in the length of a ribbon, and the extensometer can be used to determine the potential of zero charge.

The method is based on the following considerations: Suppose an unstressed metal ribbon and a spring, one end of each is fixed. The ribbon of length L is immersed into the electrolyte solution in the extensometer. There is a gap L_0 between the other ends, as shown in Fig. 4.5, case 1. If the ribbon and spring are stretched to connect their free ends, the ribbon is stretched by Δx_1 (case 2 in Fig. 4.5), and the spring force F_1 is

$$F_1 = k_r \Delta x_1 = k_s(\Delta L_0 - \Delta x_1),$$

where k_s is the spring constant of the spring. With the bulk elastic modulus (Young's modulus, E_b) and the cross-sectional area (A) of the ribbon, respectively, the spring constant of the ribbon, k_r, can be given as

$$k_r = \frac{E_b A}{L}.$$

Eliminating Δx_1 gives

$$F_1 = \frac{k_r k_s \Delta L_0}{k_r + k_s}.$$

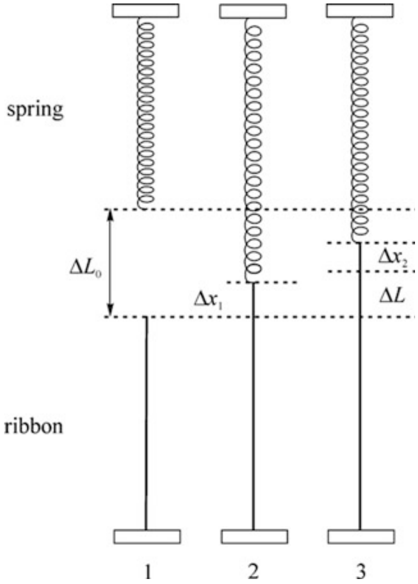

Fig. 4.5 Schematic diagram of the spring and ribbon system: (1) nonstretched ribbon and spring, without potential applied; (2) stretched ribbon and spring, without potential applied; and (3) stretched ribbon and spring, with potential applied [81]

If the electrode potential is applied in the extensometer experiment (the ribbon in contact with the electrolyte solution serves as the working electrode), the ribbon is increased (decreased) in length by an amount ΔL.

Suppose that the free ends are again connected, and the ribbon is stretched by $\Delta L + \Delta x_2$. Assuming, that since ΔL is very small, the spring constant of the ribbon remains the same after the change in length, the new force F_2 on the ribbon and spring is

$$F_2 = k_r \Delta x_2 = k_s(\Delta L_0 - \Delta L - \Delta x_2).$$

After eliminating Δx_2, we have

$$F_2 = \frac{k_r k_s(\Delta L_0 - \Delta L)}{k_r + k_s},$$

and

$$\Delta F = F_2 - F_1 = \frac{-k_r k_s \Delta L}{k_r + k_s}.$$

If $k_r \gg k_s$, then

$$\Delta F \approx -k_s \Delta L. \tag{4.1}$$

In [81], it has been assumed that the force on the ribbon is resisted by separable bulk and surface stresses, σ_b and σ_s, respectively. The surface stress has been assumed to be in a region of atomic thickness on the surface of the metal ribbon. Thus,

$$F = \sigma_{\mathrm{b}}A + \sigma_{\mathrm{s}}P$$

and

$$\Delta F = \sigma_{\mathrm{b}}\Delta A + A\Delta\sigma_{\mathrm{b}} + \sigma_{\mathrm{s}}\Delta S_{\mathrm{r}} + S_{\mathrm{r}}\Delta\sigma_{\mathrm{s}}, \tag{4.2}$$

where S_{r} is the periphery of the cross section of the ribbon.

According to Hooke's law,

$$\Delta\sigma_{\mathrm{b}} = E_{\mathrm{b}}\frac{\Delta L}{L}. \tag{4.3}$$

It has been assumed that E_{b} remains unchanged if the electrode potential changes. If t is the thickness and w is the width of the metal ribbon, the change in area is

$$\Delta A = (t + \Delta t)(w + \Delta w) - tw,$$

therefore,

$$\frac{\Delta A}{A} = \left(1 + \frac{\Delta t}{t}\right)\left(1 + \frac{\Delta w}{w}\right) - 1. \tag{4.4}$$

According to Poisson's law,

$$\frac{\Delta t}{t} = -\nu\frac{\Delta L}{L}$$

and

$$\frac{\Delta w}{w} = -\nu\frac{\Delta L}{L}. \tag{4.5}$$

From Eq. (4.4), by neglecting the quadratic term,

$$\frac{\Delta A}{A} = \left(1 - \nu\frac{\Delta L}{L}\right)^2 - 1 \approx -2\nu\frac{\Delta L}{L}. \tag{4.6}$$

By combining Eqs. (4.3) and (4.6),

$$\left|\frac{\sigma_{\mathrm{b}}\Delta A}{A\Delta\sigma_{\mathrm{b}}}\right| = \frac{2\nu\sigma_{\mathrm{b}}}{E_{\mathrm{b}}}. \tag{4.7}$$

The bulk strain $\sigma_\mathrm{b}/E_\mathrm{b}$ is expected to be very small; thus,

$$A\Delta\sigma_\mathrm{b} \gg \sigma_\mathrm{b}\Delta A. \tag{4.8}$$

In [81] a constant elastic modulus E_s has been defined for the atomic layer on the surface of the metal ribbon. This assumption is rather questionable since E_s may be affected by adsorption or absorption. The change in the surface stress has been expressed as

$$\Delta\sigma_\mathrm{s} = E_\mathrm{s}\frac{\Delta L}{L}, \tag{4.9}$$

and the periphery of the cross section of the ribbon has been approximated as $S_\mathrm{r} \approx 2w$. This means that

$$\frac{\Delta S_\mathrm{r}}{S_\mathrm{r}} \approx \frac{\Delta w}{w} = -\nu\frac{\Delta L}{L}. \tag{4.10}$$

Since the surface linear strain $\sigma_\mathrm{s}/E_\mathrm{s}$ is very small, from Eqs. (4.9) and (4.10),

$$S_\mathrm{r}\Delta\sigma_\mathrm{s} \gg \sigma_\mathrm{s}\Delta S_\mathrm{r}. \tag{4.11}$$

From Eqs. (4.1), (4.2), (4.8), and (4.11)

$$\Delta F \approx A\Delta\sigma_\mathrm{b} + S_\mathrm{r}\Delta\sigma_\mathrm{s} \approx -k_\mathrm{s}\Delta L.$$

On the other hand,

$$A\Delta\sigma_\mathrm{b} = AE_\mathrm{b}\frac{\Delta L}{L} = k_\mathrm{r}\Delta L,$$

$$S_\mathrm{r}\Delta\sigma_\mathrm{s} \approx -(k_\mathrm{r} + k_\mathrm{s})\Delta L,$$

and since $k_\mathrm{r} \gg k_\mathrm{s}$,

$$\Delta\sigma_\mathrm{s} \approx -\frac{AE_\mathrm{b}}{S_\mathrm{r}L}\Delta L. \tag{4.12}$$

This means that the variation in surface stress can be obtained from the change in the ribbon length.

The most serious problem to overcome in the design of the extensometer is minimizing errors due to thermal expansion. Even very small temperature variations can cause changes in the length of the ribbon which are expected to be considerably larger than those produced by changes in the surface stress.

Several design considerations were made to minimize the effects of thermal expansion [80]:

- Invar and quartz, each having low thermal expansion coefficients, were used for the measuring head above the ribbon out of the electrolyte solution. [Invar, also known generically as FeNi36 (64FeNi in the US), is a nickel steel alloy notable for its uniquely low coefficient of thermal expansion. The name, Invar, comes from the word invariable, referring to its lack of expansion or contraction with temperature changes.]
- The whole instrument was placed in a thermally insulated box and measurements were made after the thermal drift has decreased to a low value.
- The potential sweep rate was high to provide adequate resolution from residual thermal drift.
- The measurements were limited to metals, electrolyte solutions, and potential ranges in which electrolysis current and consequently the heating effects are minimum.

However, none of these measures can completely eliminate thermal effects due to Joule heating or electrochemical polarization. It has been therefore suggested that the method be limited to systems with low electrochemical activity. Nevertheless, as pointed out by Morcos [71], unless the effect of electrochemical processes on thermal expansion can be quantitatively accounted for, the results of the extensometer method cannot be conclusively interpreted.

The temperature sensitivity of the extensometer can be estimated using the data presented in Table 4.2. The difference between the thermal expansion coefficients ($\Delta\alpha_t$) of gold and crown glass is about 5×10^{-6} K^{-1}. If $l_\mathrm{r} = 50$ cm length of the metal ribbon is immersed in the electrode solution, the differential thermal expansion ($\alpha_t l_\mathrm{r}$) is on the order of 2,500 nm K^{-1}. This means that at a sensitivity of the order of 1 nm [86], a temperature stability of

$$\Delta t = \frac{\Delta l}{\alpha_t \cdot l_\mathrm{t}} = \frac{1\,\mathrm{nm}}{2,500\,\mathrm{nm}\,\mathrm{K}^{-1}} = 4 \times 10^{-4}\,\mathrm{K},$$

is required.

In [89], the effect of mechanical stress on electrode potential, E, was studied under zero current conditions. The experimental setup was very similar to the extensometer described above. A tensile stress machine was used for mechanical characterization of the samples. A two-electrode geometry was used for the potential measurements; the potential of a thin Ag wire made taut vertically in an electrolyte solution ($AgNO_3$) was measured against a reference electrode with a

Table 4.2 Coefficients of thermal expansion (α_t, $t = 20$°C)

Au: 14.2×10^{-6} K^{-1}	Pt: 8.9×10^{-6} K^{-1}
Ag: 19.7×10^{-6} K^{-1}	Quartz: 0.16–14.5 $\times 10^{-6}$ K^{-1}
Optical glass: 7.6×10^{-6} K^{-1}	Crown glass: 9.65×10^{-6} K^{-1}

high input impedance voltmeter. (The total length of the wire was 50 mm; the portion in contact with the electrolyte solution was 30 mm.) One end of the wire was fixed to one arm of a balance; the other arm of which was loaded with standard weights. The applied force was low enough to maintain proportionality between stress and strain (elastic deformation conditions). A schematic diagram of the apparatus is shown in Fig. 4.6.

The numerically large response reported in [89] has been questioned in [90]. It has been pointed out that the dE/dσ values (where σ is a measure for tangential stress, which scales with the elastic strain ε) reported in the literature [89, 91, 92] differ by several orders of magnitude and even by sign. In [90], the measurement of the response, ΔE, of the electrode potential of a polarizable electrode (gold 10 mmol dm^{-3} aqueous perchloric acid solution) to elastic strain under open circuit has been described. A lock-in technique was used to measure the potential variation during cyclic elastic deformation of a thin-film electrode supported on a polymer substrate. The method allowed the potential–strain response to be accurately resolved for elastic strain amplitudes as small as 10^{-4}. It has been shown that the approach similar to that originally suggested by Gokhshtein (see the piezoelectric method discussed above [39, 46]) can provide quantitative data for dE/dε. The results reported in [90] were commented in [93]. As a response to the criticism, the experiment with Ag was repeated [94] using the identical electrolyte as in [89] (aqueous 10 mmol dm^{-3} $AgNO_3$ and 0.1 mmol dm^{-3} KNO_3). According to the authors of [94], the results confirmed the prediction that $\varsigma = \partial E/\partial e$ is small and ς at the potential of zero charge should be negative for Ag, similar to Au.

Figure 4.7 shows the experimental setup used in [90, 94]. The entire apparatus was housed in a stainless steel chamber. Before experiments, the chamber was flushed repeatedly with Ar and then sealed in Ar at atmospheric pressure.

Au layers for the experiments were prepared by dc magnetron sputtering onto the top of a thin Ti adhesion layer on much thicker polyimide substrates. The principle of operation can be understood by referring to Fig. 4.8. The entire gold surface was wetted during the measurements. The surrounding regions of wetted substrate are insulating. The electrode has been strained by applying a uniaxial stress at the open circuit potential (E_{ocp}). When the axial strain imposed on the

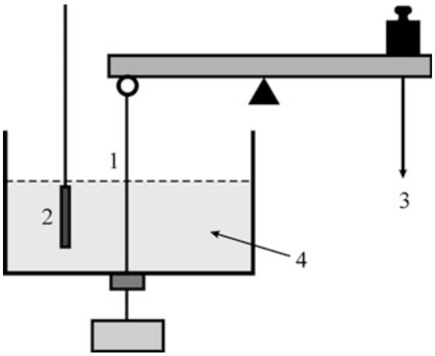

Fig. 4.6 Schematic drawing of the apparatus: (1) metal (Ag) wire; (2) reference electrode; and (3) force ($F = mg$, where m is the load mass and g is the local acceleration of free fall)

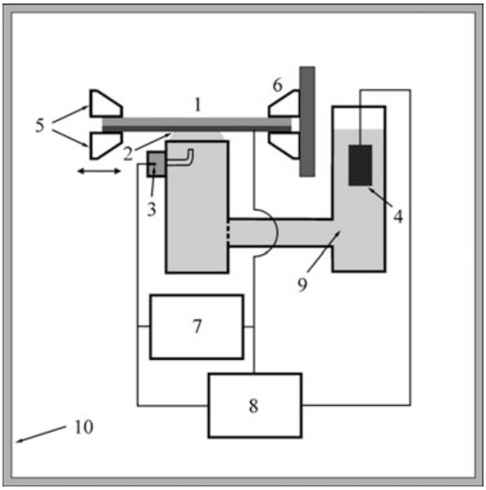

Fig. 4.7 Schematic representation of the experimental setup in [90]: (1) sample with Au layer; (2) working electrode; (3) reference electrode with Luggin capillary; (4) auxiliary electrode; (5) mobile grip; (6) fixed grip; (7) lock-in amplifier; (8) potentiostat; (9) electrolyte solution; and (10) stainless steel chamber

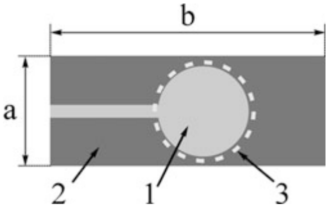

Fig. 4.8 The sample with gold film in Fig. 4.7: (1) gold layer; (2) substrate (Kapton®); (3) three-phase boundary between the surface of the sample, the electrolyte solution, and the gas phase; *a*: 10 mm; *b*: 25 mm

substrate is $\Delta l/l$ (l is an axial linear dimension), then the area strain of the substrate is $\Delta\varepsilon = (1 - \nu)\cdot\Delta l/l$, with ν is the substrate Poisson's ratio. This strain is transferred to the electrode.

In the experiments, the substrate was strained by displacing one of two grips using a computer-controlled piezoactuator equipped with a calibrated displacement sensor that serves to record the time dependence of Δl. A gentle prestraining prevented the buckling of the substrate in the negative-going part of the strain cycle. The sample was mounted horizontally with the gold film facing down and was contacted from below by a meniscus of electrolyte solution. To assure constant wetted Lagrangian area (constant number of surface metal atoms in contact with the electrolyte solution) throughout the strain cycles, the wetted region was larger than the circular electrode section (see the boundary 3 in Fig. 4.8). The reference electrode was separated from the main body of the cell (made of Teflon®) by a Luggin capillary. Au wire in a compartment separated from the main reservoir by a channel served as the counter electrode. The frequency of the cyclic strain was limited to 100 Hz.

According to the authors, their results demonstrate that, when artifacts from Faraday currents and adsorbate coverage are avoided, the prediction that "electrical work–mechanical response is the same as mechanical work–electrical response" (as proposed almost 40 years ago by Gokhshtein) could be confirmed experimentally.

Cyclic voltammetric experiments combined with dilatometric detection of the length change have been reported in [95, 96]. Nanoporous Pt samples prepared by consolidating commercial Pt black having a grain size of 6 nm were immersed in different aqueous electrolyte solutions (H_2SO_4, $HClO_4$, and KOH), and the strain upon varying the electrode potential E was measured in situ by dilatometry and diffractometry. According to the results, reversible strain amplitudes comparable to those of commercial piezoceramics could be induced in metals by introducing a continuous network of nanometer-sized pores with a high surface area and by controlling the surface charge density through an applied potential [95]. In [96], the experimental results for cuboids of porous gold of dimension $1.2 \times 1.2 \times 1\ \mathrm{mm}^3$ were reported.

In [97, 98], a laser technique, based on optical fiber interferometry, is described for in situ measurements of electrode strain during electrode reactions. The basic concept utilizes a metal coated optical fiber in contact with an electrolyte solution as the working electrode in an electrochemical cell, while simultaneously using the fiber as one arm of a Mach–Zehnder interferometer (see later). The optical path length of the metal coated fiber was monitored during the electrochemical process. Strain induced in the working electrode also strained the fiber and modified its effective optical path length.

The measurement system is shown schematically in Fig. 4.9.

Light from the He–Ne laser is split into two parts which are introduced into two single-mode optical fibers using microscope objectives. Both fibers pass through the electrolyte solution and are brought together on a microscope slide to which they are glued. The interference fringe pattern in the diode array is sent to the computer. The light beams coming from the two fiber ends interact to produce an interference pattern.

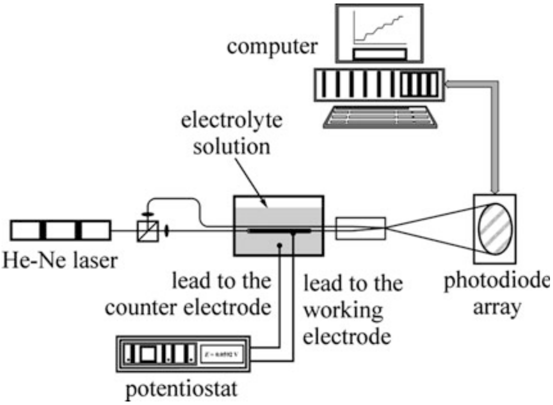

Fig. 4.9 Schematic diagram of the system for in situ measurement of strain during electrode reaction (adapted from [97, 98])

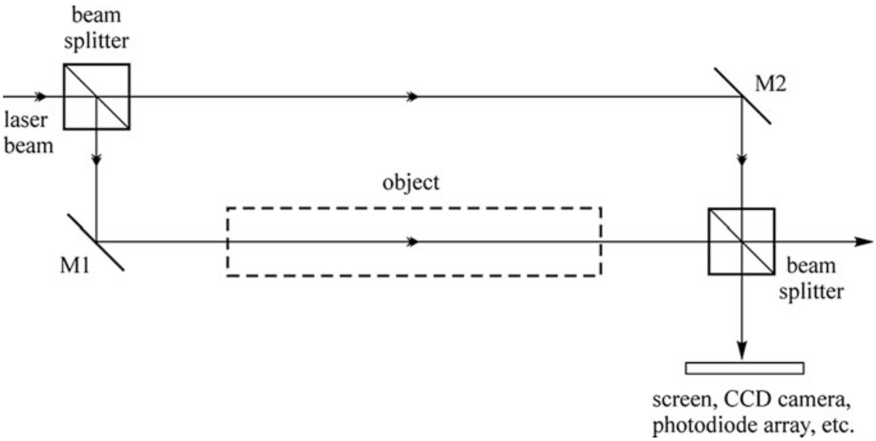

Fig. 4.10 Rectangle arrangement of a Mach–Zehnder interferometer. M1, M2: reflecting mirrors

The Mach–Zehnder interferometer is a classical mirror interferometer [99, 100]. For a long time, it was the most common dual-beam interferometer used to measure continuously refractive index distributions or thickness variation of transparent objects. Figure 4.10 shows a Mach–Zehnder interferometer with a “phase object” in its measuring beam (“phase object” is a transparent object which influences the phase of light passing through it).

It consists of two reflecting and two beam-splitting mirrors in a rectangle (can also be a parallelogram) arrangement. A light beam from a source, say a He–Ne laser, is first split into two parts by a beam splitter and then recombined by a second beam splitter. First, the interferometer has to be adjusted in such a way that the two beams have equal optical path lengths. When all reflecting surfaces are perfectly parallel, the recombined beams do not produce interference fringes. When the physical process of interest, e.g., strain, heat transfer, etc., is introduced into the measuring beam, an optical path difference between reference and measuring beam is produced. A superposition of the two beams then generates an interference pattern.

4.4 Contact Angle Measurements

The direct measurement of the potential dependence of contact angles in systems with a solid phase started with the work of Möller [101, 102]. Later, Frumkin observed [103] that the shape of a drop of water placed on a solid electrode could be altered by varying the electrode potential: The stronger the polarization, the flatter the drop. This phenomenon, commonly known as electrowetting, has numerous applications from liquid lenses to moving drops in microfluidic devices.

Contact angles can either be measured directly or obtained indirectly. In the latter case, the rise of a liquid meniscus at a partially immersed plate or the capillary rise inside a metal capillary is measured. The contact angle is then obtained by using a relationship connecting the measured parameter with the contact angle. The potential dependence of contact angles can be measured on metals, semiconductors, and semimetallic electrodes of both single-crystal and polycrystalline type, as well as on conductive polymers [71, 104].

An interesting example for the direct measurement of the potential dependence of contact angles can be found in [105]. In this study, the potential dependence of the contact angle between perfluorodecaline ($C_{10}F_{18}$) and copper, copper(I) sulfide, and copper telluride (Cu_4Te_3) in aqueous sodium acetate solution (concentration, 0.1 M) was investigated. The contact angles were measured in a plane–parallel quartz cuvette with a metallographic microscope. The contact angle was determined using a goniometer.

Contact angle measurements between water and a poly(vinylferrocene) film on a potential-controlled platinum electrode have been reported in [106].

In [107], an unwalled electrochemical cell formed by a sessile droplet of 1-butyl-3-methylimidazolium hexafluorophosphate resting on electroactive surfaces was used to investigate the voltammetry and surface energy of different electroactive film/ionic liquid interfaces. The following films were investigated: ferrocene films, Au_{140} nanoparticle films, and Au_{38} nanoparticle films. The substrate was a 200-nm Au film formed by evaporation of Au onto a glass substrate, with a 10-nm Cr undercoat. The contact angles were measured with a Rame-Hart optical goniometer.

Very little potential dependence of the contact angle between an electrolyte solution droplet and an etched germanium surface was reported in [108]. The variations of the advancing and receding contact angles during a potential scan have been measured by a gravimetric method for Si and Ge in different acid solutions [109]. For *p*-Si in dilute fluoride electrolyte solutions, the change from the reduced state to the oxidized state (electropolishing regime) is associated with a large decrease of the contact angles. In accordance with the results reported in [108], for Ge in H_2SO_4 or $HClO_4$ solutions, the change of the contact angles between the reduced state and the oxidized state is much smaller than for silicon and is dependent upon crystal orientation.

The principles of the indirect measurement of contact angles by meniscus-rise techniques in electrochemical systems have been reported by Morcos [71, 104]. Experimental data on the potential dependence of contact angles on solid electrodes have been obtained by the method of meniscus rise at partially immersed plates. The equation relating the meniscus rise h at an infinitely wide vertical plate to the contact angle θ is [110, 111]

$$\sin\theta = 1 - \frac{g\rho}{2\gamma_L}h^2,$$

where γ_L and ρ are the liquids surface tension and density and g is the local acceleration of free fall. Taking into account that h is the difference between the

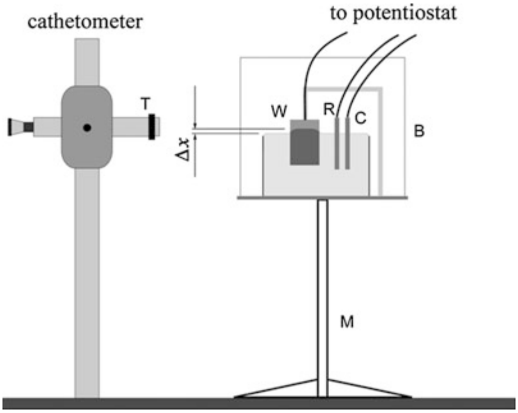

Fig. 4.11 Schematic of the apparatus for measuring of meniscus rise. W: test electrode; R: reference electrode; C: counter electrode; B: box; M: adjustable stand; T: telescope

level of the meniscus at the solid surface and the level of the liquid surface in the cell, the heights of both levels must be experimentally determined. The measurement can be accurately performed, e.g., by a cathetometer (Fig. 4.11). According to [111], the advantage of this method compared to the direct measurement of contact angle lies in the fact that it is much easier to measure the height of a meniscus than to measure a contact angle between a sessile drop and a solid plate. It is important that the cell used for this purpose should be made of a material that is not wetted by the solvent.

A method, based on the response of a thickness shear mode sensor to electrocapillary phenomena, for determination of the potential of zero charge and changes in the surface stress at solid metal/solution interfaces has been described in [112]. Essentially, the method involves measuring the change in the rise of the solution meniscus due to electrocapillary phenomena at the surface of a partially immersed vertical metal plate. This change has been determined by a thickness shear mode (TSM) bulk acoustic wave sensor.

The principle of the measurement can be summarized as follows: Changing the electrode potential E causes a change in the contact angle and meniscus rise and its associated height h (see Fig. 4.12). The change of h causes a change in the electrode mass and the mass of solution adhering to the piezoelectric quartz crystal sensor (PQC). As Δh is very small, the effect of the change of oscillating medium on the resonant frequency of the PQC–TSM sensor (such as viscosity, surface stress, and static pressure) can be neglected. A similar method, but with an electrochemical quartz crystal impedance system, was used in [113].

However, contact-angle methods are not without drawbacks. The most important disadvantages of these methods are as follows:

- In a three-phase system, the risk of surface contamination is high.
- Hysteresis complicates the measurements and the interpretation of the data.

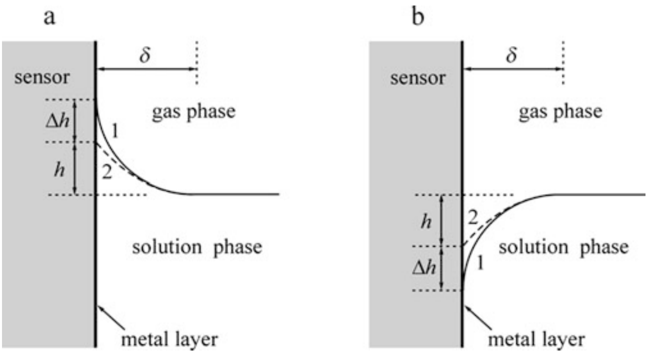

Fig. 4.12 The height of the solution meniscus at two-electrode potentials: (1) E_1; (2) E_2; a: wettable metal surface; b: nonwettable metal surface; δ: the characteristic attenuation length of the shear wave of the TSM sensor

- The evaluation of experimental data usually involves questionable assumptions and complicated correction procedures.

4.5 Bending Plate and Bending Beam Methods

The theory of the bending of a film–substrate system is an old problem dating back at least to 1909. The principles of the "bending beam" ("bending cantilever," "laser beam deflection," "wafer curvature," etc.) method were first stated by Stoney [114, 115], who derived an equation relating the isotropic surface stress in the film (γ_s) to the radius of curvature (R) of the beam

$$\gamma_s = \frac{E_S t_S^2}{6R}, \tag{4.13}$$

where t_S is the substrate thickness and E is the modulus of elasticity of the substrate.

Early attempts to obtain the potential dependence of surface stress from measurement of the deformation of electrodes as a function of electrode potential have been reported in [30, 31]. The deflection of the electrode was measured with a laser optical lever. The measuring apparatus consisted of a He–Ne laser, optical components, and a detector.

Measuring the bending of a plate or strip to determine surface stress change or the stress in thin films is a common technique today, even in electrochemistry [71, 115, 116]. It has been used, for instance, for the investigation of the origin of electrochemical oscillations at silicon [117] or in the course of galvanostatic oxidation of organic compounds on platinum [78, 82], for the study of volume changes in polymers during redox processes [118], for the investigation of the response kinetics of the bending of polyelectrolyte membrane platinum composites

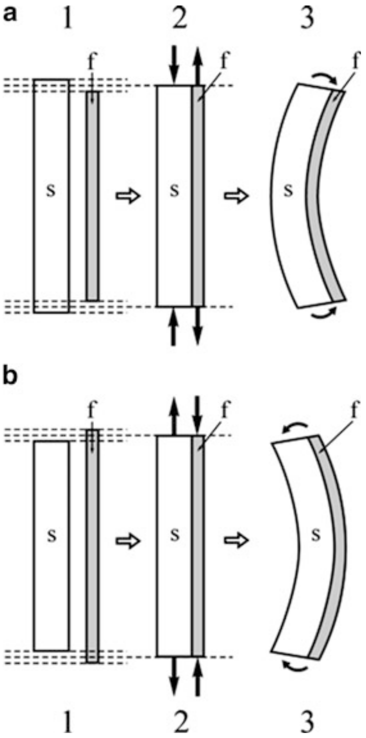

Fig. 4.13 Events leading to: (**a**) internal tensile stress in film or (**b**) internal compressive stress in film. (1) Film and substrate are separated; (2) the film is firmly attached to the substrate; balanced external forces are applied on the film and the substrate to compensate for the difference in length; (3) the substrate–film system bends; S: substrate; f: film

by electric stimuli [119], for the experimental verification of the adequacy of the "brush model" of polymer modified electrodes [120], etc.

The generation of internal (residual) stress during the electrochemical deposition of films on substrates is illustrated in Fig. 4.13. Static equilibrium requires that no net forces and no body torques act of an infinitesimal volume element. In particular, the net force (F) and bending moment (M) vanish on the film–substrate cross section; thus,

$$F = \int \sigma \mathrm{d}A = 0, \tag{4.12}$$

$$M = \int \sigma z \mathrm{d}A = 0, \tag{4.13}$$

where z is the distance from the neutral axis, and A is the sectional area, respectively.

In case (a) shown in Fig. 4.13, the growing film initially shrinks relative to the substrate. There can be a multitude of reasons for this to happen, e.g., surface tension forces or lattice mismatch during epitaxial growth. However, compatibility requires that both the film and the substrate have the same length (and width); consequently, the film stretches while the substrate contracts to accommodate the constraints. The tensile forces developed within the film are balanced by the compressive forces in the substrate. The film–substrate system is still not in mechanical equilibrium because of the uncompensated end moments. If the substrate is not rigidly held, i.e., the film–substrate pair is not restrained from moving, it will elastically deform to counteract the unbalanced moments.

Thus, films containing internal (residual) tensile stresses bend the substrate concavely, as shown in Fig. 4.13a. Similarly, a film which develops residual compressive stresses (i.e., the film wants to be larger than the substrate) will expand relative to substrates and elastically bend the substrate, but in the opposite direction (Fig. 4.13b). By convention, the radius of curvature, R, of the substrate–film structure is positive for concave curvature (tensile stress) and negative for convex curvature (compressive stress). These results are perfectly general regardless of the specific mechanisms that cause the film to stretch or shrink relative to the substrate [121].

In the derivation of Eq. (4.13), Stoney considered a "thin steel rule" with a thin nickel layer of a thickness t_f deposited on it. Assuming that the thickness of the rule (t_S) is very small in comparison with the radius of curvature (R), the following equation can be written for the bending moments in the steel:

$$\int_{t_s}^{0} \frac{E}{R}(b - x)x\mathrm{d}x = 0, \tag{4.16}$$

where is the depth from the surface of the rule to the neutral axis (Fig. 4.14).

Since

$$\int_{t_S}^{0} \frac{E}{R}(b - x)x\mathrm{d}x = \frac{E}{R}\left(-\frac{bt_S^2}{2} + \frac{t_S^3}{3}\right),$$

so that $b = 2t_S/3$.

On the other hand,

$$\sigma_f t_f = \int_{t_s}^{0} \frac{E}{R}(b - x)\mathrm{d}x = \frac{E}{R}\left(bt_S - \frac{t_S^2}{2}\right) = \frac{Et_S^2}{6R}, \tag{4.17}$$

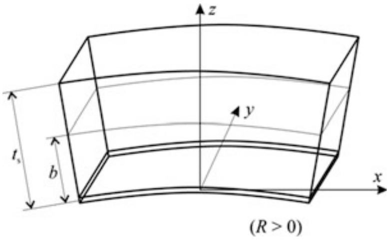

Fig. 4.14 The coordinate system for the derivation of Stoney's equation

which is identical with Eq. (4.13) since $\gamma_s = \sigma_f \cdot t_f$, where σ_f is the film stress.

Equation (4.17) or its variants have been used in almost all experimental determinations of film stress or surface stress.

As has been pointed out in several publications (see, e.g., [122, 123]) that the effect of stress in two dimensions has been neglected in the original derivation. A modified equation can be obtained by referring to Fig. 4.15, which depicts a film–substrate system of width w. The thickness of the film and Young's modulus are denoted by t_f and E_f, respectively, and the corresponding parameters of the substrate are t_S and E_S (see Fig. 4.15a). The interfacial forces can be replaced by a force acting on the entire cross section of the film (or substrate) and a corresponding moment as shown in the force diagram ("free body diagram") in Fig. 4.15b. The statically equivalent combinations of forces and moments are (F_f, M_f) in the film and (F_S, M_S) in the substrate. The force F_f must be equal to the force F_S and can be imagined to act uniformly over the cross-sectional area, $A_f = t_f{\cdot}w$, giving rise to the (tensile or compressive) film stress. The bending of the sample results from the moments M_f and M_S of the film and substrate, respectively. Since according to Eq. (4.13), the total moment in the system must be zero, the sum of the counter-clockwise moments M_f and M_S must be equal to the clockwise moment acting on the entire system:

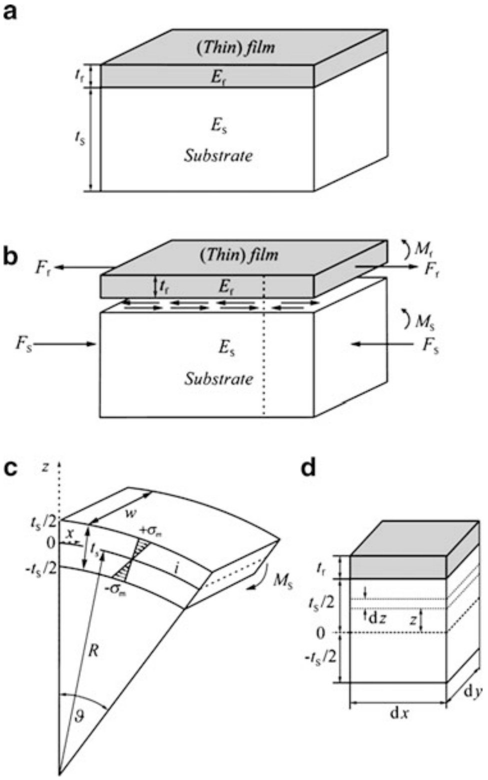

Fig. 4.15 Illustration of the relationship between film stress and substrate curvature: (**a**) The composite structure; (**b**) force diagram of film and substrate; (**c**) bending of the beam under an applied moment; and (**d**) an element of the substrate–film combination

$$\frac{t_\mathrm{f}}{2}F_\mathrm{f}+\frac{t_\mathrm{s}}{2}F_\mathrm{S}=\frac{t_\mathrm{f}+t_\mathrm{s}}{2}F_\mathrm{f}=M_\mathrm{f}+M_\mathrm{S}. \tag{4.18}$$

Since the film–substrate system is not restrained from moving, it will bend to counteract the unbalanced moments, and it can be treated as a beam with the radius of curvature R defined as (Fig. 4.15c):

$$\frac{1}{R}=\frac{1}{\mathrm{d}i/\mathrm{d}\vartheta}=\mathrm{C}\frac{\mathrm{d}^2z}{\mathrm{d}x^2}, \tag{4.17}$$

where

$$C=\left[1+\left(\frac{\mathrm{d}z}{\mathrm{d}x}\right)^2\right]^{-3/2}.$$

For small deflections, $\mathrm{d}z/\mathrm{d}x \ll 1$; therefore, $C \approx 1$ and the radius of curvature can be approximated as

$$R\approx\frac{1}{\mathrm{d}^2z/\mathrm{d}x^2}.$$

If the longitudinal strain varies linearly with the distance z from the neutral axis and is proportional with the curvature of the beam, then according to Hooke's law:

$$\sigma_\mathrm{S}(z)=\frac{E_\mathrm{S}z}{R}.$$

In case of an isolated beam (made of the substrate material) bent by the moment M_s (Fig. 4.15c), the stress varies linearly across the section from maximum tension ($+\sigma_\mathrm{m}$) to maximum compression ($-\sigma_\mathrm{m}$). In terms of R and ϑ, Hooke's law yields

$$\pm\sigma_\mathrm{m}=\left[\frac{\left(R\pm\frac{t_\mathrm{S}}{2}\right)\vartheta-R\vartheta}{R\vartheta}\right]E_\mathrm{S}=\pm\frac{E_\mathrm{S}t_\mathrm{S}}{2R}.$$

The bending moment corresponding to this stress distribution can be given as (Fig. 4.15d)

$$M_\mathrm{S}=\int_{-t_\mathrm{S}/2}^{t_\mathrm{S}/2}\sigma_\mathrm{S}(z)z\mathrm{d}A=\int_{-t_\mathrm{S}/2}^{t_\mathrm{S}/2}\frac{E_\mathrm{S}}{R}z^2\mathrm{d}A=\int_{-t_\mathrm{S}/2}^{t_\mathrm{S}/2}\frac{E_\mathrm{S}}{R}z^2w\mathrm{d}z=\frac{E_\mathrm{S}t_\mathrm{S}^3w}{12R}.$$

By analogy,

$$M_\mathrm{f} = \frac{E_\mathrm{f} t_\mathrm{f}^3 w}{12R}.$$

Substituting the expressions for M_S and M_f into Eq. (4.18) gives

$$\frac{t_\mathrm{f} + t_\mathrm{S}}{2} F_\mathrm{f} = \frac{w}{12R} \left(E_\mathrm{f} t_\mathrm{f}^3 + E_\mathrm{S} t_\mathrm{S}^3 \right). \tag{4.20}$$

In order to account for the biaxial nature of the stress, we have to replace E_f by $E_\mathrm{f}/(1 - \nu_\mathrm{f})$ and, similarly, E_S by $E_\mathrm{S}/(1 - \nu_\mathrm{S})$, where ν_f and ν_S are the film and substrate Poisson's ratios, respectively. Thus,

$$\frac{t_\mathrm{f} + t_\mathrm{S}}{2} F_\mathrm{f} = \frac{w}{12R} \left(\frac{E_\mathrm{f}}{1 - \nu_\mathrm{f}} t_\mathrm{f}^3 + \frac{E_\mathrm{S}}{1 - \nu_\mathrm{S}} t_\mathrm{S}^3 \right). \tag{4.21}$$

Since t_S is usually much larger than t_f, the film stress can be given by

$$\sigma_\mathrm{f} = \frac{F_\mathrm{f}}{t_\mathrm{f} w} = \frac{E_\mathrm{S} t_\mathrm{S}^2}{6(1 - \nu_\mathrm{S})\, t_\mathrm{f}} \cdot \frac{1}{R} \tag{4.22}$$

and

$$\Delta\gamma_\mathrm{s} = \frac{F_\mathrm{f}}{w} = \frac{E_\mathrm{S} t_\mathrm{S}^2}{6(1 - \nu_\mathrm{S})} \cdot \frac{1}{R}. \tag{4.23}$$

Both Eqs. (4.22) and (4.23) are referred to as Stoney's formula or Stoney's equation and are valid under the following conditions: (a) The substrate is homogeneous, linearly elastic, and uniformly thick. (b) The stress is uniform throughout the film thickness. (c) The substrate thickness is much greater than the film thickness (according to [124]); the $t_\mathrm{f}/t_\mathrm{S}$ ratio should be $\leq 10^{-3}$. (d) The radius of curvature of the substrate is much greater than the thickness of the composite structure, i.e., the bending displacement is small compared to the thickness of the substrate.

It should be noted here that an average stress can be defined by the relation [124]

$$\bar{\sigma}_\mathrm{f} = \frac{1}{t_\mathrm{f}} \int_0^{t_\mathrm{f}} \sigma_\mathrm{f}(z) \mathrm{d}z,$$

where $\sigma_\mathrm{f}(z)$ is the stress distribution through the film thickness t_f. Experimentally, data are usually obtained for the product of the average stress and the film thickness.

Stoney's equation has become the standard expression for the analysis of surface stress problems in materials physics. It has been pointed out [125, 126] that the equation holds for thickness ratios much larger than expected in the context of the thin-film approximation. This can be attributed to self-compensating errors in its derivation [127, 128].

The calculation of the bending of a sheet material subject to a change in the surface stress on one side has been carried out for two boundary conditions in [29]. One of them is that the sheet is allowed to bend only in one direction, the other one is that the sheet can bend freely in both principal directions. For simplicity in [29] a crystal plate is considered to be oriented such that the surfaces are (1 0 0) surfaces and that the sides of the rectangular shaped sheet coincide with the $\langle 1\ 0\ 0 \rangle$ direction. The solution satisfying the second boundary condition is formally identical with Eq. (4.23). For the case of a bending only in one direction the corresponding expression for the interface stress has been given as

$$\tau_{11}^{S} = \frac{Et^2}{6(1 - \nu^2)} \cdot \frac{1}{R},$$

where E is Young's modulus, ν is Poisson's ratio, and t is the thickness of the crystal.

As it has already been mentioned earlier, the "bending beam" method can be effectively used in electrochemical experiments, since the changes of the surface stress ($\Delta\gamma_s$) for a thin metal film on one side of an insulator (e.g., glass) strip (or a metal plate, one side of which is coated with an insulator layer) in contact with an electrolyte solution can be estimated from the changes of the radius of curvature of the strip. If the potential of the electrode changes, electrochemical processes resulting in the change of γ_s can take place exclusively on the metal side of the sample. The change in the surface stress induces a bending moment and the strip bends. In case of a thin metal film on a substrate if the thickness of the film t_f is sufficiently smaller than the thickness at of the plate, $t_S \gg t_f$, the change of γ_s can be obtained by an expression based on a generalized form of Stoney's equation

$$\Delta\gamma_s = k_i \Delta\left(\frac{1}{R}\right), \tag{4.24}$$

where k_i depends on the design of the electrode. In the simplest case [see Eq. (4.23)]:

$$k_i = \frac{E_S t_S^2}{6(1 - \nu_s)}, \tag{4.25}$$

where E_S, ν_S, and R are Young's modulus, Poisson's ratio, and radius of curvature of the plate, respectively. It should be noted that a number of authors have tried to modify Stoney's approach over the years, and several modified equations have been derived; however, these equations can usually be written in a form equivalent to Eq. (4.24) [126–129].

The values of $\Delta(1/R) = \Delta\gamma_{\mathrm{s}}/k_{\mathrm{i}}$ can be calculated (a) if the changes of the deflection angle of a laser beam mirrored by the cantilever are measured using an appropriate experimental setup (Fig. 4.16) (the optical detection techniques most used are optical beam deflection and interferometry, discussed in Chap. 5) or (b) the deflection of the plate is determined directly, e.g., with a nanoindenter, an atomic force microscope (AFM), or a scanning tunneling microscope, etc. (discussed in Chap. 6).

The combination of the two methods was used in [130–132]. In order to improve the sensitivity and stability of the technique, microfabricated cantilevers, usually employed in atomic force microscopes, were used instead of thin, but still macroscopic plates [131], and the deflection of the cantilever was measured with an optical lever using the head of a commercially available atomic force microscope. The deflection detection has been calibrated before each experiment: The end of the cantilever was pushed a defined distance upward by a piezoelectric crystal, and the corresponding change in the photodiode signal was measured. However, as it is well known from elasticity theory, when pushing the end of the cantilever (a bar with rectangular cross section) downward or upward ("concentrated load mode"), its shape is not circular anymore, but it is described by a third-order polynomial. Using the notation in Fig. 4.15

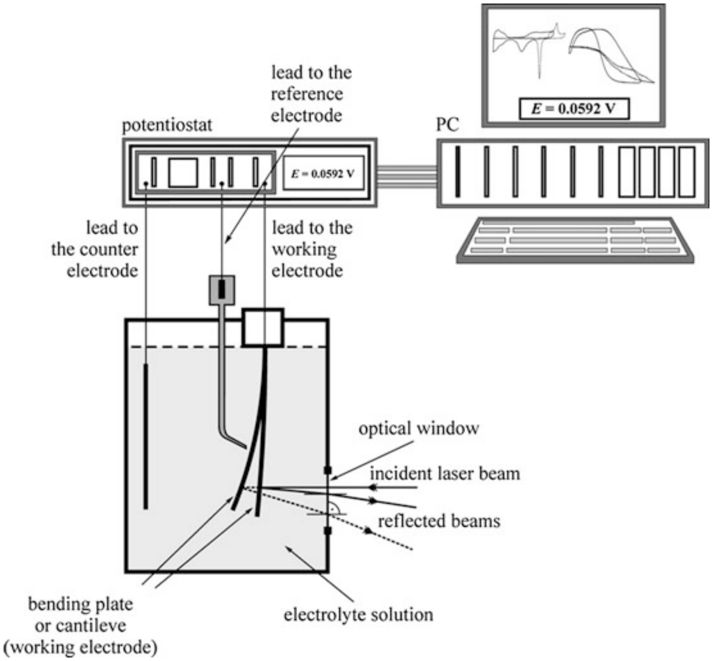

Fig. 4.16 Schematic of experimental setup for electrochemical bending beam measurements

$$z(x) = -\frac{F}{EI}\left(\frac{lx^2}{2} - \frac{x^3}{6}\right), \tag{4.26}$$

where l is the length of the cantilever and I is the second moment of area (moment of inertia)

$$I = \int_A z^2 \mathrm{d}A.$$

The slope of the beam is

$$\frac{\mathrm{d}z(x)}{\mathrm{d}x} = -\frac{F}{EI}\left(lx - \frac{x^2}{2}\right), \tag{4.27}$$

and in case of small deflections ($l \approx L$) at the end of the cantilever,

$$\frac{\mathrm{d}z(L)}{\mathrm{d}x} \approx -\frac{FL^2}{2EI} = \frac{3}{L}z(L). \tag{4.28}$$

For circular bending, the deflection can be calculated as (Fig. 4.17)

$$z(x) = (R^2 - x^2)^{1/2} - R. \tag{4.29}$$

The slope of the beam is

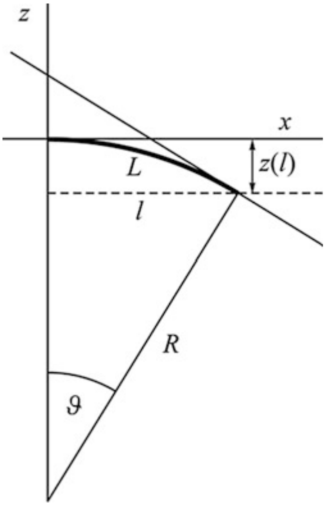

Fig. 4.17 The cylindrical bending of the cantilever. At small deflection, $z(l) \ll R$ and $L \approx l$

$$\frac{\mathrm{d}z(x)}{\mathrm{d}x} = -\frac{x}{\left(R^2 - x^2\right)^{1/2}}. \tag{4.30}$$

At the end of the beam, at small deflections,

$$\frac{\mathrm{d}z(L)}{\mathrm{d}x} \approx -\frac{L}{\left(R^2 - L^2\right)^{1/2}}, \tag{4.31}$$

and so

$$\frac{1}{R} \approx \frac{2z(L)}{L^2}. \tag{4.32}$$

It is clear that if the beam is pushed upward or downward at its end (i.e., during calibration), the inclination cannot be described by Eq. (4.31).

In [130, 131], the deflection, z, and inclination were related by

$$\frac{\mathrm{d}z(L)}{\mathrm{d}x} = \frac{3}{2L} z(L), \tag{4.33}$$

since the shape of V-shaped cantilevers was taken to be equivalent to two rectangular cantilevers of the same length [133, 134]. During surface stress measurements, the signal of a photodiode was recorded. Since the instrument was calibrated, this signal corresponded to a "virtual" deflection, i.e., the deflection it would have if the cantilever were not bent circular, as described by Eq. (4.31), but if it was pushed by a force applied to its end, as described by Eq. (4.33). With Eq. (4.33), the "virtual" deflection has been converted into d$z(L)$/dx. The reciprocals radius of curvature was calculated by comparing Eqs. (4.31) and (4.33):

$$\frac{1}{R} = \frac{3z(L)}{L\left[4L^2 + 9z(L)^2\right]^{1/2}} \approx \frac{3z(L)}{2L^2}, \tag{4.34}$$

where $z(L)$ is the deflection signal of the calibrated instrument. The accuracy of the method has been reported to be better than 0.005 J m^{-2}. A similar calibration of the cantilever setup was performed in other studies [135, 136]. A condition for the validity of the calibration procedure is that the laser is reflected from the same position along the length of the cantilever in each experiment, typically near the free end of the cantilever. Nevertheless, this is often not easy to accomplish. Measurements of the bending of commercial rectangular cantilevers under the concentrated load mode and the bending moment mode were reported in [137]. A detailed theoretical study of the effects of homogeneous surface stress on rectangular AFM cantilever plates has been presented in [138, 139].

It has been found in [140] that as long as the deflection is much smaller than the overall length of the cantilever, the radius of curvature of the cantilever is to a good approximation constant over its length when exposed to an isotropic surface stress.

As it has already been mentioned above, if the equation of the bending plate is known, the corresponding radius of curvature can be therefore calculated using Eq. (4.35), which is analogous to Eq. (4.17):

$$\frac{1}{R} = -\frac{z''(x)}{\left\{1 + [z'(x)]^2\right\}^{3/2}}. \tag{4.35}$$

According to the theory of elasticity, the deflected shape of a composite beam can be represented in terms of elementary functions. Since the deflection is smaller than the specimen length, the quadratic function,

$$z(x) = ax^2 + bx + c, \tag{4.36}$$

is a reasonable approximation of the bending profile [141]. It has been shown in [142] that in case of coated plates, the bending of the sample is accurately fitted by the quadratic function. The theory was also confirmed in [143, 144]. In [142], the equation for the bending plate could be written as $y = ax^2$, and so

$$\frac{1}{R} = -\frac{2a}{\left\{1 + (2ax)^2\right\}^{3/2}}.$$

Since $2ax \ll 1$, R is well approximated by

$$R = -\frac{1}{2a}, \tag{4.37}$$

and a can be determined as a function of the geometrical parameters of the bending beam setup and then related to R.

Nevertheless, it can be shown that the fact that there is practically no difference between "parabolic" and "circular" approaches is a mathematical consequence of the small deflection approximation.

Let us consider a circle C of radius R centered at a point O (Fig. 4.18). The equation of the circle

$$x^2 + (z + R)^2 = R^2,$$

can be written as

$$x^2 + z(z + 2R) = 0.$$

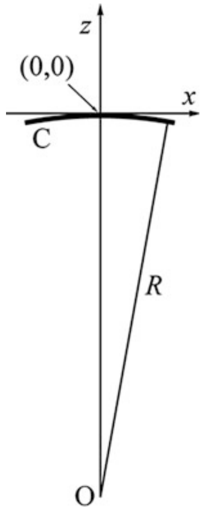

Fig. 4.18 A circle centered at (0, $-R$) with radius R

For $z \ll R$,

$$x^2 + 2Rz \approx 0,$$

and so

$$z \approx -\frac{1}{2R}x^2. \tag{4.38}$$

[Alternatively,

$$z = \sqrt{R^2 - x^2} - R = R\sqrt{1 - \frac{x^2}{R^2}} - R \approx R\left(1 - \frac{x^2}{2R^2}\right) - R = -\frac{1}{2R}x^2,$$

and the result is identical to Eq. (4.38).]

By comparing Eq. (4.38) with Eq. (4.36), we get Eq. (4.37). On the other hand Eq. (4.36), can be rewritten as

$$x^2 + \frac{b}{a}x + \frac{c}{a} = \frac{z}{a}.$$

With $c = 0$

$$x^2 + z^2 - z^2 - \frac{z}{a} + \frac{b}{a}x = 0,$$

or

$$x^2 + \left(z - \frac{1}{2a}\right)^2 = \frac{1 - 4abx + 4a^2z^2}{4a^2}.$$

If $|4a(bx - az^2)| \ll 1$, then

$$x^2 + \left(z - \frac{1}{2a}\right)^2 = \frac{1}{4a^2}.$$

The last being the equation of a circle centered at $(0, \frac{1}{2a})$ and radius $R = \frac{1}{2a}$.

It should be noted that in the case of a cubic polynomial, the situation is much more complicated, and the shape of the cantilever cannot be characterized by a single radius of curvature.

References

1. Linford RG (1978) Chem Rev 78:81–95
2. Láng G, Heusler KE (1994) J Electroanal Chem 377:1–7
3. Heusler KE, Láng G (1997) Electrochim Acta 42:747–756
4. Guidelli R (1998) J Electroanal Chem 453:69–77
5. Láng G, Heusler KE (1999) J Electroanal Chem 472:168–173
6. Guidelli R (1999) J Electroanal Chem 472:174–177
7. Valincius G (1999) J Electroanal Chem 478:40–49
8. Lipkowski J, Schmickler W, Kolb DM, Parsons R (1998) J Electroanal Chem 452:193–197
9. Couchman PR, Jesser WA, Kuhlmann-Wilsdorf D (1972) Surf Sci 33:429–436
10. Couchman PR, Jesser WA (1973) Surf Sci 34:212–224
11. Couchman PR, Everett DW, Jesser WA (1975) J Colloid Interface Sci 52:410–411
12. Rusanov AI (1978) J Colloid Interface Sci 63:330–345
13. Rusanov AI (1989) Pure Appl Chem 61:1945–1948
14. Rusanov AI (1996) Surf Sci Rep 23:173–247
15. Everett DW, Couchman PR (1976) J Electroanal Chem 67:382–386
16. Grafov BM, Paasch G, Plieth W, Bund A (2003) Electrochim Acta 48:581–587
17. Marichev VA (2006) Surf Sci 600:4527–4536
18. Marichev VA (2007) Chem Phys Lett 434:218–221
19. Marichev VA (2008) Prot Met 44:99–104
20. Marichev VA (2010) Adv Colloid Interface Sci 157:34–60
21. Marichev VA (2010) Prot Met 46:383–402
22. Bikerman JJ (1978) Surface energy of solids. In: Dewar MJS, Hafner K, Heilbronner E, Ito S, Lehn J-M, Niedenzu K, Rees CW, Schaefer K, Wittig G, Boschke FL (eds) Topics in current chemistry, vol 77. Springer, Berlin
23. Adamson AW (1967) Physical chemistry of surfaces. Interscience, New York (Chap. 5)
24. Mays CW, Vermaak JS, Kuhlmann-Wilsdorf D (1968) Surf Sci 12:134–140
25. Wassermann HJ, Vermaak JS (1970) Surf Sci 22:164–172
26. Wassermann HJ, Vermaak JS (1972) Surf Sci 32:168–174
27. Cammarata RC, Sieradzki K (1994) Annu Rev Mater Sci 24:215–234
28. Cammarata RC (1994) Prog Surf Sci 46:1–38

29. Ibach H (1997) Surf Sci Rep 29:193–263
30. Fredlein RA, Damjanovic A, Bockris JO'M (1971) Surf Sci 25:261–264
31. Fredlein RA, Bockris JO'M (1974) Surf Sci 46:641–652
32. Sahu SN, Scarminio J, Decker F (1990) J Electrochem Soc 137:1150–1154
33. Tian F, Pei JH, Hedden DL, Brown GM, Thundat T (2004) Ultramicroscopy 100:217–233
34. Cattarin S, Pantano E, Decker F (1999) Electrochem Commun 1:483–487
35. Cattarin S, Decker F, Dini D, Margesin B (1999) J Electroanal Chem 474:182–187
36. Raiteri R, Butt HJ, Grattarola M (1998) Scanning Microsc 12:243–251
37. Kongstein OE, Bertocci U, Stafford GR (2005) J Electrochem Soc 152:C116–C123
38. Stafford GR, Bertocci U (2006) J Phys Chem B 110:15493–15498
39. Gokhshtein AYa (1976) Surface tension of solids and adsorption. Nauka, Moscow
40. Gokhshtein AYa (1966) Elektrokhimiya 2:1318–1326
41. Gokhshtein AYa (1968) Elektrokhimiya 4:619–624
42. Gokhshtein AYa (1968) Elektrokhimiya 4:665–670
43. Gokhshtein AYa (1968) Dokl Akad Nauk SSSR 181:385–388
44. Gokhshtein AYa (1969) Elektrokhimiya 5:637–638
45. Gokhshtein AYa (1969) Dokl Akad Nauk SSSR 187:601–604
46. Gokhshtein AYa (1970) Electrochim Acta 15:219–223
47. Gokhshtein AYa (1970) Elektrokhimiya 6:979–985
48. Gokhshtein AYa (1971) Elektrokhimiya 7:3–17
49. Gokhshtein AYa (1971) Dokl Akad Nauk SSSR 200:620–623
50. Gokhshtein AYa (1972) Elektrokhimiya 8:1260–1260
51. Gokhshtein A (1975) Ya. Russ Chem Rev 44:921–932
52. Gokhshtein AYa (2000) Physics-Uspekhi 43:725–750
53. Malpas RE, Fredlein RA, Bard AJ (1979) J Electroanal Chem 98:171–180
54. Malpas RE, Fredlein RA, Bard AJ (1979) J Electroanal Chem 98:339–343
55. Handley LJ, Bard AJ (1980) J Electrochem Soc 127:338–343
56. Dickinson KM, Hanson KE, Fredlein RA (1992) Electrochim Acta 37:139–141
57. Seo M, Makino T, Sato N (1986) J Electrochem Soc 133:1138–1142
58. Seo M, Jiang XC, Sato N (1987) J Electrochem Soc 134:3094–3098
59. Seo M, Jiang XC, Sato N (1989) Electrochim Acta 34:1157–1158
60. Jiang XC, Seo M, Sato N (1990) Corros Sci 31:319–324
61. Jiang XC, Seo M, Sato N (1990) J Electrochem Soc 137:3804–3808
62. Jiang XC, Seo M, Sato N (1991) J Electrochem Soc 138:137–140
63. Seo M, Aomi M (1992) J Electrochem Soc 139:1087–1090
64. Seo M, Aomi M (1993) J Electroanal Chem 347:185–194
65. Seo M, Aomi M, Yoshida K (1994) Electrochim Acta 39:1039–1044
66. Seo M, Ueno K (1996) J Electrochem Soc 143:899–904
67. Ueno K, Seo M (1998) Denki Kagaku 66:713–719
68. Ueno K, Seo M (1999) J Electrochem Soc 146:1496–1499
69. Valincius G (1998) Langmuir 14:6307–6319
70. Valincius G, Reipa V (2000) J Electrochem Soc 147:1459–1466
71. Morcos I (1978) The interfacial tension of solid electrodes. In: Thirsk HR (ed) Specialist periodical reports: electrochemistry, vol 6. The Chemical Society, Burlington House, London
72. Morcos I, Fischer H (1968) J Electroanal Chem 17:7–11
73. Morcos I (1972) J Phys Chem 76:2750–2753
74. Morcos I (1972) J Chem Phys 56:3996–4000
75. Jaeckel L, Láng G, Heusler KE (1994) Electrochim Acta 39:1031–1038
76. Ibach H, Bach CE, Giesen M, Grossmann A (1997) Surf Sci 375:107–119
77. Haiss W (2001) Rep Prog Phys 64:591–648
78. Láng G, Seo M, Heusler KE (2005) J Solid State Electrochem 9:347–353
79. Trasatti S, Parsons R (1986) Pure Appl Chem 58:437–454
80. Beck TR (1969) J Phys Chem 73:466–468

81. Lin KF, Beck TR (1976) J Electrochem Soc 123:1145–1151
82. Láng GG, Ueno K, Ujvári M, Seo M (2000) J Phys Chem B 104:2785–2789
83. Láng G, Heusler KE (1997) J Chem Soc Faraday Trans 93:583–589
84. Láng G, Heusler KE (1995) J Electroanal Chem 391:169–179
85. Láng G, Heusler KE (1995) Russ J Electrochem 31:759–767
86. Beck TR, Beach KW (1974) Measurement of changes in surface stress of electrodes. In: Breiter MW (ed) Proceedings of the symposium on electrocatalysis. The Electrochemical Society, Princeton
87. Lin KF (1978) J Electrochem Soc 125:1077–1078
88. Beck TR, Lin KF (1979) J Electrochem Soc 126:252–256
89. Horváth Á, Schiller R (2001) Phys Chem Chem Phys 3:2662–2667
90. Smetanin M, Kramer D, Mohanan S, Herr U, Weissmüller J (2009) Phys Chem Chem Phys 11:9008–9012
91. Craig PP (1969) Phys Rev Lett 22:700–703
92. Unal K, Wickramasinghe HK (2007) Appl Phys Lett 90:113111
93. Horváth Á, Nagy G, Schiller R (2010) Phys Chem Chem Phys 12:7290–7290
94. Smetanin M, Deng Q, Kramer D, Mohanan S, Herr U, Weissmüller J (2010) Phys Chem Chem Phys 12:7291–7292
95. Weissmüller J, Viswanath RN, Kramer D, Zimmer P, Würschum R, Gleiter H (2003) Science 300:312–315
96. Kramer D, Viswanath RN, Weissmüller J (2004) Nano Lett 4:793–796
97. Butler MA, Ginley DS (1987) J Electrochem Soc 134:510–511
98. Butler MA, Ginley DS (1988) J Electrochem Soc 135:45–51
99. Zehnder L (1891) Z Instrumentenk 11:275–285
100. Mach L (1892) Z Instrumentenk 12:89–93
101. Möller G (1908) Ann Physik 27:665–711
102. Möller G (1908) Z Phys Chem 65:226–234
103. Froumkin AN (1936) Actualites Scientifiques et Industrielles 373:5–36
104. Morcos I (1975) J Electroanal Chem 62:313–340
105. Batrakov VV, Makarov AG (2003) Russ J Electrochem 39:1351–1511
106. Willman KW, Murray RW (1983) Anal Chem 55:1139–1142
107. Wang W, Murray RW (2007) Anal Chem 79:1213–1220
108. Sparnaay MJ (1964) Surf Sci 1:213–224
109. Chazalviel JN, Maroun F, Ozanam F (2004) J Electrochem Soc 151:E51–E55
110. Neumann AW (1964) Z Phys Chem Neue Folge 41:339–352
111. Morcos I (1971) J Colloid Interface Sci 37:410–421
112. Chen JH, Nie LH, Yao SZ (1996) J Electroanal Chem 414:53–59
113. Xie Q, Zhang Y, Xiao X, Guo Y, Wang X, Yao S (2001) Anal Sci 17:265–275
114. Stoney GG (1909) Proc Roy Soc London A 32:172–175
115. Láng GG (2008) Bending beam method. In: Bard AJ, Inzelt G, Scholz F (eds) Electrochemical dictionary. Springer, Berlin
116. Láng GG, Sas Ns, Vesztergom S (2009) Chem Biochem Eng Q 23:1–9
117. Lehmann V (1996) J Electrochem Soc 143:1313–1318
118. Pei Q, Inganas O (1992) J Phys Chem 96:10507–10514
119. Asaka K, Oguro K (2000) J Electroanal Chem 480:186–198
120. Láng GG, Ujvári M, Rokob TA, Inzelt G (2006) Electrochim Acta 51:1680–1694
121. Ohring M (1992) The materials science of thin films. Academic, San Diego
122. Hoffman RW (1966) The mechanical properties of thin condensed films. In: Hass G, Thun RE (eds) Physics of thin films, vol 3. Academic, New York
123. Brenner A, Senderoff S (1949) J Res Nat Bur Stand 42:105–123
124. Klokholm E (1969) Rev Sci Instrum 40:1054–1058
125. Klein C, Miller RP (2000) J Appl Phys 87:2265–2272
126. Klein C (2000) J Appl Phys 88:5487–5489

127. Pureza JM, Lacerda MM, De Oliveira AL, Fragalli JF, Zanon RAS (2009) Appl Surf Sci 255:6426–6428
128. Pureza JM, Neri F, Lacerda MM (2010) Appl Surf Sci 256:4408–4410
129. Janssen GCAM, Abdalla MM, van Keulen F, Pujada BR, van Venrooy B (2009) Thin Solid Films 517:1858–1867
130. Raiteri R, Butt HJ (1995) J Phys Chem 99:15728–15732
131. Butt HJ (1996) J Coll Interf Sci 180:251–260
132. Raiteri R, Butt HJ, Grattarola M (2000) Electrochim Acta 46:157–163
133. Gould SAC, Drake B, Prater CB, Weisenhorn AL, Manne S, Kelderman GL, Butt HJ, Hansma H, Hansma PK, Magonov S, Cantow HJ (1990) Ultramicroscopy 33:93–98
134. Butt HJ, Siedle P, Seifert K, Fendler K, Seeger T, Bamberg E, Weisenhorn AL, Goldie K, Engel A (1993) J Microsc 169:75–84
135. Friesen C, Dimitrov N, Cammarata C, Sieradzki K (2001) Langmuir 17:807–815
136. Vasiljevic N, Trimble T, Dimitrov N, Sieradzki K (2004) Langmuir 20:6639–6643
137. Miyatani T, Fujihira M (1997) J Appl Phys 81:7099–7115
138. Sader JE (2002) J Appl Phys 89:2911–2921
139. Sader JE (2002) J Appl Phys 91:9354–9361
140. Godin M, Tabard-Cossa V, Grütter P (2001) Appl Phys Lett 79:551–553
141. Suhir E (1988) J Appl Mech 55:143–148
142. Moulard G, Contoux G, Motyl G, Gardet G, Courbon M (1998) J Vac Sci Technol 16:736–742
143. Schwarzer N, Richter F, Hecht G (1993) Surf Coat Technol 60:396–400
144. Ramsey PM, Chandler HW, Page TF (1990) Surf Coat Technol 43(44):223–233

Chapter 5
Optical Detection of the Deformation

5.1 Direct Optical Position Sensing

5.1.1 Experimental Arrangements

Measuring the bending of a plate or strip to determine surface (interface) stress change or the stress in thin films is a common technique, even in electrochemistry [1–13].

Figure 5.1 shows a typical arrangement for electrochemical bending beam (bending cantilever, wafer curvature measurement) experiments with optical detection [13]. Such a setup can be used mainly for the investigation of small deflections, and several details may be different in special cases. For instance, the cantilever (beam) can also be mounted horizontally (Fig. 5.2). The advantage with this arrangement is that no optical window is necessarily required; however, it suffers from the fact that the clamping of the cantilever is immersed into the solution. This may cause electrical connection problems in electrochemical systems, and may constitute a source of contamination. In addition, the maintenance of an inert gas atmosphere without traces of oxygen is very often essential to perform electrochemical measurements. The use of an electrochemical cell open to air can lead to significant experimental errors.

On the other hand, optical lever detection is currently used in all but a few commercial AFM instruments. Cantilever-based sensors have been shown to be capable of measuring surface stress changes [14, 15]. The experimental arrangement used, for example, in [16–18], is presented in Fig. 5.3.

Another method particularly suitable for in situ curvature monitoring is the multiple-beam optical sensor (MOS) technique [19], inspired by the two-beam sensor studied in [20]. With this technique, the distances between a one-dimensional array of multiple laser reflections of the cantilevered substrate can be continuously monitored with a charge-coupled device (CCD) camera.

One advantage of using a multibeam configuration instead of a single-beam one is a reduced sensitivity toward vibrations, while maintaining a high time resolution

G.G. Láng and C.A. Barbero, *Laser Techniques for the Study of Electrode Processes*,
Monographs in Electrochemistry, DOI 10.1007/978-3-642-27651-4_5,

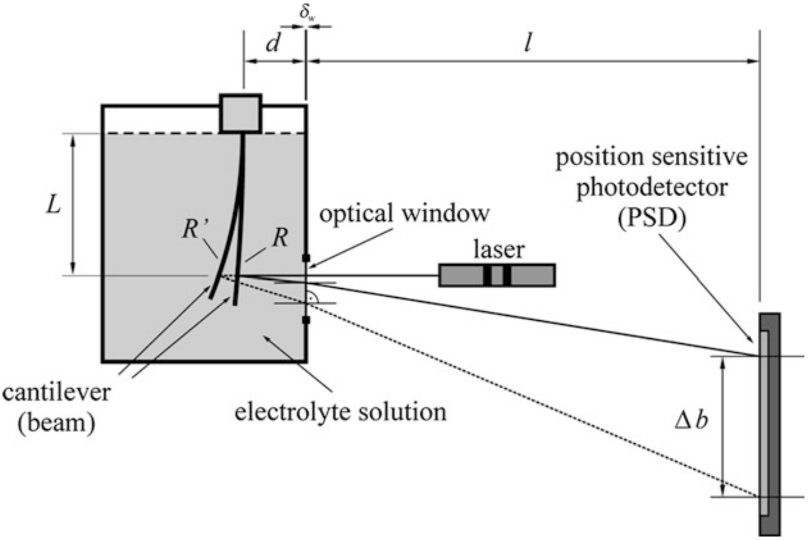

Fig. 5.1 Schematic representation of a typical electrochemical (optical) bending beam setup. Δb is the displacement of the light spot on the position-sensitive detector (PSD) if the radius of curvature changes from R to R', d is the distance between the clamped end of the probe (cantilever, electrode) and the optical window, l is the distance between the optical window and the photodetector (PSD), L is the distance between the solution level and the reflection point, and δ_w is the thickness of the optical window, respectively

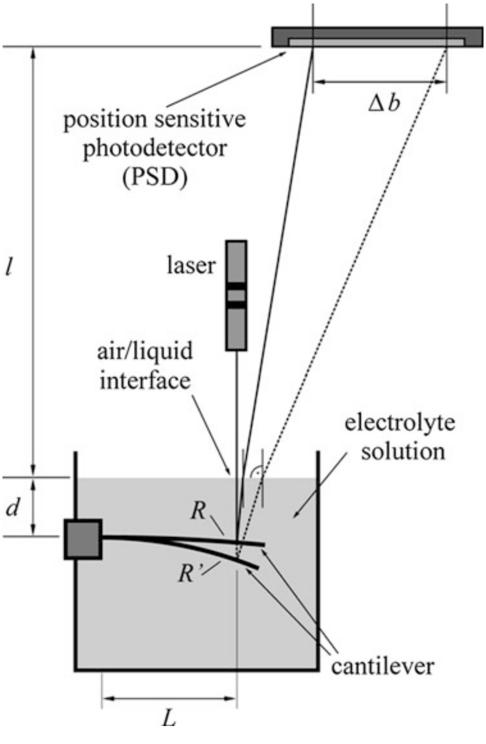

Fig. 5.2 Optical bending beam setup with horizontally mounted cantilever

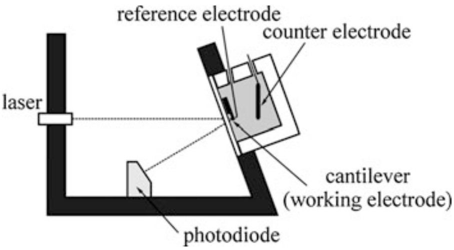

Fig. 5.3 Schematic diagram of the AFM detection system combined with an electrochemical cell. Adapted from [16]

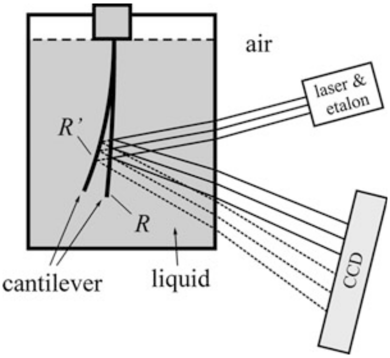

Fig. 5.4 The MOS setup in electrochemical systems

(Fig. 5.4). Vibrations of the sample, laser source, and detector are expected to affect every laser beam in the same manner so that the instantaneous spacings are expected to be virtually unaffected.

The multibeam technique has been successfully used for in situ monitoring of the stresses generated in metal or ceramic thin films deposited in vacuum by chemical vapor deposition, physical vapor deposition, or molecular beam epitaxy [21–28].

5.1.2 Basic Principles

The classical bending beam method (with single laser beam optical detection) is based on the specular (mirrorlike) reflection of light from surfaces. The law of reflection states that the angle of incidence (incoming light ray) is equal to the angle of reflection (reflected light ray). The angles are measured from a normal line (perpendicular) drawn to the surface at the point of reflection. With spherical or cylindrical mirrors, reflection of light occurs at a curved surface. The law of reflection holds since at each point on the curved surface one can draw a surface tangent and erect a normal to a point P on the surface where the light is incident, as shown in Fig. 5.5.

One then applies the law of reflection at point P, with the incident and reflected rays making the same angles (α and β) with the normal to the surface at P.

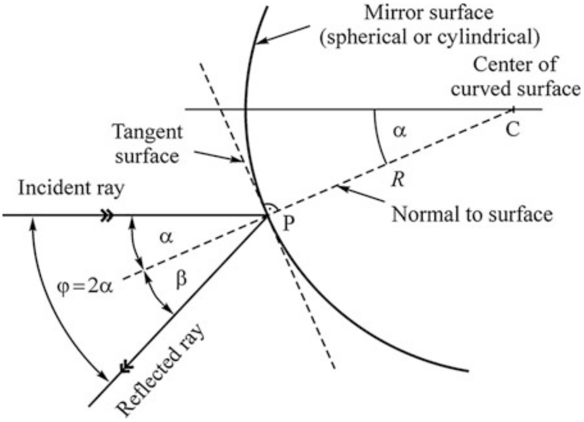

Fig. 5.5 Reflection from a convex-mirroring surface. The incident ray is parallel to the mirror axis (principal axis)

Since point *P* can be moved anywhere along the curved surface and a normal drawn there, we can always find the direction of the reflected ray by applying the law of reflection. One has to apply this technique when studying the way mirrors (or segments of mirrors) reflect light to form images [29–32].

According to Fig. 5.5, the total angle of deflection of the ray is

$$\varphi = 2\alpha. \tag{5.1}$$

In Fig. 5.6, the reflection by a concave surface is shown. By using the trigonometric small-angle approximation $\sin\theta \approx \tan\theta \approx \theta$, $\sin 2\theta \approx \tan 2\theta \approx 2\theta$, and $\cos\theta \approx 1$, the following equations can be derived:

$$L = 2R\sin\theta\cos\theta \approx 2R\theta, \tag{5.2}$$

and

$$\frac{1}{R} \approx \frac{2\theta}{L}. \tag{5.3}$$

By taking into account the law of reflection, it can be seen from Fig. 5.6 that the total angle of deflection of the light beam is

$$\varphi = 4\theta. \tag{5.4}$$

The optical scheme of the bending beam arrangement in air or vacuum is shown in Fig. 5.7. In this case, the expression for the deflection of the laser beam can be given as:

$$b = w\sin\varphi \approx s\varphi = 4s\theta; \tag{5.5}$$

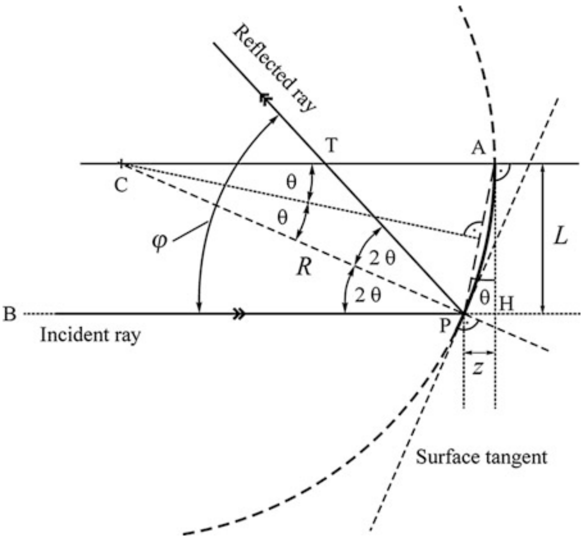

Fig. 5.6 Scheme for the derivation of the relationship between the deflection angle (φ) and the radius of curvature (R)

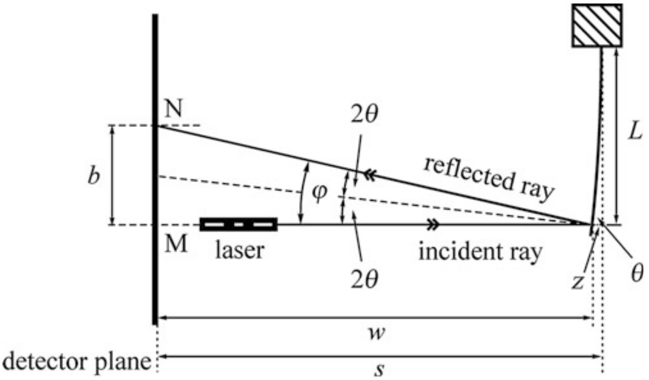

Fig. 5.7 Optical configuration of the bending beam setup in vacuum or air (z is the deflection of the cantilever, s is the distance between the clamped end of the cantilever and the detector plane, and w is the distance between the detector plane and the reflection point, respectively)

therefore

$$\theta \approx \frac{b}{4s}, \tag{5.6}$$

and by substituting Eq. (5.6) into Eq. (5.3), we arrive at the approximate equation

$$\frac{1}{R} \approx \frac{b}{2Ls}. \tag{5.7}$$

(Recently, it has been claimed [33] that Eq. (5.7) is incorrect, and the correct expression for $1/R$ is

$$\frac{1}{R} \approx \frac{b}{Ls}.$$

However, it has been shown [34] that the proposed equation is clearly erroneous due to an error in the derivation [35].)

5.1.3 Effect of Refraction

Although the bending beam technique is already well established for monitoring of curvature changes in vacuum or in gaseous environment, its application in multiphase systems is not without problems.

In many papers reporting results on electrochemical bending beam experiments (i.e., experiments carried out in systems consisting a liquid phase), schemes of experimental arrangements can be found in which the direction of the reflected beam before and after passing the optical window or the air/solution boundary is indicated incorrectly since the effect of refraction is ignored. In addition, no reference is made to the refractive index of the solution, or the value of the refractive index is not reported in the papers [see, e.g., 1, 2, 4–7, 36].

This problem was first discussed in [37] for the special case of normal incidence. It is clear that if the incident beam is exactly perpendicular to the optical window (or to the air/solution interface [38]), no refraction occurs, which makes the situation simpler and the calculations easier. Consequences of refraction for the MOS technique have been outlined in [24].

As seen in Fig. 5.8, a laser beam coming from a direction normal to the plane of the optical window is reflected by the surface of the cantilever (point A). The incident beam is perpendicular to the optical window; therefore, no refraction occurs at C. The direction of the reflected beam is AC′, which coincides with the direction of C′M. Let the angle between CA and AC′ be φ. Without refraction at the optical window plane (at C′), the reflected beam would result in a light spot at M on the detector plane. [It is assumed that the (not necessarily lateral) shift of the light ray due to the optical window is negligible.]

However, because of the refraction at C′, the direction of the beam changes, its new direction is C′N, and a light spot at N can be detected. Let us denote the distance between P and M by a, the distance between P and N by b, and the angle between P′C′ (or PC) and C′N by β and consider the situation depicted in Fig. 5.8.

Obviously, only b can be determined by direct measurement because the light spot is located at position N, and there is no light spot on the detector at M. The distance between the cantilever and the photodetector is

$$w = d' + l, \tag{5.8}$$

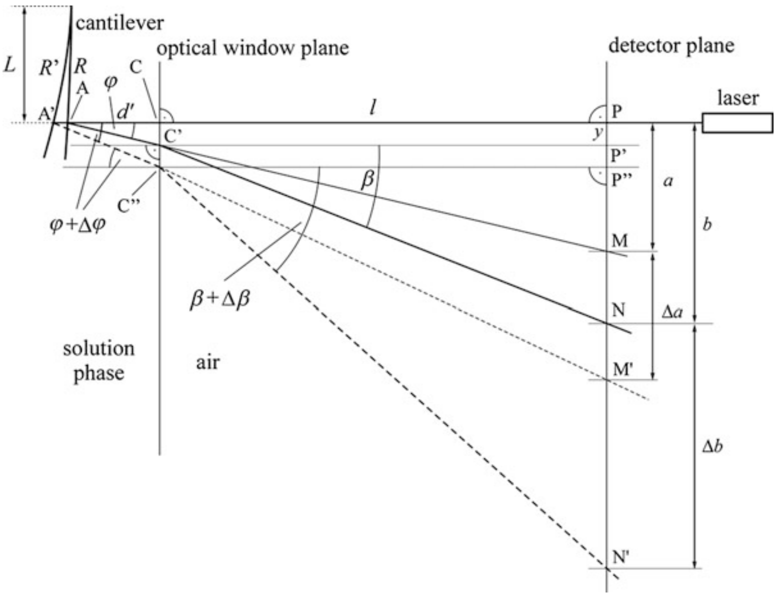

Fig. 5.8 Optical configuration of the bending beam setup in a system consisting a liquid phase

where d' is the distance between the optical window and the reflection point A and l is the distance between the optical window and the detector plane.

It should be noted here that d' differs from d in Fig. 5.1 by the deflection z of the cantilever (see Figs. 5.6 and 5.7), that is, $d' = d + z$.

If φ is very small, the radius of curvature of the cantilever can be well approximated as

$$R \approx \frac{2L}{\varphi}, \tag{5.9}$$

where L is the distance between the solution level (or the clamping of the cantilever) and the reflection point [see Eqs. (5.3) and (5.4)]. Sometimes, the half of the total deflection angle is denoted by ϑ, then $\vartheta = \varphi/2$, and $R \approx L/\vartheta$.

If y is the distance between P and P′ in the framework of the small-angle approximation, φ can be expressed as

$$\varphi \approx \tan\varphi = \frac{a}{w} = \frac{a-y}{l}. \tag{5.10}$$

The direct measurement of y is extremely difficult, if not impossible, in the usual experimental setup; however, it is practically always possible to arrange the electrode and the detector in such a manner that $l >> d'$. In this case, $y << a$, and with good approximation:

$$\varphi \approx \tan \varphi = \frac{a}{l} \approx \frac{a}{w}. \tag{5.11}$$

From the practical point of view, Eq. (5.11) means that for the determination of φ, the determination of the distances a and l (or a and w) is necessary.

However, it is well known that in the case of nonnormal incidence, if the deflection of a light beam is measured outside the phase where the mirroring surface is located, the deflection angle should usually be corrected. According to the Snellius–Descartes law of refraction (also known as law of refraction, Snell's law, Snel's law, or Snell–Descartes law), when light travels from one medium into another, the incident and refracted rays lie in one plane with the normal to the surface, are on opposite sides of the normal, and make angles with the normal whose sines have a constant ratio to one another. It means that due to the refraction, we cannot obtain a light spot on the detector plane at M (the position of which could be used for the determination of a and φ); only the light spot at N can be detected. As a consequence, only b is accessible experimentally.

According to the experimental setup in Figs. 5.1 and 5.8, the laser beam reflected from the lower end of the cantilever is incident on a position-sensitive detector. For small deflections,

$$\beta \approx \tan(\beta) = \frac{b - y}{l} = \frac{b - y}{w - d'}, \tag{5.12}$$

and if $l >> d'$ and $b >> y$, then

$$\frac{b}{w} \approx \tan(\beta) \approx \beta. \tag{5.13}$$

Thus, by measuring b and w, the approximate value of β can be determined experimentally. The problem is, however, that according to Eq. (5.9), for the correct determination of R, the value of φ (and not that of β) is necessary.

The relationship between φ and β can be obtained from the law of refraction:

$$\frac{\sin \varphi}{\sin \beta} = n_{\mathrm{a,s}} \approx \frac{1}{n_{\mathrm{s}}}, \tag{5.14}$$

where $n_{\mathrm{a,s}}$ is the (relative) refractive index of air with respect to the solution and n_{s} is the (absolute) refractive index of the solution. For small deflections,

$$\frac{\sin \varphi}{\sin \beta} \approx \frac{\varphi}{\beta} \approx \frac{1}{n_{\mathrm{s}}}; \tag{5.15}$$

therefore,

$$\varphi \approx \frac{\beta}{n_\mathrm{s}}, \tag{5.16}$$

and with Eqs. (5.13) and (5.16), the angle of deflection can be calculated as

$$\varphi \approx \frac{b}{n_\mathrm{s} w}. \tag{5.17}$$

Thus, taking into account Eq. (5.9), the radius of curvature of the cantilever can be given by the following approximate relationship:

$$R \approx \frac{2 n_\mathrm{s} L w}{b}. \tag{5.18}$$

If the conditions $l >> d'$ and $b >> y$ are not fulfilled (e.g., the detector is close to the optical window), Eq. (5.12) should be used instead of Eq. (5.13).

In this case, the expressions for φ and R are the following:

$$\varphi \approx \frac{b - y}{n_\mathrm{s} l}, \tag{5.19}$$

and

$$R \approx \frac{2 n_\mathrm{s} L l}{b - y}. \tag{5.20}$$

That is, the determination of R requires the accurate measurement of b, L, l, n_s, and y.

Equation (4.24) establishes a linear relationship between the surface stress change and the change in the curvature (reciprocal radius of curvature). This means that for the determination of the change in $\Delta\gamma_\mathrm{s}$, the value of $\Delta(1/R)$ is necessary.

Applying Eq. (5.18) for two different deflections of the cantilever (see Figs. 5.1 and 5.6), we arrive at the (approximate) equation

$$\Delta\left(\frac{1}{R}\right) \approx \frac{\Delta b}{2 L w n_\mathrm{s}} \approx \frac{\Delta b}{2 L w n_\mathrm{s,a}}, \tag{5.21}$$

where Δb is the displacement of the light spot on the position-sensitive detector due to the bending of the electrode and $n_\mathrm{s,a}$ is the refractive index of the solution with respect to air.

Equation (5.21) implies that without the refractive index of the solution, it is impossible to determine accurately the values of the radius of curvature (or the change of the reciprocal value of the radius of curvature) of the electrode. Since refractive indices of aqueous solutions are about 1.33–1.48, the complete neglect of the bending of the laser beam due to refraction at the optical window may cause an error of about 25–30% in the determination of $\Delta(1/R)$ or $\Delta\gamma_s$.

It should also be stressed that the dependence of on the wavelength of the light, that is, the dispersion, has to be taken into account.

In the light of the above results, it is clear that in electrochemical bending beam experiments, the effect of refraction at the optical window cannot be ignored.

5.1.4 Effects of Nonnormal Incidence

The effects of nonnormal incidence on the measured data have been discussed in [12, 33].

The optical configuration of the arrangement for electrochemical bending beam experiments with nonnormal incidence of the laser beam on the optical window is presented in Fig. 5.9.

As seen in Fig. 5.9, w is the distance between the cantilever (electrode) and the photodetector (PSD), d' is the distance between the optical window and the reflection point (B) on the cantilever, l is the distance between the optical window and the detector plane, and i is the length of the cantilever in the solution between the

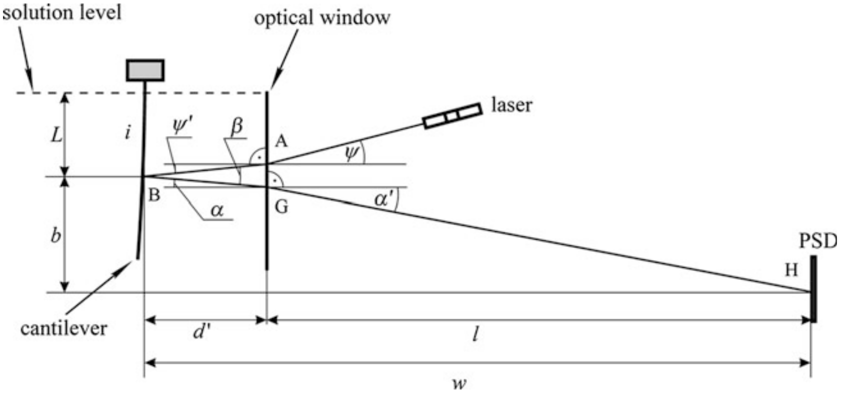

Fig. 5.9 Optical configuration of the arrangement for electrochemical bending beam experiments with nonnormal incidence. ψ is the angle of incidence of the light beam coming directly from the laser (in air), ψ' is the angle of refraction at point A, α is the angle of incidence at point G (the reflected light is coming from the solution phase), α' is the angle of refraction at G (a light spot on the detector can be observed at point H), w is the distance between the cantilever (electrode) and the photodetector, d' is the distance between the optical window and the reflection point (B) on the cantilever, l is the distance between the optical window and the position-sensitive detector (PSD), i is the length of the electrode in the solution, and L is the distance between the solution level and B, respectively

solution level and the reflection point, respectively. The angle of incidence of the light beam coming directly from the laser (located in air) is ψ. Due to refraction at the optical window (at point A), the direction of the beam changes, its new direction (in the solution) is AB, and the angle of refraction is ψ'. In the following derivations, for simplicity, the shift of the path of light in the glass wall is neglected.

The laser beam arriving from the direction AB (in the solution) is reflected at point B on the surface of the cantilever. The direction of the reflected beam (which strikes the surface of the optical window with an angle of incidence of α) is BG. Because of refraction at G, the direction of the reflected beam changes again, the new direction of it (in air) is GH, and the angle of refraction is α'. (Similarly to the incident beam, the lateral displacement of the path of light in the glass wall is neglected.) The reflected beam results in a light spot at H on the detector plane. If the radius of curvature of the electrode changes, a displacement of the light spot on the position-sensitive detector can be observed.

The w distance between the reflection point B and the position sensing photodetector can be given as

$$d' + l = w. \tag{5.22}$$

The distance b can be expressed with the help of the corresponding triangles:

$$b = d' \tan\alpha + l \tan\alpha'. \tag{5.23}$$

From Figs. 5.10 and 5.11 (in which the corresponding segment of the electrode with the incident and reflected light beam is magnified), we can see that

$$\alpha + \psi' = \beta, \tag{5.24}$$

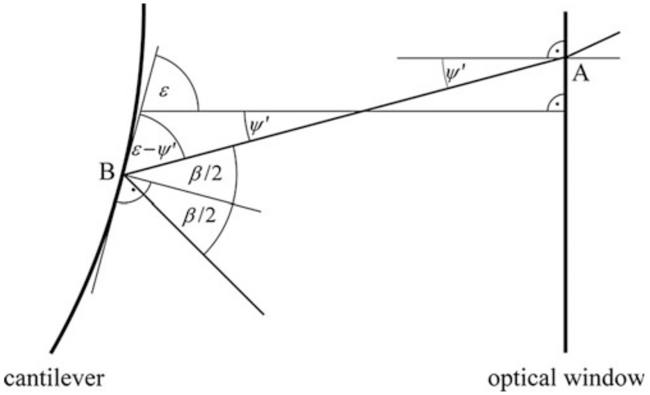

Fig. 5.10 Enlargement of the region around the reflection point B with the magnified segment of the cantilever and the (incident and reflected) light beams

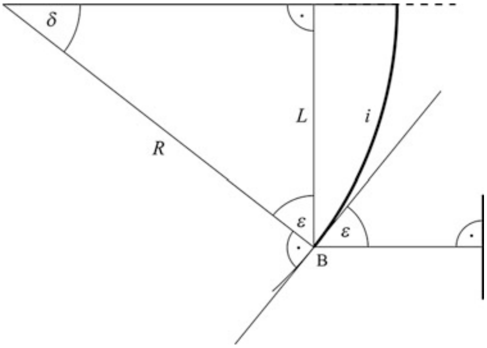

Fig. 5.11 The cantilever with the radius of curvature *R*

and

$$\delta = 90^\circ - \varepsilon. \tag{5.26}$$

Taking into account the rectangle triangle shown in Fig. 5.11, the angle δ can be expressed as

$$\frac{\beta}{2} = 90^\circ - (\varepsilon - \psi'). \tag{5.25}$$

By combining the above equations, one obtains

$$\alpha = 2\delta + \psi'. \tag{5.27}$$

To express α', that is, the angle between the normal to the optical window and the light beam exiting the electrochemical cell, we use Snell's law:

$$\frac{\sin \alpha'}{\sin \alpha} = n_{\mathrm{s,a}}, \tag{5.28}$$

where $n_{\mathrm{s,a}}$ is the refractive index of the solution with respect to air.

According to Eq. (5.22),

$$b = d' \tan \alpha + l \frac{\sin \alpha'}{\sqrt{1 - \sin^2 \alpha'}}, \tag{5.29}$$

and with Eqs. (5.27) and (5.28),

$$b = d' \tan(2\delta + \psi') + n_{\mathrm{s,a}} l \frac{\sin(2\delta + \psi')}{\sqrt{1 - n_{\mathrm{s,a}}^2 \sin^2(2\delta + \psi')}}. \tag{5.30}$$

The right-hand side of Eq. (5.30) contains only experimentally accessible quantities: d' and l are measurable (at least in principle) and the values of δ and ψ' can be determined knowing the incident angle of the beam, the refractive index ($n_{\mathrm{s,a}}$), and the radius of curvature of the plate (R). This means that Eq. (5.30) can be applied directly for the determination of b.

On the other hand, by using this expression, we can derive simpler equations for the change in b with δ. Differentiating the $b(\delta)$ function with respect to δ, we have

$$\frac{\mathrm{d}b}{\mathrm{d}\delta} = 2d'\frac{1}{\cos^2(2\delta+\psi')} + 2n_{\mathrm{s,a}}l\frac{\cos(2\delta+\psi')}{\left[1-n_{\mathrm{s,a}}^2\sin^2(2\delta+\psi')\right]^{\frac{3}{2}}}. \tag{5.31}$$

By taking into account Eqs. (5.27) and (5.28), the above equation can be rewritten into a simpler form:

$$\frac{\mathrm{d}b}{\mathrm{d}\delta} = 2d'\frac{1}{\cos^2\alpha} + 2n_{\mathrm{s,a}}l\frac{\cos\alpha}{\cos^3\alpha'}. \tag{5.32}$$

It can be easily shown that the factor multiplying $n_{\mathrm{s,a}}$ in the second term of the RHS of Eq. (5.31) is always greater than one:

Obviously, $\alpha' \geq \alpha$ since the solution is the optically denser medium. However, from $\alpha' \geq \alpha$ follows that

$$\cos^3\alpha' \leq \cos\alpha' \leq \cos\alpha \leq 1,$$

and therefore,

$$\frac{\cos\alpha}{\cos^3\alpha'} \geq 1. \tag{5.33}$$

Since

$$\mathrm{d}\delta = i\mathrm{d}\left(\frac{1}{R}\right), \tag{5.34}$$

by using Eq. (5.24), the following expression can be obtained:

$$\frac{\mathrm{d}b}{\mathrm{d}(1/\mathrm{R})} = 2id'\frac{1}{\cos^2((2i/R)+\psi')} + 2in_{\mathrm{s,a}}l\frac{\cos((2i/R)+\psi')}{\left[1-n_{\mathrm{s,a}}^2\sin^2((2i/R)+\psi')\right]^{3/2}}. \tag{5.35}$$

It should be stressed that except for the assumption that the thickness of the optical window is zero (see later), no approximations were used in the derivation of Eq. (5.35).

Let us now express Δb (i.e., the change of the position of the light spot on the position-sensitive detector plane) by using Snell's law

$$\frac{\sin\psi}{\sin\psi'} = n_{\mathrm{s,a}},$$

and the following assumptions: $\Delta(1/R)$ is small enough to use first-order approximation for the changes, $i \approx L$, and

$$2i/R = 2\delta << \psi'.$$

According to the above derivations,

$$\Delta b \approx \frac{\mathrm{d}b}{\mathrm{d(1/R)}}\Delta\left(\frac{1}{R}\right) \approx \\ \left[2Ld'\frac{1}{1-n_{\mathrm{s,a}}^{-2}\sin^2\psi} + 2Ln_{\mathrm{s,a}}l\frac{\left(1-n_{\mathrm{s,a}}^{-2}\sin^2\psi\right)^{1/2}}{\left(1-\sin^2\psi\right)^{3/2}}\right]\Delta\left(\frac{1}{R}\right). \tag{5.36}$$

In addition, if $d' << l$, that is, $w \approx l$,

$$\Delta b \approx 2Lwn_{\mathrm{s,s}}\left[\frac{\left(1-n_{\mathrm{s,a}}^{-2}\sin^2\psi\right)^{1/2}}{\left(1-\sin^2\psi\right)^{3/2}}\right]\Delta\left(\frac{1}{R}\right), \tag{5.37}$$

or

$$\Delta\left(\frac{1}{R}\right) \approx \frac{\Delta b}{2Lwn_{\mathrm{s,a}}}\left[\frac{\left(1-\sin^2\psi\right)^{3/2}}{\left(1-n_{\mathrm{s,a}}^{-2}\sin^2\psi\right)^{1/2}}\right] = \frac{\Delta b}{2Lwn_{\mathrm{s,a}}}\xi\left(\psi, n_{\mathrm{s,a}}\right). \tag{5.38}$$

The function $\xi(\psi, n_{\mathrm{s,a}})$ in square brackets in the above equation, expressing the effect of the incident angle, is monotonously decreasing with ψ (see Fig.5.12), and for $n_{\mathrm{s,a}} \approx 1.333$ (pure water at 20°C) and for $\psi = 10°$, it has the value of 0.963.

Selected values of $\xi(\psi, n_{\mathrm{s,a}})$ are presented in Table 5.1.

If the deflection of the electrode is small and ψ tends to zero ("normal incidence"), we get back the formula derived earlier for perpendicular incident light:

$$\Delta\left(\frac{1}{R}\right) \approx \frac{\Delta b}{2Lwn_{\mathrm{s,a}}}. \tag{5.39}$$

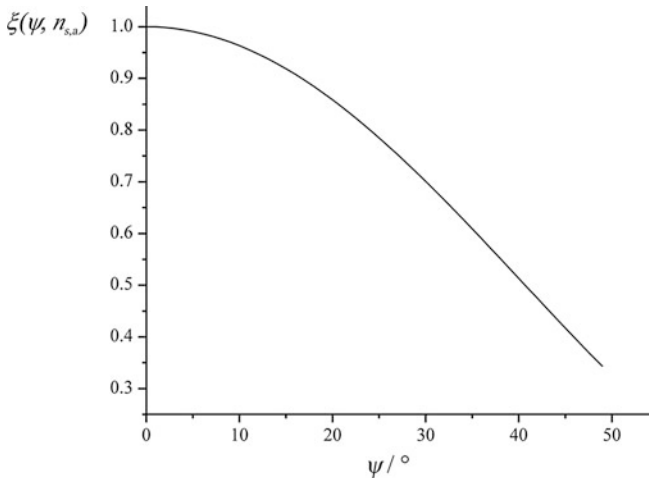

Fig. 5.12 The dependence of $\xi(\psi, n_{s,a})$ on the angle of incidence (ψ) for $n_{s,a} \approx 1.333$

Table 5.1 The dependence of $\xi(\psi, n_{s,a})$ on ψ for $n_{s,a} \approx 1.333$

ψ (deg.)	$n_{s,a}$	$\xi(\psi, n_{s,a})$
0	1.333	1
2	1.333	0.9985
5	1.333	0.9908
10	1.333	0.9633
20	1.333	0.8585
30	1.333	0.7007
40	1.333	0.5131
0	1.420	1
2	1.420	0.9985
5	1.420	0.9905
10	1.420	0.9623
20	1.420	0.8549
30	1.420	0.6940
40	1.420	0.5041

The above results are reassuring in that a slight optical misalignment resulting in nonnormal incidence of the laser beam (i.e., when ψ is in the range of 1°) will cause an error of only about 0.1% in the value of $\Delta(1/R)$. However, neglecting refraction and ignoring the effect of nonnormal incidence can lead to both erroneous conclusions and inaccurate results.

Of course, for accurate calculations, the dependence of $n_{s,a}$ on the wavelength of the light and temperature has to be taken into account. The data in Table 5.2 can provide an estimate of the error associated with these effects. (The 0.1 M aqueous sulfuric acid solution has been selected as an illustrative example.)

Table 5.2 The refractive index of 0.1 M H_2SO_4 solution (with respect) to air in dependence on wavelength at 25°C

Wavelength, λ (nm)	Refractive index, $n_{s,a}$
435.9 (Hg g)	1.34072
480.0 (Cd F′)	1.33799
546.1 (Hg e)	1.33500
587.6 (He d)	1.33359
643.8 (Cd C′)	1.33204
589.0 (calculated)	1.33353
632.8 (calculated)	1.33232

Refractive indexes were measured with a Zeiss PR 2 refractometer [Láng GG, Ujvári M (unpublished results)]

Table 5.3 Cauchy coefficients

Temperature, t (°C)	$A(t)$	$B(t)$ (nm^2)	10^{-8}°C(t) (nm^4)
25.0	1.324060	3,433.19221	5.11397529

For approximation of the presented data (rows 1–5), Cauchy's formula (with temperature-dependent coefficients) has been used:

$$n_{s,a}(\lambda, t) = A(t) + \frac{B(t)}{\lambda^2} + \frac{C(t)}{\lambda^4}.$$

The three Cauchy coefficients can be obtained by nonlinear least squares fitting (Table 5.3).

The refractive indices at 589.0 and 632.8 nm were calculated with the help of these coefficients. The latter value is important since He–Ne lasers operate at 632.8 nm. On the other hand, the refractive indices of liquids are conventionally measured by using an Abbe refractometer at sodium d-line wavelength (589.3 nm). If instead of the refractive index for 632.8 nm (red light, He–Ne laser) the value measured at 589.3 nm is used in the calculation, the estimated error in the deflection is about 0.1%.

From the data presented in Tables 5.2 and 5.4, it can be also concluded that a monochromator is essential if a broadband light source (with polychromatic or white light) is used in bending beam experiment. Since laser light is effectively monochromatic, the bending beam setup with laser light can be used without a monochromator. As a result, there is little loss of light, the beam remains sharp and narrow, and the apparatus can be made compact.

The effects arising from changes in the refractive index of the medium and initial bending of cantilevers were discussed in [40–42]. The refractive index of air depends strongly on the pressure, temperature, and humidity. Theoretical conversion from pressure to refractive index can be made by using the formulas given in [43]. The refractive index of dry CO_2-free air is to a very good approximation linear with pressure (p) in the range of interest $n_a = 1 + 2.5834 \times 10^{-7}\ p$/mbar. Initial bending is mainly a problem when using very sensitive polymer-based cantilevers,

Table 5.4 Refractive index of water [39]

Temperature (°C)	Wavelength (nm)		
	404.4	589.0	632.8
20	1.34315	1.33336	1.33211
25	1.34260[a]	1.33283[a]	1.33158[a]
30	1.34205	1.33230	1.33105

[a] Interpolated value

for example, for biochemical detection: polymer-based cantilevers can be a factor of 20 more sensitive to surface stress changes than the traditional cantilevers due to the much lower Young's modulus. On the other hand, the cantilevers are so sensitive to surface stress that a functionalization of individual cantilevers will change their bending with a magnitude depending on the specific surface coating and application method.

It has been shown in [42] that the use of cantilevers with significant initial bending may lead to appreciable errors when changing the refractive index of the environment by only 10^{-4}; a change easily happens in liquids due changes in composition and due to variations in temperature (see Table 5.4). Therefore, it is important to have control of pressure and temperature during measurements in order to avoid spurious signals from the cantilever-based sensor.

5.1.5 Other Possible Sources of Errors

One source of error is associated with the lateral shift of the reflected laser beam due to the optical window [44]. This effect has been ignored in the previous derivations.

The laws of refraction can be used to examine the passage of light through a transparent plate with plane-parallel surfaces.

Figure 5.13 shows a beam incident on the surface of a glass plate (optical window) at point F. When light is passing from the solution to glass, that is, from a rarer medium to a denser medium, the refracted beam bends toward the normal drawn at the point of incidence (F). The refracted beam FD travels inside the glass, and at point D, it emerges into air. When the light is passing from glass to air, the refracted ray bends away from the normal at point D. This means that the light beam is refracted at two points: first at F, when it enters glass, and then at D, when it emerges out. Let us denote the angle of incidence by α, the angle of refraction by ϕ, and the angle of emergence by β.

It is well known that in case of a glass plate in air (or more generally, a transparent plate bounded by the same medium), the emergent beam is displaced parallel to the incident ray. This shift is often called the "lateral shift" or "lateral displacement" of the light beam. The lateral shift L_s can be given by the formula

$$L_s = \frac{t_w \sin(\alpha - \phi)}{\cos \phi}. \tag{5.40}$$

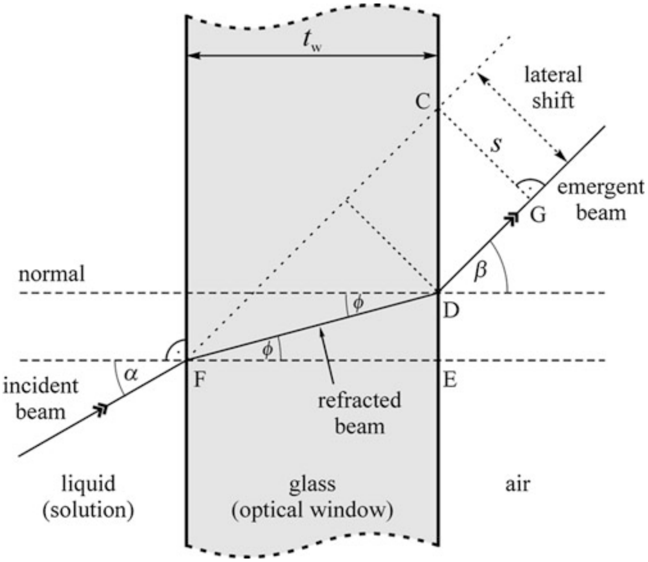

Fig. 5.13 Refraction of light through a plan-parallel glass plate (the plate is bounded by two different media)

The situation is quite different in electrochemical bending beam experiments, where the optical window is bounded by two different media, that is, the electrolyte solution and air, with refractive indexes of n_s and n_a, respectively.

As indicated in Fig. 5.13, DG is the direction of the light beam passing through an optical window of thickness t_w. If the optical window would not be present, the direction of the emergent beam would be FC, that is, the emergent beam is displaced by s with respect to the line FC. Considering the notations in Fig. 5.13,

$$s = \overline{\mathrm{CD}} \cdot \cos\beta = t_w \cdot \cos\beta \cdot (\mathrm{tg}\beta - \mathrm{tg}\phi). \tag{5.41}$$

With

$$\frac{\sin\alpha}{\sin\beta} = \frac{n_a}{n_s} \quad \text{and} \quad \frac{\sin\alpha}{\sin\phi} = \frac{n_a}{n_s},$$

where n_g is the refractive index of glass, we find

$$s = t_w \frac{n_s}{n_a} \sin\alpha \left[1 - \frac{n_s}{n_g} \frac{\sqrt{1 - (n_s/n_a)^2 \sin^2\alpha}}{\sqrt{1 - (n_s/n_g)^2 \sin^2\alpha}} \right]. \tag{5.42}$$

Usually, $n_g > n_s > n_a$, but this does not affect the final result. The angle of incidence (α) is small; therefore, the approximation

$$\sqrt{1 - ax^2} \approx 1 - \frac{ax^2}{2}$$

can be used. The approximate expression for s then becomes

$$s = t_w \frac{n_s}{n_a} \sin\alpha \left(1 - \frac{n_a}{n_g}\right) = t_w \frac{n_s}{n_a} \frac{n_g - n_a}{n_g} \sin\alpha. \tag{5.43}$$

The magnitude of error due to the change of the angle of incidence α during the measurement can be estimated as

$$\Delta s \approx t_w \cos\alpha \frac{n_s}{n_a} \frac{n_g - n_a}{n_g} \Delta\alpha \approx t_w \frac{n_s}{n_a} \frac{n_g - n_a}{n_g} \Delta\alpha. \tag{5.44}$$

As seen from Fig. 5.8, the displacement of the light spot on the detector can be estimated as

$$\Delta b \approx l \cos\alpha \frac{n_s}{n_a} \Delta\alpha \approx l \frac{n_s}{n_a} \Delta\alpha. \tag{5.45}$$

This means that the relative error

$$\frac{\Delta s}{\Delta b} \approx \frac{t_w}{l} \frac{n_g - n_a}{n_a} \tag{5.46}$$

becomes smaller the longer the distance and/or the smaller the thickness of the optical window. In a typical bending beam measurement, l is in the 1-m range, t_w is in the 1-mm range, and $(n_g - n_a)/n_a \approx 0.5$. Consequently, $\Delta s/\Delta b \approx 0.0005$, and the error caused by the shift at the optical window can be safely neglected.

It should be noted that the thickness of the glass plate should be great enough to secure sufficient mechanical properties including strength and rigidity since the deformation of the optical window under hydrostatic pressure can be a further source of error.

Another possible source of error is related to the structure of the (cantilever) probe consisting of a thin metal film coated on one side of a glass substrate. In some experimental arrangements, the laser beam is reflected from the "back side" of the cantilever, that is, by the metal surface in contact with the glass plate (see, e.g., [3, 45–48]). The changes in curvature radius of bending of the substrate are then obtained from the changes in reflection angle of the laser beam irradiated to the cantilever. However, the direction of the reflected beam may also change due to refraction in the substrate.

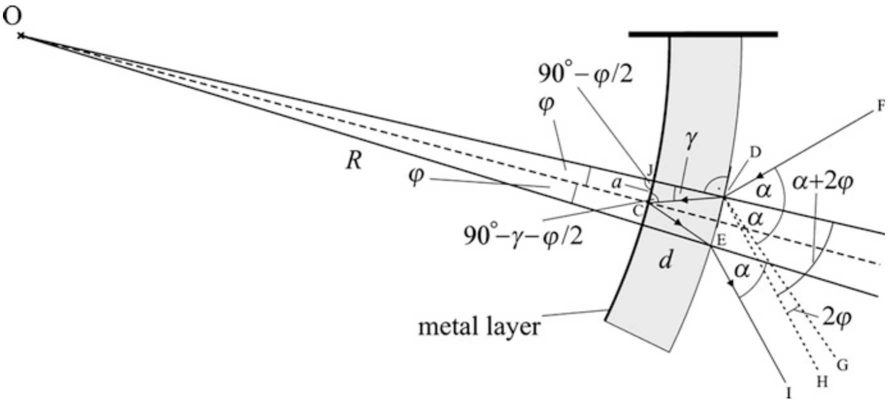

Fig. 5.14 Refraction and reflection of the laser beam inside the cantilever

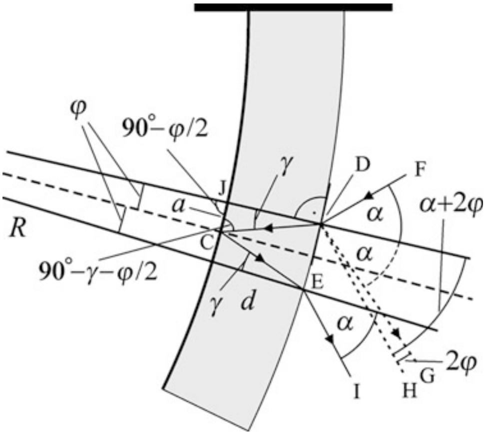

Fig. 5.15 Enlarged section of Fig. 5.14

In order to estimate the error introduced by neglecting the refraction inside the cantilever, let us consider the situation represented in Figs. 5.14 and 5.15. In both figures, FD is the direction of the light beam incident on the surface of the glass plate at point D. When light is passing from the solution to glass, that is, from a rarer medium to a denser medium, the refracted beam bends toward the normal drawn at the point of incidence (D). The refracted beam DC travels inside the glass; it is reflected at point C and is refracted again at the glass to solution surface (E). This means that the light beam FD is refracted at two points: first at D, when it enters the glass substrate, and then at E, when it enters the liquid phase again. The direction of the emergent beam is EI.

Let us denote the angle of incidence at point D by α, the angle of refraction by γ, the thickness of the glass substrate by d, the length of the segment JC by a, and the radius of curvature by R, respectively.

From the triangle CDJ,

$$\frac{\sin\gamma}{\sin(90^\circ - \gamma - \varphi/2)} = \frac{a}{d} = \frac{2R\sin(\varphi/2)}{d}. \tag{5.47}$$

Using the trigonometric identity

$$\sin(x \pm y) = \sin x \cos y \pm \cos x \sin y,$$

we obtain

$$\frac{d}{2R} = \frac{\sin(\varphi/2)\cos(\gamma + \varphi/2)}{\sin\gamma}, \tag{5.48}$$

and by using the small-angle approximation $\sin(\varphi/2) \approx \varphi/2$, $\sin\gamma \approx \gamma$, and $\cos(\gamma + \varphi/2) \approx 1$,

$$\frac{d}{R} \approx \frac{\varphi}{\gamma}. \tag{5.49}$$

From the law of refraction,

$$\frac{\sin\gamma}{\sin\alpha} = \frac{n_\mathrm{s}}{n_\mathrm{g}}, \tag{5.50}$$

where n_s and n_g are the indexes of refraction of the solution and glass, respectively. By using the small-angle approximation, $\sin\gamma \approx \gamma$ and $\sin\alpha \approx \alpha$. Thus,

$$\gamma = \frac{n_\mathrm{s}}{n_\mathrm{g}}\alpha, \tag{5.51}$$

and with Eq. (5.49),

$$\frac{\varphi}{\alpha} \approx \frac{n_\mathrm{g}}{n_\mathrm{s}}\frac{d}{R}. \tag{5.52}$$

It can be seen from Fig. 5.15 that without refraction at the solution/glass surface (at point D), the light would be reflected along direction DG. This means that due to refraction at the interface, the direction of the reflected beam (EI or DH) changes by about 2φ with respect to the “ideally” reflected beam DG.

In a typical bending beam measurement, R is in the 10–100-m range, d is in the 0.1-mm range, and the ratio of the refractive index of the glass to that of the solution is close to unity; consequently, the estimated relative error of the deflection angle is about

$$\frac{2\varphi}{\alpha} \approx \frac{2n_\mathrm{g}}{n_\mathrm{s}} \frac{d}{R} \approx \frac{2 \times 10^{-4}\,\mathrm{m}}{10\,\mathrm{m}} = 2 \times 10^{-5}.$$

Remarks:

The refraction/reflection in the probe may also cause a shift (similar to that caused by the optical window) in the position of the light spot on the detector. Nevertheless, this effect is expected to be negligible for aqueous solutions and glass substrates.

The composition of a solution in the interfacial region may differ from that in the bulk (e.g., due to adsorption/desorption phenomena or due to other electrochemical processes). The same is true for the refractive index. This can cause errors if the laser beam is reflected from the "front side" of the cantilever, that is, by the metal surface in contact with the electrolyte solution. In principle, this problem can be analyzed similarly to the case discussed above.

5.2 Interferometric Detection

The deflection of a strip or a plate can also be measured interferometrically, with the help of a Kösters interferometer. In electrochemistry, this technique can be used for the determination of changes of surface stress (specific surface energy) by the resulting deformation of an elastic plate. The principle of this method is analogous to "bending beam" techniques. However, using a suitable experimental arrangement, changes in surface stress, mass, and charge can be measured simultaneously.

5.2.1 Principles of Interferometry

The history of interferometers began in 1881 with a setup created by Michelson [49], which later results in the definition of the basic meter in units of light wavelengths. Many different types of optical interferometers were demonstrated shortly before the turn of the nineteenth century. They include devices by Fizeau [50], Fabry and Perot [51], and Michelson. These devices had an immediate and far-ranging application in several areas of experimentation.

Optical interferometers are designed to exploit the interference of light and the fringe patterns that result from optical path differences. To achieve interference patterns, that is, interference between two coherent light beams, an interferometer divides an initial beam into two parts that travel different optical paths and then reunites the beams to produce an interference pattern. “Wave-front division interferometers” sample portions of the same wave front of a coherent beam of light, while “amplitude-division interferometers” use a beam splitter that divides the initial beam into two parts [52]. Other classification schemes distinguish between those interferometers that make use of the interference of two beams and those that operate with multiple beams.

Interferometry is the process of making measurements by allowing light, sound, or other kinds of waves to interfere with each other. In interferometry, coherent wave fronts are superimposed on each other resulting in a fringe pattern known as an interferogram. When two beams interfere, each fringe represents a constant phase difference between both waves. In standard interferometry, the interference occurs between two beams at the same wavelength (or carrier frequency). The conventional design of an interferometer for shape testing includes a collimated coherent light source, which is divided into two beams by a beam splitter. The beam splitting is usually controlled by a semireflecting (semitransparent) metallic or dielectric film.

When two waves with the same frequency combine, the resulting pattern is determined by the phase difference between the two waves; waves that are in phase can add (constructive interference) and waves that are out of phase can subtract (destructive interference) (Fig. 5.16). The phase difference between the two beams results in a change in the intensity of the light on the detector. Measuring the resulting intensity of the light after the mixing of these two light beams is known as

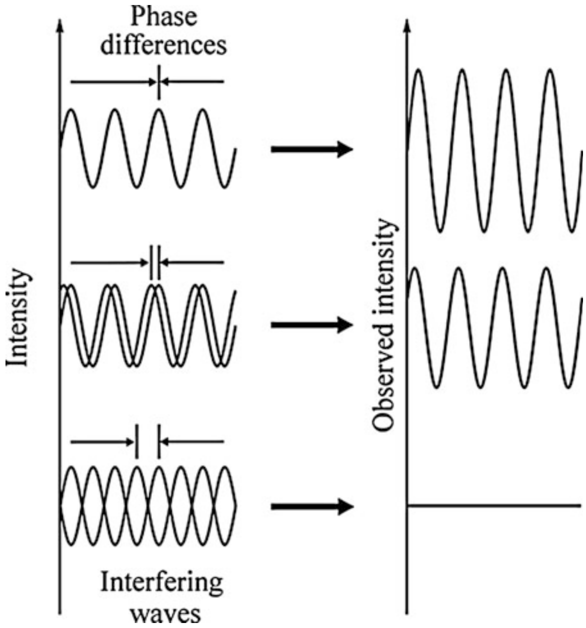

Fig. 5.16 Interference principle

homodyne detection. In heterodyne detection, one modulates, usually by a frequency shift, one of two beams prior to detection.

Among the optical measuring techniques, interferometry is capable of the highest accuracy. However, before the invention of the laser, its usefulness was quite limited, particularly when looked at in today's perspective. The accuracy attainable in interferometric setups is primarily determined by the quality of the optical components, stability of the system, and coherence and stability of the light source.

The restricted coherence of nonlaser light sources was most probably the main cause of the limited use of interferometers before the discovery of lasers. The term "nonlaser interferometer" refers to systems with conventional light sources. Obviously, this does not mean that these interferometers cannot be used with laser light. In fact, in most cases, the converse is true: laser light improves significantly the performance of the system. Usually, nonlaser interferometers have to utilize very small optical path differences between the interfering beams. This results in a relatively high stability, but the sensitivity may be relatively low. Nevertheless, these interferometers can be used under various conditions, even in quite hostile environments. On the other hand, when accuracy requirements are more stringent, laser interferometry may be the most effective method [53]. It should be noted that even laser interferometers are strongly affected by environmental noise and special designs are required for high-accuracy measurements. Three major factors limit the accuracy attainable with laser interferometers: uncertainty in the wavelength of the source, uncertainty in the refractive index of the medium, and the resolution of the interferometer [54, 55].

5.2.2 *The Kösters Laser Interferometer*

The Kösters laser interferometer (Kösters-prism [56] interferometer) is a laser-illuminated double-beam interferometer [53, 57, 58]. The main advantage of this type of interferometer is its high immunity to environmental noise due to the close vicinity of the two interfering beams. This immunity makes it an ideal tool for high-precision measurements.

Figure 5.17 is a simplified illustration of Kösters-prism interferometry.

The central constituent of the interferometer is the Kösters-prism beam splitter (BS), which produces two parallel coherent beams (Fig. 5.17). Transparent samples may be inserted in region R1, while reflective samples will replace one or both reflecting mirrors (RM1, RM2) at position R2. The two reflected beams recombine in the prism, and an interference pattern can be observed. Kösters prisms consist of two identical prism halves, which are cemented together. Usually, the Kösters prisms are constructed of two halves of fused silica joined together along a coated surface, which acts as a beam splitter. The angles of the prism halves are 30–60–90°, with high angular accuracy, and one long cathetus side is semitransparent (the reflection and transmission coefficients are equal). The semitransparent

Fig. 5.17 The principle of the Kösters-prism interferometer

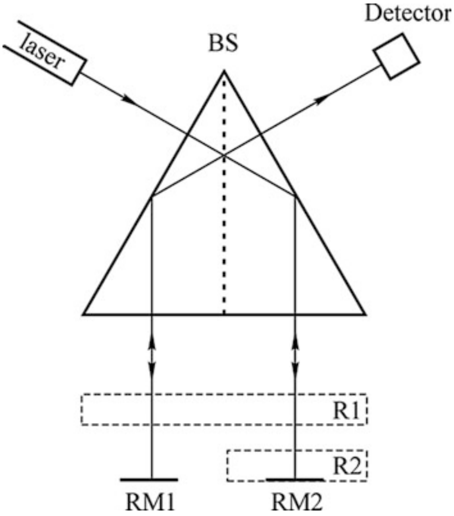

layer performs an equal intensity division of the beam, reflecting half and transmitting half, imparting a 90° phase lag in the transmitted beam. This division and phase shift gives the Kösters prism its interferometric properties: the beam reflected from one side of the prism interferes constructively or destructively with the beam transmitted from the other side.

5.2.3 Electrochemical Application

Figure 5.18 shows the principle of the electrochemical Kösters laser interferometer, which can be used for the determination of changes of surface stress by the resulting deformation of an elastic plate. Not shown in Fig. 5.18 are the adjustment devices for rotating and turning the optical components in three directions, tilting the electrochemical cell with the quartz plate at its bottom with respect to the prism, and the damping elements.

As seen in Fig. 5.18, the light from the laser is reflected by mirrors M1 and M2 in the direction perpendicular to the entrance side of the prism. The point of entrance determines the distance of the two beams emerging from the base of the prism. They are reflected at a nearly zero angle of incidence from the plate. The interfering light leaves the Kösters prism through the exit side, and it is projected onto a screen with a hole of a given diameter and a photodiode behind it. The deformation of the plate causes sinusoidal changes of the light intensity at the point of measurement in the interference pattern (Fig. 5.18). After normalizing the observed sinusoidal current change to 1 at the maximum and -1 at the minimum and taking the arcus sinus, multiplication with $\lambda/4$ yields the deformation ΔZ_{C} at R (i.e., at the center of the quartz plate). The optical path lengths at the point of interference differ by $\lambda/2$,

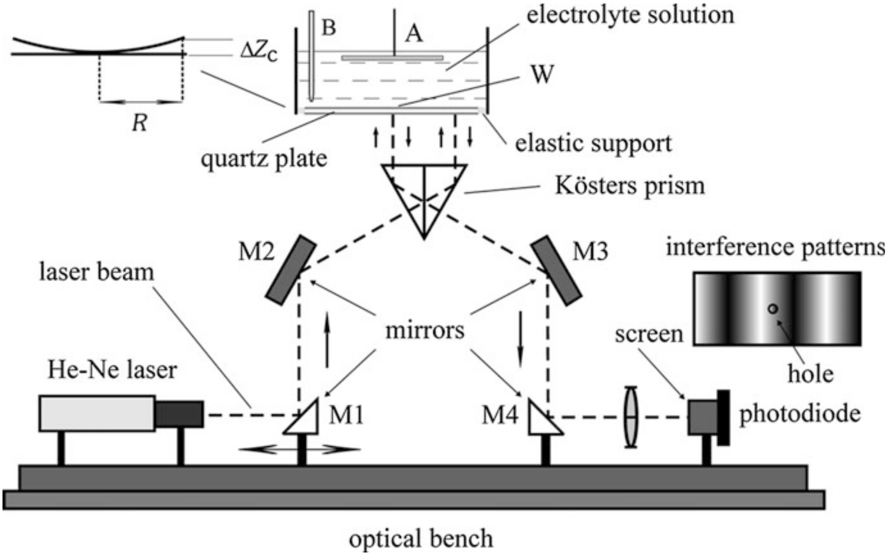

Fig. 5.18 Interferometric apparatus for electrochemical purposes with He–Ne laser and Kösters prism. *W* working electrode, *A* counter electrode, *B* reference electrode, *M1*, *M2*, *M3*, *M4* mirrors

if the distances between the exit side of the Kösters prism and the two points of reflection differ by $\lambda/4$, since the light has to go back and forth. This means that the difference between the optical path lengths ($2 \times \Delta Z_C$) can be determined from the change in light intensity detected by the photodiode.

The height change ΔZ_C of the center of the plate with respect to a plane at a given radius yields $\Delta\gamma_s$ from the appropriate form of Hooke's law:

$$\Delta\gamma_s = k\Delta Z_C. \tag{5.53}$$

The constant k in Eq. (5.53) is determined by the mechanical properties of the plate and by the type and quality of the support at the edge of the plate. It was derived [59, 60] for an unsupported circular AT quartz plate that a change of the specific surface energy is related to the change of the deformation ΔZ_C at the center of the plate with respect to a plane at the radius R by

$$\Delta\gamma_s = \frac{\Delta Z_C d^2}{3R^2\left(((1-\nu_{xy})/E_x)\cos^2\varphi + ((1-\nu_{yx})/E_y)\sin^2\varphi\right)} \tag{5.54}$$

in polar coordinates, where φ is the angle and d is the thickness of the plate. Young's moduli are $E_x = 7.831 \times 10^{10}$ Pa and $E_y = 9.066 \times 10^{10}$ Pa in the two perpendicular principal directions. The respective Poisson's coefficients are $\nu_{xy} = 0.277$ and $\nu_{yx} = 0.321$. The sensitivity is of the order 0.1 nm with respect to ΔZ_C and 1 mN/m with respect to $\Delta\gamma_s$.

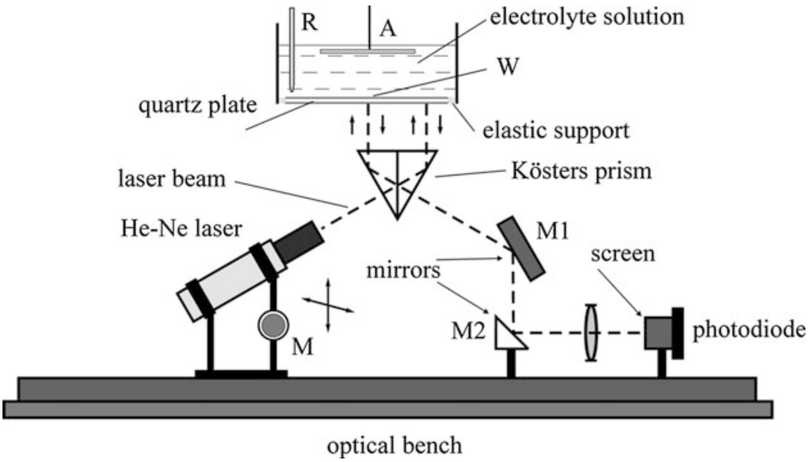

Fig. 5.19 Compact design of the electrochemical Kösters laser interferometer

Remarks:

1. In the first published paper dealing with electrochemical Kösters interferometry [61], a slightly different experimental setup was used, where a beam splitter splits the light from a He–Ne laser into a "reference" beam and a "measuring" beam. The beams were chopped at different rates. The measuring beam was reflected by a metal mirror in the direction perpendicular to the entrance side of the Kösters prism. The interfering light left the Kösters prism through the exit side, it was reflected at a second mirror, and the measuring and the reference beam were recombined in a second beam splitter.
2. It should be noted that the Kösters interferometer setup can be designed in a more compact form with reduced optical path length. As seen in Fig. 5.19, the mounting of the laser is equipped with a micrometer stage (M) which makes both height and angle adjustment both accurate and easy.

5.2.4 *Adjustment of the Interferometer*

Adjustment of the interferometer starts by making parallel the two beams leaving the Kösters prism. This is achieved when the distance between the light spots on a screen immediately behind the prism coincides with the distance measured between the spots far from the prism (e.g., 2 m). After installing the cell, one of the beams should be adjusted to the center of the gold mirror on the quartz plate at its bottom side. The other beam is reflected by the gold ring at the edge of the plate. The distance of the beams can be changed by moving the mirror (M1) in Fig. 5.18

horizontally. The two reflected light beams can be made parallel by tilting the cell until the interference pattern is perpendicular to the optical axis, and only one set of interference fringes can be observed.

5.2.5 Design of the Electrochemical Cell

Choosing a circular AT-cut quartz plate with a thin metal layer on it in contact with the solution being the working electrode in an electrochemical cell provides the advantage to measure simultaneously surface energy, mass, and charge [61–63]. (If the metal layers on both sides of the quartz disk are connected to an appropriate oscillator circuit, the device can be used as an electrochemical quartz crystal microbalance, EQCM.) In addition, since the light beams do not pass the air/solution interface, the effects of light refraction at the surface are excluded.

Even though there are great advantages of the interferometric detection, there are still some problems connected with this method. As mentioned above, the type and quality of the support at the edge of the plate are extremely important. The shape and the magnitude of the deformation $Z(r,\varphi)$ as a function of the radial distance r and the angle φ depend on the type of support at the edge of the circular plate. The largest deformation and thus the highest sensitivity for measurements of the surface stress change are expected for the "unsupported" plate. A plate is also unsupported if a mounting is present but exerts no forces on the edge. The unsupported plate will be deformed like a bubble under the influence of pressure and surface energy. If both the surface energy and the elastic constants of the wall of the bubble are isotropic, it has the shape of a perfect sphere (or a paraboloid). The shape of the unsupported plate will be a cap of a sphere. Anisotropies of the elastic constants or of the surface energy will result in some deviation from a perfect sphere. Evidently, the design and realization of such a device is very difficult.

In [61], a cylindrical electrochemical cell containing a quartz plate in a sample holder was used (Fig. 5.20). Gold layers were sputtered on thin layers of chromium onto both sides of the polished and flat 10-MHz AT-cut quartz plate of 20-mm diameter after its careful cleaning. One of the gold layers in contact with the electrolyte solution served as working electrode in the electrochemical cell. It had a diameter of 17 mm except for an extension to the edge of the plate for the electrical connection. The second metal layer on the quartz disk (outside the cell) with the diameter of 8 mm was surrounded at the edge of the plate by a 3-mm wide electrically insulated gold ring serving as a mirror in the interferometer. After connecting (with silver paint) both electrodes to copper wires of 0.2-mm diameter, the quartz plate was glued into the plastic sample holder by a ring of elastic silicone rubber with a width of 1 mm as shown in Fig. 5.21. Before use, the silicone was aged at room temperature for at least 3 weeks.

The electrochemical cell shown in Fig. 5.20 contained the quartz disk (working electrode) in the sample holder at the bottom connected by glass tubing to the head of the cell with the counter electrode which was a circular platinum or gold sheet

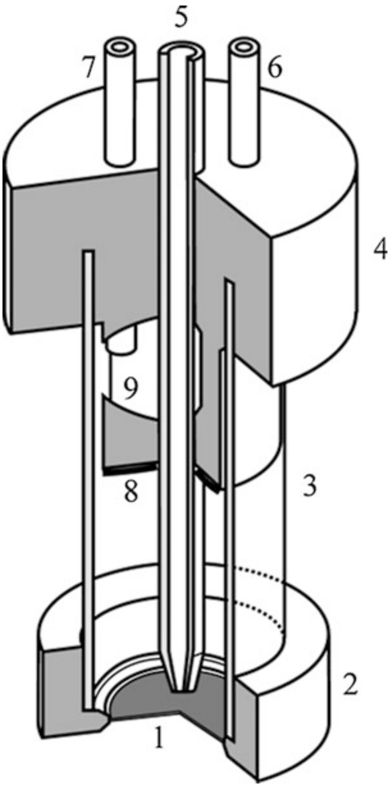

Fig. 5.20 Electrochemical cell with quartz crystal covered with a metal layer (working electrode) (1) sample holder (2) connected by glass tubing (3) to the head of the cell (4) containing tubing for the Luggin capillary (5), for the inlet (6) and outlet (7) of the electrolyte solution, the counter electrode (8), and a void (9). Adapted from [61]

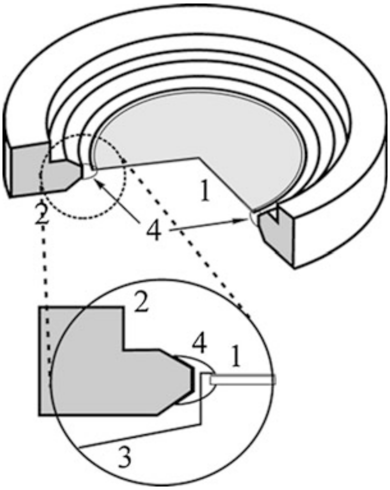

Fig. 5.21 The quartz plate (1) glued with elastic silicone (4) into the quartz holder (2) and with electrical connections (3). Adapted from [61]

with a central hole for the Luggin capillary and with glass tubes for the inlet and outlet of the electrolyte solution. The cell was assembled by first screwing the sample holder with the glass tubing to the top of the adjustment devices of the interferometer. The head of the cell was fastened airtight to the top of the cell with silicone glue, when necessary.

5.2.6 Calibration

The calibration procedures used in [61] have proven that within the limits of experimental accuracy, the shape of the deformation by normal pressure for $p \to 0$ is identical to the one provided by Eq. (5.53) for the deformation by the surface stress change ($\Delta\gamma_s$) of the unsupported plate. The silicone mounting exerts negligible forces on the plate because Young's modulus of silicone is several orders of magnitude smaller than Young's modulus of quartz. This means that the mounting very closely corresponds to the limiting case of an unsupported plate. Thus, the change of the surface stress was calculated from ΔZ_C using Eqs. (5.53) and (5.54).

With $d = 0.167$ mm and $R = 8.5$ mm, one obtains $\mathrm{d}\gamma_s/\mathrm{d}Z_C = 15.39$ mN m^{-1} nm^{-1} for $\varphi = 45°$.

The device to change the pressure in the cell by about ±3 kPa consisted of U-tubing half filled with distilled water. The connection of one leg to the outlet at the head of the cell was filled with high-purity nitrogen gas. A peristaltic pump pumped water into the other leg open to the air. The deformations $Z(r)$ have been measured with a profilometer. Figure 5.22 shows the experimental data for three pressures and the best fits to the function

$$Z(r) = A\left[1 - (r/R)^2\right]^n, \tag{5.55}$$

where A is an amplitude factor.

The parameters A and n were estimated by nonlinear least squares fitting method. The exponent was $n = 1.02$ for $p = 0\ 05$ kPa and grew approximately linearly with pressure to $n = 1.14$ at $p = 14.5$ kPa, the 95% confidence limit being about 0.04. Simultaneously, the slope $\mathrm{d}Z/\mathrm{d}p$ decreased. The deformation in the x and y directions was expected to deviate 10.4% from the mean. Experimentally, the deviation was $(8.1 \pm 0.4)\%$.

The deformation Z_C was a linear function of pressure up to about 5 kPa with the slope 11.75 nm Pa^{-1} and a regression coefficient of 0.99994.

In [61, 64], the relation between the deformations $Z(r,p)$ due to changes of pressure and $Z(r,\gamma_s)$ due to changes of the surface stress was calculated assuming a bubble model. With the notations of (Fig. 5.23), one finds

$$Z(r) = R_K\sqrt{1 - \left(\frac{r}{R_K}\right)^2} - R_K + Z_C, \tag{5.56}$$

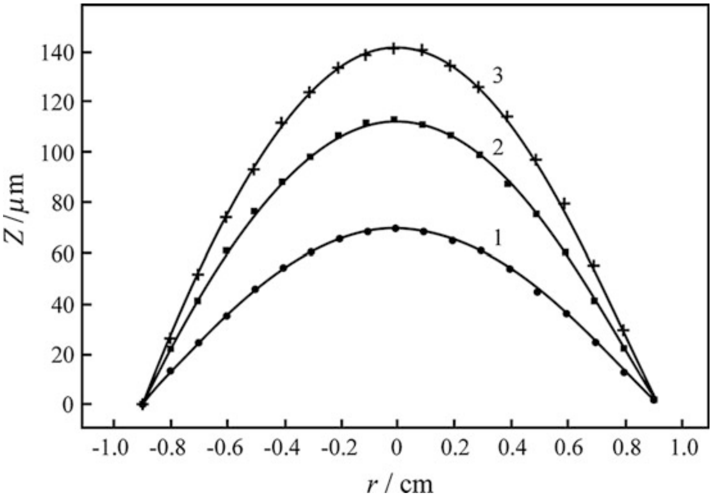

Fig. 5.22 Deformation of a quartz plate (Z) as a function of the radial distance r from the center at different pressures. (1) $p = 5.158$ kPa (*filled circle*); (2) $p = 9.787$ kPa (*filled square*); (3) $p = 14.465$ kPa (*plus*). Solid lines are the best fits to the function [Eq. (5.55)]. Adapted from [61]

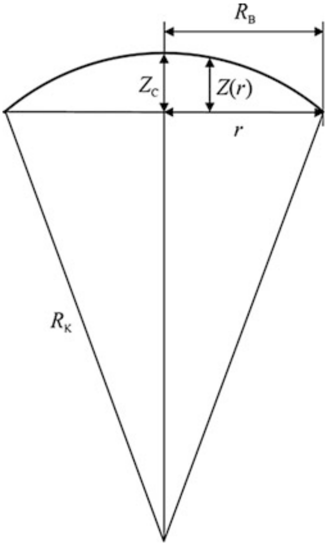

Fig. 5.23 The section of a spherical cap. Coordinate system for representing the deformations $Z(r)$

where R_K is the radius of the sphere (radius of curvature) and $Z(r)$ is the deformation at a given pressure,

$$\frac{r^2}{R_K^2} << 1.$$

Making use of the series expansion of the square root term in Eq. (5.56) and neglecting the high-order terms, the approximated result is as follows:

$$\sqrt{1-\left(\frac{r}{R_{\mathrm{K}}}\right)^{2}} \approx 1-\frac{1}{2}\frac{r^{2}}{R_{\mathrm{K}}^{2}}. \tag{5.57}$$

For $Z_{\mathrm{C}} < < R_{\mathrm{K}}$, the relation

$$R_{\mathrm{B}}^{2} = R_{\mathrm{K}}^{2} - (R_{\mathrm{K}} - Z_{\mathrm{C}})^{2} \tag{5.58}$$

can be approximated by

$$R_{\mathrm{B}}^{2} = 2R_{\mathrm{K}}Z_{\mathrm{C}}, \tag{5.59}$$

where R_{B} denotes the distance between the two beams reflected by the metal layer on the bottom side of the quartz. With Eqs. (5.57) and (5.59), one obtains the expression for the deformation:

$$Z(r) = \frac{R_{\mathrm{B}}^{2} - r^{2}}{2R_{\mathrm{K}}}. \tag{5.60}$$

In the linear relation [the left-hand side of Eq. (5.61) follows from Eq. (5.60) at $r = 0$]

$$Z_{\mathrm{C}} = \frac{R_{\mathrm{B}}^{2}}{2R_{\mathrm{K}}} = kp, \tag{5.61}$$

the constant k can be determined experimentally. A formal (purely geometrical) comparison to an equal deformation by changes of surface stress [see Eq. (5.54)] yields

$$k\Delta p = 3\frac{\Delta\gamma_{\mathrm{s}}R_{\mathrm{B}}^{2}}{d^{2}}\Phi, \tag{5.62}$$

where

$$\Phi = \left(\frac{1-\nu_{xy}}{E_{x}}\cos^{2}\varphi + \frac{1-\nu_{yx}}{E_{y}}\sin^{2}\varphi\right).$$

Consequently,

$$\Delta\gamma_{\mathrm{s}} = \frac{\Delta Z_{\mathrm{C}}d^{2}}{3R^{2}\Phi}. \tag{5.63}$$

In [61, 64], the experimental value of k, $d = 0.167$ mm, and $R = 8.5$ mm yielded $\Delta\gamma_s/\Delta p = 0.108$ m which is by a factor of 2.75 larger than the value calculated from the assumption of no support for deformation by surface energy and flexible elastic support for deformation by pressure [60].

5.2.7 Detection of the Light Intensity

As it has been mentioned earlier, the difference between the optical path lengths can be calculated from the changes in light intensity measured by a photodiode.

In case of a photodiode, any incident photon whose energy exceeds the bandgap energy is absorbed to produce an electron–hole pair by photoelectric excitation of a valence electron into the conduction band. The charge carriers are swept out of the crystal by the internal electric field to appear as a photocurrent at the terminals. The photocurrent is proportional to light intensity over a range of several orders of magnitude. Inherent limitations of photodiode response are due to structure and specific junction design, the wavelength of incoming radiation, and the presence of an externally applied bias. The inherent time constant of a photodiode causes a delay in the generated photocurrent. This time constant is typically in the range of tens to hundreds of nanoseconds.

In the case of the electrochemical Kösters interferometer, the distribution of the intensity of light in the interferogram is measured by a photodiode behind a small hole in the screen onto which the interferogram was projected. However, the accurate measurement of the photocurrent is difficult, due to the low intensity of the detected light. The acquired data are often quite noisy and hard to analyze. Noise can be diminished by measuring the photovoltage generated by the photodiode, instead of the photocurrent. Unfortunately, the photovoltage V_{ph} is a nonlinear function of the intensity. Thus, a special calibration procedure is necessary to convert the voltage to displacement [65].

5.2.8 Fast Kösters Interferometry

In [66], time-dependent changes of surface stress and changes of the specific surface energy of sputtered gold were measured by Kösters laser interferometry and coulometry. The transients were induced by potential steps. Quantitative differences could be attributed to excess nonequilibrium stresses, which change during times of the order 0.1 s.

For fast measurements, the noise was reduced by using a very stable He–Ne laser. Noise was further diminished by measuring the photovoltage of the photodiode, instead of the photocurrent. It is known that in such cases, the photovoltage V_{ph} is a nonsinusoidal function of the deformation.

In order to relate ΔZ_C to the intensity in the interferogram, a new calibration procedure was developed: The formula

$$U = U_0 \left\{ \left[\exp\left(-I_0 + I_1 \cos \frac{4\pi \ \Delta Z_C}{\lambda} \right) \right] - 1 \right\} \tag{5.64}$$

describes the response of a photodiode in the photovoltaic regime [66]. In Eq. (5.64), the exponent represents the usual distribution of the intensity of light with the wavelength $\lambda = 632.8$ nm in an interferogram with the amplitude I_1 and the background intensity I_0.

During calibration, the voltage U was measured at three points: at the minimum of the interference pattern where $\cos(4\pi\Delta Z_C/\lambda) = -1$, exactly at the middle point where $\cos(4\pi\Delta Z_C/\lambda) = 0$, and at the maximum where $\cos(4\pi\Delta Z_C/\lambda) = 1$. The unknown parameters U_0, I_0, and I_1 were obtained by using Eq. (5.64). Equation (5.64) could also be used for the calculation of the deformations ΔZ_C during the experiments.

5.2.9 Measurement of (Surface) Mass Changes

The EQCM [or electrochemical quartz crystal nanobalance (EQCN)] is a mass sensing device with the ability to measure very small changes in mass per unit area in real time. The QCM measures the changes in mass per unit area by measuring the shifts in the frequency of a quartz crystal resonator. The sensitivity of the QCM is several hundred times higher than an electronic fine balance with a sensitivity of 0.1 mg, that is, EQCMs are capable of measuring mass changes as small as a fraction of a monolayer or single layer of atoms. Mass changes occurring during adsorption, absorption, deposition, dissolution, etc., can be followed effectively, which is very useful in exploring reaction mechanisms. The EQCM is sensitive toany interfacial mass change, especially to the mass (density) and viscoelastic changes at the solid–liquid interface [67–74]. The high sensitivity and the real-time monitoring of mass changes on the sensor crystal make the EQCM a widely used technique in several areas of electrochemistry and electroanalytical chemistry.

The quartz crystal microbalance can be combined with many electrochemical methods, such as voltammetry, amperometry, chronoamperometry, chronocoulometry, etc. [75]. It can be further combined with other techniques, for example, with optical spectroscopies [76], probe beam deflection [77], different microscopies [78, 79], and, of course, with electrochemical Kösters interferometry.

The physical basis of operation of the EQCM originates in the converse piezoelectric effect. This means that the application of an electric field across a piezoelectric material induces a deformation of the material. It is known that mechanical stress applied to the surface of acentric materials (like quartz, Rochelle salt, and tourmaline), that is, those that crystallize into noncentrosymmetric space group, results in generation of an electrical potential across the crystal, whose magnitude is proportional to the applied stress.

Quartz is the most stable form of silica (or silicon dioxide SiO_2). In QCM devices, the so-called alpha-quartz crystals are employed because of their superior mechanical and piezoelectric properties. The cut angle with respect to crystal orientation determines the mode of oscillation. AT-cut crystals, which are the most commonly used for EQCM applications, are fabricated by slicing through a quartz rod at a cut angle of 35.17° with respect to the optical axis. The advantage of the AT-cut quartz crystal is that it has nearly zero frequency drift with temperature around room temperature. The quartz crystals used in EQCM devices are sandwiched between two electrically conducting layers, for example, metal layers that are vapor-deposited on either side of the crystal. Gold layers have been the most commonly used in EQCM studies because of the ease with which Au is evaporated. However, Cu, Ni, Pt, and other metals have also been employed. When an alternating electric field is applied over the metal layers, the quartz crystal starts to oscillate. These oscillations are stable only at the resonance frequency of the crystal. The vibration motion of the quartz crystal results is the establishment of a transverse acoustic wave. A standing wave condition is fulfilled when the acoustic wavelength is equal to twice the combined thickness of the crystal and the metal layers. The resonance frequency (f_r) can be related to the thickness of the crystal (d_q) by

$$f_\mathrm{r} = \frac{1}{2}\frac{v_\mathrm{q}}{d_\mathrm{q}}, \tag{5.65}$$

where v_q is the speed of the acoustic wave in AT-cut quartz given by

$$v_\mathrm{q} = \sqrt{\frac{\mu_\mathrm{q}}{\rho_\mathrm{q}}} = 3,336\,\mathrm{ms}^{-1}$$

and $\rho_\mathrm{q} = 2.648$ gcm^{-3} and $\mu_\mathrm{q} = 2.947 \times 10^{10}$ nm^{-2} are the density and the shear modulus of quartz, respectively. Relation [Eq. (5.65)] assumes that the velocities of sound in the electrodes and in quartz are identical, and the thicknesses of the metal layers are small in comparison with that of quartz. Typical operating frequencies of the EQCM lie within the range of 5–10 MHz.

The quartz oscillator circuit used in [61] and in [62,64-66] was similar to the one used in [80]. The digital data from the frequency counter were transferred via GPIB to a computer. The changes of superficial mass Δm were calculated from changes Δf of the frequency using Sauerbrey's equation [81], which describes the relationship between the resonant frequency shift (Δf) and the added mass (Δm):

$$\Delta f = f_\mathrm{r} - f_0 = -\frac{2f_0^2\Delta m}{A(\rho_\mathrm{q}\mu_\mathrm{q})^{1/2}} = -C_\mathrm{f}\Delta m, \tag{5.66}$$

where f_0 is the fundamental resonance frequency of the quartz crystal, A is the (acoustically) active surface area, and C_f is the integral mass sensitivity. For the most frequently used crystals, $C_\mathrm{f}(f_0 = 5\ \mathrm{MHz}) = 5.660 \times 10^7\ \mathrm{Hz\ cm^2\ g^{-1}}$ and $C_\mathrm{f}(f_0 = 10\ \mathrm{MHz}) = 2.264 \times 10^8\ \mathrm{Hz\ cm^2\ g^{-1}}$, respectively.

Equation (5.66) can be rewritten as

$$\Delta m = -\frac{1}{C_\mathrm{f}}\Delta f = -K_\mathrm{f}\Delta f, \tag{5.67}$$

where Δf is the frequency change corresponding to the mass change Δm per area and K_f is a proportionality constant characteristic of the quartz crystal. Small changes Δf of frequency are linearly related to mass changes. Changes of 0.1 Hz at a fundamental frequency $f = 10$ MHz could be measured, corresponding to a sensitivity of about 0.442 ng $\mathrm{cm^{-2}}$. Effects of mechanical deformation on frequency [60] should be kept negligible by avoiding stresses in the quartz as much as possible. The uniform distribution of the mass over the active area of the quartz plate is very important because the differential mass sensitivity (c_f) varies across this area. Considering a disk-shaped crystal with radius r [68, 69, 82, 83],

$$C_\mathrm{r} = 2\pi \int_0^r r c_\mathrm{f}(r)\mathrm{d}r.$$

The resonant frequency of the EQCM also depends on the density and viscosity of the contacting media. The frequency shift associated with the influence of the viscosity and density of a liquid can be written as

$$\Delta f = -f_0^{3/2}\left(\frac{\rho_\mathrm{l}\eta_\mathrm{l}}{\pi\rho_\mathrm{q}\mu_\mathrm{q}}\right)^{1/2},$$

where η_l and ρ_l are the viscosity and density of the liquid. This simple relation is justified only if the surface of the QCM in contact with the liquid is ideally flat.

5.2.10 Holographic Interferometry

In all the two-beam interferometric techniques, one beam serves as reference for comparison with the test beam. The position of the fringes shifts when there is any perturbance in the test beam. In these methods, the test beam and the reference beam travel through two different paths before they are incident on the plane of observation. In contrast to two-beam interferometry, holographic interferometry is a common path interferometry. The reconstructed wave front of a scene from a hologram (which can serve as the comparison beam) travels the same path as the test scene wave front is traveling. Because both beams are traveling through the same optical arrangements, whatever optical imperfection exists for one beam exists for the other as well, and the effects cancel out. This is unique for holographic interferometry [84].

Holographic interferometry has been proposed for measurement of small elastic deformations of electrodes caused by surface forces [85]. It can be applied when the investigated metal strip is mounted in a transparent cell. In the experimental setup, a laser beam was split into two components. One passed through a semitransparent mirror and an objective lens. After reflection from the metal plate, it reached a photographic plate. The second part of the laser beam was reflected from two mirrors, passed the objective lens, and fell also on the photographic plate. By the superposition of the two wave fronts, a hologram was recorded. The bending of the strip resulted in the appearance of interference fringes.

References

1. Fredlein RA, Damjanovic A, Bockris JO’M (1971) Surf Sci 25:261–264
2. Fredlein RA, Bockris JO’M (1974) Surf Sci 46:641–652
3. Ueno K, Seo M (1999) J Electrochem Soc 146:1496–1499
4. Sahu SN, Scarminio J, Decker F (1990) J Electrochem Soc 137:1150–1154
5. Cattarin S, Pantano E, Decker F (1999) Electrochem Commun 1:483–487
6. Cattarin S, Decker F, Dini D, Margesin B (1999) J Electroanal Chem 474:182–187
7. Lehmann V (1996) J Electrochem Soc 143:1313–1318
8. Láng G, Ueno K, Ujvári M, Seo M (2000) J Phys Chem B 104:2785–2789
9. Pei Q, Inganas O (1992) J Phys Chem 96:10507–10514
10. Asaka K, Oguro K (2000) J Electroanal Chem 480:186–198
11. Láng G, Seo M, Heusler KE (2005) J Solid State Electrochem 9:347–353
12. Rokob TA, Láng GG (2005) Electrochim Acta 51:93–97
13. Láng GG, Sas NS, Vesztergom S (2009) Chem Biochem Eng Q 23:1–9
14. Raiteri R, Butt HJ (1995) J Phys Chem 99:15728–15732
15. Butt H-J (1996) J Colloid Interface Sci 180:251–260
16. Brunt TA, Chabala ED, Rayment T, O’Shea SJ, Weiland ME (1996) J Chem Soc Faraday Trans 92:3807–3812
17. Brunt TA, Rayment T, O’Shea SJ, Weiland ME (1996) Langmuir 12:5942–5946
18. O’Shea SJ, Welland ME, Brunt TA, Ramadan AR, Rayment T (1996) J Vac Sci Technol B 14:1383–1385
19. Floro JA, Chason E, Lee SR (1996) Mater Res Soc Symp Proc 405:381–386
20. Kobeda E, Irene EA (1986) J Vac Sci Technol B 4:720–722
21. Floro JA, Chason E (1996) Appl Phys Lett 69:3830–3832
22. Hearne S, Chason E, Han J, Floro JA, Figiel J, Hunter J, Amano H, Tsong IST (1999) Appl Phys Lett 74:356–358
23. Proost J, Spaepen F (2002) J Appl Phys 91:204–216
24. Van Overmeere Q, Vanhumbeeck JF, Proost J (2010) Rev Sci Instrum 81:045106
25. Vanhumbeeck JF, Proost J (2007) In-situ monitoring of the growth stress evolution during galvanostatic anodizing of aluminum thin films. In: Moffat TP, Stickney J, Deligianni H, Dukovic J (eds) ECS transactions. Electrochemical Society, Pennington, NJ
26. Vanhumbeeck JF, Proost J (2008) Electrochim Acta 53:6165–6172
27. Van Overmeere Q, Nysten B, Proost J (2009) Appl Phys Lett 94:074103
28. Van Overmeere Q, Blaffart F, Proost J (2010) Electrochem Commun 12:1174–1176

29. Frank NH (1940) Introduction to electricity and optics. McGraw-Hill Inc., New York, NY
30. Duncan J, Starling SG (1950) A text book of physics. MacMillan Co., London
31. Southall JPC (1950) Mirrors, prisms and lenses. MacMillan Co., New York
32. Pedrotti LS (2008) Basic geometrical optics. In: Roychoudhuri C (ed) Fundamentals of photonics, vol TT79 CD-ROM. SPIE Press Book, Cardiff
33. Xiao X, Schleh D (2010) J Appl Phys 107:013508-1-5
34. Láng GG (2010) J Appl Phys 107:116104-1-3
35. Xiao X, Schleh D (2010) J Appl Phys 107:116105
36. Tian F, Pei JH, Hedden DL, Brown GM, Thundat T (2004) Ultramicroscopy 100:217–233
37. Láng GG, Seo M (2000) J Electroanal Chem 490:98–101
38. Láng GG, Rokob TA, Horányi G (2005) Ultramicroscopy 104:330–332
39. Lide DR (ed) (2005) CRC handbook of chemistry and physics. CRC, Boca Raton, FL
40. Huang Y, Liu H, Li K, Chen YY, Zhang QC, Wu XP (2008) Sens Actuator A 148:329–334
41. Huber F, Lang HP, Hegner M, Despont M, Drechsler U, Gerber C (2008) Rev Sci Instrum 79:086110
42. Dohn S, Greve A, Svendsen WE, Boisen A (2010) Rev Sci Instrum 81:065104
43. Owens JC (1967) Appl Opt 6:51–59
44. Peterson JP, Peterson RB (2006) Appl Opt 45:4916–4926
45. Lang GG, Ueno K, Ujvári M, Seo M (2000) J Phys Chem 104:2785–2789
46. Ueno K, Pyun SI, Seo M (2000) J Electrochem Soc 147:4519–4523
47. Pyun SI, Go JY, Jang TS (2004) Electrochim Acta 49:4477–4486
48. Kim YH, Pyun SI, Go JY (2005) Electrochim Acta 51:441–449
49. Michelson AA (1882) Phil Mag 13:236–242
50. Fizeau H (1862) Ann Chim Phys 66:429–482
51. Fabry C, Perot A (1899) Ann Chim Phys 16:115–144
52. Al-Azzawi A (2007) Physical optics, principles and practices. CRC, Boca Raton, FL
53. Shamir J (1998) Interferometric methods for the determination of thin-film parameters. In: Palik ED (ed) Handbook of optical constants of solids, vol 5. Academic, San Diego, CA
54. Zagar BG (1999) Laser interferometer displacement sensors. In: Webster JG (ed) The measurement, instrumentation and sensors handbook. CRC, Roca Baton, FL
55. Lee WK, Suh HS, Kang CS (2011) Opt Eng 50
56. Kösters W (1934) Interferenzdoppelprisma für Messzwecke. German patent:595211
57. Láng GG (2008) Kösters laser interferometer. In: Bard AJ, Inzelt G, Scholz F (eds) Electrochemical dictionary. Springer-Verlag, Berlin
58. Láng GG (2009) Application of the Koesters interferometer in electrochemistry. In: Raynor W, Halsey D (eds) Handbook of interferometers: research technology and applications. Nova Science Publishers Inc., Hauppauge, NY
59. Janda M, Stefan O (1984) Thin Solid Films 112:127–137
60. Heusler KE, Pietrucha J (1992) J Electroanal Chem 329:339–350
61. Jaeckel L, Láng G, Heusler KE (1994) Electrochim Acta 39:1031–1038
62. Heusler KE, Láng G (1995) Elektrokhimiya 31:826–835
63. Heusler KE, Láng G (1995) Russ J Electrochem 31:759–767
64. Jaeckel L (1994) Spezifische Oberflächenenergien fester Elektroden und Mechanische Spannungen in dünnen Schichten. Dissertation, Technische Universität Clausthal
65. Husfeld N (1997) Einfluss der Adsorption von Metallen an Gold auf die spezifische Oberflächenenthalpie. Dissertation, Technische Universität Clausthal
66. Efimov IO, Heusler KE (2000) J Electroanal Chem 490:1–6
67. Uida E (1995) Optoelectronics. Prentice-Hall, Englewood Cliffs
68. Lu C, Czanderna AW (eds) (1984) Applications of piezoelectric quartz crystal microbalances. Elsevier, New York
69. Buttry DA (1991) Applications of the quartz crystal microbalance to electrochemistry. In: Bard AJ (ed) Electroanalytical chemistry, vol 17. Marcel Dekker, New York
70. Buttry DA, Ward MD (1992) Chem Rev 92:1355–1379

71. Grate JW, Martin SJ, White RM (1993) Anal Chem 65:940A–948A
72. Grate JW, Martin SJ, White RM (1993) Anal Chem 65:987A–996A
73. Hepel M (1999) Electrode-solution interface studied with electrochemical quartz crystal nanobalance. In: Wieczkowski A (ed) Interfacial electrochemistry. Marcel Dekker, New York
74. Tsionsky V, Daikhin L, Urbakh M, Gileadi E (2004) Looking at the metal/solution interface with electrochemical quartz-crystal microbalance: theory and experiment. In: Bard AJ, Rubinstein I (eds) Electroanalytical chemistry, vol 22. Marcel Dekker, New York
75. Inzelt G (2010) Electrochemical quartz crystal nanobalance. In: Scholz F (ed) Electroanalytical methods. Springer, Berlin
76. Kim JM, Chang SM, Muramatsu H (1999) J Electrochem Soc 146:4544–4550
77. Henderson MJ, Hillman AR, Vieil E (1998) J Electroanal Chem 454:1–8
78. Friedt JM, Choi KH, Frederix F, Campitelli A (2003) J Electrochem Soc 150:H229–H234
79. Gollas B, Bartlett PN, Denault G (2000) Anal Chem 72:349–356
80. Grzegorzewski A, Heusler KE (1987) J Electroanal Chem 228:455–470
81. Sauerbrey G (1959) Z Phys 155:206–222
82. Bácskai J, Láng G, Inzelt G (1991) J Electroanal Chem 319:55–69
83. Buck RP, Lindner E, Kutner W, Inzelt G (2004) Pure Appl Chem 76:1139–1160
84. Srinivasan VS (1973) Holography and holographic interferometry in electrochemistry. In: Delahay P, Tobias CW (eds) Advances in electrochemistry and electrochemical engineering, vol 9, Muller RH (ed) Optical techniques in electrochemistry. Wiley, New York
85. Pangarov N, Kolarov G (1978) J Electroanal Chem 91:281–285

Chapter 6
Detection of the Cantilever Deflection by Microscopy

6.1 Scanning Tunneling Microscopy

Since its invention following that of the scanning tunneling microscope (STM), the atomic force microscope (AFM) has been increasingly used in studying surface forces and surface structures of a wide range of materials [1–5].

A rather elegant method to measure the bending of a strip or a plate is to use the scanning tunneling microscope (STM) [6–13]. The STM may be used then as a means to simultaneously investigate the structure of the surface (Fig. 6.1). Advantages and limitations of the technique have been discussed in excellent reviews [14, 15].

However, even this method is not without pitfalls. In electrolyte solutions, there is a double-layer-like structure also around the STM tip [16]. Consequently, there are some interactions between the tip of the STM and the sample that seem to be unavoidable [17, 18]. These are long-range electrostatic interactions between electrical (electrochemical) double layers and structural/dispersion/hydration forces that dominate the interaction at very short ranges. Most of these contributions have been widely studied, but some are marginally understood. The repulsion of two double layers was discussed, e.g., in [19–22]. As it has been noted in [23], "… one can lift solids by the electrical forces in the double layer." We note here that attractive forces were observed also between two gold spheres used in vacuum tunneling [24]. Interaction forces between surfaces with high electric potentials in aqueous electrolyte solutions were investigated in [25]. The electrostatic force between a sphere and a flat plate has been calculated using simple continuum theory. Similar experiments have been reported in [26].

In experiments reported in [10, 11], a small circular portion of the liquid was removed by a syringe in the vicinity of the tip (Fig. 6.2). According to the authors, with this simple procedure, the tip remained dry, and the electrochemical offset current with its concomitant noise was eliminated. The values of the surface stress changes derived from the Stoney formula were corrected for the small area not covered by the solution. The uncertainty incurred by this procedure has been

G.G. Láng and C.A. Barbero, *Laser Techniques for the Study of Electrode Processes*,
Monographs in Electrochemistry, DOI 10.1007/978-3-642-27651-4_6,

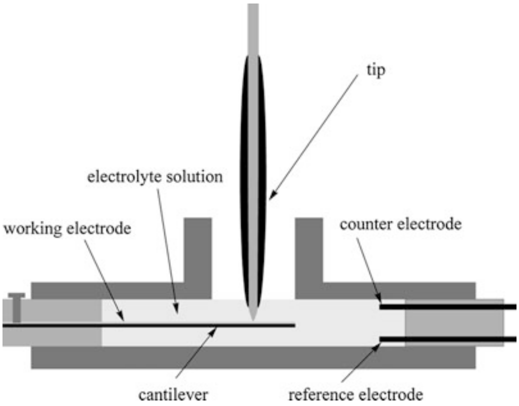

Fig. 6.1 Schematic illustration of a typical arrangement for STM studies at the solid–liquid interface which allows simultaneous measurement of the bending of the cantilever when the electrode potential is varied

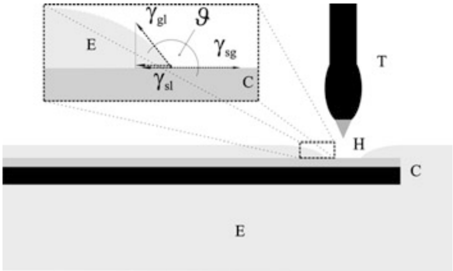

Fig. 6.2 *A* bending cantilever setup with a "hole" in the liquid layer at the vicinity of the STM tip. *E*: electrolyte solution, *C*: cantilever sample, *H*: hole, *T*: STM tip, ϑ: contact angle. γ_{sg}, γ_{sl}, and γ_{gl} are the surface tension at the solid-gas, solid–liquid, and liquid–gas interfaces, respectively

estimated at most 5%. Obviously, in this setup, the error due to the interaction between double layers is eliminated, but a new source of error, namely, that due to the creation of a three-phase boundary, is introduced (Fig. 6.2).

It is well known that in a three-phase system, there is a greater likelihood of surface contamination from organic and oxygen impurities present in the gas phase. On the other hand, the wetting of such metals as gold and platinum is still a subject of controversy among those who consider these metals to be hydrophobic in nature and others who report low or zero contact angle. It is clear that if the surface tension of the liquid–gas interface or/and the contact angle changes during the experiment, the results obtained may be incorrect.

As pointed out in [14], another source of error, which can be important, arises because the exact elastic behavior of membranes is strongly dependent on the boundary conditions, which are not well defined in many experiments. For example, in the study reported in [7], the bending of a crystal disk was measured. This disk was clamped on the entire circular boundary. For a flat disk which is clamped on the perimeter, a bending in either direction increases the area of both surfaces (Fig. 6.3). Consequently, a tensile stress applied to either surface would not bend the plate at all [6]. In reality, a disk or a plate is always slightly deformed, and one

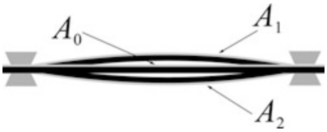

Fig. 6.3 The bending of a rigidly clamped plate. Bending to either side enlarges the area of both surfaces. A_0: surface area without bending; A_1, A_2: surface area of the deformed sample. Obviously, A_1,A_2 > A_0

would, therefore, observe also a linear effect on such a sample. However, the magnitude of the bending effect would depend on the initial bending of the crystal.

The small volume of the electrolyte solution in the cell and the small distance between working and counter electrode may be an additional source of errors. By applying the "phase-shifted dual cyclic voltammetry" method, it could be shown that the reduction of the surface oxide layer of the polycrystalline gold disk immersed into sulfuric acid solutions is accompanied by the formation of soluble, electroreducible gold species which can be detected on the ring electrode [27]. A similar effect has been observed in EQCM studies using Pt layers deposited on quartz crystals [28–30].

6.2 Atomic Force Microscopy

The past two decades have seen increasing use of AFM cantilevers to measure changes in surface stresses. An internet search using the keywords "AFM" and "surface stress" generates a list of hundreds of papers. In fact, the AFM is a combination of the principles of the scanning tunneling microscope and the stylus profilometer (SP), where the stylus in the profilometer is carried by a cantilever beam and it rides on the sample surface [31]. Most of the positioning, vibration isolation, and feedback hardware used for STM can be adapted for use in any scanning probe instrument. The additional instrumental requirement for AFM is only the ability to detect sub-nm deflections of a cantilever. A typical AFM consists of three essential components: (a) a sharp tip mounted on the end of a flexible-force-sensing microcantilever, (b) a force transducer, which is the cantilever with a laser beam bouncing off the backside of the cantilever onto a multiple-segment photodiode called the position-sensitive detector, and (c) a piezoelectric scanner, which precisely positions the tip and scans the sample relative to the tip in three orthogonal directions. An excellent review of cantilever-like micromechanical sensors is provided in [32].

In the first experiments, surface stress changes were generally a result of molecular adsorption from the gas phase, or photon adsorption giving rise to either thermally or chemically induced stress in the cantilever [33–36]. Lately, measurements have been extended to electrochemical systems [37–40]. Measurements were performed using microcantilever-based sensors where the cantilever in contact

Fig. 6.4 Schematic illustration of the laser beam deflection system of a commercial AFM. In the special case when the resulting bending over the whole length is circular with a constant radius of curvature R, then $\beta = 2\alpha$

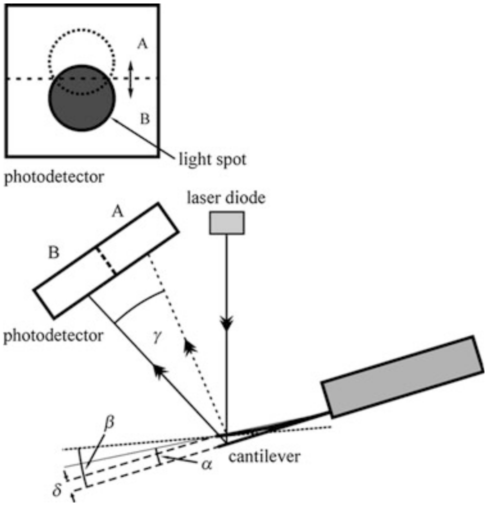

with the electrolyte solution is also the working electrode in a three-electrode electrochemical system. Usually, AFM tips and cantilevers utilized in surface stress measurements are microfabricated from Si or Si_3N_4. Typical tip radius is from a few to tens of nanometer.

Unlike STM, in which the probe signal is always detected with a preamplifier in series with the tunneling current, there are a number of ways to detect the deflection of the cantilever in an AFM [41]. Today, most AFMs use a laser beam deflection system, where laser light is reflected from the back of the reflective AFM lever onto a position-sensitive detector [42]. This method was used also in [37, 43, 44]. In order to improve the sensitivity and stability of the technique, microfabricated cantilevers were used instead of thin but still macroscopic plates, and the deflection of the cantilever was measured with an optical lever using the head of a commercially available AFM.

Figure 6.4 shows a typical optical lever arrangement of the AFM. The cantilever beam is clamped on one side on which there is no deflection and zero slope [45]. Evidently, the basic principles of the measurement of the cantilever's deflection are the same as those discussed in Chap. 5

References

1. Binning G, Rohrer H (1982) Helv Phys Acta 55:726–735
2. Binning G, Quate CF, Gerber Ch (1986) Phys Rev Lett 56:930–933
3. Sarid D (1991) Scanning force microscopy. Oxford University Press, New York
4. Eastman T, Zhu DM (1996) Langmuir 12:2859–2862
5. Butt HJ, Jaschke M, Drucker W (1995) Bioelectrochem Bioenerg 38:191–201
6. Ibach H, Bach CE, Giesen M, Grossmann A (1997) Surf Sci 375:107–119
7. Haiss W, Sass JK (1995) J Electroanal Chem 386:267–270

8. Haiss W, Sass JK (1996) J Electroanal Chem 410:119–124
9. Haiss W, Sass JK (1996) Langmuir 12:4311–4313
10. Haiss W, Nichols RJ, Sass J-K (1997) Surf Sci 388:141–149
11. Haiss W, Nichols RJ, Sass JK, Charle KP (1998) J Electroanal Chem 452:199–202
12. Nichols RJ, Nouar T, Lucas CA, Haiss W, Hofer WA (2002) Surf Sci 513:263–271
13. Láng GG, Sas NS, Vesztergom S (2009) Chem Biochem Eng Q 23:1–9
14. Ibach H (1997) Surf Sci Rep 29:193–263
15. Haiss W (2001) Rep Prog Phys 64:591–648
16. Conroy JFT, Bruckner-Lea CJ, Janata J (1997) Solid State Ionics 94:161–164
17. Conroy JFT, Caldwell K, Bruckner-Lea CJ, Janata J (1996) J Phys Chem 100:18222–18228
18. Conroy JFT, Hlady V, Bruckner-Lea CJ, Janata J (1996) J Phys Chem 100:18229–18233
19. Bockris JO'M, Parry-Jones R (1953) Nature 171:930–931
20. Bockris JO'M, Argade SD (1969) J Chem Phys 50:1622–1623
21. Bockris JO'M, Sen RK (1972) Surf Sci 30:237–241
22. Voronaeva TN, Deryagin BV, Kabanov BN (1962) Kolloid Zhurnal (USSR) 26:396–404
23. Bockris JO'M (1992) Electrons, interfaces, and societies in the 21st century. In: Murphy OJ, Srinivasan S, Conway BE (eds) Electrochemistry in transition. Plenum Press, New York
24. Teague EC (1986) J Res Natl Bur Stand 91:171–233
25. Raiteri R, Preuss M, Grattarola M, Butt HJ (1998) Colloids Surf A 136:191–197
26. Arai T, Fujihira M (1996) J Vac Sci Technol B 14:1378–1382
27. Vesztergom S, Ujvári M, Láng GG (2011) Electrochem Commun 13:378–381
28. Inzelt G, Berkes BB, Kriston Á (2010) ECS Trans 25:137–156
29. Inzelt G, Berkes BB, Kriston Á (2010) Electrochim Acta 55:4742–4749
30. Inzelt G, Berkes BB, Kriston Á, Székely A (2011) J Solid State Electrochem 15:901–915
31. Binnig G, Quate CF, Gerber CH (1986) Phys Rev Lett 56:930–933
32. Boisen A, Dohn S, Keller SS, Schmid S, Tenje M (2011) Rep Prog Phys 036101 (30 pp)
33. Chen GY, Thundat T, Wachter EA, Warmack RJ (1995) J Appl Phys 77:3618–3622
34. Manne S, Gaub HE (1997) Curr Opin Colloid Interface Sci 2:145152
35. Barnes JR, Stephenson RJ, Weiland ME, Gerber Ch, Gimzewski JK (1994) Nature 372:79–81
36. Thundat T, Sharp SL, Fisher WG, Warmack RJ, Wachter EA (1995) Appl Phys Lett 66:1563–1565
37. Raiteri R, Butt HJ (1995) J Phys Chem 99:15728–15732
38. O'Shea SJ, Welland ME, Brunt TA, Ramadan AR, Rayment TJ (1996) J Vac Sci Technol B 14:1383–1385
39. Brunt TA, Chabala ED, Rayment T, O'Shea SJ, Weiland ME (1996) J Chem Soc Faraday Trans 92:3807–3812
40. Brunt TA, Rayment T, O'Shea SJ, Weiland ME (1996) Langmuir 12:5942–5946
41. Putman CAJ, De Grooth BGD, Van Hulst NF, Greve J (1992) J Appl Phys 72:6–12
42. Meyer G, Amer NM (1990) Appl Phys Lett 56:2100–2101
43. Butt HJ (1996) J Colloid Interface Sci 180:251–26
44. Raiteri R, Butt HJ, Grattarola M (2000) Electrochim Acta 46:157–163
45. Miyatani T, Fujihira M (1997) J Appl Phys 81:7099–7115

Chapter 7
Applications: Selected Experimental Results

7.1 Introduction

In contrast to most other areas of electrochemistry, the thermodynamics of electrified solid/liquid interfaces is characterized more by theories and speculations than by systematic experimental investigations—though the number of the latter is steadily increasing. Although much of the previous research has focused on the development of experimental techniques, the scarcity of reliable experimental data is due at last in part to the difficulty to perform precise and reliable measurements of interfacial stress changes. On the other hand, experiments frequently are not carried out with sufficient care, leading to the neglect of certain physical and/or electrochemical effects. This might be attributed to that the design and construction of measuring devices and electrochemical cells appropriate for such measurements require the knowledge of several disciplines including (electro)chemistry, physics, optics, electronics, etc. There are several examples in the literature where published data have required subsequent correction due to neglect of important physical phenomena in the original data analysis. For instance, as it has been pointed out in the previous chapters, the neglect of refraction effects resulted in false conclusions and misinterpretation of data (see, e.g., [1–5] and references cited therein). In fact, all data from bending beam experiments [6] with optical detection published before the year 2000 should be treated with caution.

In the present chapter, the results of selected bending beam (bending plate) experiments are presented and discussed as illustrative examples.

7.2 Platinum and Gold in Contact with Electrolyte Solutions

Inert metals like platinum and gold in contact with electrolyte solutions are frequently used to study electrode processes. It is well known that the Au|H_2SO_4(aq) system can be treated as ideally polarizable electrode in a certain potential region

G.G. Láng and C.A. Barbero, *Laser Techniques for the Study of Electrode Processes*,
Monographs in Electrochemistry, DOI 10.1007/978-3-642-27651-4_7,

(“double-layer region”), and the platinum|H_2SO_4(aq) electrode is assumed to be reversible with respect to the adsorption processes of hydrogen or oxygen and of ions. For these reasons, Au and Pt are frequently used in interfacial stress change measurements in electrochemical systems. (The thermodynamic theory of surface phenomena at platinum group metals was discussed, e.g., in [7–11])

Early experimental results obtained with platinum in sulfuric acid solution ($8.3{\cdot}10^{-4}$ mol dm^{-3}) are presented in Fig. 7.1a (curve 1) [12]. The bending beam method, with optical detection, was used. The cantilever consisted of a glass strip of 13 × 1.5 × 0.0085 cm with Pt vacuum deposited on one side. The thickness of the metal layer was about 100 nm. Because of the inaccuracies in the measurement and errors in the equations used for the calculation of stress changes, the uncertainty is high. It should be noted that the angular deflection in this case has been measured point by point, in contrast to the continuous stress vs. potential plot (Fig. 7.1a, curve 2) [13].

Voltdeflectograms ($\Delta(1/R)$ vs. E curves, R is the radius of curvature of the strip) and simultaneously recorded cyclic voltammograms (CVs) of platinum and gold in 0.1M H_2SO_4 solution are shown in Fig. 7.1a, b (curves 2 and 3, respectively, sweep rates $v = 50$ mV s^{-1}) [13]. (Since the correct value of k_i in Eq. (4.24) is uncertain, only the values of $\Delta(1/R)$ are shown in some figures.)

Cantilever probes for the above measurement were prepared by evaporating a 150-nm-thick gold or an 80-nm-thick platinum layer on a very thin layer of titanium evaporated on one side of a glass strip after careful cleaning of the surface. (Dimensions and physical properties of the glass substrate: total length: $l_s = 60.0$ mm; width: $w_s = 5.0$ mm; thickness: $t_s = 147$ μm; Poisson’s ratio: $\nu_s = 0.230$; Young’s modulus: $E_s = 7.09 \times 10^{10}$ N m^{-2}; and index of refraction: $n_g = 1.522$, i.e., $k_i \cdot t_f = 331.6$ N for the present case, see, e.g., Eqs. (4.22), (4.24), and (4.25).) The geometrical area of the electrode (the area of the metal layer in contact with the electrolyte solution) was 2.0 cm^2.

As it can be seen from Fig. 7.1a, b, the change in the radius of curvature in case of gold is about 0.0046 m^{-1}, in the potential range from −0.3 to 1.5 V vs. SCE (saturated calomel electrode [KCl]), while in case of platinum, the changes are greater; the difference between the maximum and minimum value in the potential range from −0.3 to 1.2 V vs. SCE is about 0.0069 m^{-1}. Hysteresis was observed both in the hydrogen and oxygen adsorption/desorption regions.

In [14, 15], simultaneously measured changes of interfacial stress, mass, and charge at sputtered platinum in acid sulfate solutions ($0 < pH < 6.5$) were reported. The deformations of the disk-shaped probe were measured with an electrochemical Kösters laser interferometer [16]. Figure 7.2 shows the time dependence of the interfacial stress change of platinum in contact with 0.3M sulfuric acid and the changes of the quartz oscillator frequency during pulse experiments starting from a bias potential $E = 0.1$ V vs. SCE. Potential pulses of different heights and 150 s duration were applied. After stepping the potential, the mass changed rapidly simultaneously with a fast decay of the current.

The $\Delta\gamma_s$ vs. E curve and the simultaneously recorded cyclic voltammogram of platinum in potassium sulfate solution (acidified with H_2SO_4, pH 3.43) at a sweep

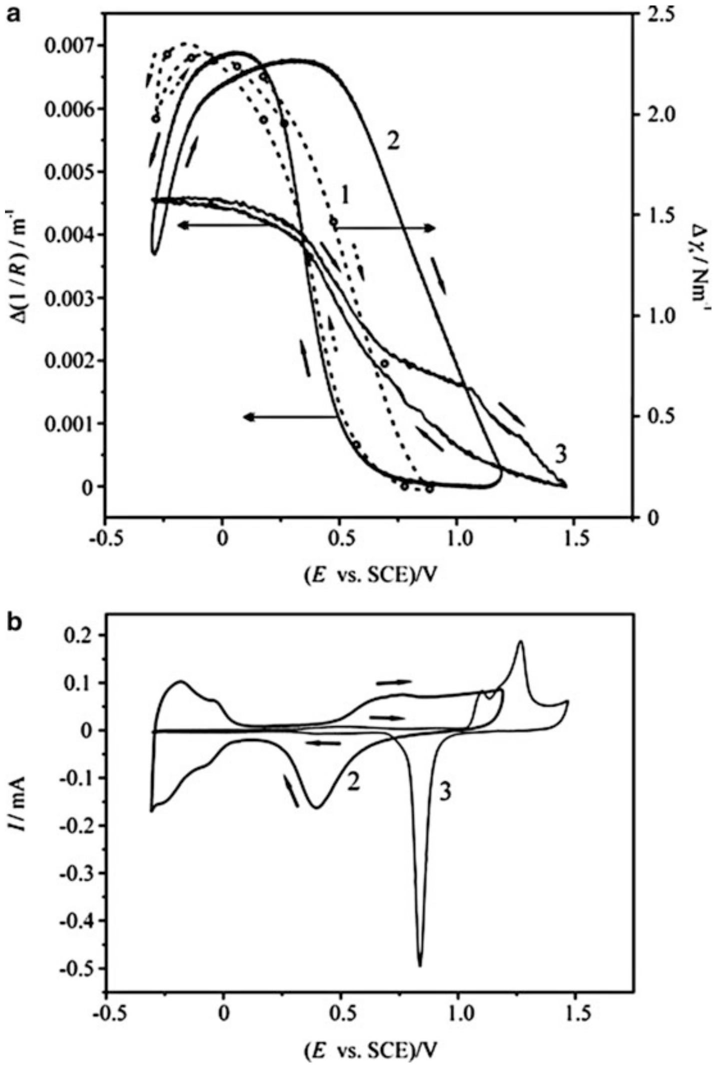

Fig. 7.1 (**a**) Curve 1: Interfacial stress vs. *E* curve for platinum in 8.3×10^{-4} mol dm^{-3} M H_2SO_4 solution (adapted from [12]). *Curves* 2, 3: $\Delta(1/R)$ vs. *E* curves of platinum (2) and gold (3) (deposited on glass strips by vacuum evaporation, surface area: $A = 2$ cm^2) recorded in $c = 0.1$ mol dm^{-3} H_2SO_4 solution at 25°C (sweep rate: $v = 50$ mV s^{-1}). (**b**) *Curves* 2, 3: Cyclic voltammograms recorded simultaneously (platinum (2) and gold (3)). *E*: electrode potential; *I*: current; *R*: radius of curvature of the cantilever; SCE: saturated calomel electrode (KCl)

rate of $v = 10$ mV s^{-1} is displayed in Fig. 7.3. In the hydrogen adsorption region ($-0.4 < E/\mathrm{V} < 0$), the voltammogram exhibits two current peaks in the positive-going scan ($E \approx -0.13$ V and -0.28 V vs. SCE). The interfacial stress in Fig. 7.3

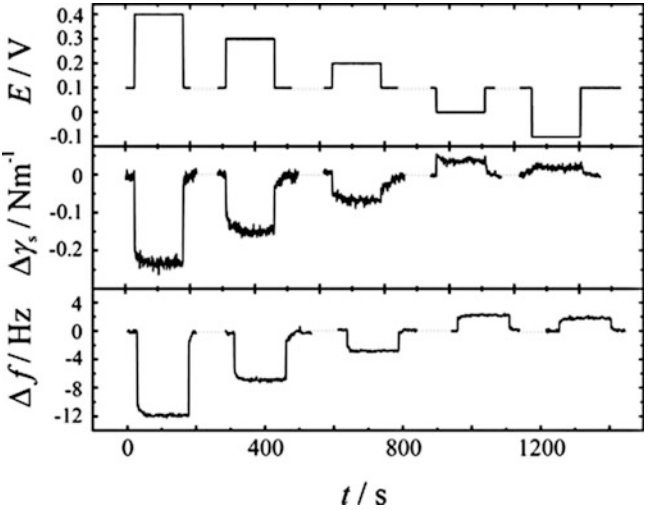

Fig. 7.2 Pulse experiments with platinum in 0.3 M H_2SO_4. *Top*: Applied electrode potential E vs. SCE. *Center*: Change of interfacial stress. *Bottom*: Frequency change of the EQCM t is the time. (Adapted from [17])

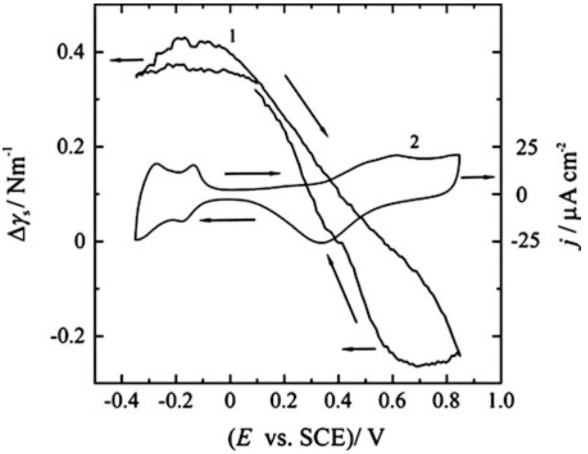

Fig. 7.3 Curve 1: Current density j as a function of electrode potential E for platinum in 0.3 M K_2SO_4, pH = 3.43, at $v = 10$ mV s^{-1}. 2: Changes of interfacial stress with the electrode potential under the same conditions. Adapted from [14, 15]

($\Delta\gamma_s$ vs. E curve) during the positive potential scan appears to have two not very pronounced maxima at about $E = -0.08$ V and -0.18 V vs. SCE.

Figure 7.4 shows the time dependence of the interfacial stress change and the changes of the quartz oscillator frequency during pulse experiments starting from a bias potential $E = 0$ V vs. SCE.

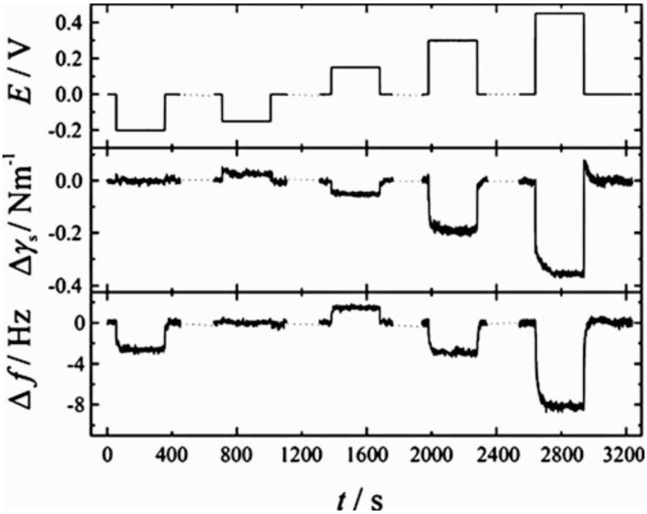

Fig. 7.4 Time dependence of the interfacial stress change and the changes of the quartz oscillator frequency during pulse experiments starting from a bias potential $E = 0$ V vs. SCE. The conditions are the same as in Fig. 7.3. Adapted from [15]

In [17, 18], simultaneous oscillations of electrode potential, surface mass, and specific surface energy have been detected in the course of galvanostatic oxidation of formic acid on platinum by using the Kösters interferometer combined with an electrochemical quartz crystal microbalance. Changes of interfacial stress data measured with the electrochemical Kösters laser interferometer and with the electrochemical bending beam method have been shown to be equivalent.

Figure 7.5 shows a typical pattern of the simultaneous oscillations of the electrode potential, the interfacial stress, and the frequency of the EQCM determined with the electrochemical Kösters interferometer setup. A constant current $I = 0.35$ mA was applied to the electrode immersed in a $c(H_2SO_4) = 0.5$ mol dm^{-3} sulfuric acid solution containing 0.9 mol dm^{-3} formic acid. Oscillations started after an induction period. In general, under the same conditions of current density and composition of the solution, the oscillation experiment could be repeated several times. The induction period is most likely due to the slow accumulation of adsorbed species poisoning the electrode. According to curves a and c, the rapid decrease of the potential apparently is accompanied by a fast increase of the superficial mass, i.e., by a fast decrease of the frequency. As the potential increases again, the frequency of the EQCM also increases. In both directions of the potential scan, the changes of the frequency are somewhat slower than that in both directions, which indicate that the rate of chemisorption is somewhat higher than the oxidation of the chemisorbed particles. The changes of γ_s also follow the changes of the electrode potential. As the potential increases, the specific surface energy decreases. The rapid decrease of the potential is accompanied by a rapid increase of γ_s.

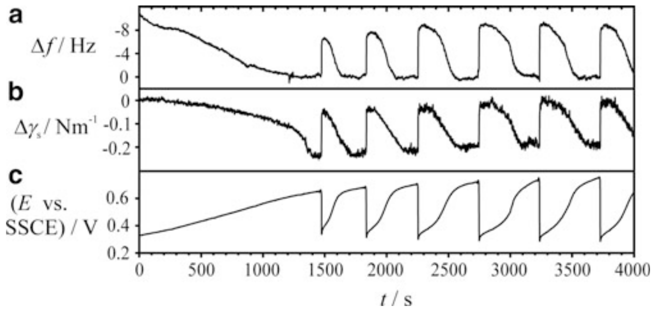

Fig. 7.5 Typical oscillation patterns for the galvanostatic oxidation (current density: $j = 0.15$ mA cm^{-2}) of formic acid at Pt in a solution containing 0.5 mol dm^{-3} sulfuric acid and 0.9 mol dm^{-3} formic acid. (**a**) Changes of frequency (Δ*f*) of the EQCM (10 MHz, AT-cut quartz), (**b**) changes in the interfacial stress ($\Delta\gamma_s$), (**c**) electrode potential *E* as a function of time *t*. Adapted from [18]

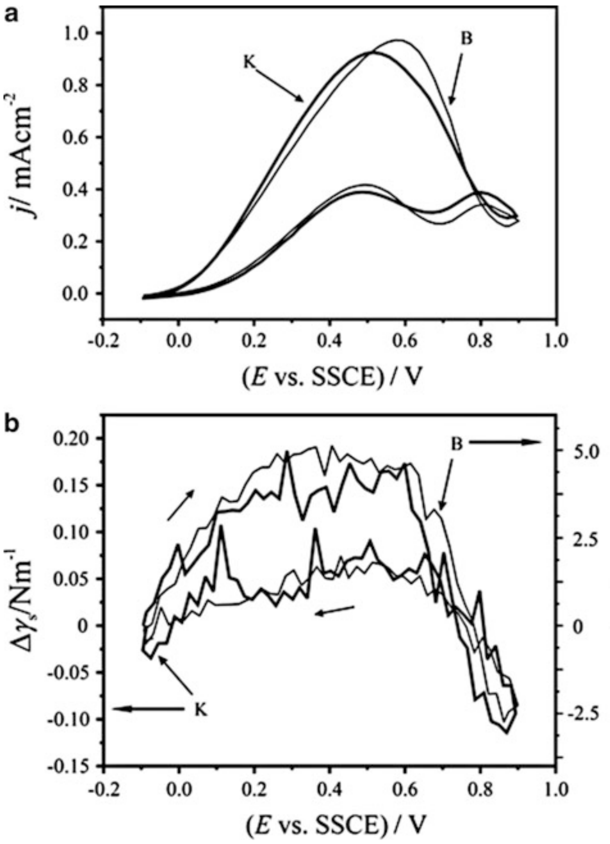

Fig. 7.6 (**a**) Cyclic voltammograms; (**b**) changes of interfacial stress (*K*) and changes in the reciprocal radius of curvature (*B*) with electrode potential *E* obtained for platinum in contact with solutions containing 1.0 mol dm^3 sulfuric acid and 0.8 mol dm^3 formic acid. Sweep rate: $v = 20$ mV/s. (*K*) from experiments with the Kösters laser interferometer and (*B*) from bending beam experiments. Adapted from [18]

In Fig. 7.6, results of experiments with the electrochemical bending beam setup and with the Kösters laser interferometer are compared. Both setups yield practically identical cyclic voltammograms for the sputtered platinum layers in contact with mixtures of sulfuric acid and formic acid (1 mol dm^{-3} and 0.8 mol dm^{-3}, respectively), at a sweep rate of $v = 20$ mV s^{-1}. On the other hand, the simultaneously recorded $\Delta\gamma_s$ vs. E curves from the interferometer experiments and the $\Delta(1/R)$ vs. E curves measured with the bending beam method have very similar shapes.

Experimental results obtained by the bending beam technique on gold have been reported in [19].

A cantilever bending investigation into the variation of surface stress, with surface charge density for (1 1 1)-textured thin films of gold in aqueous NaF and $HClO_4$, has been reported in [20]. A linear correlation between surface stress and charge in a significant potential interval around the pzc has been found. Changes of the interfacial stress of sputtered gold films (deposited on an oscillating quartz plate) in contact with aqueous $K_2SO_4 + H_2SO_4$ solutions were measured by Kösters laser interferometry simultaneously with changes of mass and current density as functions of the electrode potential and of the concentration of sulfate ions at different pH [21]. Changes in the interfacial stress of gold in contact with HCl solutions are reported in [22, 23].

In [24], in situ stress measurements were carried out during copper electrodeposition onto (1 1 1)-textured Au from acidic sulfate electrolyte using the bending beam method. When deposition was interrupted, both tensile and compressive components of the stress relaxed somewhat, but were quickly reestablished when deposition was resumed. The development of the growth stress was very similar to that reported for Cu deposition from the vapor phase. The changes in interfacial stress of the evaporated gold (mainly oriented to the (1 1 1) plane) in 0.1M sulfuric acid medium or 0.1M perchloric acid medium with and without sulfate or chloride during underpotential deposition (UPD) of copper were measured using the bending beam method [25]. It has been found that the coadsorption of (bi)sulfate or chloride ions with copper atoms induced the compressive surface stress to promote the Cu-UPD. The factors influencing the surface stress or surface elastic strain were discussed in relation to the Cu-UPD structure. The bending beam method was used for the investigation of anodic oxidation and cathodic reduction processes at Cu/Cu_2O multilayer films and pure Cu films in pH 8.4 borate buffer solutions [26].

In [27], results from simultaneous measurements of the changes of specific surface energy, mass, and charge for the adsorption of KF and the UPD of Pb, Tl, and Zn on polycrystalline gold are compared to theoretical predictions.

In [28], experimental results are presented for the systems Pb^{2+}/Au(111), Pb^{2+}/Ag(1 1 1), and Ag^{+}/Au(1 1 1) in 0.1M $HClO_4$. In [29], surface stress changes during Pb UPD on (1 1 1)-textured Au in perchloric acid-supporting electrolyte have been investigated. The sweep rate dependence in peak height and the stress relaxation hump at the transition between submonolayer to monolayer were interpreted as the result of kinetically controlled surface alloying and dealloying processes. The stress change associated with the electrodeposition of Pd onto

(1 1 1)-textured Au cantilever electrodes in 0.1M H_2SO_4-supporting electrolyte has been examined in [30].

In [31, 32], interfacial stress changes associated with the UPD of bismuth and thallium (Tl) on (1 1 1)-textured Au in acidic perchlorate- and nitrate-supporting electrolyte solutions were examined using the bending beam method.

Results of the measurements of interfacial stress changes with gold immersed in equilibrated partially miscible water—isobutyl alcohol—hydrochloric acid phases have been reported in [33]. According to thermodynamic considerations, changes of the surface energy of a given electrode with the intensive parameters such as electrode potential, chemical potential of a component, and temperature should be the same in either phase of equilibrated partially miscible electrolytes. The changes of the interfacial stress with electrode potential were measured by Kösters laser interferometry. Although no structural resemblance follows from thermodynamics properties, the experimental results indicate similar structures of the interfacial layers formed in the coexisting equilibrium phases.

7.3 Stress Changes in Thin Films and Layers on Metals

7.3.1 Anodic Films and Passive Layers

High-resolution curvature measurements have been performed in situ during aluminum thin film anodized in sulfuric acid [34, 35]. A well-defined transition in the rate of internal stress-induced curvature change was shown to allow for the accurate, real-time detection of porosity initiation. In conclusion, it has been shown that the initiation of porosity during aluminum anodizing in sulfuric acid can be accurately detected in situ by high-resolution curvature measurements.

The relationship between the microstructural and internal stress evolution during Ti anodizing has been discussed in [36, 37]. Correlations have been found between the microstructural and internal stress evolution during galvanostatic Ti thin-film anodization. Stresses in anodic oxide film on titanium thin film/glass electrode in pH 8.4 borate solution were investigated by using the bending beam method [38].

The changes of the interfacial stress of a thin Ni plate in contact with a 0.1 mol dm^{-3} perchloric acid solution were estimated from the changes in the bending of the plate (only one side of the plate was in contact with the electrolyte solution; the other side of it was covered with a nonconducting film) [39]. As it can be seen in Fig. 7.7, the mechanical properties of the passive layer on nickel are influenced by the presence of Cl^- ions.

The shape of the voltstressogram recorded in 0.1M perchloric acid solution (curve 1) changes substantially if the solution contains 10^{-4}M chloride ions (curve 2). The increase in the deflection is more pronounced at higher Cl^- concentrations. It is known from the literature that chloride ions are incorporated in the passive film on nickel, if the film is formed in Cl^--containing solutions [40,

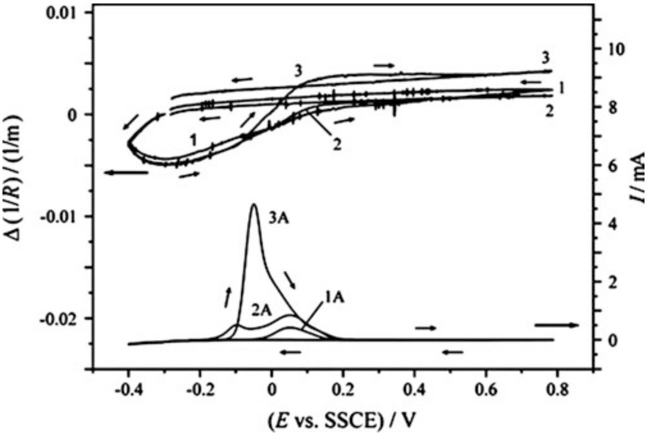

Fig. 7.7 Changes in the radius of curvature of a Ni plate (one side of it covered with a Teflon® foil) and the current during potential sweep in a 0.1 mol dm^{-3} perchloric acid solution (curves 1 and 1A), in the same solution containing 10^{-4} mol dm^{-3} Cl^- ions (2, 2A), and in the same solution containing 2.5×10^{-4} mol dm^{-3} Cl^- ions (3, 3A) (sweep rate: 3 mV s^{-1}) (SSCE: calomel electrode, the electrolyte solution is saturated with NaCl). Adapted from [39]

41]. Since the change of the stress is positive (tensile stress), it can be assumed that chloride ions incorporated in the passive film facilitate the formation of a more ordered structure.

From thermodynamic point of view, perchlorate ions at solution/metal electrode interfaces, mainly in acidic medium, should be instable against reductive attacks in a wide potential range [42]. In contrast to this, it is a general view in the electrochemical literature that ClO_4^- ions are very resistant to reduction. Therefore, perchlorates (e.g., perchloric acid and sodium perchlorate) are widely used as supporting electrolytes in electrochemical studies. Among these investigations, reports concerning dissolution, deposition, passivation, and corrosion of iron group metals can also be found (see, e.g., [43–46] and literature cited therein). However, it has been already demonstrated that the reduction of perchlorate ions takes place during the corrosion of Co, Ni, and Fe in $HClO_4$ solutions. A survey of the literature can be found in reviews [44, 45, 47]. The bending beam method can be considered as an appropriate tool for the in situ monitoring of these effects.

7.3.2 *Monitoring of the Electrochemical Degradation of Polymer Films*

In recent years, there has been great progress in research on electronic and electrochemical devices based on organic materials. Such devices are, e.g., light emitting diodes, organic thin film transistors, solar cells, memory devices, ion-selective electrodes, microelectrode arrays, fuel cells, etc. [48–57]. The monitoring of the degradation of polymer layers is of great importance for the long-term use of the devices. Among the organic-conducting polymers, poly(3,4-ethylenedioxythiophene), often abbreviated as PEDOT, and its derivatives appear to be among the most stable organic-conducting polymers currently available. Previous studies have shown that PEDOT is electroactive in aqueous solutions [58–60], changes its color depending on the applied potential, is transparent in the oxidized state, is highly insoluble in almost every solvents, and exhibits quite a high conductivity (ca. 300 S cm^{-1}). According to experimental results, during oxidation or reduction processes, the mechanical properties of conductive polymers may change significantly [61, 62].

Considerable stress changes in dodecylbenzenesulfonate-doped polypyrrole films have been detected by using a micromechanical cantilever-based sensor [63]. In these experiments, the polymer was electrochemically switched between its oxidized and neutral state by cyclic voltammetry.

In [64], results obtained during the overoxidation of PEDOT on gold in aqueous sulfuric acid and sodium sulfate solutions have been reported. It has been shown that the electrochemical bending beam method is a useful tool for the in situ monitoring of the degradation of polymer films in electrochemical systems. Unfortunately, in the case of polymer-modified electrodes, the change in the interfacial stress of the metal/electrolyte interface with electrode potential (E) occurs simultaneously with the change of the film stress. Both processes can lead to a change of the radius of curvature of the beam. It has been concluded that overoxidation of PEDOT takes place when the electrode potential is more positive than about +0.80 V vs. SCE, but the effect of overoxidation on the electrochemical/electromechanical properties is small if the positive potential limit is kept below 1.20 V vs. SCE. When the positive potential limit was extended to 1.5 V, the cyclic voltammetric wave characteristic of gold oxide reduction appeared after a few cycles in the negative-going potential scan. Similarly, the "deflectograms" recorded by using the bending beam technique before and after overoxidation of the polymer showed significant differences. During subsequent overoxidation cycles, the deflection vs. electrode potential curves more and more resembled that of gold contacting the same solution (see Fig. 7.1a).

A series of cyclic voltammetric curves recorded for a gold/PEDOT/0.1M sulfuric acid (aq) electrode ($t_F \approx 1.4\ \mu m$) at a sweep rate of $v = 50\ mV\ s^{-1}$ are presented in Figs. 7.8b and 7.9b. The corresponding potential programs are given in Figs. 7.8a and 7.9a. After completion of the potential program shown in Fig. 7.8a, six additional triangular potential cycles (between -0.4 and 1.5 V vs. SCE) were applied to the electrode (not shown in the figures). Finally, the four potential cycles shown in Fig. 7.9a were applied. The corresponding $\Delta(1/R)$ vs. E curves are plotted in Figs. 7.8c and 7.9c.

The changes in the $\Delta(1/R)$ vs. E curves become more and more pronounced with the increase of the number of cyclic voltammograms recorded in the potential range where (over)oxidation of the polymer occurs (Fig. 7.9c) and the shape of the curve begins to resemble more and more that of the ΔR^{-1} vs. E curve for PPD on gold (curves 1–2 in Fig. 7.9c). These differences suggest that the film undergoes a

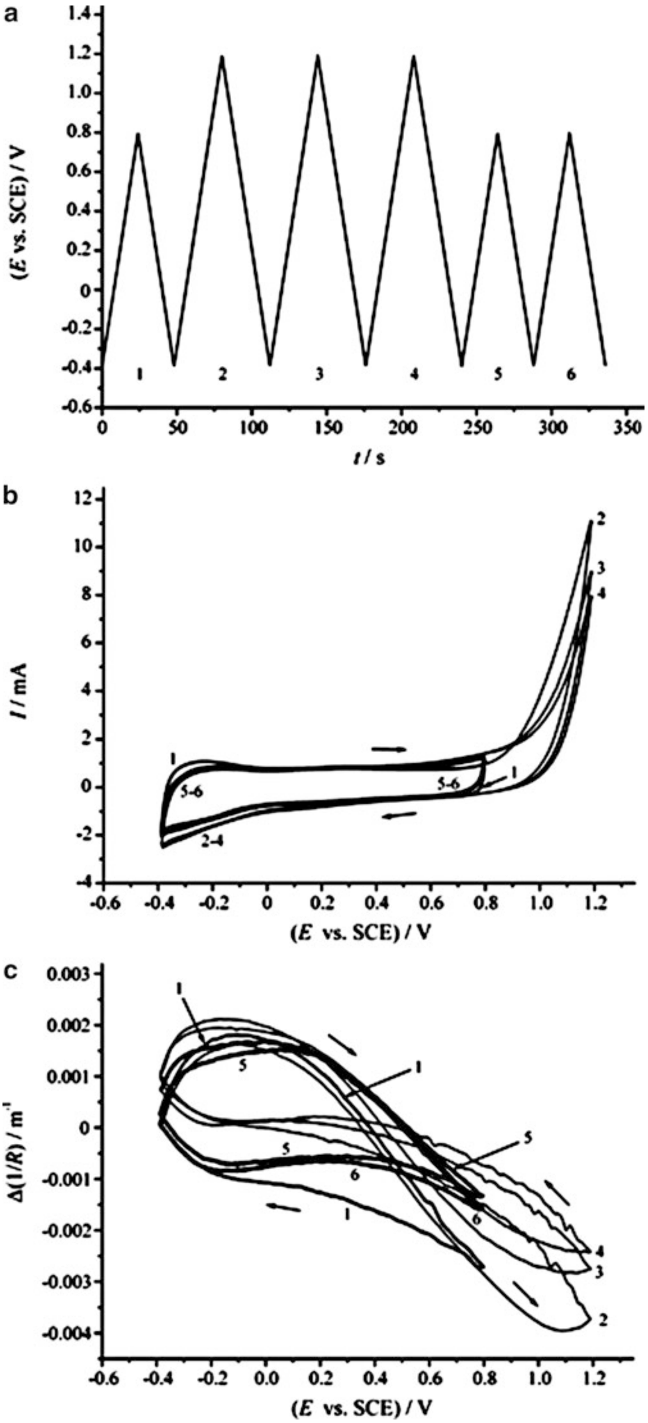

Fig. 7.8 (**a**) Potential program applied to the Au/PEDOT/0.1 M sulfuric acid electrode. Sweep rates $v = 50$ mV s^{-1}. (**b**) The series of cyclic voltammetric curves corresponding to the potential program indicated in (a). (**c**) The simultaneously recorded $\Delta(1/R)$ vs. E curves. Adapted from [64]

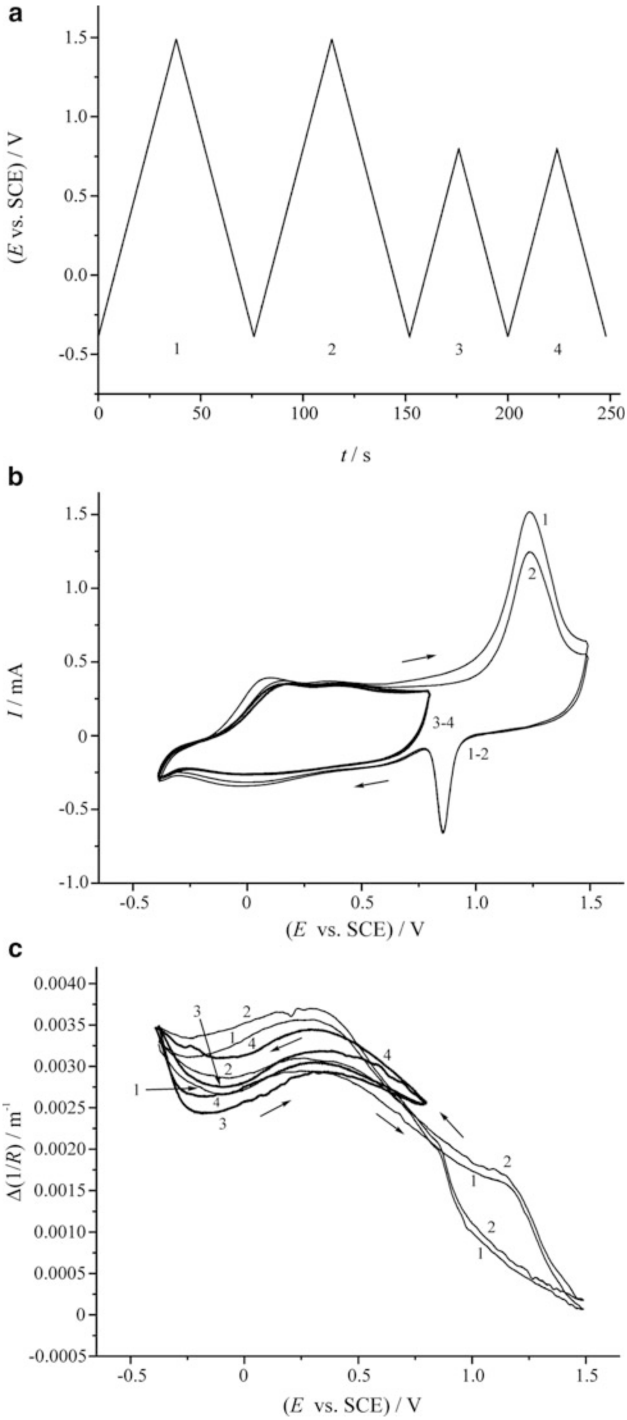

Fig. 7.9 (**a**) Potential program applied to the Au/PEDOT/0.1 M sulfuric acid electrode after the treatment is shown in Fig. 7.8 and six additional potential cycles between −0.4 and 1.5 V vs. SCE

degradation process of some sort upon its (over)oxidation above 0.8 V. After the application of eight potential cycles up to 1.5 V vs. SCE, only a slight change in $1/R$ can be observed in the potential range −0.4 to 0.8 V vs. SCE during subsequent potential cycles (curves 3–4 in Fig. 7.9c). In this potential region, the $\Delta(1/R)$ vs. E curve is of a very characteristic shape with a maximum and a minimum indicating that the polymer layer is still present on the gold surface.

The same conclusion can be drawn on the basis of cyclic voltammetry. When the positive potential limit was extended until 1.5 V, the cyclic voltammetric wave characteristic to gold oxide reduction appeared after a few cycles in the negative-going potential scan (curves 1–2 in Fig. 7.9b). On the other hand, the CVs recorded in the potential range from −0.4 to 0.8 V vs. SCE clearly show the presence of a significant amount of polymer in direct (electrical) contact with the gold surface (curves 3–4 in Fig. 7.9b).

Most of the results could be explained by the assumption that the observed electrochemical/mechanical behavior of the Au/PEDOT/0.1M sulfuric acid (aq) electrodes before and after overoxidation is directly related to the internal structure of the polymer, i.e., by supposing structural changes in the originally compact and strongly adherent polymer film during the overoxidation (degradation) process. An alternative explanation is that during overoxidation, the film gradually delaminates from the gold layer, exposing the underlying gold substrate to the electrolyte solution. It has been shown in [13] that both interpretations outlined in the introduction can be considered as correct. The most important point is that structural changes in (Au, Pt)/PEDOT films due to overoxidation are associated with the formation of cracks or crevices and occur almost simultaneously with the initiation of delamination.

7.3.3 Insertion of Species into Materials, Absorption, and Intercalation

In [65], the stress change generated during lithium transport through the rf-sputter-deposited $Li_{1-\delta}CoO_2$ films in contact with 1M solution of lithium perchlorate in propylene carbonate was determined as a function of the lithium stoichiometry, $(1 - \delta)$, using the bending beam method combined with cyclic voltammetry, galvanostatic intermittent titration technique, and potentiostatic current transient technique. (Note that the results in [65] have been corrected in [66].) The stress changes generated during lithium transport through the sol/gel-derived $Li_xMn_2O_4$

Fig. 7.9 (continued) (not shown in the figures). Sweep rates $v = 50$ mV s^{-1}. (**b**) The series of cyclic voltammetric curves corresponding to the potential program indicated in (a). (**c**) The simultaneously recorded $\Delta(1/R)$ vs. E curves. Adapted from [64] films annealed at 773 and 873 K were quantitatively determined as a function of the lithium stoichiometry (electrolyte solution used in the experiments: manganese acetylacetonate $Mn(CH_3COCHCOCH_3)_3$ and lithium acetylacetonate ($LiCH_3$-$COCHCOCH_3$) dissolved in 1-butanol and acetic acid).

In [67], the stresses generated during cyclic voltammetric measurements on a Pd foil electrode in 0.1M NaOH solution have been analyzed by using the bending beam technique combined with cyclic voltammetry. The stress behavior of hydrogen adsorption/absorption into Pd layers electrodeposited on (1 1 1)-textured gold has been investigated in alkaline solution [68] and in 0.1M H_2SO_4 [69].

In situ measurements of stress evolution in a silicon thin-film electrode during electrochemical lithiation and delithiation by using the multibeam optical sensor (MOS) technique were reported in [70].

References

1. Láng GG, Seo M (2000) J Electroanal Chem 490:98–101
2. Rokob TA, Láng GG (2005) Electrochim Acta 51:93–97
3. Tian F, Pei JH, Hedden DL, Brown GM, Thundat T (2004) Ultramicroscopy 100:217–223
4. Tabard-Cossa V, Godin M, Beaulieu LY, Grütter P (2006) Sensor Actuator B Chem 119:352–354
5. Láng GG, Rokob TA, Horányi G (2005) Ultramicroscopy 104:330–332
6. Láng GG (2008) Bending beam method. In: Bard AJ, Inzelt G, Scholz F (eds) Electrochemical dictionary. Springer, Berlin
7. Frumkin AN (1963) Holography and holographic interferometry in electrochemistry. In: Delahay P, Tobias CW (eds) Advances in electrochemistry and electrochemical engineering. Muller RH (ed) Optical techniques in electrochemistry, vol 3. Wiley, New York, NY
8. Plieth WJ, Vetter KJ (1968) Ber Bunsenges Phys Chem 72:673–680
9. Plieth WJ, Vetter KJ (1969) Ber Bunsenges Phys Chem 73:79–86
10. Soffer A (1972) J Electroanal Chem 40:153–165
11. Frumkin AN, Petrii OA (1975) Electrochim Acta 20:347–359
12. Fredlein RA, Damjanovic A, Bockris JO'M (1971) Surf Sci 25:261–264
13. Láng GG, Ujvári M, Bazsó F, Vesztergom S, Ujhelyi F (2012) Electrochim Acta http://dx.doi.org/10.1016/j.electacta.2012.01.068; http://www.sciencedirect.com/science/article/pii/S0013468612001065
14. Láng G, Torma V, Heusler KE (1997) Changes of the specific surface energy of platinum in aqueous sulfate solutions. In: Korzeniewski C, Conway BE (eds) The electrochemical double layer, physical electrochemistry, proceedings volume 97-17. The Electrochemical Society Inc., Pennington NJ
15. Láng GG (2009) Application of the koesters interferometer in electrochemistry. In: Halsey D, Raynor W (eds) Handbook of interferometers; research, technology and applications. Nova Science Publishers, New York, NY
16. Láng GG (2008) Kösters laser interferometer. In: Bard AJ, Inzelt G, Scholz F (eds) Electrochemical dictionary. Springer, Berlin
17. Láng G, Ueno K, Ujvári M, Seo M (2000) J Phys Chem B 104:2785–2789
18. Láng GG, Seo M, Heusler KE (2005) J Solid State Electrochem 9:347–353
19. Fredlein RA, Bockris JO'M (1974) Surf Sci 46:641–652
20. Smetanin M, Viswanath RN, Kramer D, Beckmann D, Koch T, Kibler LA, Kolb DM, Weissmüller J (2008) Langmuir 24:8561–8567

21. Láng G, Heusler KE (1995) J Electroanal Chem 391:169–179
22. Láng G, Heusler KE (1995) Russ J Electrochem 31:759–767
23. Láng G, Heusler KE (1995) Elektrokhimiya 31:826–835
24. Kongstein OE, Bertocci U, Stafford GR (2005) J Electrochem Soc 152:C116–C123
25. Seo M, Yamazaki M (2007) J Solid State Electrochem 11:1365–1373
26. Seo M, Hagioi M (2007) Corros Sci 49:176–185
27. Jaeckel L, Láng G, Heusler K (1994) Electrochim Acta 39:1031–1038
28. Friesen C, Dimitrov N, Cammarata RC, Sieradzki K (2001) Langmuir 17:807–815
29. Shin JW, Bertocci U, Stafford GR (2010) J Phys Chem 114:7926–7932
30. Stafford GR, Bertocci U (2009) J Phys Chem C 113:261–268
31. Stafford GR, Bertocci U (2006) J Phys Chem B 110:15493–15498
32. Shin JW, Bertocci U, Stafford GR (2010) J Phys Chem C 114:17621–17628
33. Láng G, Heusler KE (1997) J Chem Soc Faraday Trans 93:583–589
34. Van Overmeere Q, Nysten B, Proost J (2009) Appl Phys Lett 94:074103
35. Van Overmeere Q, Blaffart F, Proost J (2010) Electrochem Commun 12:1174–1176
36. Vanhumbeeck J-F, Tian H, Schryvers D, Proost J (2010) Corr Sci 53:1269–1277
37. Proost J, Vanhumbeeck J-F, Van Overmeere Q (2009) Electrochim Acta 55:350–357
38. Kim J-D, Pyun S-I, Seo M (2003) Electrochim Acta 48:1123–1130
39. Láng GG, Rokob TA, Ujvari M, Horányi G (2005) Electrochemical aspects of the behavior of perchlorate ions in the presence of iron group metals. In: Marcus P, Maurice V (eds) Passivation of metals and semiconductors, and properties of thin oxide layers. Elsevier, Amsterdam
40. Herbelin JM, Barbouth N, Marcus P (1990) J Electrochem Soc 137:3410–3414
41. Marcus P, Herbelin JM (1993) Corros Sci 34:1123–1145
42. Charlot G, Collumeau A, Marchon MJC (1971) Oxidation-reduction potentials of inorganic substances in aqueous solution. Butterworths, London
43. Zucchi F, Fonsati M, Trabanelli G (1998) J Appl Electrochem 28:441–447
44. Láng GG, Horányi G (2003) J Electroanal Chem 552:197–211
45. Ujvári M, Láng G (2011) J Electrochem Sci Eng 1:1–26
46. Horányi G (1996) Electrosorption studies in electrocatalysis. In: Spivey JJ (ed) Catalysis. A specialist periodical report. The Royal Society of Chemistry, Cambridge, MA
47. Láng GG, Ujvári M (in press) Trends in the study of the electrochemical stability of perchlorate ions against reductive attacks. In: Matthews LE (ed) Perchlorates: production, uses and health effects. Nova Science Publishers, Hauppauge NY
48. Lang U, Naujoks N, Dual J (2009) Synthetic Met 159:473–479
49. Lilliedala MR, Medforda AJ, Madsena MV, Norrmana K, Krebs FC (2010) Sol Energ Mat Sol C 94:2018–2031
50. Nasybulin E, Wei S, Cox M, Kymissis I, Levon K (2011) J Phys Chem C 115:4307–4314
51. Scott JC (2004) Science 304:62–63
52. Möller S, Perlov C, Jackson W, Taussig C, Forrest SR (2003) Nature 426:166–169
53. Cui X, Martin DC (2003) Sensor Actuator B Chem 89:92–102
54. Vázquez M, Danielsson P, Bobacka J, Lewenstam A, Ivaska A (2004) Sensor Actuat B-Chem 97:182–189
55. Bobacka J (1999) Anal Chem 71:4932–4937
56. Drillet JF, Dittmeyer R, Jüttner K, Li L, Mangold KM (2006) Fuel Cells 6:432–438
57. Drillet JF, Dittmeyer R, Jüttner K (2007) J Appl Electrochem 37:1219–1226
58. Bobacka J, Lewenstam A, Ivaska A (2000) J Electroanal Chem 489:17–27
59. Yamato H, Ohwa M, Wernet W (1995) J Electroanal Chem 397:163–170
60. Sakmeche N, Aeiyach S, Aaron JJ, Jouini M, Lacroix JC, Lacaze PC (1999) Langmuir 15:2566–2574
61. Pei Q, Inganaes O (1992) J Phys Chem 96:10507–10514
62. Pei Q, Inganaes O (1993) J Phys Chem 97:6034–6041

63. Tabard-Cossa V, Godin M, Grütter P, Burgess I, Lennox RB (2005) J Phys Chem B 109:17531–17537
64. Ujvári M, Takács M, Vesztergom S, Bazsó F, Ujhelyi F, Láng GG (2011) J Solid State Electrochem 15(11–12):2341–2349. doi:10.1007/s10008-011-1472-y
65. Pyun SI, Go JY, Jang TS (2004) Electrochim Acta 49:4477–4486
66. Go JY, Shin HC, Pyun SI (2005) Electrochim Acta 51:566–567
67. Han JN, Lee JW, Seo M, Pyun SI (2001) J Electroanal Chem 506:1–10
68. Shin JW, Bertocci U, Stafford GR (2011) J Electrochem Soc 158:F127–F134
69. Stafford GR, Bertocci U (2009) J Phys Chem C 113:13249–13256
70. Sethuramana VA, Chon MJ, Shimshak M, Srinivasan V, Guduru PR (2010) J Power Sources 195:5062–5066

Chapter 8
Mathematical Methods in Interfacial Thermodynamics

8.1 Important Mathematical Concepts

8.1.1 *Homogeneous Functions*

8.1.1.1 Definition

A homogeneous function is a function of one or several variables that satisfies the following condition: when all independent variables of a function are simultaneously multiplied by the same (arbitrary) factor, the value of the function is multiplied by some power of this factor.

Let $f(x_1, x_2, \ldots, x_m)$ a real function of variables $x_1, x_2, \ldots, x_m$ such that

$$f(kx_1, kx_2, \ldots, kx_m) = k^n f(x_1, x_2, \ldots, x_m) \tag{8.1}$$

for all $k > 0$, and then f is said to be a *homogeneous function of degree n.*

8.1.1.2 Euler's Theorem

Euler's theorem states that the differentiable function f of m variables is homogeneous of degree n if and only if

$$nf(x_1, x_2, \ldots, x_m) = \sum_{i=1}^{m} x_\mathrm{i} \frac{\partial f}{\partial x_i}. \tag{8.2}$$

Proof. Let

$$f(\hat{x}_1, \hat{x}_2, \ldots, \hat{x}_m)$$

G.G. Láng and C.A. Barbero, *Laser Techniques for the Study of Electrode Processes*,
Monographs in Electrochemistry, DOI 10.1007/978-3-642-27651-4_8,

be a homogeneous function of degree n such that

$$f(\kappa\hat{x}_1,\kappa\hat{x}_2,\ldots,\kappa\hat{x}_m)=\kappa^n f(\hat{x}_1,\hat{x}_2,\ldots,\hat{x}_m) \tag{8.3}$$

and

$$k\neq 0,\,\frac{1}{k}=\kappa,\quad x_i=\frac{1}{k}\hat{x}_i=\kappa\hat{x}_i,\quad kx_i=\hat{x}_i.$$

Evidently,

$$f(\kappa\hat{x}_1,\kappa\hat{x}_2,\ldots,\kappa\hat{x}_m)=f(x_1,x_2,\ldots,x_m)=\left(\frac{1}{k}\right)^n f(kx_1,kx_2,\ldots,kx_m) \tag{8.4}$$

and

$$k^n f(x_1,x_2,\ldots,x_m)=f(kx_1,kx_2,\ldots,kx_m)=f(\hat{x}_1,\hat{x}_2,\ldots,\hat{x}_m), \tag{8.5}$$

that is, $f(x_1,x_2,\ldots,x_m)$ is also a homogeneous function of degree n.

To prove Euler's theorem, differentiate each side of Eq. (8.3) with respect to κ to give

$$\begin{aligned}&\frac{\partial f(\kappa\hat{x}_1,\kappa\hat{x}_2,\ldots,\kappa\hat{x}_m)}{\partial\kappa\hat{x}_1}\hat{x}_1+\frac{\partial f(\kappa\hat{x}_1,\kappa\hat{x}_2,\ldots,\kappa\hat{x}_m)}{\partial\kappa\hat{x}_2}\hat{x}_2+\ldots\\&+\frac{\partial f(\kappa\hat{x}_1,\kappa\hat{x}_2,\ldots,\kappa\hat{x}_m)}{\partial\kappa\hat{x}_m}\hat{x}_m=n\kappa^{n-1}f(\hat{x}_1,\hat{x}_2,\ldots,\hat{x}_m).\end{aligned} \tag{8.6}$$

By introducing $\kappa=1/k,\ x_i=\kappa\hat{x}_i,\ \hat{x}_i=kx_i$,

$$\begin{aligned}&\frac{\partial f(x_1,x_2,\ldots,x_m)}{\partial x_1}kx_1+\frac{\partial f(x_1,x_2,\ldots,x_m)}{\partial x_2}kx_2+\ldots\\&+\frac{\partial f(x_1,x_2,\ldots,x_m)}{\partial x_m}kx_m=n\left(\frac{1}{k}\right)^{n-1}f(kx_1,kx_2,\ldots,kx_m).\end{aligned} \tag{8.7}$$

Taking into account that according to Eq. (8.4)

$$k^n f(x_1,x_2,\ldots,x_m)=f(kx_1,kx_2,\ldots,kx_m), \tag{8.8}$$

Eq. (8.7) can be rewritten as

$$\begin{aligned}&\frac{\partial f(x_1,x_2,\ldots,x_m)}{\partial x_1}kx_1+\frac{\partial f(x_1,x_2,\ldots,x_m)}{\partial x_2}kx_2+\ldots+\frac{\partial f(x_1,x_2,\ldots,x_m)}{\partial x_m}kx_m\\&=n\left(\frac{1}{k}\right)^{n-1}k^n f(kx_1,kx_2,\ldots,kx_m).\end{aligned} \tag{8.9}$$

This means that

$$\sum_{i=1}^{m} \frac{\partial f(x_1, x_2, \ldots, x_m)}{\partial x_i} x_i = nf(x_1, x_2, \ldots, x_m), \tag{8.10a}$$

or, obviously,

$$\sum_{i=1}^{m} \frac{\partial f(\hat{x}_1, \hat{x}_2, \ldots, \hat{x}_m)}{\partial \hat{x}_i} \hat{x}_i = nf(\hat{x}_1, \hat{x}_2, \ldots, \hat{x}_m), \tag{8.10b}$$

which is exactly *Euler's theorem*.

Alternatively, by differentiating the homogeneity condition [Eq. (8.1)] with respect to k,

$$\frac{\partial}{\partial k} f(kx_1, kx_2, \ldots, kx_m) = \frac{\partial}{\partial k} k^n f(x_1, x_2, \ldots, x_m), \tag{8.11}$$

and thus

$$\sum_{i=1}^{m} \frac{\partial f(kx_1, kx_2, \ldots, kx_m)}{\partial kx_i} x_i = nk^{n-1} f(x_1, x_2, \ldots, x_m). \tag{8.12}$$

Then, setting $k = 1$, we have

$$\sum_{i=1}^{m} x_i \frac{\partial f(x_1, x_2, \ldots, x_m)}{\partial x_i} = nf(x_1, x_2, \ldots, x_m), \tag{8.13}$$

which was to be proved.

We can show that *the converse theorem also holds*, that is, if Eq. (8.2) holds, then the function f is homogeneous of degree n.

Suppose that Eq. (8.2) is true, that is,

$$nf(x_1, x_2, \ldots, x_m) = \sum_{i=1}^{m} x_i \frac{\partial f}{\partial x_i}.$$

Let us fix $(x_1, \ldots, x_m)$ and define the function g of a single variable as

$$g(t) = t^{-n} f(tx_1, \ldots, tx_m) - f(x_1, \ldots, x_m). \tag{8.14}$$

Differentiate each side of this equation with respect to t to give

$$\frac{\partial g(t)}{\partial t} = -nt^{-n-1} f(tx_1, \ldots, tx_m) + t^{-n} \sum_{i=1}^{m} x_i \frac{\partial f(tx_1, \ldots, tx_m)}{\partial tx_i}. \tag{8.15}$$

By Euler's theorem (see, e.g., 8.10b), we have

$$\sum_{i=1}^{m} \frac{\partial f(tx_1, \ldots, tx_m)}{\partial tx_i} tx_i = nf(tx_1, \ldots, tx_m) \tag{8.16}$$

so that

$$\frac{\partial g(t)}{\partial t} = -nt^{-n-1} f(tx_1, \ldots, tx_m) + t^{-n} \frac{1}{t} nf(tx_1, \ldots, tx_m) = 0. \tag{8.17}$$

Thus, $g(t)$ is constant for all t. It is clear that $g(1) = 0$; therefore, $g(t) = 0$ for all t, and with Eq. (8.14), we get

$$t^{-n} f(tx_1, \ldots, tx_m) - f(x_1, \ldots, x_m) = 0, \tag{8.18}$$

that is,

$$f(tx_1, \ldots, tx_m) = t^n f(x_1, \ldots, x_m)$$

for all $t > 0$, which means that f is homogeneous of degree n.

Example 1. Consider the following function:

$$f(x, y, z) = -\frac{x^3}{yz}.$$

Since

$$f(kx, ky, kz) = -\frac{(kx)^3}{(ky)(kz)} = k\left(-\frac{x^3}{yz}\right) = kf(x, y, z),$$

this function is homogeneous of the first degree in the variables x, y, and z, and the partial derivatives are

$$\frac{\partial f}{\partial x} = -\frac{3x^2}{yz}, \quad \frac{\partial f}{\partial y} = \frac{x^3}{y^2 z}, \quad \text{and} \quad \frac{\partial f}{\partial z} = \frac{x^3}{yz^2}.$$

Thus, applying Euler's theorem,

$$f(x, y, z) = \frac{\partial f}{\partial x} \cdot x + \frac{\partial f}{\partial y} \cdot y + \frac{\partial f}{\partial z} \cdot z = \left(-\frac{3x^2}{yz}\right) x + \left(\frac{x^3}{y^2 z}\right) y + \left(\frac{x^3}{yz^2}\right) z = -\frac{x^3}{yz}.$$

Remarks. (i) A homogeneous function of degree n gives rise to a set of derivative functions that are homogeneous in the same set of variables and of degree $n - 1$, that is, partial derivatives of a homogeneous function of degree n are homogeneous functions of degree $n - 1$.

Proof. Differentiate both sides of Eq. (8.1) with respect to x_i (for $i = 1, \ldots, m$) to get

$$k\frac{\partial f(kx_1,\ldots,kx_m)}{\partial kx_i} = k^n\frac{\partial f(x_1,\ldots,x_m)}{\partial x_i}$$

and then divide both sides by k to get

$$\frac{\partial f(kx_1,\ldots,kx_m)}{\partial kx_i} = k^{n-1}\frac{\partial f(x_1,\ldots,x_m)}{\partial x_i}.$$

Hence, the derivatives of f are homogeneous of degree $n - 1$.

(ii) In thermodynamics, extensive thermodynamic functions are homogeneous functions of degree $n = 1$ (homogeneous linear functions), that is,

$$f(kx_1,\ldots,kx_m) = kf(x_1,\ldots,x_m), \tag{8.19}$$

and so

$$\sum_{i=1}^{m}\frac{\partial f}{\partial x_i}x_i = f(x_1,\ldots,x_m). \tag{8.20}$$

Partial derivatives of a homogeneous linear functions are homogeneous functions of degree $n = 0$ (homogeneous function of 0th degree), that is,

$$f(kx_1,\ldots,kx_m) = f(x_1,\ldots,x_m) \tag{8.21}$$

and

$$\sum_{i=1}^{m}\frac{\partial f}{\partial x_i}x_i = 0. \tag{8.22}$$

(iii) Suppose that the domain of definition of the function f lies in the first quadrant, $x_1 > 0, \ldots, x_m > 0$, and contains the whole ray $(kx_1, \ldots, kx_m)$, $k > 0$, whatever it contains $(x_1, \ldots, x_m)$. Then f is homogeneous of degree n if and only if there exists a function w of $m - 1$ variables defined on the set of points of the form $(x_2/x_1, \ldots, x_m/x_1)$ such that, for all $(x_1, \ldots, x_m)$ in the domain of definition,

$$f(x_1,\ldots,x_m) = x_1^n w(x_2/x_1,\ldots,x_m/x_1). \tag{8.23}$$

(see, e.g., [1, 2]).

Proof. Let $f(x_1, x_2, \ldots, x_m)$ a homogeneous function of degree n of variables $x_1, x_2, \ldots, x_m$ such that

$$f(kx_1, \ldots, kx_m) = k^n f(x_1, \ldots, x_m)$$

for all $k > 0$. Obviously,

$$f(x_1, x_2, \ldots, x_m) = f\left(x_1, \frac{x_2}{x_1} x_1, \ldots, \frac{x_m}{x_1} x_1\right).$$

If we set $k = 1/x_1$, we have

$$f(x_1, x_2, \ldots, x_m) = x_1^n f\left(1, \frac{x_2}{x_1}, \ldots, \frac{x_m}{x_1}\right),$$

that is, f is represented by

$$f = x_1^n w\left(\frac{x_2}{x_1}, \ldots, \frac{x_m}{x_1}\right)$$

with some function w. Since, conversely, every f function formed by means of an appropriate function w of $n - 1$ variables satisfies the condition of homogeneity, f represents the totality of homogeneous functions of degree n.

8.1.1.3 The Gibbs–Duhem Equation

If the function $f(x_1, \ldots, x_m)$ is homogeneous of degree $n = 1$ with respect to the variables $x_1, \ldots, x_m$, then one has the identity

$$f(kx_1, kx_2, \ldots, kx_m) = kf(x_1, x_2, \ldots, x_m).$$

Let us set

$$\frac{\partial f}{\partial x_1} = f_1', \ldots, \frac{\partial f}{\partial x_m} = f_m',$$

etc. and apply Euler's theorem to the function f.

We will have

$$f = x_1 f_1' + x_2 f_2' + \ldots + x_m f_m'. \tag{8.24}$$

It results from this formula that the functions

$$f_1', f_2', \cdots, f_m'$$

are quantities (functions) of the same type as the quotient of an energy or a work by a charge, mass, etc. Hence, these are quantities of the same type as a potential (function).

In thermodynamics, if f means, e.g., the internal energy function, and x_is mean the amounts of substances, we can call them *partial molar internal energies of the constituents* 1, …, m in the system (thermodynamic potentials).

On the basis of remarks *(i)* and *(ii)*, the functions

$$f_1', f_2', \ldots, f_m'$$

are homogeneous functions of degree zero in the variables $x_1, \ldots, x_m$.

To each of these functions, we can apply Euler's theorem, and we will find the identities

$$\begin{aligned} &x_1 \frac{\partial f'_1}{\partial x_1} + x_2 \frac{\partial f'_1}{\partial x_2} + \ldots + x_m \frac{\partial f'_1}{\partial x_m} = 0 \\ &\vdots \\ &x_1 \frac{\partial f'_m}{\partial x_1} + x_2 \frac{\partial f'_m}{\partial x_2} + \ldots + x_m \frac{\partial f'_m}{\partial x_m} = 0. \end{aligned}$$

The identities

$$\frac{\partial f'_i}{\partial x_j} = \frac{\partial f'_j}{\partial x_i},$$

which result from the definition of the functions (the mixed second partial derivatives are equal), permit the substitution of equations

$$\begin{aligned} &x_1 \frac{\partial f'_1}{\partial x_1} + x_2 \frac{\partial f'_2}{\partial x_1} + \ldots + x_m \frac{\partial f'_m}{\partial x_1} = 0 \\ &\vdots \\ &x_1 \frac{\partial f'_1}{\partial x_m} + x_2 \frac{\partial f'_2}{\partial x_m} + \ldots + x_m \frac{\partial f'_m}{\partial x_m} = 0, \end{aligned} \tag{8.25}$$

and therefore

$$x_1 \mathrm{d}f_1' + x_2 \mathrm{d}f_2' + \ldots + x_m \mathrm{d}f_m' = 0. \tag{8.26}$$

This relation is known as *Gibbs–Duhem equation* or *Gibbs–Duhem relation.*

Example 2. Consider the following function:

$$f(x, y, z) = -\frac{x^3}{yz}$$

homogeneous of degree 1 (see Example 1).

The partial derivatives with respect of x, y, and z are

$$f'_x = \frac{\partial f}{\partial x} = -\frac{3x^2}{yz}, \quad f'_y = \frac{\partial f}{\partial y} = \frac{x^3}{y^2 z}, \quad \text{and} \quad f'_z = \frac{\partial f}{\partial z} = \frac{x^3}{yz^2}.$$

The partial derivatives of f'_x, f'_y, and f'_z with respect to x can be given as

$$\frac{\partial f'_x}{\partial x} = -\frac{6x}{yz}, \quad \frac{\partial f'_y}{\partial x} = \frac{3x^2}{y^2 z}, \quad \text{and} \quad \frac{\partial f'_z}{\partial x} = \frac{3x^2}{yz^2}.$$

In accordance with Eq. (8.25),

$$x\frac{-6x}{yz} + y\frac{3x^2}{y^2 z} + z\frac{3x^2}{yz^2} = \frac{-6x^2 + 3x^2 + 3x^2}{yz} = 0.$$

Alternatively, we can formally write

$$\mathrm{d}f'_x = \frac{-6xyz \cdot \mathrm{d}x + 3x^2 z \cdot \mathrm{d}y + 3x^2 y \cdot \mathrm{d}z}{y^2 z^2},$$

$$\mathrm{d}f'_y = \frac{3x^2 y^2 z \cdot \mathrm{d}x - 2x^3 yz \cdot \mathrm{d}y - x^3 y^2 \cdot \mathrm{d}z}{y^4 z^2},$$

, and

$$\mathrm{d}f'_z = \frac{3x^2 yz^2 \cdot \mathrm{d}x - x^3 z^2 \cdot \mathrm{d}y - 2x^3 yz \cdot \mathrm{d}z}{y^2 z^4}.$$

Thus,

$$\begin{aligned} x\mathrm{d}f'_x + y\mathrm{d}f'_y + z\mathrm{d}f'_z &= \frac{-6x^2 y^2 z^2 \cdot \mathrm{d}x + 3x^3 yz^2 \cdot \mathrm{d}y + 3x^3 y^2 z \cdot \mathrm{d}z}{z^3 y^3} \\ &+ \frac{3x^2 y^2 z^2 \cdot \mathrm{d}x - 2x^3 yz^2 \cdot \mathrm{d}y - x^3 y^2 z \cdot \mathrm{d}z}{z^3 y^3} \\ &+ \frac{3x^2 y^2 z^2 \cdot \mathrm{d}x - x^3 yz^2 \cdot \mathrm{d}y - 2x^3 y^2 z \cdot \mathrm{d}z}{z^3 y^3} = 0 \end{aligned}$$

in accordance with the Gibbs–Duhem equation (8.26).

Example 3. Consider the internal energy function U defined by

$$U = U(S, V, n_1, \ldots, n_m),$$

where S is the entropy, V is the volume, and n_i ($i = 1, \ldots, m$) is the chemical amount of component i, respectively. Since U is a homogeneous function of degree 1 with respect to all of its variables,

$$U(kS, kV, kn_1, \ldots, kn_m) = kU(S, V, n_1, \ldots, n_m).$$

The temperature (T), pressure (p), and the chemical potentials μ_i ($i = 1, \ldots, m$) of the components are

$$T = \left(\frac{\partial U}{\partial S}\right)_{V,n_1,\ldots,n_m}, \quad p = -\left(\frac{\partial U}{\partial V}\right)_{S,n_1,\ldots,n_m}, \quad \text{and} \quad \mu_i = \left(\frac{\partial U}{\partial n_i}\right)_{S,V,n_{i\neq m}},$$

respectively. (In the above equations, n_{i} means the set [$n_1, \ldots, n_m$] ($i = 1, \ldots, m$) and $n_{j\neq i}$ denotes all elements (variables) in [$n_1, \ldots, n_m$] except for the ith.) According to Euler's theorem,

$$U = TS + (-pV) + \sum_i \mu_i n_i.$$

The Gibbs–Duhem relation is written as

$$-S\mathrm{d}T + V\mathrm{d}p + n_1\mathrm{d}\mu_1 + \ldots + n_m\mathrm{d}\mu_m = 0.$$

It follows that T, p, and μ_i cannot be independently variable, that is, that the intensive variables are not independent. If we know $m - 1$ of them, the value of the mth can be determined from the Gibbs–Duhem equation. It is particularly useful in its application to changes at constant temperature and pressure, when it may be written

$$\sum_{i=1}^{m} n_i \mathrm{d}\mu_i = 0.$$

8.1.1.4 Partly Homogeneous Functions

A function f is called "partly homogeneous" of degree 1 in terms of m among p variables if

$$f\left(kx_1, \ldots, kx_m, y_1, \ldots, y_p\right) = kf\left(x_1, \ldots, x_m, y_1, \ldots, y_p\right) \quad (k>0),$$

that is, the function f is homogeneous with respect to certain variables, but not homogeneous with respect to all of the variables. These functions are important as they are frequently encountered in thermodynamics [3].

Let us introduce new variables

$$z_i = x_1 \cdot y_i \tag{8.27}$$

and the function $\hat{f}$ as

$$\hat{f}\left(x_1,\ldots,x_m,z_1,\ldots,z_p\right)=f\left(x_1,\ldots,x_m,\frac{z_1}{x_1},\ldots,\frac{z_p}{x_1}\right). \tag{8.28}$$

We can prove that $\hat{f}$ is homogeneous of the first degree with respect to all of its variables. According to Eq. (8.28),

$$\begin{aligned}\hat{f}\left(kx_1,\ldots,kx_m,kz_1,\ldots,kz_p\right)&=f\left(kx_1,\ldots kx_m,\frac{kz_1}{kx_1},\ldots,\frac{kz_p}{kx_1}\right)\\&=f\left(kx_1,\ldots kx_m,\frac{z_1}{x_1},\ldots,\frac{z_p}{x_1}\right).\end{aligned} \tag{8.29}$$

On the other hand, f is a homogeneous linear function with respect of x_i, …, x_m. Thus,

$$f\left(kx_1,\ldots,kx_m,\frac{z_1}{x_1},\ldots,\frac{z_p}{x_1}\right)=kf\left(x_1,\ldots,x_m,\frac{z_1}{x_1},\ldots,\frac{z_p}{x_1}\right). \tag{8.30}$$

By taking into account the definition of $\hat{f}$,

$$\hat{f}\left(kx_1,\ldots,kx_m,kz_1,\ldots,kz_p\right)=k\hat{f}\left(x_1,\ldots,x_m,z_1,\ldots,z_p\right), \tag{8.31}$$

which was to be proved.

The partial derivatives of f and $\hat{f}$ w.r.t. x_i, y_i, and z_i are, respectively, denoted by

$$f_i^x=\left(\frac{\partial f}{\partial x_i}\right)_{x_{j\neq i},y_j},\ f_i^y=\left(\frac{\partial f}{\partial y_i}\right)_{x_j,y_{j\neq i}},\ \hat{f}_i^x=\left(\frac{\partial\hat{f}}{\partial x_i}\right)_{x_{j\neq i},z_j},\ \hat{f}_i^z=\left(\frac{\partial\hat{f}}{\partial z_i}\right)_{x_j,z_{j\neq i}}. \tag{8.32}$$

The partial derivatives of $\hat{f}$ are given as (for $i = 1, \ldots, p$)

$$\hat{f}_i^z=\frac{\partial\hat{f}}{\partial z_i}=\frac{\partial f}{\partial y_i}\cdot\frac{1}{x_1}=f_i^y\cdot\frac{1}{x_1}, \tag{8.33}$$

and for $i = 2, \ldots, m$

$$\hat{f}_i^x=\frac{\partial\hat{f}}{\partial x_i}=\frac{\partial f}{\partial x_i}=f_i^x. \tag{8.34}$$

The total derivative of $\hat{f}$ can be written as

$$\frac{\partial\hat{f}}{\partial x_1}=\frac{\partial f}{\partial x_1}+\frac{\partial f}{\partial y_1}\cdot\left(\frac{-z_1}{x_1^2}\right)+\frac{\partial f}{\partial y_2}\cdot\left(\frac{-z_2}{x_1^2}\right)+\ldots+\frac{\partial f}{\partial y_m}\cdot\left(\frac{-z_p}{x_1^2}\right). \tag{8.35}$$

By using Eqs. (8.26) and (8.31), Eq. (8.34) can be rewritten in the form

$$\hat{f}_1^x = f_1^x + f_1^y \cdot \left(\frac{-y_1}{x_1}\right) + f_2^y \cdot \left(\frac{-y_2}{x_1}\right) + \ldots + f_p^y \cdot \left(\frac{-y_p}{x_1}\right). \tag{8.36}$$

From Eq. (8.33),

$$\frac{f_i^y}{x_1} = \hat{f}_i^z, \tag{8.37}$$

this means that

$$\hat{f}_1^x = f_1^x - \sum_{i=1}^{p} \hat{f}_i^z y_i. \tag{8.38}$$

Since $\hat{f}$ is homogeneous of the first degree with respect to all of its variables and its partial derivatives are homogeneous of degree zero, we can apply Euler's theorem. Hence,

$$\hat{f} = \sum_{i=1}^{m} x_i \hat{f}_i^x + \sum_{i=1}^{p} z_i \hat{f}_i^z, \tag{8.39}$$

and

$$0 = \sum_{i=1}^{m} x_i \mathrm{d}\hat{f}_i^x + \sum_{i=1}^{p} z_i \mathrm{d}\hat{f}_i^z. \tag{8.40}$$

With Eqs. (8.28), (8.33), (8.35), (8.38)–(8.40), we have

$$f = x_1 \left(f_1^x - \sum_{i=1}^{p} \frac{f_i^y}{x_1} y_i \right) + \sum_{i=2}^{m} x_i f_i^x + \sum_{i=1}^{p} x_1 y_i \frac{f_i^y}{x_1} \tag{8.41}$$

and

$$0 = x_1 \mathrm{d} \left(f_1^x - \sum_{i=1}^{p} \frac{f_i^y}{x_1} y_i \right) + \sum_{i=2}^{m} x_i \mathrm{d} f_i^x + \sum_{i=1}^{p} x_1 y_i \mathrm{d} \frac{f_i^y}{x_1}. \tag{8.42}$$

Consequently,

$$f = \sum_{i=1}^{m} x_i f_i^x = \sum_{i=1}^{m} x_i \left(\frac{\partial f}{\partial x_i} \right)_{x_{j \neq i}, y_j}, \tag{8.43}$$

and

$$0 = \sum_{i=1}^{m} x_i \mathrm{d}f_i^x - \sum_{i=1}^{p} f_i^y \mathrm{d}y_i. \tag{8.44}$$

The latter relation is the Gibbs–Duhem equation for “partly homogeneous functions.”

Example 4. The function

$$f = -\frac{x^2}{y}w + u^4x$$

is not fully homogeneous, since

$$f(kx, ky, ku, kw) \neq k^n f(x, y, u, w).$$

(If the powers of x, y, u, and w are added, the first term on the right-hand side of the expression yields 2 and the second term, 5.)

However, if u and w are constant, the sum of the powers of x and y for each term is 1. Therefore, the function is partly homogeneous (with respect to x and y) so that

$$f(kx, ky, u, w) = kf(x, y, u, w).$$

The partial derivatives with respect of x and y are

$$f'_x = \frac{\partial f}{\partial x} = -\frac{2xw}{y} + u^4 \quad \text{and} \quad f'_y = \frac{\partial f}{\partial y} = \frac{x^2 w}{y^2}.$$

Thus, applying Euler’s theorem,

$$f(x, y, u, w) = \left(-\frac{2xw}{y} + u^4\right)x + \left(\frac{x^2 w}{y^2}\right)y = -\frac{x^2 w}{y} + u^4 x.$$

The partial derivatives with respect of u and w are

$$f'_u = \frac{\partial f}{\partial u} = 4u^3 x \quad \text{and} \quad f'_w = \frac{\partial f}{\partial w} = -\frac{x^2}{y}.$$

We can formally write

$$x \cdot \mathrm{d}f'_x = \frac{-2wyx \cdot \mathrm{d}x - 2x^2 y \cdot \mathrm{d}w + 2x^2 w \cdot \mathrm{d}y}{y^2} + 4u^3 x \cdot \mathrm{d}u,$$

$$y \cdot \mathrm{d}f'_y = \frac{2xwy^2 \cdot \mathrm{d}x + x^2y^2 \cdot \mathrm{d}w - 2x^2wy \cdot \mathrm{d}y}{y^3},$$

$$f'_u \cdot \mathrm{d}u = 4u^3x \cdot \mathrm{d}u,$$

and

$$f'_w \cdot \mathrm{d}w = -\frac{x^2}{y} \cdot \mathrm{d}w.$$

Thus,

$$x\mathrm{d}f'_x + y\mathrm{d}f'_y - f'_u\mathrm{d}u - f'_w\mathrm{d}w = 0,$$

in accordance with the Gibbs–Duhem equation for "partly homogeneous functions" [Eq. (8.44)].

Example 5. As we have seen from the previous example, the function

$$f = -\frac{x^2}{y}w + u^4x$$

is not fully homogeneous, since

$$f(kx, ky, ku, kw) \neq k^n f(x, y, u, w).$$

Let us introduce new variables $\alpha = x \cdot u$ and $\beta = x \cdot w$, that is,

$$u = \frac{\alpha}{x}, \quad w = \frac{\beta}{x},$$

and the function $\hat{f}$ as

$$\hat{f} = -\frac{x^2}{y}\frac{\beta}{x} + \left(\frac{\alpha}{x}\right)^4 x = -\frac{x\beta}{y} + \frac{\alpha^4}{x^3}.$$

Since

$$\hat{f}(kx, ky, k\alpha, k\beta) = -\frac{kx \cdot k\beta}{ky} + \frac{k\alpha^4}{kx^3} = k\left(-\frac{x \cdot \beta}{y} + \frac{\alpha^4}{x^3}\right) = k\hat{f}(x, y, \alpha, \beta),$$

it is obvious that $\hat{f}$ is a homogeneous function of degree 1 with respect to all of its variables (x, y, α, and β).

Example 6. Let us consider the Gibbs free energy function G defined by

$$G = G(T, p, n_1, n_2, \ldots, n_m),$$

where T is the temperature, p is the pressure, and n_i ($i = 1, \ldots, m$) is the chemical amount of component i, respectively. G is partly homogeneous of degree 1 in terms of the variables $n_1, \ldots, n_m$. We thus have

$$G(T, p, kn_1, \ldots, kn_m) = kG(T, p, n_1, \ldots, n_m).$$

The total differential of G is given as

$$\mathrm{d}G = \left(\frac{\partial G}{\partial T}\right)_{p,n_i} \mathrm{d}T + \left(\frac{\partial G}{\partial p}\right)_{T,n_i} \mathrm{d}p + \sum_{i=1}^{m} \left(\frac{\partial G}{\partial n_i}\right)_{T,p,n_{j\neq i}} \mathrm{d}n_i. \tag{8.45}$$

The temperature (T), pressure (p), and the chemical potentials μ_i ($i = 1, \ldots, m$) of the components are

$$S = -\left(\frac{\partial G}{\partial T}\right)_{p,n_i}, \quad V = \left(\frac{\partial G}{\partial p}\right)_{T,n_i}, \quad \text{and} \quad \mu_\mathrm{i} = \left(\frac{\partial G}{\partial n_\mathrm{i}}\right)_{T,p,n_{j\neq i}},$$

respectively. Thus, Eq. (8.45) can be rewritten as

$$\mathrm{d}G = -S\mathrm{d}T + V\mathrm{d}p + \sum_{i=1}^{m} \mu_i \mathrm{d}n_i. \tag{8.46}$$

According to Euler's theorem,

$$G = \sum_i \mu_i n_i. \tag{8.47}$$

In order to get an expression for dG from Eq. (8.47) comparable with that in Eq. (8.45) or Eq. (8.46), we must differentiate Eq. (8.47) "generally," that is, with respect to the same variables as in Eq. (8.46), expressed explicitly or implicitly. This gives

$$\mathrm{d}G = \sum_{i=1}^{m} \mu_i \mathrm{d}n_i + \sum_{i=1}^{m} n_i \mathrm{d}\mu_i.$$

There are thus two (general) expressions for df, both of which are correct. This can only be the case if

$$S\mathrm{d}T - V\mathrm{d}p + \sum_i n_i \mathrm{d}\mu_i = 0.$$

8.1.2 Legendre Transformation

Consider an arbitrary function of

$$x_1, x_2, x_3, \ldots : f(x_1, x_2, x_3, \ldots) \tag{8.48}$$

The total derivative (full derivative) of $f(x_1, x_2, x_3, \ldots)$ with respect to x_1 is

$$\frac{\mathrm{d}f}{\mathrm{d}x_1} = \frac{\partial f}{\partial x_1} + \frac{\partial f}{\partial x_2}\frac{\mathrm{d}x_2}{\mathrm{d}x_1} + \frac{\partial f}{\partial x_3}\frac{\mathrm{d}x_3}{\mathrm{d}x_1} + \ldots \tag{8.49}$$

Multiplying both sides of the equation by the differential $\mathrm{d}x_1$,

$$\mathrm{d}f = \frac{\partial f}{\partial x_1}\mathrm{d}x_1 + \frac{\partial f}{\partial x_2}\mathrm{d}x_2 + \frac{\partial f}{\partial x_3}\mathrm{d}x_3 + \ldots = p_1\mathrm{d}x_1 + p_2\mathrm{d}x_2 + p_3\mathrm{d}x_3 + \ldots, \tag{8.50}$$

where $p_1 = \partial f/\partial x_1$, $p_2 = \partial f/\partial x_2$, $p_3 = \partial f/\partial x_3$, etc. The result will be the differential change df in the function f.

The differential of the form

$$\mathrm{d}f = \sum_{j=1}^{k} p_{\mathrm{j}}(x_1, x_2, \ldots, x_k)\mathrm{d}x_j \tag{8.51}$$

is called the total differential or the exact differential of the function f.

Let us consider a new function g of the variables p_1 and x_2, x_3, ...,

$$g(p_1, x_2, x_3, \ldots) = f\,(x_1(p_1), x_2, x_3, \ldots) - p_1 x_1(p_1). \tag{8.52}$$

A necessary condition is the existence of a one-to-one relation between p_1 and x_1; that is, the function $p_1(x_1, x_2, x_3, \ldots)$ can be inverted to give $x_1(p_1)$.

The new function $g(p_1, x_2, x_3, \ldots)$ is called the *Legendre transform* of the function $f(x_1, x_2, x_3, \ldots)$. In general, this is a special transformation that allows us to replace variables in a function in a consistent manner.

The differential of $g(p_1, x_2, x_3, \ldots)$ is

$$\mathrm{d}g = \mathrm{d}f - x_1(p_1)\mathrm{d}p_1 - p_1\,(x_1, x_2, x_3, \ldots)\,\mathrm{d}x_1. \tag{8.53}$$

With Eq. (8.50),

$$\mathrm{d}g = -x_1(p_1)\mathrm{d}p_1 + \frac{\partial f}{\partial x_2}\mathrm{d}x_2 + \frac{\partial f}{\partial x_3}\mathrm{d}x_3 + \ldots. \tag{8.54}$$

Formally, the total differential of g is

$$\mathrm{d}g = \frac{\partial g}{\partial p_1}\mathrm{d}p_1 + \frac{\partial g}{\partial x_2}\mathrm{d}x_2 + \frac{\partial g}{\partial x_3}\mathrm{d}x_3 + \ldots. \tag{8.55}$$

By comparing Eqs. (8.54) and (8.58),

$$x_1 = -\frac{\partial g}{\partial p_1},$$

$$\frac{\partial f}{\partial x_2} = \frac{\partial g}{\partial x_2},$$

$$\frac{\partial f}{\partial x_3} = \frac{\partial g}{\partial x_3},$$

etc.

Let us look at examples to see how this works out.

Example 1: One-dimensional Legendre transformation Consider an arbitrary function of x:$f(x)$. We know that locally the slope of this curve is precisely its derivative with respect to x, so the change in the function $f(x)$ at the point x for a small change in the argument dx is

$$\mathrm{d}f = \frac{\partial f}{\partial x}\mathrm{d}x \equiv p(x)\mathrm{d}x,$$

where

$$p = \frac{\partial f(x)}{\partial x} = f'(x),$$

as usual.

Now, suppose we want to find a function that reverses the roles of the slope and infinitesimal, that is, a function $g(p)$ such that $\mathrm{d}g = x\mathrm{d}p$ [where we now view x as a function of p defined by the inverse of $p = f'(x)$].

It is easy to see that the function

$$g = f(p) - px(p)$$

(the Legendre transform) has

$$\mathrm{d}g = \mathrm{d}f - x\mathrm{d}p - p\mathrm{d}x = -x\mathrm{d}p,$$

as desired. Note that since $g(p)$ is a function of p only, we must have

$$x = \frac{\mathrm{d}g(p)}{\mathrm{d}p}$$

just as we had

$$p = \frac{\partial f(x)}{\partial x}$$

before. Consequently, we have a pair of functions $f(x)$ and $g(p)$ related in the following way:

$$f(x) \to g(p) = f(x(p)) - x(p)p \quad x(p) : \frac{\mathrm{d}f(x)}{\mathrm{d}x} = p,$$

$$g(p) \to f(x) = g(p(x)) - p(x)x \quad p(x) : \frac{\mathrm{d}g(p)}{\mathrm{d}p} = x,$$

where the pair $f(x)$ and $g(p)$ are Legendre transforms of each other. There is a certain symmetry here; the same transformation takes us back and forth.

Example 2. Consider the function

$$f(x,y,z) = -\frac{x^3}{yz}.$$

The partial derivatives are

$$\frac{\partial f}{\partial x} = -\frac{3x^2}{yz} = f_x, \quad \frac{\partial f}{\partial y} = \frac{x^3}{y^2 z} = f_y, \quad \text{and} \quad \frac{\partial f}{\partial z} = \frac{x^3}{yz^2} = f_z.$$

The variable y can be expressed as

$$y = \frac{x^{3/2}}{z^{1/2} f_y^{1/2}}.$$

Define the new function $f_2(x, f_y, z)$ as follows:

$$f_2\left(x, f_y, z\right) = -\frac{x^3}{yz} - yf_y = -\frac{x^3 z^{1/2} f_y^{1/2}}{zx^{3/2}} - \frac{x^{3/2}}{z^{1/2} f_y^{1/2}} f_y = -\frac{2x^{3/2} f_y^{1/2}}{z^{1/2}}. \tag{8.56}$$

It is obvious from this definition that f_2 is the Legendre transform of f with respect to y. By taking into account that

$$\frac{\partial f_2}{\partial z} = -2x^{3/2} f_y^{1/2} \left(-\frac{1}{2} z^{-3/2}\right) = \frac{x^{3/2} f_y^{1/2}}{z^{3/2}} = f_z$$

and

$$z = \frac{x f_y^{1/3}}{f_z^{2/3}},$$

the Legendre transformation of f_2 (with respect to z) yields

$$f_3\left(x, f_y, f_z\right) = f_2\left(x, f_y, z\right) - z f_z = -\frac{2x^{3/2} f_y^{1/2}}{x^{1/2} f_y^{1/6}} f_z^{1/3} - \frac{x f_y^{1/3}}{f_z^{2/3}} f_z = -3x f_y^{1/3} f_z^{1/3}. \quad (8.57)$$

Alternatively, Eq. s) can be derived directly by performing two successive Legendre transformations:

$$f_3\left(x, f_y, f_z\right) = f(x, y, z) - y f_y - z f_z,$$

with

$$\frac{\partial f}{\partial x} = -\frac{3x^2}{yz}, \frac{\partial f}{\partial y} = \frac{x^3}{y^2 z} = f_y, \frac{\partial f}{\partial z} = \frac{x^3}{y z^2} = f_z, \quad y = x f_y^{-2/3} f_z^{1/3}, \text{and } z = x f_y^{1/3} f_z^{-2/3}.$$

We remark that f is a homogeneous function of the first degree in the variables x, y, and z (see section 8.1.1.2, Example 1).

Example 3. Consider the function

$$f(x, y, u, w) = -\frac{x^2 w}{y} + u^4 x.$$

Since

$$f_y = \frac{\partial f}{\partial y} = \frac{x^2 w}{y^2},$$

the Legendre transformation of f with respect to y yields

$$f(x, f_y, u, w) = -2x w^{1/2} f_y^{1/2} + u^4 x.$$

Note that f is a partly homogeneous function of degree 1 in the variables x and y (see section 8.1.1.4, Example 4).

Example 4. Consider the function

$$f(x, y, u, w) = -\frac{x^2}{y} + u^4 x + w^2.$$

Since

$$f_y = \frac{\partial f}{\partial y} = \frac{x^2}{y^2}$$

and therefore

$$y = \frac{x}{f_y^{1/2}},$$

the Legendre transformation of f with respect to y yields

$$f_2\left(x, f_y, u, w\right) = -\frac{x^2 f_y^{1/2}}{x} + u^4 x + w^2 - \frac{x}{f_y^{1/2}}\left(\frac{x^2 f_y}{x^2}\right) = -2x f_y^{1/2} + u^4 x + w^2.$$

Example 5. The Gibbs free energy function ($G(T, p, n_1, \ldots, n_m)$) is obtained from the internal energy function ($U = U(S, V, n_1, \ldots, n_m)$) via appropriate Legendre transformations as $G = U - TS + pV,$

where S is the entropy, V is the volume, p is the pressure, T is the temperature, and n_i is the chemical amount of component i, respectively. p and T are given as $p = -\partial U/\partial V$ and $T = \partial U/\partial S$.

References

1. Kudryavtsev LD (2002) Homogeneous function. In: Hazewinkel M (ed) Encyclopaedia of mathematics. Springer, Berlin
2. Courant R, Hilbert D (1966) Methods of Mathematical Physics, vol II, Partial differential equations. Interscience, New York
3. Annamalai K, Puri IK (2002) Advanced thermodynamics engineering, CRC series in computational mechanics and applied analysis. CRC, Boca Raton, FL

Part II
Probe Beam Deflection (PBD)

Chapter 9
Introduction to Probe Beam Deflection Techniques

9.1 Introduction

The mechanism of detection in probe beam deflection (PBD) involves deflection (refraction) of the probe beam by the refractive index gradient. If a refractive index gradient is present in transparent medium, different parts of a beam traveling perpendicular to the gradient would traverse zones of different refractive index. The speed of light would be different for each part of the beam. Therefore, the beam will deviate. The theory of PBD for different perturbations and including redox reaction in solution has been described before [1]. In that way, similar to dynamic electrochemistry, a simple technique develops into different techniques. As it was noted there [1], while PBD techniques could be used to measure any electrochemical phenomena, it is difficult to relate the observed signal with electrochemical reactions when there are reactions in solution or several ions are exchanged. On the other hand, the ion exchange coupled to electrochemical reactions, between an electrode surface and a film confined at it, and the electrolyte solution is quite straightforward to be studied by PBD techniques.

9.2 Importance of the Field

Classic electrochemical studies are based on the study of electron fluxes at the electrode/electrolyte interface [2]. Using different ways of system perturbation and/or to measure the current-potential response of electrochemical systems, together with studies on the effect of electrolyte media (e.g., pH), it has been possible to obtain some information about electrochemical mechanisms. However, it has become clear that purely electrochemical techniques have significant limitations. To overcome those deficiencies, a plethora of in situ spectroscopic techniques has been developed in recent years. In those techniques, spectroscopies have been

G.G. Láng and C.A. Barbero, *Laser Techniques for the Study of Electrode Processes*,
Monographs in Electrochemistry, DOI 10.1007/978-3-642-27651-4_9,

combined with electrochemical perturbations to help to understand complex electrochemical phenomena. Most of those techniques have been applied to study the electrode/electrolyte interface [3, 4] by measuring changes occurring at the interface itself (e.g., in situ FTIR [5–7]) or on the whole electrode (e.g., electrochemical quartz crystal microbalance) [8] (see Chap. 14 for a detailed account).

On the other hand, studies of the ion fluxes from/to the electrode/electrolyte interface coupled to electrochemical reactions have been less common. One reason is that few techniques are able to measure concentration gradients coupled to electrochemical reactions. The oldest of those techniques is optical interferometry. It has relatively low sensitivity, slow response, and both complex experimental setup and analysis. Therefore, it was used mainly to study metal electrodeposition in electroplating cells and similar systems [9, 10]. More recently, some other techniques have been used to detect ion fluxes in solution. Among them are radiotracer detectors [11], pH sensors [12], fluorescence or absorption measurement on grid electrodes [13–15], scanning electrochemical microscopy [16–18], ring-disk voltammetry [19], surface plasmon resonance [20–22], confocal microscopy [23], etc. McCreery and coworkers performed diffraction spectroelectrochemistry in the visible optical region [24]. Kragt et al. [25] used an interferometric microscope to measure concentration gradients in front of an electrode. Most of those techniques have not gain widespread use due to complex experimental setup or too slow response.

Probe Beam Deflection (PBD), which is able to measure concentration gradients in a fast and simple manner by optical detection of refractive index gradients, has been used extensively to study a variety of electrochemical systems.

9.3 History

PBD techniques were first used by scientific groups working in photothermal deflection spectroscopy (PDS). PDS is a technique based on the detection of thermal gradients, which are due to the heat produced by light absorption, through the measurement of the refractive index gradients induced by the thermal gradients, using the refraction of a probe laser beam [26–31] (see Chap. 13 for a detailed description of the technique). During the application of PDS to electrochemical systems, it was found that the probe beam suffers a significant deviation in the absence of light. It was reasoned that electrochemical reactions could also produce refractive index gradients due to gradients of concentration of reactants/products [32, 33]. Since the refractive index depends on concentration and temperature, the photothermal effect is mixed up with a concentration effect. While, in principle, simple light sources (e.g., lamps) and position detectors (e.g., pinhole in front of photodiodes) could be used to detect the deflection of the beams, it was the availability of affordable lasers and dedicated position detectors which made the technique development possible. Therefore, the concentration gradients were measured through its effect on the refractive index, and PBD was born.[1] The technique was then adopted by electrochemists and develops further. Decker and coworkers at the University of Campinas (Brazil) used the technique to study model electrochemical [34] and photoelectrochemical systems [35]. They develop the theoretical framework for PBD measurement under controlled current [36] and sinusoidal perturbations. Cairns and coworkers (at Lawrence Berkeley Laboratory (LBL), USA) used PDS and PBD to study Cu dissolution [28, 37]. Haas used the technique, during a research stay at LBL, to study the ion exchange in redox and conductive polymer films [38, 39]. Then, he installed the technique at the Paul Scherrer Institut (Switzerland) where it was further developed and used extensively to study different systems by O. Haas, R. Kötz, M.C. Miras, and C. Barbero [40–44]. Independently, PBD technique was applied by Plichon and coworkers (Ecole Supérieure de Physique et de Chimie Industrielles, ESPCI, Paris, France). They developed a PBD setup in collaboration with A. Boccara and used it to study the ion exchange of solid metallic complexes [45]. E. Vieil (Universite J. Fourier, Grenoble, France) used the technique at ESPCI [46] and then installed it at Grenoble. There he develops the convolution method for data processing of PBD data [47]. He used the method to study different systems [48–50]. C.A. Barbero installed a new PBD set-up at the National University of Rio Cuarto (UNRC, Argentina) in 1996. The technique was used there to study electroactive films [51–53] and nanostructured materials [54, 55]. The theoretical framework was developed further [56–59], and the application of PBD to study ion exchange was reviewed [60]. Brolo and coworkers set up a PBD system at the University of Victoria (UV, Canada) and used it to study metal deposition and corrosion [61]. Scherson and coworkers install a PBD setup at Case Western Reserve University (CWRU, USA). They develop the theoretical framework of the technique [62], and combine it with in situ infrared spectroscopy [63], to study electrocatalysis.

Acknowledgments The author wishes to thank Otto Haas and Ruediger Koetz for introducing him to the probe beam deflection techniques at Paul Scherrer Institut (Switzerland). The excellent working environment and freedom enjoyed there allow developing the understanding of the technique. The author also thanks all the students and fellow researchers who perform the work described here.

Cesar Barbero is a permanent fellow of CONICET. The financial support of FONCYT, CONICET, MinCyT-Cordoba, and SECY-UNRC during the writing of this book is gratefully acknowledged.

---

[1] The technique has also been known as “mirage effect” or, less commonly, “optical beam deflection.” While the name “mirage effect” predates the other names, given the physical phenomena it describes, it seems more appropriate to leave such name for thermal (*PDS*) and not for techniques measuring concentration gradients.

References

1. Barbero C, Miras MC (2003) Tecnicas deflectometricas aplicadas al estudio de procesos electroquímicos. In: Alonso-Vante N (ed) Electroquimica y electrocatalisis. e-libro net, Buenos Aires
2. Bard AJ, Faulkner L (1984) Electrochemical methods. Wiley, New York, NY
3. Abruña HD (1991) Electrochemical interfaces. Modern techniques for in-situ interface characterization. VCH, Weinheim
4. Gale RJ (1988) Spectroelectrochemistry. Theory and practice. Plenum Press, New York, NY
5. Iwasita T, Nart F (1997) In situ infrared spectroscopy at electrochemical interfaces. Progr Surf Sci 55:271–340. doi:10.1016/S0079-6816(97)00032-4
6. Bittins-Cattaneo B, Cattaneo E, Königshoven P, Vieltisch W (1991) New developments in electrochemical mass spectroscopy. In: Bard AJ (ed) Electroanalytical chemistry: a series of advances, vol 17. Marcel Dekker, New York, NY, pp 181–220
7. Baltruschat H (1999) Differential electrochemical mass spectrometry as a tool for interfacial studies. In: Wieckowski A (ed) Interfacial electrochemistry. Theory, experiments and applications. Marcel Dekker, New York, NY
8. Buttry DA (1991) Applications of the quartz crystal microbalance in electrochemistry. In: Bard AJ (ed) Electroanalytical chemistry. Marcel Dekker, New York, NY, p 17
9. Mueller RH (1973) Optical techniques in electrochemistry. In: Muller RH (ed) Advances in electrochemistry and electrochemical engineering, vol 9. Wiley-Interscience, New York, NY.
10. Shaposhnik VA, Vasileva VI, Praslov DB (1995) Concentration fields of solutions under electrodialysis with ion-exchange membranes. J Membr Sci 101:23–30. doi:10.1016/0376-7388(94)00270-9 DOI:dx.doi.org
11. Horanyi G, Inzelt G (1988) Anion involvement in electrochemical transformations of polyaniline. A radiotracer study. Electrochim Acta 33:947–952. doi:10.1016/0013-4686(88)80093-8
12. Shimazu K, Murakoshi K, Kita H (1990) Quantitative and in-situ measurements of proton transport at polyaniline film electrodes. J Electroanal Chem 277:347–353. doi:10.1016/0022-0728(90)85114-K
13. Rajeshwahr K, Lezna RO, de Tacconi NR (1992) Light in an electrochemical tunnel? solving analytical problems in electrochemistry via spectroscopy. Anal Chem 64:429A–441A. doi:10.1021/ac00031a001
14. Lapkowski M, Genies EM (1990) Spectroelectrochemical studies of proton exchange processes in the electrochemical reactions of polyaniline using pH indicators. J Electroanal Chem 284:127–140. doi:10.1016/0022-0728(90)87067-T
15. Nath A, Kanungo M, Contractor AQ (2003) In situ measurement of pH in the interior of conducting polymer microtubules. J Electroanal Chem 557:119–125. doi:10.1016/S0022-0728(03)00354-1 DOI:dx.doi.org
16. Bard AJ, Denault G, Lee C, Mandler D, Wipf DO (1990) Scanning electrochemical microscopy: a new technique for the characterization and modification of surfaces. Acc Chem Res 23:357–363. doi:10.1021/ar00179a002
17. Troise Frank MH, Denuault G (1993) Scanning electrochemical microscopy: probing the ingress and egress of protons from a polyaniline film. J Electroanal Chem 354:331–339. doi:10.1016/0022-0728(93)80347-K
18. Troise Frank MH, Denuault G (1994) Scanning electrochemical microscope (SECM) study of the relationship between proton concentration and electronic charge as a function of ionic strength during the oxidation of polyaniline. J Electroanal Chem 379:399–406. doi:10.1016/0022-0728(94)87163-9
19. Kobayashi T, Yoneyama H, Tamura H (1984) Oxidative degradation pathway of polyaniline film electrodes. J Electroanal Chem 177:293–297. doi:10.1016/0022-0728(84)80230-2

20. Wang S, Huang X, Shan X, Foley KJ, Tao N (2010) Electrochemical surface plasmon resonance: basic formalism and experimental validation. Anal Chem 82:935–941. doi:10.1021/ac902178f
21. Andersson O, Ulrich C, Björefors F, Liedberg B (2008) Imaging SPR for detection of local electrochemical processes on patterned surfaces. Sensor Actuator B Chem 134:545–550. doi:10.1016/j.snb.2008.05.042
22. Iwasaki Y, Horiuchi T, Morita M, Niwa O (1999) Electrochemical reaction of Fe(CN)3−/4−6 on gold electrodes analyzed by surface plasmon resonance. Surf Sci 427–428:195–198. doi:10.1016/S0039-6028(99)00264-2 DOI:dx.doi.org
23. Cannan S, Macklam ID, Unwin PR (2002) Three-dimensional imaging of proton gradients at microelectrode surfaces using confocal laser scanning microscopy. Electrochem Comm 4:886–892. doi:10.1016/S1388-2481(02)00482-4 DOI:dx.doi.org
24. McCreery RL (1988) Electronic and vibrational spectroscopy of electrode surfaces. Prog Analyt Spectrosc 11:141–178
25. Kragt HJ, Smith CP, White HS (1990) Refractive index mapping of concentration profiles. J Electroanal Chem 378:403–407. doi:10.1016/0022-0728(90)85152-U
26. Boccara AC, Fournier D, Badoz J (1980) Thermo-optical. Spectroscopy: detection by the mirage effect. Appl Phys Lett 36:130–132. doi:10.1063/1.91395
27. Murphy JC, Aamodt LC (1980) Photothermal spectroscopy using optical beam probing: mirage effect. J Appl Phys 51:4580–4588. doi:10.1063/1.328350
28. Russo RE, McLarnon FR, Spear JD, Cairns EJ (1987) Probe beam deflection for in situ measurements of concentration and spectroscopic behavior during copper oxidation and reduction. J Electrochem Soc 134:2783–2787. doi:10.1149/1.2100287
29. Royce BSH, Voss D, Bocarsly A (1983) Mirage effect studies of electrochemical processes. J Phys Colloq 44:C6-325–C6-329. doi:10.1051/jphyscol:1983653
30. Mandelis A, Royce BSH (1984) Fundamental-mode laser-beam propagation in optically inhomogeneous electrochemical media with chemical species concentration gradients. Appl Opt 23:2892–2901. doi:10.1364/AO.23.002892
31. Tam AC (1986) Applications of photoacoustic sensing techniques. Rev Mod Phys 58: 381–431. doi:10.1103/RevModPhys.58.381
32. Barbero CA, Miras MC (2003) Probe beam deflection: a novel in-situ electrochemical technique. J Arg Chem Soc 91:1–40
33. Trigueiro JPC, Matencio T, Moraga GA, Lopez C (2006) Principles and use of the mirage effect technique—mirage effect of concentration. Quim Nova 29:1078–1085, S0100-40422006000500031
34. Decker F, Neuenschwander RT, Cesar CL, Penna AFS (1987) The mirage effect in electrochemistry. J Electroanal Chem Interf Electrochem 228(1-2):481–486. doi:10.1016/0022-0728(87)80125-0
35. Decker F, Fracastoro-Decker M (1988) The mirage effect in photoelectrochemistry. J Electroanal Chem Interf Electrochem 243:187–191. doi:10.1016/0022-0728(88)85038-1
36. Fracastoro-Decker M, Decker F (1989) The mirage effect under controlled current conditions. J Electroanal Chem Interf Electrochem 266:215–225. doi:10.1016/0022-0728(89)85069-7
37. Brisard GM, Rudnicki JD, McLarnon FR, Cairns EJ (1995) Application of probe beam deflection to study the electrooxidation of copper in alkaline media. Electrochim Acta 40:859–865. doi:10.1016/0013-4686(94)00360-D
38. Haas O (1989) Probe beam deflection spectroscopy as a tool for mechanistic investigations of modified electrodes. Faraday Discuss Chem Soc 88:123–131. doi:10.1039/DC9898800123
39. Haas O, Rudnicki J, McLarnon FR, Cairns EJ (1991) Mechanistic investigations of redox polymer-coated electrodes using probe-beam deflection and cyclic voltammetry. J Chem Soc Faraday Trans 87:939–945. doi:10.1039/FT9918700939
40. Barbero C, Miras MC, Kötz R, Haas O (1991) Alteration of the ion exchange mechanism of an electroactive polymer by manipulation of the active site: probe beam deflection and quartz

crystal microbalance study of poly(aniline) and poly(N-methylaniline). J Electroanal Chem 310:437–443

41. Barbero C, Miras MC, Haas O, Kötz R (1991) Direct in situ evidence for proton/anion exchange in polyaniline films by means of probe beam deflection. J Electrochem Soc 138:669–672. doi:10.1149/1.2085655
42. Barbero C, Miras MC, Haas O, Kötz R (1993) Comparative study of the ion exchange and electrochemical properties of sulfonated polyaniline (SPAN) and polyaniline (PANI). Synth Met 55–57:1539–1544. doi:10.1016/0379-6779(93)90281-Z
43. Barbero C, Kötz R, Kalaji M, Nyholm L, Peter LM (1993) Ion exchange and memory effects in polyaniline. Synth Met 55–57:1545–1551. doi:10.1016/0379-6779(93)90282-2
44. Barbero C, Miras MC, Kötz R (1997) Sulphonated polyaniline (SPAN) films as cation insertion electrodes battery applications part II: exchange of mobile species in aqueous and non-aqueous solutions. J Electroanal Chem 437:191–198. doi:10.1016/S0022-0728(97)00357
45. PlichonV BS (1990) Mirage detection of counter-ion flux between Prussian blue films and electrolyte solutions. J Electroanal Chem Interf Electrochem 284:141–153. doi:10.1016/0022-0728(90)87068-U
46. Vieil E, Matencio T, Plichon V, Servagent S (1991) Hysteresis, relaxation and ionic movements in conducting polymers studied by in-situ quartz microbalance, ESR and mirage effect. Synth Met 43:2837. doi:10.1016/0379-6779(91)91186-E
47. Vieil E (1994) Mass transfer and convolution. Part 1. Theory. J Electroanal Chem 364:9–15. doi:10.1016/0022-0728(93)02925-8
48. Correia JP, Vieil E, Abrantes LM (2004) Electropolymerization of 3-methylthiophene studied by multiflux convolution. J Electroanal Chem 573:299–306. doi:10.1016/j.jelechem.2004.06.036
49. Csahok E, Vieil E, Inzelt G (1998) Probe beam deflection study of the transport of ions during the redox reaction of indium-hexacyanoferrate films. J Electroanal Chem 457:251–255. doi:10.1016/S0022-0728(98)00290-3
50. French HM, Henderson MJ, Hillman AR, Vieil E (2002) Temporal resolution of ion and solvent transfers at nickel hydroxide films exposed to LiOH. Solid State Ionics 150:27–37. doi:10.1016/S0167-2738(02)00261-8
51. Barbero C, Calvo EJ, Miras MC, Koetz R, Haas O (2002) A probe beam deflection study of Ion exchange at poly(vinylferrocene) films in aqueous and nonaqueous electrolytes. Langmuir 18:2756–2764. doi:10.1021/la010999j
52. Barbero C, Planes GA, Miras MC (2001) Redox coupled ion exchange in cobalt oxide films. Electrochem Comm 3:113–116. doi:10.1016/S1388-2481(01)00107-2
53. Yánez-Heras J, Planes GA, Williams F, Barbero CA, Battaglini F (2010) Sequential electrochemical polymerization of aniline and their derivatives showing electrochemical activity at neutral pH. Electroanalysis 22:2801–2808. doi:10.1002/elan.201000325
54. Planes GA, Miras MC, Barbero CA (2005) Double layer properties of carbon aerogel electrodes measured by probe beam deflection and AC impedance techniques. Chem Commun. 2146–2148. DOI: 10.1039/B419448A
55. Garcia G, Bruno MM, Planes GA, Rodriguez JL, Barbero CA, Pastor E (2008) Phys Chem Chem Phys 10:6677–6685. doi:10.1039/B806938G
56. Garay F, Barbero CA (2006) Charge neutralization process of mobile species at Any distance from the electrode/solution interface. 1. Theory and simulation of concentration and concentration gradients developed during potentiostatic conditions. Anal Chem 78:6733–6739. doi:10.1021/ac0603678
57. Garay F, Barbero CA (2006) Charge neutralization process of mobile species at any distance from the electrode/solution interface. 2. Concentration gradients during potential pulse experiments. Anal Chem 78:6740–6746. doi:10.1021/ac0603680
58. Garay F, Barbero CA (2008) Charge neutralization process of mobile species developed during potentiodynamic conditions. Part 1: theory. J Electroanal Chem 624:218–227. doi:10.1016/j.jelechem.2008.09.010

59. Garay F, Iglesias RI, Barbero CA (2008) Charge neutralization process of mobile species developed during potentiodynamic conditions. Part 2: simulation and fit of probe beam deflection experiments. J Electroanal Chem 624:211–217. doi:10.1016/j.jelechem.2008.09.009
60. Barbero C (2005) Ion exchange at the electrode/electrolyte interface studied by probe beam deflection techniques. Phys Chem Chem Phys 7:1885–1899. doi:10.1039/b419382b
61. Brolo AG, Yang Y (2004) Investigating mechanisms of anodic film formation by electrochemical probe beam deflection (EPBD). Electrochim Acta 49:339–347. doi:10.1016/j.electacta.2003.08.016
62. Wang J, Wang Z, Scherson D (2007) Beam probe deflection analysis of redox active species irreversibly adsorbed on electrode surfaces. J Electrochem Soc 154(9):F165–F171. doi:10.1149/1.2754070
63. Shi P, Fromondi J, Shi Q, Wang Z, Scherson DA (2007) Simultaneous in situ reflectance and probe beam deflection measurements at solid electrode−aqueous electrolyte interfaces. Anal Chem 79:202–207. doi:10.1021/ac061452i

Chapter 10
Basic Principles of Probe Beam Deflection Techniques

10.1 Optical Principles

A laser beam traveling parallel to an electrode of an electrochemical cell could be deflected by different phenomena. One of them is the instantaneous concentration gradient associated with the electrochemical process. The technique is called "probe beam deflection (PBD)." On the other hand, a thermal gradient associated with the Joule generation of heat will produce the deflection. This phenomenon has not been used to investigate materials but cell calorimetry (see below).

In the present chapter, the theory and applications of PBD will be discussed. The usual scheme of a probe beam deflection experiment is depicted in Fig. 10.1. A solid/fluid (liquid in the case of electrochemistry) is created, and a laser beam is set up to travel parallel to the surface.[1]

The deflection of a probe beam, which travels close to an electrode along a path length l, in an electrolyte of refractive index n (Fig. 10.1) could be understood as a distortion in the wave front of the beam. The wave speed increases according to $v = c/n$. In conditions of small deflection, the geometric optics approximation could be used [1]:

$$\theta(x,t) = \left(\frac{l}{n}\frac{\mathrm{d}n}{\mathrm{d}C}\right)\left(\frac{\partial C(x,t)}{\partial x}\right), \tag{10.1}$$

where C is the concentration, l is the interaction path length, n is the refractive index of the bulk, and $\mathrm{d}n/\mathrm{d}C$ is the variation of refractive index with concentration. The sign of the deflection depends on the change of refractive index with concentration ($\mathrm{d}n/\mathrm{d}C$).

---

[1] The interface is usually planar; however, spherical or cylindrical solids can be used. The only difference is the geometry of the interaction between probe beam and the interface.

G.G. Láng and C.A. Barbero, *Laser Techniques for the Study of Electrode Processes*, Monographs in Electrochemistry, DOI 10.1007/978-3-642-27651-4_10,

This constant is positive for liquids or solids dissolved in a solvent because the refractive index increases with concentration. Therefore, an increase of concentration at the electrode surface (Fig. 10.1) will be accompanied by a negative deflection. However, when gases are dissolved in a liquid phase, the refractive index decreases; therefore, dn/dc has negative values. This has to be taken into account when the data is analyzed.

One way to make both signals proportional is to make the beam-electrode distance close to zero. However, the beam waist cannot be zero. From laser beam optics [2], it is known that a beam can be focused to a small spot, but there is a relationship between the waist ($w(x)$) and the path length (l) of the beam in front of the electrode:

$$w^2(z) = w_0^2\left[1 + \left(\frac{\lambda z}{\pi w_0^2}\right)^2\right]. \tag{10.2}$$

This can be seen in Fig. 10.2.

Since the interaction between the probe beam and the concentration gradient assumes that the beam is nearly cylindrical with a fixed waist, the electrode width has to be smaller than b. Otherwise, the waist at the extremes ($w(z)$) will be very different from w_0, and the probe beam will sample different concentration gradients.

Using Eq. (10.2), the error incurred by using the cylindrical beam approximation can be calculated. The typical setup uses a 632.8-nm He–Ne probe beam. If an electrode of $L = 0.5$ cm is used, and the minimum beam-electrode distance w_0 is

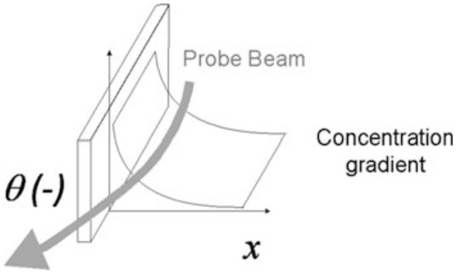

Fig. 10.1 Probe beam deflection in a concentration gradient

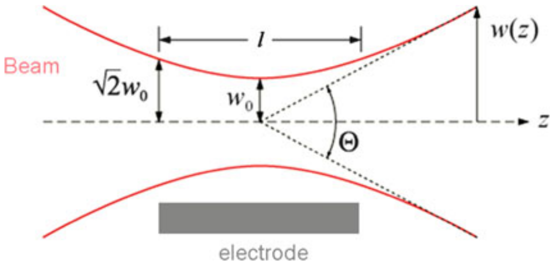

Fig. 10.2 Scheme of the probe beam shape in front of the electrode

30 μm, the waist ($w(z)$) at the extremes of the electrode ($z = L/2$) will be 34 μm (13% error). On the other hand, if the beam to the electrode distances is smaller (e.g., $w_0 = 10$ μm), an electrode width (L) of 0.055 cm is necessary to get the same error degree. Such electrode will not behave as a planar electrode but will show strong border effects, since the width will be comparable to the diffusion layer. Moreover, it has to be protruding from the base substrate. Otherwise, the beam will refract or be blocked at the base substrate. Therefore, the most usually used beam-electrode distance (w_0) is of ca. 30 μm. This size allows using normal planar electrodes (0.5–1 cm width).

10.2 Theoretical Framework of Probe Beam Deflection

The possible perturbations used in PBD are as diverse as those used in electrochemistry. Therefore, the basic principles will be initially stated, and then, details for each experimental technique will be described. To obtain the equations governing the PBD signal for different electrochemical techniques, the concentration gradient has to be obtained. An electrochemical system could be modeled as a planar electrode[2] of width w in contact with a semi-infinite fluid layer where diffusion occurs (being the diffusion layer several times thinner than w). The latter condition implies that border effects could be neglected and that interaction path length is $l = w$. Using the mass transport equations and the boundary conditions, the variation of concentration gradient with time and distance could be obtained. Since electrochemical reactions occur in the electrode surface ($x = 0$), the diffusion of a species in the diffusion layer obeys Eq. (10.3):

$$\frac{\partial^2 C}{\partial x^2} = \frac{1}{D}\frac{\partial C}{\partial t} \tag{10.3}$$

with the boundary conditions

$$C(x,0) = C^* \quad \text{for all}\, x, \tag{10.4}$$

$$\lim_{x\to\infty} C(x,t) = C^* \quad \text{for all}\, t. \tag{10.5}$$

Once the concentration gradient $\dfrac{\partial C(x,t)}{\partial x}$ is calculated, the deflection can be obtained from Eq. (10.1).

---

[2] In principle, any geometry of the electrode could be used. The planar case is described here for the sake of simplicity.

In electrochemistry, the concentration gradient is usually calculated at the electrode surface ($x = 0$) because, in that way, the mass transport is directly related with the electron flux (current) through Faraday equation:

$$i = n_e FA \left[\frac{\partial C(x,t)}{\partial x} \right]_{x=0}. \tag{10.6}$$

Nevertheless, in PBD, it is necessary to calculate the flux at a finite distance (x) where the center of the probe beam is. In principle, a laser beam could be focused in a point, as small as its wavelength. However, the path length would be also of the size of the wavelength. Applying Eq. (10.1), the signal would be vanishing small. For finite path lengths (e.g., 1 cm), the beam cannot be focused below a waist (given by Gaussian optics) of ca. 60 μm. Therefore, the center of the beam would be at ca. 30 μm away from the electrode surface. This means that since the probe beam center is at a finite distance of the electrode (typically 30–180 μm), the PBD signal is delayed in time with respect to the current signal due to diffusion of the ions. Such delay is the time that it takes for the concentration perturbation to travel between $x = 0$, where it is produced, and the beam center, where it is monitored. Rudnicki et al. [3] calculated the PBD signal from a given flux at $x = 0$ and used digital simulation to evaluate the effect of the diameter of the beam and other experimental parameters. It was found [4] that a beam of diameter inferior to 100 μm can be considered thin for the deflection, that is, the measured deflection is equivalent to that one measured for a point beam.

In general, to obtain the equations to simulate the PBD response, the following steps have to be carried out:

1. Obtain the concentration profile at distance x: $C(x,t)$ for the technique under study.
2. Differentiate with respect to x to obtain $\frac{\partial C(x,t)}{\partial x}$.
3. Combine with Eq. (10.1) to obtain $\theta(x,t)$.

One characteristic of the technique is its lack of specificity. That is, not individual concentration gradients but the sum of all concentration gradients is detected. This could be an advantage because it allows measuring all possible ion exchange not only of some ions (e.g., massive ions for EQCM) like other techniques. In the case of surface and film species, only concentration gradients due to ion exchange will be detected. Moreover, if the measurements are carried out in presence of binary electrolytes, that is, electrolyte containing only one anion and one cation (e.g., NaCl), the diffusion of ions and its migration are necessarily coupled [5]. In that way, the diffusion of one ion is coupled to the other, and a single gradient will be measured.

A different situation exists when redox reactions in solution are monitored (e.g., Fe^{+2} oxidation). There, the gradient of reactants, products, and supporting electrolyte (if present) has to be considered. Then, the interpretation of the PBD signal in terms of chemical reactions is more difficult.

10.3 Probe Beam Deflection Techniques

Those electrochemical systems where a soluble substance is produced, consumed, or transformed in a continuous way (e.g., Fe^{+2} reduced to Fe^{+3} on a Pt electrode) are called continuous processes. If a binary electrolyte is present (only two species, e.g., HCl), the migration and diffusion are coupled through the electroneutrality condition. That is, the species cannot move faster than an arithmetic median of the diffusion coefficient of anions and cations. This fact simplifies the analysis when binary electrolytes are present.

10.3.1 Potential Step Chronodeflectometry

This technique consists in applying a potential pulse to the system, from a potential where there is no reaction to one where the reaction is complete, and monitor the time evolution of the PBD signal. It is of simple mathematic treatment.

10.3.1.1 Continuous Case (Diffusion Control)

We considered an experiment involving an instantaneous change in potential from a value where no electrolysis occurs to a value in the mass-transfer-controlled region.

A planar electrode (e.g., a gold film on glass) is presumed.

We can consider the general reaction:

$$\mathrm{O} + n\,\mathrm{e}^- \rightarrow \mathrm{R} \tag{10.7}$$

The electrode kinetics of this process can be activated by a sufficiently negative potential (unless the solvent or supporting electrolyte is reduced first), so that the surface concentration of O becomes effectively zero. This condition will then hold at any more extreme potential.

Solution of the Diffusion Equation

The calculation of the concentration profile, $C_\mathrm{O}(x, t)$, involves the solution of the linear diffusion equation:

$$\frac{\partial C_\mathrm{O}(x,t)}{\partial x} = D_\mathrm{O}\frac{\partial^2 C_\mathrm{O}(x,t)}{\partial x^2} \tag{10.8}$$

under the boundary conditions:

$$C_{\mathrm{O}}(x,0) = C_{\mathrm{O}}^{*}, \tag{10.9}$$

$$\lim_{x\to\infty} C_{\mathrm{O}}(x,0) = C_{\mathrm{O}}^{*}, \tag{10.10}$$

$$C_{\mathrm{O}}(0,t) = 0 \quad (\text{for}\, t>0). \tag{10.11}$$

The *initial condition*, (10.9), means that the solution is homogenous before the experiment starts at $t = 0$. The *semi-infinite condition*, (10.10), means that the concentration of substance far away from the electrode is unperturbed by the experiment. The third condition, (10.11), indicates that all O is converted to R at the electrode surface after the potential step. This is only true when the electrode kinetics is very fast, because the redox couple is reversible and/or the potential is large enough to make the charge transfer rate high.

Using Laplace transform, the partial differential (Eq. (10.8)) could be converted into the following:

$$s\overline{C_{\mathrm{O}}}(x,\mathrm{s}) - C_{\mathrm{O}}^{*} = D_{\mathrm{O}}\frac{\partial^{2}\overline{C_{\mathrm{O}}}(x,s)}{\partial x^{2}}, \tag{10.12}$$

$$\frac{\partial^{2}\overline{C_{\mathrm{O}}}(x,s)}{\partial x^{2}} - \frac{s}{D_{\mathrm{O}}}\overline{C_{\mathrm{O}}}(x,\mathrm{s}) = -\frac{C_{\mathrm{O}}^{*}}{D_{\mathrm{O}}}. \tag{10.13}$$

This can be solved to give

$$\overline{C_{\mathrm{O}}}(x,s) = \frac{C_{\mathrm{O}}^{*}}{s} + A'\mathrm{e}^{\left(-\sqrt{s/D_{\mathrm{O}}x}\right)} + B'(s)\mathrm{e}^{\left(\sqrt{s/D_{\mathrm{O}}x}\right)}. \tag{10.14}$$

The semi-infinite limit is Laplace transformed to

$$\lim_{x\to\infty} \overline{C_{\mathrm{O}}}(x,\mathrm{s}) = \frac{C_{\mathrm{O}}^{*}}{s}. \tag{10.15}$$

Therefore, $B'(s)$ have to be zero. The equation simplify to

$$\overline{C_{\mathrm{O}}}(x,s) = \frac{C_{\mathrm{O}}^{*}}{s} + A'\mathrm{e}^{\left(-\sqrt{s/D_{\mathrm{O}}x}\right)}. \tag{10.16}$$

Applying inverse Laplace transform, we obtain

$$C_{\mathrm{O}}(x,t) = C_{\mathrm{O}}^{*} + L^{-1}\left\{A'(s)\mathrm{e}^{\left(-\sqrt{s/D_{\mathrm{O}}x}\right)}\right\}. \tag{10.17}$$

By applying the third condition, (10.11), the function $A'(s)$ can be evaluated, and then, $C_{\mathrm{O}}(x, s)$ can be inverted to obtain the concentration profile for the species O. Laplace transforming (10.9) gives

$$\overline{C_{\mathrm{O}}}(0,s) = 0 \tag{10.18}$$

which implies that

$$\overline{C_{\mathrm{O}}}(x,s) = \frac{C_{\mathrm{O}}^{*}}{s} - \frac{C_{\mathrm{O}}^{*}}{s}\mathrm{e}^{\left(-\sqrt{s/D_{\mathrm{O}}}x\right)} \tag{10.19}$$

solves into the concentration profile equation:

$$C_{\mathrm{O}}(x,t) = C_{\mathrm{O}}^{*}\left(1 - \mathrm{erfc}\left(\frac{x}{\sqrt{4D_{\mathrm{O}}t}}\right)\right) \tag{10.20}$$

or

$$C_{\mathrm{O}}(x,t) = C_{\mathrm{O}}^{*}\mathrm{erf}\left(\frac{x}{\sqrt{4D_{\mathrm{O}}t}}\right), \tag{10.21}$$

where C is the concentration, x is the beam-electrode distance, t is the time, and D_{o} is the diffusion coefficient. The concentration profiles are shown in Fig. 10.3.

As it can be seen, the laser beam (shown as a gray circle) will detect the changes in the concentration profile during time. This pictorial representation is very useful because it shows that some time is required for the concentration gradient to reach the beam. First, it means that the deflection signal has a time delay compared to the current signal (proportional to the concentration gradient at $x = 0$).

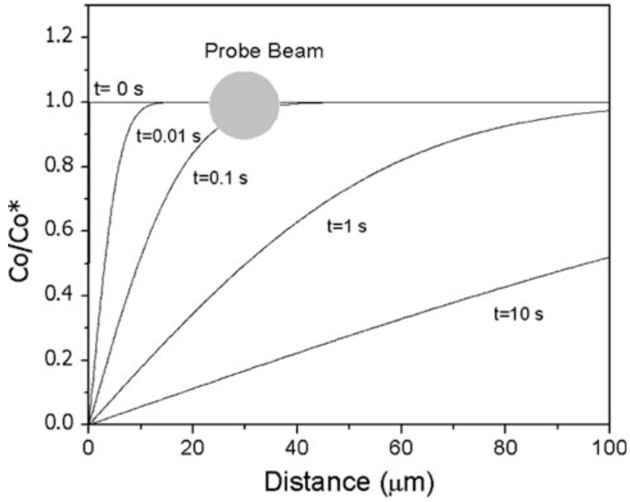

Fig. 10.3 Concentration profiles for several times after the application of a potential pulse. $D_{\mathrm{O}} = 1.0 \times 10^{-5}$ cm^{2} s^{-1}

According to Eq. (10.1), the PBD signal will be proportional to the derivative of concentration: $\left(\frac{\partial C(x,t)}{\partial x}\right)$. Differentiation of the concentration gradient profile as a function of distance (x) gives

$$\frac{\partial C_{\mathrm{O}}(x,t)}{\partial x} = \frac{C_{\mathrm{O}}^{*}}{\sqrt{\pi D_{\mathrm{O}} t}} \mathrm{e}^{-x^2/4D_{\mathrm{O}}t}. \tag{10.22}$$

The formula for the PBD signal is obtained combining (10.22) and (10.1):

$$\theta(x,t) = \left(\frac{l}{n}\frac{\mathrm{d}n}{\mathrm{d}C}\right)\frac{C_{\mathrm{O}}^{*}}{\sqrt{\pi D_{\mathrm{O}} t}} \mathrm{e}^{-x^2/4D_{\mathrm{O}}t}. \tag{10.23}$$

Simulated graphs of chronodeflectometry, using Eq. (10.23), are shown in Fig. 10.4.

As it can be seen, the signal shows a maxima at a given time, which depends on the distance. Finding the maxima by differentiation of Eq. (10.1) with respect to time renders

$$\sqrt{t_{\max}} = \frac{(x - x_0)}{\sqrt{2D}}. \tag{10.24}$$

Using Eq. (10.24), the diffusion coefficients (D), of binary electrolytes, could be measured by chronodeflectometry [6]. To do that, chronodeflectometric profiles are

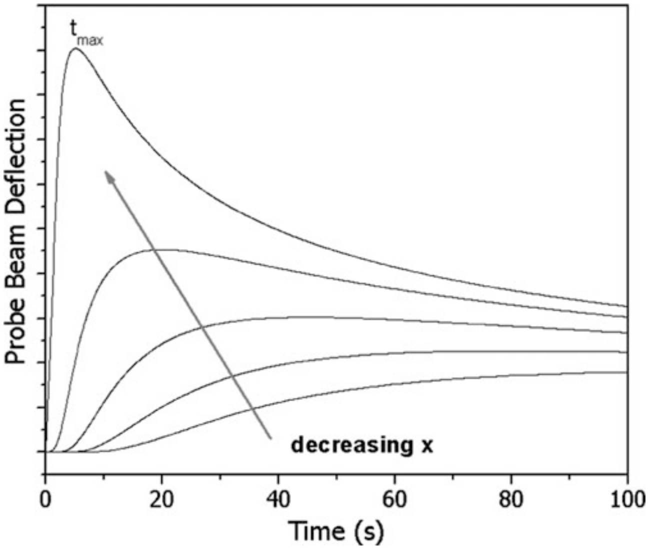

Fig. 10.4 Probe beam deflection signal as a function of times, at different beam-electrode distances

obtained while the beam-electrode distance is changed from an initial value x_0. Additionally, the initial beam-electrode distance could be obtained.

The value of PBD signal at the maxima only depends on C_O^* and x (Eq. 10.25):

$$\theta_{\max}(x) = 0.484 \times \left(\frac{l}{n}\frac{\mathrm{d}n}{\mathrm{d}C}\right)\frac{C_O^*}{x}. \tag{10.25}$$

Equations (10.23) to (10.25) are only valid for systems where a sole substance is generated or consumed (e.g., metal deposition). If a substance is converted into another by a redox change (e.g., $Fe(CN)_6{}^{-4}$ into $Fe(CN)_6{}^{-3}$ by oxidation), the contribution of both components has to be taken into account, and a more complex formula is obtained:

$$\theta(x,t) = \left(\frac{l}{n}\right)\left\{\left[\left(\frac{\mathrm{d}n}{\mathrm{d}C_O}\right)\frac{C_O^*}{\sqrt{\pi D_O t}}\,\mathrm{e}^{-x^2/4D_O t}\right] - \left[\left(\frac{\mathrm{d}n}{\mathrm{d}C_R}\right)\frac{C_O^*\left(\frac{D_O}{D_R}\right)}{\sqrt{\pi D_R t}}\,\mathrm{e}^{-x^2/4D_R t}\right]\right\} \tag{10.26}$$

where O and R have the usual meaning.

Then, the shape of the chronodeflectometric profile would depend on the relative values of the diffusion coefficients (D_O and D_R) and refractive index gradients ($\mathrm{d}n/\mathrm{d}C_R$ and $\mathrm{d}n/\mathrm{d}C_O$).

For some values of R and P diffusion coefficients (such as those of the $[Fe(CN)_6]^{-4}/[Fe(CN)_6]^{-3}$ couple), even prepeaks of opposite sign could be observed (Fig. 10.5, full line).

If we assume that $D_R = D_O$, a common assumption in electrochemistry, Eq. (10.26) reduces to

$$\theta(x,t) = \left(\frac{l}{n}\right)\left(\frac{\mathrm{d}n}{\mathrm{d}C_O} - \frac{\mathrm{d}n}{\mathrm{d}C_R}\right)\frac{C_O}{\sqrt{\pi D t}}\mathrm{e}^{-x^2/4Dt}. \tag{10.27}$$

From this peak (using Eq. (10.24)), it is possible to measure a mean diffusion coefficient, similar to those usually measured by electrochemical techniques. For species with different $\mathrm{d}n/\mathrm{d}C$, it is possible to simulate different profiles including null deflection or inverted sign (decrease of deflection during conversion). Therefore, it is important to know the values of $\mathrm{d}n/\mathrm{d}C$ before performing an experiment. Those values could be obtained, for stable species, measuring the refractive index of solutions with different concentrations. In Table 10.1 are shown the values of $\mathrm{d}n/\mathrm{d}C$ which are calculated from literature reported refractive index data. It is noteworthy that $\mathrm{d}n/\mathrm{d}C$ values could vary up to 2 orders of magnitude. Therefore, it could be possible detect concentration changes of one species with a big $\mathrm{d}n/\mathrm{d}C$ in presence of another with smaller coefficients, even if the concentration of the later changes more significantly.

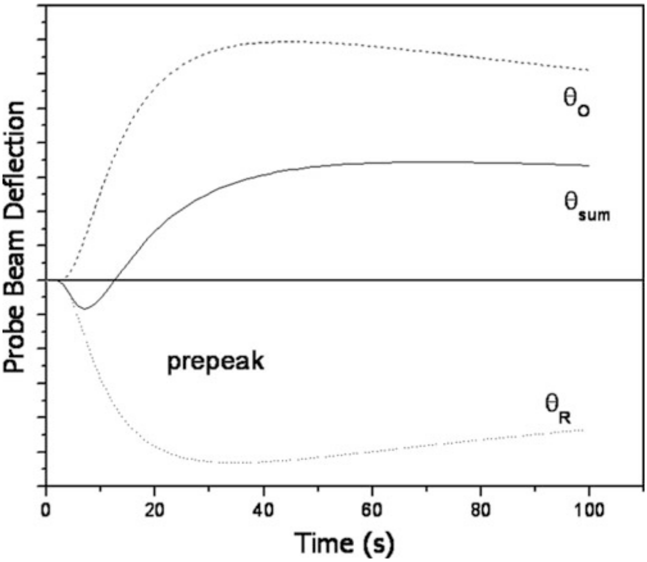

Fig. 10.5 Probe beam deflection signal during reduction of a soluble reactant (O) to a product (R). dn/dC_R= 0.07174, dn/dC_R= 0.07055, D_O =7.4 × 10^{-6} cm^2 s^{-1}, D_R = 9.4 × 10^{-6} cm^2 s^{-1}. Beam-electrode distance (x) = 150 μm. The *dashed line* is the contribution of the reactant, *dotted line* is the contribution of the product, and the *full line* is the sum deflection. The magnitude of the sum has been increased to reveal the details

10.3.1.2 Discontinuous Case (Instantaneous Process)

The complexities of PBD response in redox systems make the technique of little use when redox transformation of solution species is considered. As it will be seen, the forte of the technique is to study exchange of ions by solid state (redox oxides, metals, conductive polymers, etc.) species.

The application of the technique to the study of instantaneous or discontinuous processes will be described. In this kind of systems, the amount of species produced or consumed during the potential excursion is finite. Important examples are

1. Stripping of a thin layer (some monolayers) of a metal deposit
2. Ion exchange occurring when a film of a solid electroactive substance (redox oxide, conductive polymer, electroactive polymer, etc.) is oxidized or reduced
3. Charging/discharging of the electrochemical double layer of an electrode surface
4. Stripping of metal ions from a Hg amalgam
5. Dissolution of a deposit where one redox form is soluble and the other insoluble
6. Photoelectrochemical induced process when a light pulse is used
7. Stripping of and adsorbed monolayer (or submonolayer) of a redox adsorbate

If the rate of ion transport inside the layer has to be taken into account, it is necessary to know the kinetics of the process. On the other hand, PBD data could provide information on the mass transport inside the layer, if this process controls the overall mass transport. To do that, it is assumed that production/consumption of all species occurs in a time span negligible with respect to time width of the PBD pulse. Therefore, the concentration profile at the initial time corresponds to a Dirac delta function. The approximation is valid for thin electroactive films with a thickness of several monolayers. However, it is important to remember that the switching time has to be negligible relative to the time of the measurement. Using the assumption, Fick's law is solved for semi-infinite linear diffusion, giving the dependence of concentration with time and distance:

$$C(x,t) = \frac{C_S}{\sqrt{\pi D t}}\,\mathrm{e}^{-x^2/4Dt} \tag{10.28}$$

where C_S is the total concentration of ions exchanged in the process. Differentiation with respect to x and combining with Eq. (10.1) give the expression for deflection:

$$\theta(x,t) = \left(\frac{l}{n}\frac{\mathrm{d}n}{\mathrm{d}C}\right)\frac{C_S}{\sqrt{\pi D t}}\,\frac{x}{2Dt}\mathrm{e}^{-x^2/4Dt}. \tag{10.29}$$

The plot of PBD signal (θ) as a function of time (Fig. 10.6) presents a maximum value at a time value which depends on the beam-electrode distance.

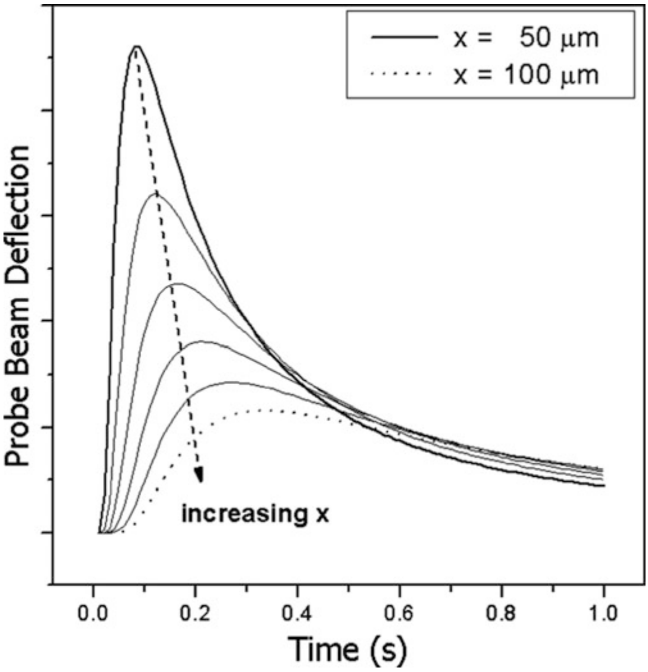

Fig. 10.6 Simulated potential pulse chronodeflectometry plots during a discontinuous process. Effect of beam-electrode distance

If 10.29 is derived, as a function of time, and equated to 0, the dependence of the signal maxima with beam-electrode distance can be calculated:

$$\sqrt{t_{\max}} = \frac{(x - x_0)}{\sqrt{6D}}. \tag{10.30}$$

The equation could be used to estimate diffusion coefficients (D) and x_0 from chronodeflectometric data. The PBD magnitude at the maximum only depends on C_s and x:

$$\theta_{\max}(x) = 0.925 \times \left(\frac{l}{n}\frac{dn}{dC}\right)\frac{C_S}{x^2}. \tag{10.31}$$

Since dissolution of a thin metal film can be studied by PBD, the reduction of Ag^+ to metal and the layer dissolution was used to check the validity of chronodeflectometric equations.

While the chronodeflectometric data measured during deposition obeys a continuous process [10.29], the dissolution of the thin metal layer obeys a discontinuous process (Fig. 10.7). Using the dependence of the time of the maximum on the beam-electrode distance, a value of $D_{Ag^+} = 1.5 \times 10^{-5}$ cm^2 s^{-1} was calculated. The value agrees well with those reported in literature [9].

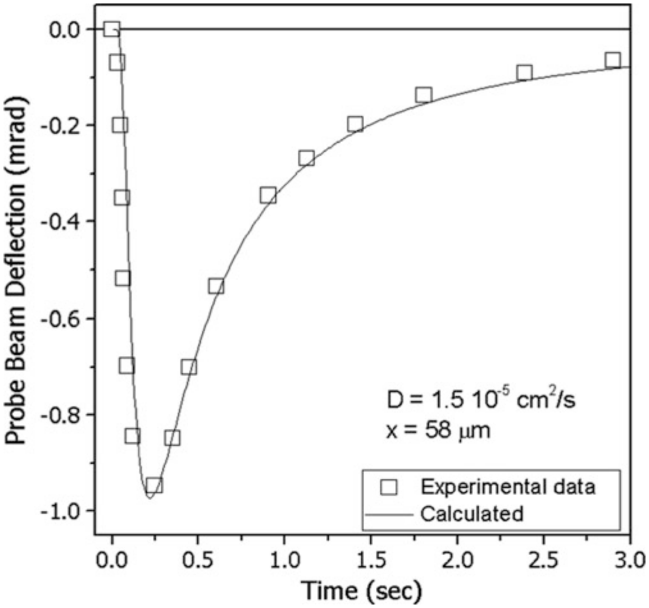

Fig. 10.7 Chronodeflectometry of the dissolution of a Ag thin film. Solution = 1.5 mM $AgClO_4$ in 2 M $HClO_4$. $D = 1.5 \times 10^{-5}$ cm^2 s^{-1}. $X = 58$ μm. Initial potential = 0.3 V_{SCE}. Final potential = 0.9 V_{SCE}. *Open squares* = experimental data. *Full line*: simulated with a discontinuous process

A similar behavior was observed for other discontinuous processes, such as the ion exchange of electrochromic oxide or electroactive polymer films [10], suggesting that the equations for a discontinuous process could successfully be applied to the ion exchange to/from thin electroactive films.

10.3.1.3 Multiflux Diffusion

PBD techniques are able to elucidate ion fluxes when only one ion (or a binary electrolyte) is moving. However, more complex systems exist. When the redox system is present in solution, the signal will depend on the relative values of $\mathrm{d}n/\mathrm{d}C$ (see above and Chap. 12). Therefore, the interpretation could be ambiguous. When the redox system is confined to the surface, only the charge-compensating ions have to be taken into account. While usually only one ion is moving, diffusion of more than one ion occurs frequently. At first sight, it could be thought that the assumption used to treat the instantaneous or discontinuous case implies that electrochemical kinetic information is lost, but that is not the case.

While the redox process has to occur in a time negligible compared with the chronodeflectometric measurement, the latter is quite large (milliseconds to seconds) for usual electrochemical process. Additionally, it can be made even larger by increasing the beam-electrode distance. Therefore, multiple or sequential electron transfer could occur which will show in the PBD signal. As an example, consider a gold electrode covered with a thin layer (e.g., 100 nm) of Ag, which is covered by a thin layer (e.g., 100 nm) of Cu. If the potential is stepped from 0.0 $\mathrm{V_{RHE}}$ to 1.0 $\mathrm{V_{RHE}}$, both layers will oxidize and dissolve sequentially. Therefore, two concentration pulses will appear, and the chronodeflectometric signal will show a contribution of both processes. If the experiment is performed in nitrate solution, Ag and Cu will produce negative PBD signals (increasing $\mathrm{Me^+}$ concentration in front of the electrode). The chronodeflectometry profile will show the sum of both contributions If the delay is relatively large, a shoulder can be seen (Fig. 10.8a). Otherwise, the interpretation could be ambiguous. On the other hand, if the experiment is performed in a chloride solution, the copper film will dissolve (negative deflection), but the silver film will produce AgCl, decreasing the chloride concentration in front of the electrode positive deflection. There will be two opposite but time-delayed concentration pulses which will give a prepeak (Fig. 10.8b). The situation is typical of other instantaneous processes, and the simulation has been used with success to understand processes like ion exchange in layer-by-layer multilayer [11] or oxidation of adsorbed CO on a mesoporous Pt electrode [12].

Unlike the experiment proposed above, the opposite fluxes could have different magnitude. The magnitude ratio can be obtained from the fitting of the experimental data with simulated CD profiles, as those depicted in Fig. 10.9. This flux ratio could have important information about, for example, the ion exchange mechanism (cation/anion ratio). The simplicity of Eq. (10.29) allows to simulate the chronodeflectometric data using simply a spreadsheet program [13], as it has been done successfully in our laboratory.

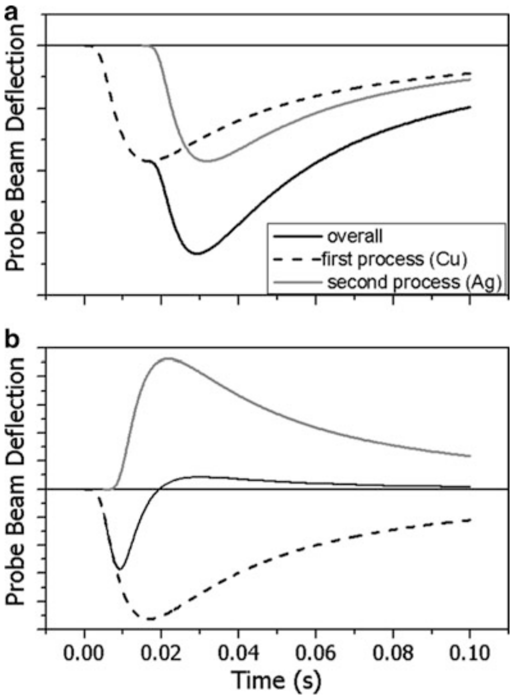

Fig. 10.8 Calculated chronodeflectometric profiles for a surface-confined sequential process with the same (**a**) and opposite sense flux (**b**). The time delay in the panel (**a**) is larger than in (**b**). The *dashed line* is the PBD due to the first process, the *gray line* is the PBD due to the second process, and the *full line* is the overall PBD signal

10.3.2 Pulse Voltadeflectometry (PVD)

10.3.2.1 General Equations

Chronodeflectometry has the advantage, over other PBD techniques such as cyclic deflectometry, to have a closed analytical form for the equations describing the process. However, it only allows studying the changes between two extreme states. To be able to study the dependence of the ion fluxes on the applied potential, the general dependence of PBD with potential has to be obtained. If we apply potential pulse between a fixed potential at different potentials, the concentration gradients will depend on time and potential. Each plot has a profile similar to the one found for chronodeflectometry, but the intensity depends on E (Fig. 10.9 (upper plot)).

Assuming that the amount of ions exchanged ($C_s(E)$) at $x = 0$ does not depend on time, the general expression of PBD could be obtained:

$$\theta(E,t) = \left[\left(\frac{l}{n}\frac{\mathrm{d}n}{\mathrm{d}C}\right)\frac{C_S}{\sqrt{\pi D t}}\frac{x}{2Dt}\mathrm{e}^{-x^2/4Dt}\right]C_{\mathrm{ion}}(E) \tag{10.32}$$

where all temporal parameters, which are independent of E, are inside brackets. In Fig. 10.10 (lower plot), the $\theta(E,t)$ profile is shown, where the dependence of $C_s(E)$ was assumed to follow Nernst equation.

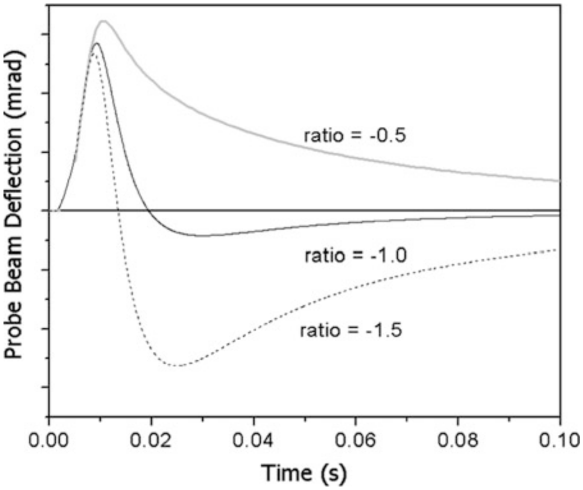

Fig. 10.9 Calculated chronodeflectometric profiles for a surface-confined sequential process opposite sense flux and different ratios of negative and positive flux

The value of deflection could be obtained at any point of the PBD chronodeflectometric curve. However, the maximum value (at $t = t_{\max}$) would have the best signal/noise ratio. In that case, the terms inside brackets reduce to a factor dependent only on x (Eq. 10.8). The dependence of PBD signal with E at $t = t_{\max}$ measures effectively the concentration of exchanged species at each potential. Such a profile (Fig. 10.10 (upper plot)) could be called normal pulse voltadeflectometry (NPVD(E)), in analogy to the normal pulse voltammetry. It represents the dependence of surface concentrations with applied potential. Its derivative with respect to the applied potential could be similarly called differential pulse voltadeflectometry (DPVD(E)). In the case of immobilized redox species, it will relate directly with the voltammetric current.

10.3.2.2 Surface Redox Process

In the case of redox coupled ion exchange in electroactive films, the charge compensation could occur via anions, cations, or both. This is described in the equations

$$\mathrm{R} - n\mathrm{e}^- + n\mathrm{A}^- = \mathrm{O} \tag{i}$$

$$\mathrm{R} - n\mathrm{e}^- = \mathrm{O} + n\mathrm{C}^+ \tag{ii}$$

$$\mathrm{R} - n\mathrm{e}^- + t_\mathrm{f} n\mathrm{A}^- = \mathrm{O} + (1 - t_\mathrm{f}) nC^+ \tag{iii}$$

For cases (i) and (ii), the NPVD(E) signal obeys Eq. (10.16):

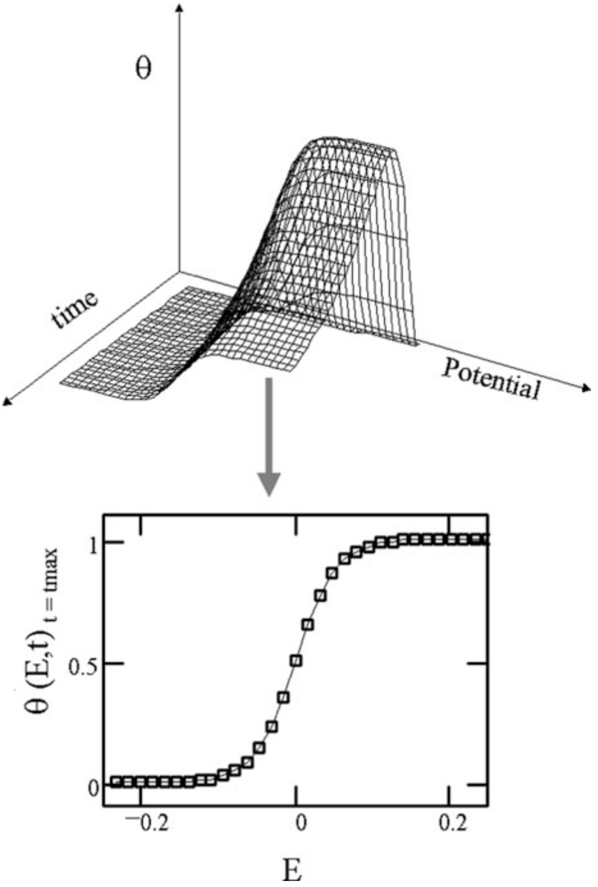

Fig. 10.10 Simulated curves for pulse potential deflectometry of a nernstian system (*upper plot*). Plot of θ (E,t) for a nernstian discontinuous process (*lower plot*). Profile of NPVD(E) for the process described above

$$\mathrm{NPVD}(E) = \theta(E)_{t=t_{\max}} = U(t_{\max})\left(\frac{\mathrm{d}n}{\mathrm{d}C}\frac{l}{n}\right)t_{\mathrm{f}}\left(\frac{Q(E)}{n_{\mathrm{e}}F}\right) \tag{10.33}$$

where t_{f} is the transference number, which is +1 (i) or −1 for (i), n_{e} is the number of electrons exchanged by each redox center, $Q(E)$ is the charge, and F is the Faraday constant. As the charge is also related with n_{e}, a straight line of unitary slope between NPVD(E) and $Q(E)$ implies only one ion used to balance charge.

In the case (iii), the equation describing the process is

$$\mathrm{NPVD}(E) = \theta(E)_{t=t_{\max}} = U(t_{\max})\left(\frac{\mathrm{d}n}{\mathrm{d}C}\frac{l}{n}\right)[2t_{\mathrm{f}}(E)-1]\left(\frac{Q(E)}{n_{\mathrm{e}}F}\right). \tag{10.34}$$

If the plot of NPVD(E) vs. $Q(E)$ is not a straight line, it is possible to detect potential ranges where a simple ion flux exists and obtain the transference number (t_{f} (E)) for each ion. If it is a straight line, the slope could be nonunitary, indicating that a mixed exchange exists and a common (t_f (E)) value could be calculated using Eq. (10.34).

Similarly, the differential pulse deflectometry (DPVD(E)) of a surface species represents a capacity of ion movement and is related with the electric capacitance and the voltammetric current by

$$\mathrm{DPVD}(E) = U(t_{\max})\frac{\partial C_s(E)}{\partial E} = \frac{t_f}{n_e F}\frac{\partial Q}{\partial E} = \frac{t_f}{n_e F}C_{\mathrm{ele}} = \frac{t_f}{n_e F}\frac{i(E)}{v} \qquad (10.35)$$

where C_{ele} is the electrical capacitance in farads, t_f is the ion transference number, and v is the scan rate of the cyclic voltammogram (it is assumed thin layer conditions for the electroactive layer, in practice a small enough scan rate (v)) measured in the same experience. Equations (10.34) and (10.35) are equivalent, but it would be simpler to compare the cyclic voltammogram (normalized with v) with the DPVD(E) profile. This could be done by numerical differentiation of NPVD(E). However, such procedure decreases the signal/noise ratio. An alternative procedure to obtain DPVD(E) implies experimentally measuring the PBD signal during pulses with a fixed potential step and shifting initial potentials. The difference between PBD signals at each state is in fact DPVD(E).

From Eq. (10.34), it is possible to obtain the dependence of NPVD(E) (and DPVD(E)) with the potential for any known dependence of $C_s(E)$ with E. In the case of Nernst equation, the deflection would be

$$\mathrm{NPVD}(E) = \theta(E)_{t=t_{\max}} = U(t_{\max})\left(\frac{l}{n}\frac{\mathrm{d}n}{\mathrm{d}C}\right)C_{\mathrm{ion}}\left(\frac{\mathrm{e}^{-\frac{nF}{RT}\left(E-E^{\Theta}\right)}}{1+\mathrm{e}^{-\frac{nF}{RT}\left(E-E^{\Theta}\right)}}\right). \qquad (10.36)$$

In that way, the reversibility or ideality of a given system could be evaluated from *PBD* measurements. Similar equations could be obtained for other known ($C_S(E)$) dependences (e.g., Butler/Volmer equation).

10.3.3 Current Step Chronodeflectometry

Another possible perturbation is a current pulse. The theory was developed by Decker and coworkers [14]. Passing through the cell a current density (j) at $t = 0$, the mass flux in $x = 0$ is fixed by the current [Eq. (10.6)].

The concentration profile will be

$$C(x,t) = \frac{j}{n_e F D}\left[2\sqrt{\frac{Dt}{\pi}}\mathrm{e}^{\left(\frac{x^2}{4Dt}\right)} - x\,\mathrm{erfc}\left(\frac{x}{\sqrt{4Dt}}\right)\right] \qquad (10.37)$$

where n_e is the number of electrons exchanged. Differentiating (10.37) with respect to x and combining with (10.1) gives the expression for PBD signal at constant current:

$$\theta(x,t) = \left(\frac{l}{n}\frac{\mathrm{d}n}{\mathrm{d}C}\right)\left[\frac{j}{n_\mathrm{e}FD}\operatorname{erfc}\left(\frac{x}{\sqrt{4Dt}}\right)\right]. \tag{10.38}$$

In Fig. 10.11a are shown the PBD profiles at different current values, and in Fig. 10.11b at different beam-electrode distances. As before, decreasing the beam-electrode distance makes the signal larger. The signal is also proportional to the current, which gives a way to measure with better signal/noise ratio. It is also possible to know the concentration profile as a function of distance, at constant time. In that way, the behavior of technologically interesting systems, such as battery electrodes or metal deposition cells, could be investigated. Since such a study has been extensively made by interferometry [15], it is worthy to compare the capability of PBD in that field. The concentration profile is obtained by PBD integration in distance:

$$C(x) = \left(\frac{l}{n}\frac{\mathrm{d}n}{\mathrm{d}C}\right)^{-1}\int_0^x \theta(x)\mathrm{d}x. \tag{10.39}$$

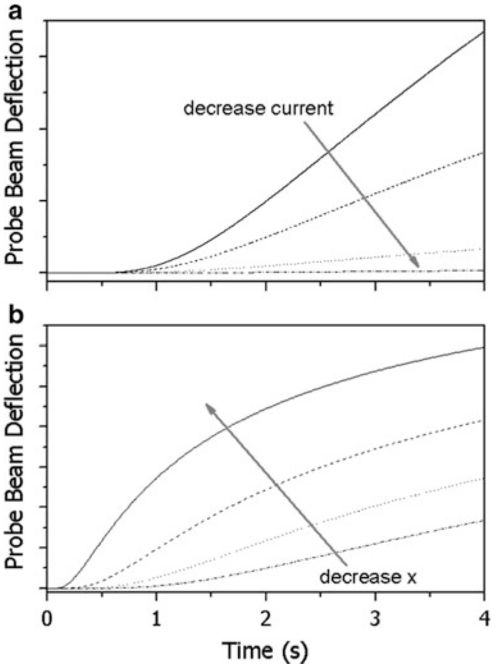

Fig. 10.11 Calculated PBD *time* profiles when the current is varied (**a**), or the beam-electrode is changed at constant current (**b**)

To calculate it experimentally, it is necessary to measure the PBD signal while the beam-electrode distance is varied. This can be done by scanning the beam, using the refraction in a moving glass slab [16], or moving the cell, using a driver, while the beam is kept stationary.

10.3.4 Alternating Current Deflectometry (ACD)

A stationary perturbation is a sinusoidal current of potential. Decker and coworkers [17] developed the theory for alternating current.

When an alternating current density $j = j_0 \sin(\omega t)$ is applied to the electrode, the concentration on the electrode surface, applying Fick's law for semi-infinite diffusion on a flat electrode, will be

$$C(x,t) = C_0 + \left(\frac{j_0}{n_\mathrm{e} F\sqrt{Dw}}\right) \mathrm{e}^{\left(-\sqrt{\frac{\omega}{2D}}x\right)} \sin\left(\omega t - \sqrt{\frac{\omega}{2D}} - \frac{\pi}{4}\right) \tag{10.40}$$

where ω is the angular frequency of the sinusoidal perturbation. Differentiation with respect to x and combining with Eq. (10.1) give the expression for PBD signal:

$$\theta(x,t) = -\left(\frac{l}{n}\frac{\mathrm{d}n}{\mathrm{d}C}\right)\left(\frac{j_0}{n_\mathrm{e} F\sqrt{Dw}}\right)\sqrt{\frac{\omega}{2D}} \mathrm{e}^{\left(-\sqrt{\frac{\omega}{2D}}x\right)} \sin\left(\omega t - \sqrt{\frac{\omega}{2D}} - \frac{\pi}{4}\right). \tag{10.41}$$

The amplitude of the signal is proportional to the perturbation amplitude (j_0) according to

$$|\theta(x,w)| = -\left(\frac{l}{n}\frac{\mathrm{d}n}{\mathrm{d}C}\right)\left(\frac{j_0}{n_\mathrm{e} F\sqrt{Dw}}\right)\sqrt{\frac{\omega}{2D}} \mathrm{e}^{\left(-\sqrt{\frac{\omega}{2D}}x\right)}. \tag{10.42}$$

The logarithm of amplitude and phase is linear with the beam-electrode distance (x), with a slope $m = -\sqrt{\frac{\omega}{2D}}$. From that slope, diffusion coefficients have been evaluated.

10.3.5 Cyclic Voltadeflectometry

Unlike the previously described case, it is not possible to obtain an analytical expression for the relationship between PBD signal and potential when the potential is scanned linearly ($E = E_\mathrm{initial} + vt$) at a constant scan rate ($v = \mathrm{d}E/\mathrm{d}t$). In such experiment, potential and time are changed simultaneously, which is equivalent to cross at same angle (defined by the scan rate) the deflection-potential-time surface Fig. 10.10 (upper plot). Therefore, cyclic voltadeflectometry (CVD) experiments, where the PBD signal is monitored along the cyclic voltamperogram, could not be simulated analytically. A similar situation exists with cyclic voltamperometry, where a closed form does not exist.

An additional problem of voltadeflectometry resides in the diffusional delay. It is caused by the fact that the probe beam is at a finite distance ($x > 0$), and the concentration perturbation takes some time to reach the beam. In CVD, the delay appears as a potential difference between the peak in voltadeflectometry and the corresponding peak in voltamperometry. In simple systems, such delay does not impede the analysis of the data. However, in some systems, it is observed a PBD signal of zero magnitude in a potential range where the current is not zero. This could be due to null ion flux (equal fluxes of opposite magnitude) or caused by the delay. To be able to compare current and PBD, the delay has to be eliminated. One possible way to do that involves measuring at very low scan rates, to minimize the potential delay. However, the magnitude of PBD signal, as any diffusion controlled flux, is proportional to the scan rate. Therefore, at low scan rates, the PBD signal will be small, and the signal/noise ratio will deteriorate.

In an analogue fashion to voltammetry, two methods could be used to overcome those problems (a) digital numeric simulation and (b) convolution of the experimental signal. Both methods could be used to simulate the PBD signal (at a beam-electrode distance, x), to compare with the experimental PBD data, or to transform the experimental PBD signal into a flux at the electrode surface ($x = 0$), to be compared with the current signal.

10.3.5.1 Digital Numeric Simulation

This is a more general approach but more difficult to be carried out. Mathias used orthogonal collocation to simulate the ion exchange of poly(1-hydroxyphenazine) in a binary electrolyte ($HClO_4$) [4]. The ion fluxes at the electrode surface ($x = 0$) were calculated from the PBD data, using the binary diffusion coefficients of the mobile species.

As it was stated before, in electrolytes containing two ions (binary electrolytes), ion diffusion is coupled to ion migration. Therefore, the interpretation of the PBD data is straightforward. On the other hand, in electrochemistry, it is customary to add supporting electrolyte to assure enough ionic conductivity and minimize migration effects on the mass transport. The interpretation of the PBD data becomes more complex, and different simulations have been performed to evaluate the effect. Vorotyntsev and Vieil [18] calculate the effect in the chronodeflectometric experiments which can be treated analytically. More recently, Garay and Barbero used digital simulation to evaluate the effect for chronodeflectometry [19, 20] and cyclic voltadeflectometry. The digital simulation program uses finite differences, a well-proven method to simulate electrochemical experiments [21, 22]. The resulting program was applied to simulate the current and deflection behavior during cyclic voltammetry experiments, with consideration of the effect of the supporting electrolyte (SE) on the deflection signal (Figs. 10.12 and 10.13) [23].

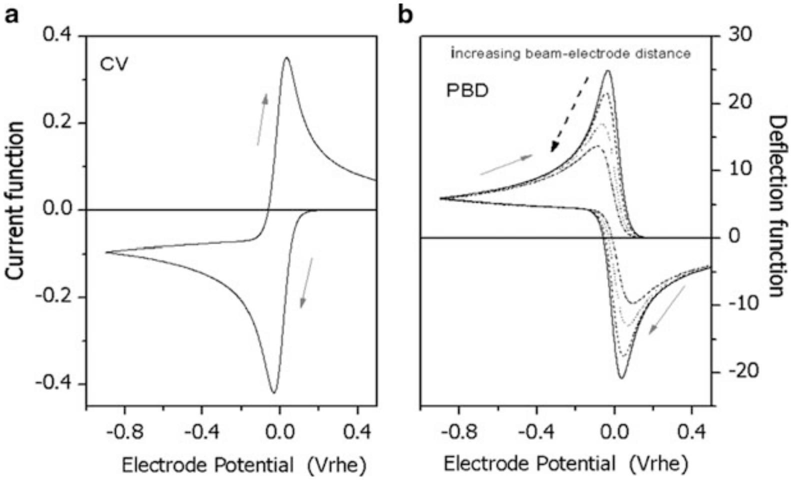

Fig. 10.12 Theoretical cyclic voltammogram (**a**) and cyclic voltadeflectograms (**b**) calculated for $x_0 = 100\ \mu\text{m}$, $E_{\text{initial}} = 0.5\ \text{V}$, $D = 1.0 \times 10^{-5}\ \text{cm}^2\ \text{s}^{-1}$, d$n$/d$C = 1$ for all species, $n_e = 1$, $v = 1\ \text{mV s}^{-1}$ [O]/[SE] $= 10^3$. The different curves in PBD were calculated with varying values of beam-electrode distance

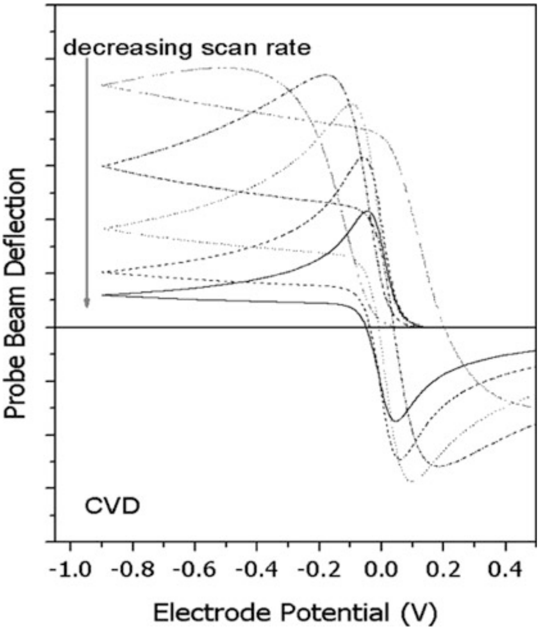

Fig. 10.13 Theoretical cyclic voltadeflectogams calculated for $x_0 = 100\ \mu\text{m}$, $E_{\text{initial}} = 0.5\ \text{V}$, [O]/[SE] $= 10^3$, $n_e = 1$, dn/d$C = 1$ for all species. Scan rate is decreased from 100 to $1\ \text{mV s}^{-1}$

Figure 10.12a shows a theoretical cyclic voltammogram where only one electron is reversibly exchanged between the electrode and a given electroactive redox species. The sweeps are started at the positive potential limit, and the reducing current is considered as negative.

Figure 10.12b shows theoretical cyclic deflectograms calculated together with the current function with different values of beam-electrode distance. The maximum values (peaks) of the cyclic deflectograms, in the forward scan, depend linearly on the square root of the beam-electrode distance. The latter is valid for reduction scans irrespectively on the amount of supporting electrolyte and on the scan rate of experiment. Such linear behavior can be observed during the backward (oxidative) scan but depends on the time spent at negative potentials. Furthermore, the separation between the positive and negative peak potentials of deflection curves is bigger as the beam is more separated from the electrode surface.

Figure 10.13 shows the calculated effect of the scan rate on the deflection responses. As it was pointed above, the shape of deflectograms is similar to the one of voltammograms when the scan rate is slow. However, cyclic voltadeflectograms cannot be normalized with v as for the case of current profiles because the shape depends on v. All the curves present positive deflection signals, but the deflection peaks shift to less negative potentials when the scan rate is decreased. An equivalent effect is observed during the positive potential scan, but in this case, the deflection do not start from zero, and the peaks are shifted to more negative potential values as the value of v is decreased. Both behaviors are the result of the intrinsic delay between the electrochemical reaction at the surface and the detection by the probe beam. In chronodeflectometry, it shows as a time delay while in cyclic voltadeflectometry shows as potential shift. It is noteworthy that the curve calculated at the larger scan rate (0.1 V s^{-1}) shows a crossing over of the curve. That is, the CVD profile of the backward scan crosses the forward scan and has more positive value than the forward scan. Such behavior is often observed in experimental CVD measurements when the scan rate or the beam-electrode distance is too large. It can be avoided by diminishing one of them or both.

The calculations were validated against experimental data (Fig. 10.14) [24]. As it can be seen, good agreement between simulation and experimental data is observed. The diffusion coefficients ($D_{\mathrm{Fe(CN)}_6^{3-}} = 7.3 \times 10^{-6}\,\mathrm{cm}^2\,\mathrm{s}^{-1}$ and $D_{\mathrm{Fe(CN)}_6^{4-}} = 6.4 \times 10^{-6}\,\mathrm{cm}^2\,\mathrm{s}^{-1}$) were obtained from chronoamperometry. The diffusion coefficients of the supporting electrolyte ions (D_{Cl^-} and $D_{\mathrm{K}^+} = 2.0 \times 10^{-5}$ cm^2 s^{-1}) were calculated from their respective individual ionic conductivities [25]. The program calculates the individual ion concentration gradients, which can be used to interpret the reaction mechanism. The lower plot, measured at the larger beam-electrode distance, shows the predicted crossing over. It is noteworthy that the program was used to calculate the third scan with good agreement.

10.3.5.2 Laplace Transform

The PBD response, during voltammetric studies of redox active species irreversibly adsorbed on a flat electrode surface, was analyzed using Week's numerical inverse Laplace transform algorithm. Excellent agreement was found between the

Fig. 10.14 Cyclic voltammogram (CV, *open circles*) and cyclic voltadeflectograms (CVD, *open squares*) obtained for a solution of $K_3Fe(CN)_6$ (1.3 mM in KCl 0.1 M), $E_{\mathrm{initial}} = E_2 = 0.5$ V, $E_1 = -0.2\ V_{\mathrm{SCE}}$, scan rate $= 6\ \mathrm{mV\ s^{-1}}$. The CVD profiles were measured at different beam-electrode distances, which are depicted in the plots. The *full lines* are theoretical calculations

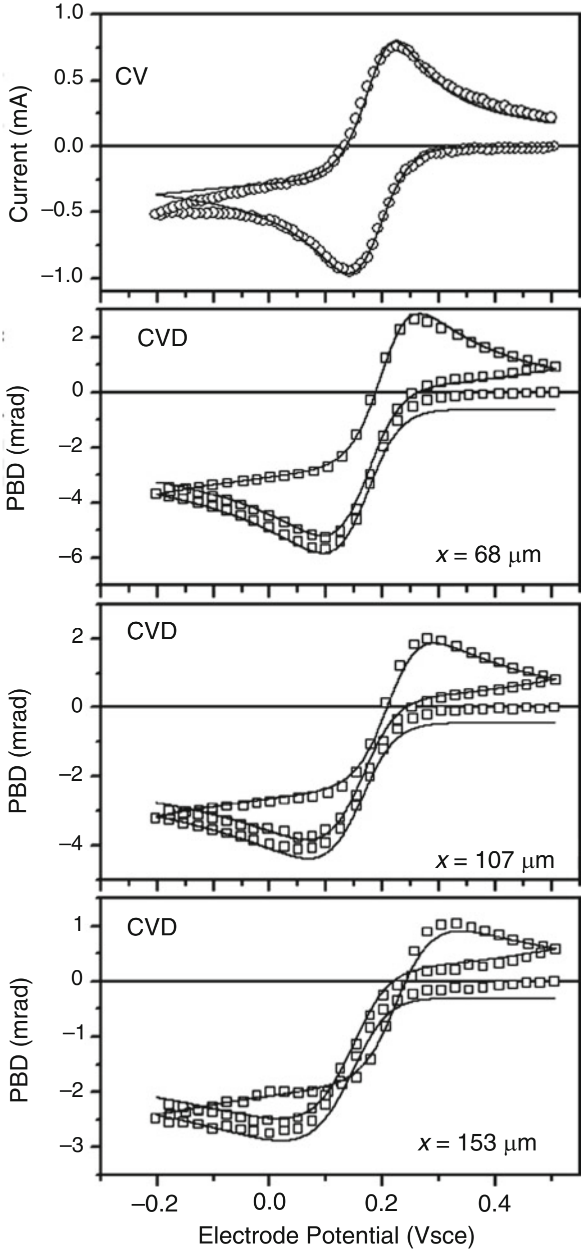

time-resolved profiles calculated based on this approach and those obtained via digital simulation [26]. It is noteworthy that the experimental data could be processed using numerical Laplace transform and compared to the simulated data in the Laplace space as it has been done to interpret purely electrochemical data [27].

10.3.5.3 Numerical Convolution

The convolution approach to data process experimental data in order to take into account diffusion effects is well known in electrochemistry. It was developed, to process cyclic voltammetry data, independently by Saveant and coworkers[28] and Oldham and coworkers [29]. The approach was applied to evaluate concentrations at a finite distance from the electrode, which is necessary to simulate or process PBD data, by Engstrom and coworkers [30] and Oldham and coworkers [31]. The numerical method could be used either to process experimental data or to simulate PBD profiles.

Data Processing by Convolution

The convolution method was proposed to process PBD data by Vieil and coworkers [32]. The idea is to calculate, from the experimental PBD data, a flux at the electrode surface which can be directly compared with the flux of electrons at the electrode, which is the electrochemical current. As it has been discussed above, the PBD data does not represent the flux of ions at the surface ($x = 0$) but at a finite distance. The method chosen implies convolution of the current to produce a calculated flux at a nonzero beam-electrode distance ($x = x_0$) and comparison with the measured PBD data.

To apply the method to cyclic voltadeflectometry data, the following assumptions are made:

1. Electron flux is directly linked to ion flux.
2. Electron exchange and ion exchange occur simultaneously.
3. All ion exchange occurs in a time period significantly lower than the time that takes the gradient to reach the electrode. This one is, in fact, the definition of a discontinuous or instantaneous process.

The measured electronic current, $i(t)$, is equal to the sum of ionic fluxes in the electrode-solution interface:

$$i(t) = FA\sum z_{\mathrm{k}}J_{\mathrm{k}}(0,t). \tag{10.43}$$

There is a contribution k for each ion exchanged, and $J_{\mathrm{k}}(0,t)$ represents the flux of each species at $x = 0$. Each mole of substance exchanged carries a charge: $z_{\mathrm{k}}F$. To evaluate the flux of each ion at a given distance and time ($J_{\mathrm{k}}(x,t)$), the convolution product of a mass transfer function is applied to the flux at the electrode surface.

$$J_{\mathrm{k}}(x,t) = H(x,t)^{*}J_{\mathrm{k}}(0,t) \tag{10.44}$$

where * indicates the convolution product. For a mass transport (in a binary electrolyte) from/to an electrode with semi-infinite diffusion, the solution of Fick's law gives the mass transfer function:

$$H(x,t) = \frac{x}{2\sqrt{(\pi D t^3)}} \mathrm{e}^{\frac{-x^2}{4Dt}}. \tag{10.45}$$

Applying Eq. (10.45) and combining with Eq. (10.1) render the deflection profile:

$$\theta(x,t) = \left(\frac{l}{n}\frac{\mathrm{d}n}{\mathrm{d}C}\right)\left(\frac{1}{D}\right)\left[\left(\frac{x}{2\sqrt{(\pi D t^3)}} \mathrm{e}^{\frac{-x^2}{4Dt}}\right) * i(t)\right]. \tag{10.46}$$

The procedure was validated using the silver deposition/stripping [33]. It is noteworthy that applying Eq. (10.46) to the concentration profile at $t = 0$, $x = 0$ in the case of potential pulse experiments would render the $\theta(t)$ profile described before. However, in that case, it is better to apply the analytical solution than numerical convolution since the concentration profiles for pulse potential present a singularity that makes the numerical procedures unstable. In fact, numerical calculations have been applied to the chronocoulometric profile, instead of the chronoamperometric one, to avoid such numerical unstability [34].

Using the method, Vieil et al. perform a quantitative analysis of the redox coupled ion exchange between poly(phenylene) films and a binary electrolyte [35]. They apply convolution to the experimental current and compare the convoluted current with the experimental PBD data. Vieil and Lopez used the method to compare the redox coupled ion exchange in polypyrrole and poly(pyrrolesulfonate) [36]. The flux of co-ions, together with counterions, was detected through the comparison of ion flux with the current. The profiles of PBD signal and EQCM have also been combined by measuring in the same electrode [37].

A parameter necessary to apply the procedure is the diffusion coefficient of the species exchanged. In a binary electrolyte, only one diffusion coefficient exists (D). One strategy to do that consists in measuring the voltadeflectogram at different distances and to compare it with the calculated PBD signal. Using literature values for $\mathrm{d}n/\mathrm{d}C$, the value of $x/\sqrt{D}$ which fits the experimental data is evaluated. Another strategy implies measuring the chronodeflectometric profiles at different distances and obtaining D and x_0 from Eq. (10.30).

If a good fitting of the current with the convoluted PBD signal is obtained, the ion exchange model (kind and number of ions) represents the system. Otherwise, some potential ranges where a different ion flux is present could be detected. An experimental drawback of the convolution method is that the potential window for voltadeflectometry is smaller than the one for voltamperometry, due to the potential gap produced by the diffusional delay. Since the extreme potentials are defined by other constraints, such as electrode or electrolyte stability, some information could be lost.

Simulation by Convolution

An alternative use of convolution, closer to digital simulation, implies the calculation of the PBD signal by convolution of an ideal current-potential profile. It is unlikely that a perfect match between experimental and simulated data could be achieved for surface films. This is due to nonidealities of the current-potential experimental profiles which also do not allow fitting cyclic voltamperograms with their ideal simulations. However, the simulations give insight on the effect of experimental parameters on the CVD profiles. It is well known that semi-integral (convolution with $t^{1/2}$) processing of adsorbed redox could render the diffusion-controlled voltammogram [38].

Using this approach, it is possible to propose a mechanism of reaction in the surface-confined redox system involving multiple electron transfer, interaction between redox centers, etc. Then, the experimental parameters such as scan rate, diffusion coefficients, and beam-electrode distance are measured and used to simulate the PBD profiles, which are then compared with the experimental data.

To assess the simulation capabilities, in Fig. 10.15, the simulated CVD profiles for an ideal one-electron/one-ion process are shown. In Fig. 10.15a, the effect of scan rate is shown, while in Fig. 10.15b, the effect of beam-electrode distance is shown. As it can be seen, increasing the scan rate or the beam-electrode distance

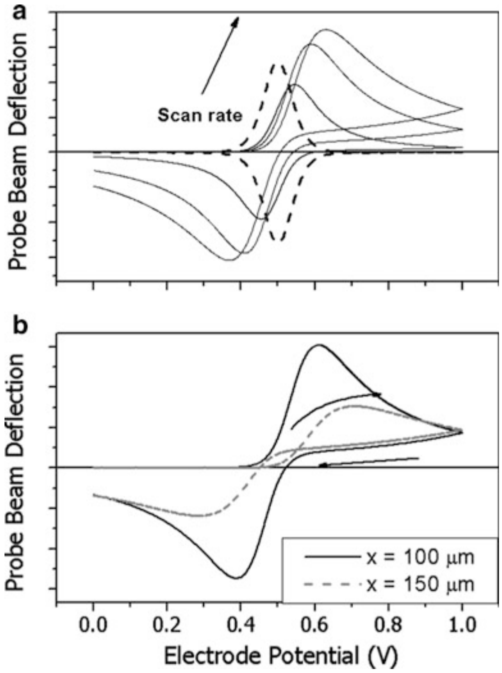

Fig. 10.15 Simulated cyclic voltadeflectograms of an immobilized coupled for one-electron/one-ion process. $C_S = 1, D_O = 1.0 \times 10^{-5}$ cm^2 s^{-1}. (**a**) Profiles calculated at different scan rates. The *dotted line* is the corresponding cyclic voltammetry signal. $x = 50$ μm. (**b**) Profiles calculated at different beam-electrode distances. Scan rate = 0.050 V s^{-1}

produces a shift in the CVD peak potential. In extreme cases, a crossing of the backward with the forward scan could be observed. Another interesting parameter in surface redox species is the existence of multiple electron steps. When the cyclic voltammogram shows a broad peak, it could be due to multiple electron steps or interaction between redox centers [39]. In those cases, the CVD profile could easily show two different processes if the ion fluxes in each process have opposite sense.

In Fig. 10.16, the simulated CV and CVD of a two successive electron steps are shown, with opposite ion exchanged in each redox step. While in the CV the two steps could not be distinguished, the CVD clearly shows two different redox processes. It is interesting to note that the simulated CVD shows two steps in the forward scan but only one in the backward scan. This feature is related with the fact that ion fluxes corresponding to the forward and backward scan are combined during the latter and occurs when the redox potential for both steps is close to each other. This feature has been observed experimentally in the ion exchange of poly (*o*-aminophenol) [40]. A qualitative analysis would lead us to believe that the ion exchange during oxidation is different to that of reduction. However, the simulation points out that an ideal two-electron transfer system which presents the same ion exchange (anion + cation) during oxidation and reduction will show a CVD profile similar to the one obtained. This result suggests that simulations of ideal systems could indeed provide great insight into the interpretation of CVD data.

It is noteworthy that simulation by convolution is quite straightforward because it uses commercial numerical convolution routines [41], unlike digital simulation where special programs have to be written. While less flexibility exists on the ion movement simulation, the method easily considers complex redox and ion exchange mechanisms in the films.

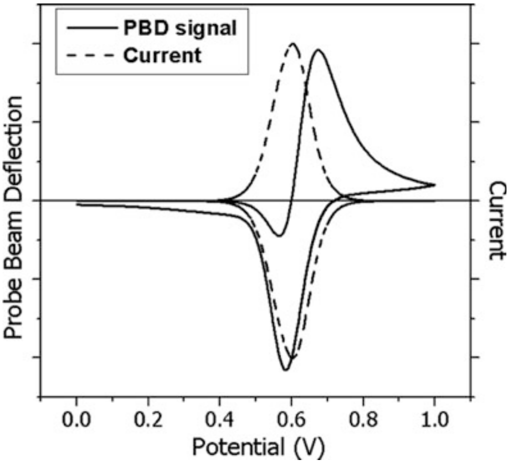

Fig. 10.16 Simulated cyclic voltammogram (*dotted line*) and cyclic voltadeflectogram (*full line*) for an electroactive film with a nernstian two-electron processes. The first redox process involves cation exchange, and the second, anion exchange

10.3.6 Water Concentration Effects

The movement of ions in solution implies changes in the water concentration since most ions are hydrated. These changes should affect the PBD signal [1]. However, water concentration effects have never been detected in PBD experiments. It should be borne in mind that water concentration is quite high, and while PBD is sensitive to the concentration gradient ($\mathrm{d}n/\mathrm{d}C$) and it does not depend on the base value, the effect of water movement is an addition/subtraction of the water concentration (55.5 M). It is unlikely that small changes of water concentration could alter the water concentration.

10.3.7 Thermal Effects

Electrochemical reactions produce thermal gradients due to resistive (Joule) or entropic (Peltier) effects. Those thermal gradients will appear as refractive index gradients and could be detected by the probe beam (see Chap. 5). However, thermal diffusivities (equivalent to the mass transport diffusion coefficient) are two orders of magnitude ($\kappa_{\mathrm{water}} = 1.36 \times 10^{-3}\ \mathrm{cm}^2\ \mathrm{s}^{-1}$ [42]) larger than the diffusion coefficient of ions. Therefore, the contribution due to thermal gradients will be negligible at the times used to measure concentration gradients. However, probe beam deflection can be used to measure cell calorimetry, under appropriate conditions [43].

10.4 Experimental Probe Beam Deflection Setup

In Fig. 10.17, a scheme of the PBD setup installed in our laboratory is shown, which is similar to the one described before [44].

The basic components of the PBD system are a He–Ne laser and a bicell position sensitive detector. The laser beam is focused by a 50-mm lens to a diameter of roughly 60 μm in front of the planar electrode. The actual beam/electrode distance is estimated by measuring chronodeflectometric pulses at different relative distances (x) and using the relationship between the time of maximum signal and distance (Eq. 10.30). The electrochemical cell is an optical glass cuvette, which is mounted on a 3 axis tilt table. The working electrodes can be any flat conductive solids such as polished glassy carbon plates, Pt plates, Au films on glass, ITO/glass transparent electrodes, and carbon aerogel plates, etc. The counter electrode is a coiled Pt wire, and the reference electrode is a conventional SCE connected with the cell by a plastic tube. The counter electrode and reference connecting tube are situated facing the working electrode outside the path of the beam. A micrometric translation stage allowed for controlled positioning of the sample with respect to the laser beam in small (μm) steps. The position sensitive detector is placed at some

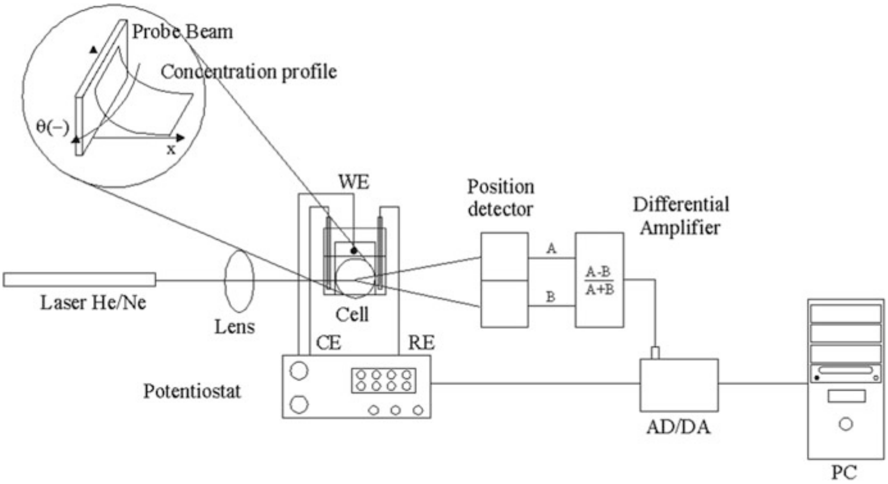

Fig. 10.17 Scheme of a probe beam deflection setup

distance (e.g., 25 cm) behind the electrochemical cell. The deflection signal was processed using a position monitor. The signal of the two photodiodes making the bicell detector was subtracted and normalized to the overall signal in order to minimize the effect of laser intensity fluctuations. All parts of the system were mounted on an optical rail, resting on a stable optical breadboard. The electrochemical control of probe beam deflection experiments is performed using a potentiostat. The entire setup is controlled by a PC, through an AD/DA card.

Positive deflections correspond to a decrease of ion concentration in the solution near the electrode, indicating ion insertion in the film. For oxidation, when positive charges are created in the film, it means that anions are inserted. During reduction, the opposite is true. Negative deflections correspond to a decrease of ion concentration in the solution near the electrode, indicating ion expulsion from the film. For oxidation, when positive charges are created in the film, it indicates that cations are expelled.

An important point is the alignment of the probe beam with the electrode surface. A similar problem exists in PDS. The ideal situation is for the probe beam to travel parallel to the electrode surface. In that way, the whole path length will sample the concentration gradients. Misalignment of flat surfaces with the beam is possible. The best solution will be to use a cylinder as an electrode and setup it perpendicular to the probe beam. Therefore, the sampling region will be always the same. However, the sampling region is only the tangent of the circle and is quite small.

10.5 Values of the Variation of Refractive Index with Concentration

Table 10.1 Variation of refractive index with concentration for common ions[a]

Species	dn/dC 10^3	Species	dn/dC 10^3	Species	dn/dC 10^3
CH_3COOH	39.9	H_3PO_4	8.35	O_2	−14.4[b]
$HONH_4$	0.91	$KHCO_3$	9.78	H_2	−12.8[b]
$ClNH_4$	9.47	$KHC_8H_4O_4$	37.64	NaH_2PO_2	22.1[c]
$(NH_4)_2SO_4$	18.54	KBr	13.71	Na_2HPO_3	10.7[c]
$BaCl_2$	28.35	K_2CO_3	21.56	$LiClO_4$	6.69[c]
$CaCl_2$	23.96	KCl	9.6	$NaCl$	9.55
$CsCl$	12.47	K_2CrO_4	38.37	$NaClO_4$	7.36
$CoCl_2$	26.58	$K_2Cr_2O_7$	51.86	$HClO_4$	6.8[c]
$CuSO_4$	26.33	$K_3Fe(CN)_6$	51.64	$NaOH$	9.76
$FeCl_3$	41.14	$K_4Fe(CN)_6$	70.55	$NaHCO_3$	10.48
$FeCl_2$	31.25	CH_3COONa	10.63	H_2SO_4	11.05
$HCOOH$	2.52	KOH	10.07	Na_2CO_3	21.25
HCl	7.94	KI	21.05	$NaCr_2O_7$	50.4
$Pb(NO_3)_2$	36.43	KNO_3	8.98	$Na_4Fe(CN)_6$	71.74
$LiCl$	8.36	$K_2C_2O_4$	20.96	Na_2MoO_4	34.06
$MgCl_2$	20.4	KH_2PO_4	14.15	$NaNO_3$	8.64
$MgSO_4$	20.8	$KHPO_4$	24.95	Na_3PO_4	37.48
$MnSO_4$	23.7	K_2SO_4	19.51	Na_2HPO_4	25.01
$NiSO_4$	29.21	$KSCN$	17.3	NaH_2PO_4	14.4
HNO_3	7.8	$AgNO_3$	17.28	Na_2SO_4	19.24
$Na_2S_2O_3$	29.69	$Na_2C_4H_4O_6$	30.35	$NaBr$	13.56
CCl_3COOH	19.5	$ZnSO_4$	25.55	$SrCl_2$	27.09
H_2O_2	1.4[c]	CO_2	−14.0[d]		

[a] The values are valid for concentrations below 2 M and were obtained from the refractive index data [7], unless otherwise stated in the table

[b] [8]

[c] Author's laboratory measurements

[d] O'Brien RN, private communication, 1994

References

1. Rudnicki JD, McLarnon FR, Cairns EJ (1991) In situ characterization of electrode processes by photothermal deflection spectroscopy. In: Varma R, Selman JR (eds) Techniques for characterization of electrodes and electrochemical processes. Plenum, New York
2. Alda J (2003) Laser and Gaussian beams propagation and transformation. In: Encyclopedia of optical engineering. Marcel Dekker, New York
3. Rudnicki JD, Brisard GM, Gasteiger HA, Russo RE, McLarnon FR, Cairns EJ (1993) Effect of the supporting electrolyte and beam diameter on probe beam deflection experiments. J Electroanal Chem 362:55–69. doi:10.1016/0022-0728(93)80006-4

4. Mathias MF (1996) Modelling probe beam deflection experiments in binary bathing electrolytes. J Electroanal Chem 407:115–122. doi:10.1016/0022-0728(95)04456-6
5. Newman JS, Thomas-Alyea KE (2004) Electrochemical systems. Wiley-IEEE, New York
6. Barbero C, Miras MC, Kötz R (1992) Electrochemical mass transport studied by probe beam deflection: potential step experiments. Electrochim Acta 37:429–437. doi:10.1016/0013-4686(92)87032-U
7. (1978) CRC handbook of chemistry and physics, 68 edn. CRC, New York
8. O'Brien RN (1972) In: Weissberger A, Rossiter BW (eds) Physical methods of chemistry. Wiley Interscience, New York
9. Lobo VMM (1989) Handbook of electrolyte solutions. Elsevier, Amsterdam
10. Barbero C, Miras MC, Koetz R, Haas O (1993) Probe beam deflection: a useful tool for the study of ion transport in polymers. Solid State Ionics 60:167–172. doi:10.1016/0167-2738(93)90292-B
11. Grumelli DE, Wolosiuk A, Forzani E, Planes GA, Barbero C, Calvo EJ (2003) Probe beam deflection study of ion exchange in self-assembled redox polyelectrolyte thin films. Chem Commun 3014–3015. doi:10.1039/B308449C
12. Garcia G, Bruno MM, Planes GA, Rodriguez JL, Barbero CA, Pastor E (2008) Phys Chem Chem Phys 10:6677–6685. doi:10.1039/B806938G
13. Channelle A (2009) Beginning OpenOffice 3: from novice to professional. Apress, New York
14. Decker F, Neuenschwander RT, Cesar CL, Penna AFS (1987) The mirage effect in electrochemistry. J Electroanal Chem 228:481–486. doi:10.1016/0022-0728(87)80125-0
15. Awakura Y, Okada M, Kondo Y (1977) Profile of the refractive index in the cathodic diffusion layer of an electrolyte containing $CuSO_4$ and H_2SO_4. J Electrochem Soc 124:1050–1057. doi:10.1149/1.2133477
16. Tamor MA, Zanini M (1986) A scanning refractometer for electrochemical studies. J Electrochem Soc 133:1399–1401
17. Decker F, Fracastoro-Decker M (1988) The mirage effect in photoelectrochemistry. J Electroanal Chem 243:187–191. doi:10.1016/0022-0728(88)85038-1
18. Vorotyntsev MA, Lopez C, Vieil E (1994) On the interpretation of optical beam deflection data at excess of a background electrolyte. J Electroanal Chem 368:155–16. doi:10.1016/0022-0728(93)03095-7
19. Garay F, Barbero CA (2006) Charge neutralization process of mobile species at any distance from the electrode/solution interface. 1. Theory and simulation of concentration and concentration gradients developed during potentiostatic conditions. Anal Chem 78:6733–6739. doi:10.1021/ac0603678
20. Garay F, Barbero CA (2006) Charge neutralization process of mobile species at any distance from the electrode/solution interface. 2. Concentration gradients during potential pulse experiments. Anal Chem 78:6740–6746. doi:10.1021/ac0603680
21. Britz D (1988) Digital simulation in electrochemistry. Springer, Berlin
22. Rudolph M, Reddy DP, Feldberg SW (1994) A simulator for cyclic voltammetric responses. Anal Chem 66:589A–600A. doi:10.1021/ac00082a002
23. Garay F, Barbero CA (2008) Charge neutralization process of mobile species developed during potentiodynamic conditions. Part 1: Theory. J Electroanal Chem 624:218–227. doi:10.1016/j.jelechem.2008.09.010
24. Garay F, Iglesias RI, Barbero CA (2008) Charge neutralization process of mobile species developed during potentiodynamic conditions. Part 2: Simulation and fit of probe beam deflection experiments. J Electroanal Chem 624:211–217. doi:10.1016/j.jelechem.2008.09.009
25. Coury L (1999) Conductance measurements Part 1: Theory. Curr Sep 18:91–96
26. Wang J, Wang Z, Scherson DA (2007) Beam probe deflection analysis of redox active species irreversibly adsorbed on electrode surfaces. J Electrochem Soc 154:F165–F171. doi:10.1149/1.2754070

27. Dauvotis VE, Moorhead ED, Stephens MM, Tomaszewski TE (1986) J Electroanal Chem 202:37–55. doi:10.1016/0022-0728(86)90106-3
28. Savéant JM, Tessier D (1975) Convolution potential sweep voltammetry V. Determination of charge transfer kinetics deviating from the Butler-Volmer behavior. J Electroanal Chem 65:57–66. doi:10.1016/0368-1874(75)85105-7
29. Oldham KB (1986) Convolution: a general electrochemical procedure implemented by a universal algorithm. Anal Chem 58:2296–2300. doi:10.1021/ac00124a040
30. Engstrom RC, Mark Wightman R, Kristensen EW (1988) Diffusional distortion in the monitoring of dynamic events. Anal Chem 60:652–656. doi:10.1021/ac00158a010
31. Myland JC, Oldham KB (1999) Concentrations of electroactive solutes, during cyclic and other voltammetries, at points away from the electrode surface. 1. Fundamental relationships and their validation. Anal Chem 71:183–195. doi:10.1021/ac980769i
32. Vieil E (1994) Mass transfer and convolution. Part 1. Theory. J Electroanal Chem 364:9–15. doi:10.1016/0022-0728(93)02925-8
33. Henderson MJ, Hillman AR, Vieil E, Lopez C (1998) Combined electrochemical quartz crystal microbalance (EQCM) and probe beam deflection (PBD): validation of the technique by a study of silver ion mass transport. J Electroanal Chem 458:241–248. doi:10.1016/S0022-0728(98)00358-1
34. Henderson MJ, Hillman AR, Vieil E (2000) Chronoamperometric resolution of ion and solvent transfers at a poly(o-toluidine) modified electrode by combined electrochemical quartz crystal microbalance (EQCM) and probe beam deflection (PBD). Electrochim Acta 45:3885–3894. doi:10.1016/S0013-4686(00)00453-9
35. Vieil E, Meerholz K, Matencio T, Heinze J (1994) Mass transfer and convolution: Part II In situ optical beam deflection study of ionic exchanges between polyphenylene films and a 1:1 electrolyte. J Electroanal Chem 368:183–191. doi:10.1016/0022-0728(93)03110-B DOI:dx.doi.org
36. Vieil E, Lopez C (1999) Quantitative discrimination of mass fluxes at electrochemical interfaces by optical beam deflection. J Electroanal Chem 466:218–233. doi:10.1016/S0022-0728(99)00153-9
37. Henderson MJ, Hillman AR, Vieil E (1998) A combined electrochemical quartz crystal microbalance (EQCM) and probe beam deflection (PBD) study of a poly(o-toluidine) modified electrode in perchloric acid solution. J Electroanal Chem 454:1–8. doi:10.1016/S0022-0728(98)00245-9
38. Bowling R, McCreery RL (1988) Diagnosis of adsorption on solid electrodes with semi-integral voltammetry. Anal Chem 60:605–608. doi:10.1021/ac00157a022
39. Barbero C, Silber JJ, Sereno L (1990) Electrochemical properties of poly-ortho-aminophenol modified electrodes in aqueous acid solutions. J Electroanal Chem 291:81–101. doi:10.1016/0022-0728(90)87179-N
40. Salavagione HJ, Arias-Pardilla J, Pérez JM, Vázquez JL, Morallón E, Miras MC, Barbero C (2005) Study of redox mechanism of poly(o-aminophenol) using in situ techniques: evidence of two redox processes. J Electroanal Chem 576:139–145. doi:10.1016/J.JELECHEM.2004.10.013
41. Higham DJ, Higham NJ (2000) MATLAB guide. Society for Industrial & Applied Mathematics, New York
42. Braslavsky S, Heihoff K (1991) Photothermal methods. In: Scaiano JC (ed) CRC handbook of organic photochemistry. CRC, Boca Raton
43. Rosolen JM, Fracastoro-Decker M, Decker F (1993) The mirage effect: a sensitive probe for electrochemical cell calorimetry. J Electroanal Chem 346:119–133. doi:10.1016/0022-0728(93)85007-4
44. Kötz R, Barbero C, Haas O (1990) Probe beam deflection investigation of the charge storage reaction in anodic iridium and tungsten oxide films. J Electroanal Chem 296:37–49. doi:10.1016/0022-0728(90)87231-8

Chapter 11
Application of Probe Beam Deflection Techniques to the Study of Surface-Confined Electrochemical Systems

11.1 Introduction

As it was stated before (Chap. 10), the interpretation of PBD results, when the concentration of several ions is changing, is difficult. On the other hand, when only one ion concentration is changing and the electrolyte is constituted by only two ions (binary electrolyte), the interpretation is straightforward. PBD studies on redox couples in solution could not meet the criteria, unless one of the redox forms is insoluble. On the other hand, if the redox couples are confined at the electrode surface, only exchanged ions are moving and can be detected by PBD. Therefore, PBD techniques are specially suited to study surface-confined systems, including monolayers and multilayers. Accordingly, most of the published data on the use of PBD techniques have been devoted to this subject.

11.2 Noble Metal Electrode Surfaces

Probably, the most thoroughly studied electrochemical system is the surface of polycrystalline Pt in aqueous media. This system was initially studied by PBD by Rudnicki et al. [1], using multiple cycles and averaging to improve the signal/noise ratio. Then, it was studied by Kersetz et al. using single cycle but with a platinized Pt electrode with a bigger area (roughness = 17) [2]. The cyclic voltammogram and the corresponding PBD signal are observed in Fig. 11.1. During oxidation, the concentration of protons increases (negative deflection) due to the oxidation of adsorbed hydrogen to protons, followed by a region with negligible signal in the double layer region and a clear increase of concentration (negative deflection) coming from the metal reaction with water to form the oxide:

$$\mathrm{Pt(H_2)ads} \xrightarrow{-2e^-} \mathrm{Pt} + 2\mathrm{H}^+, \qquad (11.1)$$

G.G. Láng and C.A. Barbero, *Laser Techniques for the Study of Electrode Processes*, Monographs in Electrochemistry, DOI 10.1007/978-3-642-27651-4_11,

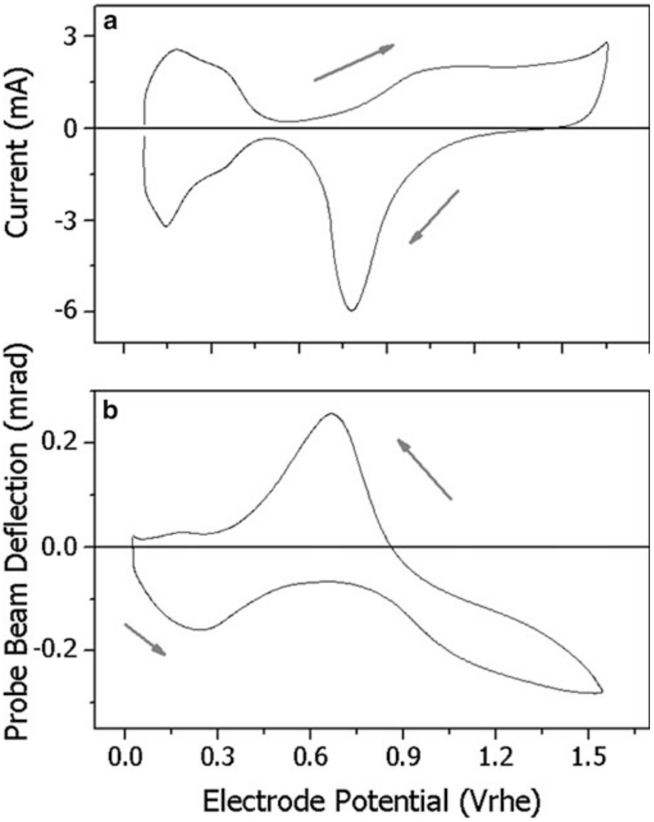

Fig. 11.1 Cyclic voltamperogram (CV) and voltadeflectogram (PBD) of a polycrystalline Pt electrode in 1 M $HClO_4$. $v = 100$ mV s^{-1}

$$\mathrm{Pt} + \mathrm{H_2O} \xrightarrow{-2e^-} \mathrm{PtO} + 2\mathrm{H}^+. \tag{11.2}$$

During reduction, the opposite reactions seem to occur, as the opposite PBD signal is observed.

Other systems studied are gold electrodes in acid media [3]. In this metal, hydrogen adsorption is minimal. Only the signals due to oxide formation:

$$\mathrm{Au} + \mathrm{H_2O} \xrightarrow{-2e^-} \mathrm{AuO} + 2\mathrm{H}^+ \tag{11.3}$$

are detected. In such system, the adsorption of anions in the double layer region was also detected. The PBD signal switch sign at the potential of zero charge ($E_{\mathrm{pzc}} = -0.2\ \mathrm{V_{SCE}}$).

11.3 Carbon Materials

Carbon materials show a more complex chemistry than noble metals. Electrochemical oxidation at high anodic potentials (>2.0 V_{RHE}) produces the irreversible formation of oxide layers, with their own electrochemical response [4]. The most commonly used electrode material, glassy carbon, was also studied by PBD [3]. In this case, the polished electrode has a weak current and PBD signal. However, after electrochemical activation (oxidation at 2.0 V_{SCE} in acid media during 3 min), a broad current peak and a related PBD signal are observed. During oxidation, a negative deflection is measured (proton concentration increases), with the opposite signal during reduction. The surface reaction is assigned to

$$QH_2 \xrightarrow{-2e^-} Q + 2H^+, \tag{11.4}$$

where Q and QH_2 are the quinone and hydroquinone surface groups, respectively. The groups are created during electrochemical activation [5]. The fluxes observed in polished electrodes are in the same direction, suggesting that the polished surface is covered by a thin layer of native oxide.

PBD has been also used to study the intercalation of anions in graphite [6] and in thin films of fullerenes [7]. In the latter system, each redox peak is correlated with cation insertion in the film, but anion contribution is also detected.

11.4 Underpotential Deposition

An interesting electrochemical system involves the deposition of metals, on noble metal surfaces, at potentials more anodic than the standard potential for the reduction of the metal ions (underpotential deposition, UPD). The UPD of copper on Pt was studied using PBD [2]. As it can be seen in Fig. 11.2, it is possible to detect the different forms of metals adsorption (shown as peaks in CV and CVD profiles). As it can be seen, the current peaks due to hydrogen desorption and PtO formation have a similar magnitude than those due to Cu desorption (Fig. 11.2a). On the other hand, the CVD peaks due to Cu desorption (Fig. 11.2b) are several orders of magnitude larger than the ones due to Pt surface electrochemistry. Therefore, CVD is much more sensitive than CV, being able to detect 2% of a Cu monolayer. It is likely that the higher value of dn/dC for $CuSO_4$ than for H_2SO_4 (Table 10.1) bears some responsibility on the increased sensitivity.

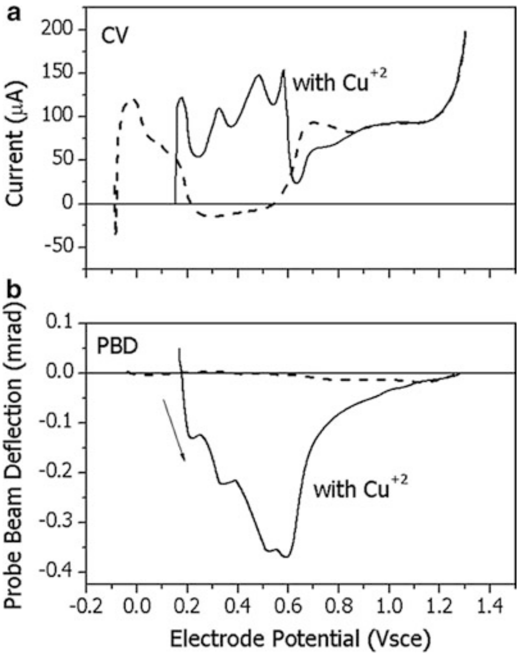

Fig. 11.2 Cyclic voltamperogram (**a**) and voltadeflectogram (**b**) for a Pt electrode in 0.1 M $HClO_4$. Scan rate = 100 mV s^{-1}. The *broken lines* represent the measurement in absence of Cu^{2+}, while the *full lines* show the measurement in presence of 10^{-3} M Cu^{2+}

11.5 Anion Adsorption on Metals

The charging of the double layer of an electrode involves the adsorption of ions from the solution onto the electrode surface. Besides the double layer process, specific adsorption of ions could occur. The ion adsorption driven by the potential will appear as a discontinuous consumption/production of ions in front of the electrode which could be detected by PBD. However, since the maximum coverage is only one monolayer of ions (ca. 10^{-9} mol cm^{-2}), the signal is weak. Bidoia et al. [8] were able to detect the anion adsorption on platinum during a cyclic voltammetry experiment. Also, they measure the potential-dependent extent of adsorption of various anions including ClO_4^-, $H_2PO_4^-$, and Cl^- on the Pt electrode surface. If a rough electrode is used instead of a flat one, the signal/noise ratio would be larger and the detection of anions by PBD easily performed. We have used a mesoporous Pt electrode (MP-Pt) to study the adsorption of anions [9]. The PBD response, measured along the cyclic voltammogram, of an MP-Pt electrode in $HClO_4$ is shown in Fig. 11.3.

In principle, the features in the cyclic voltadeflectogram can be interpreted in terms of the production and consumption of protons at the Pt interface. The following reactions have to be considered:

Between 0.05 and 0.40 V, the hydrogen adsorption/desorption occurs:

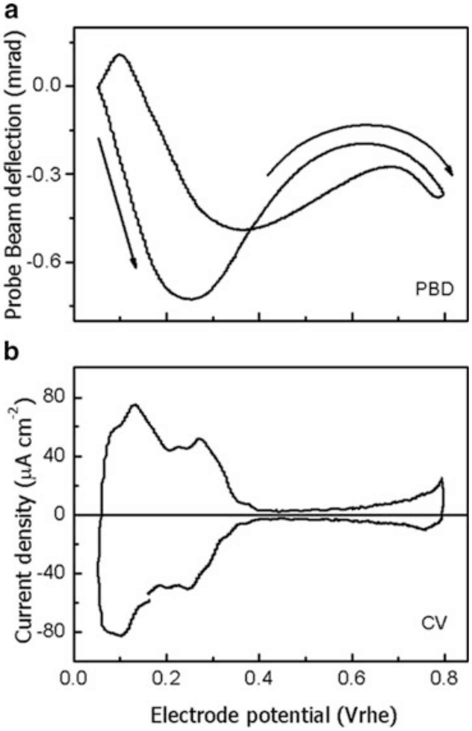

Fig. 11.3 Cyclic voltammogram (**a**) and cyclic voltadeflectogram (**b**) of an MP-Pt in 1 M $HClO_4$. Scan rate = 0.01 V s^{-1}

$$\mathrm{Pt}-(\mathrm{H})+\mathrm{H_2O}\xrightarrow{-e^-}\mathrm{Pt}+\mathrm{H_3O^+}. \tag{11.5}$$

Between 0.40 and 0.75 V is the double layer region, where water and hydroxyl ions adsorb on the surface without faradaic transfer, but partial electron transfer occurs at $E > 0.60\ V_{RHE}$ corresponding to the reaction [7]

$$\mathrm{Pt}+2\mathrm{H_2O}\xrightarrow{-e^-}\mathrm{Pt}-(\mathrm{OH})+\mathrm{H_3O^+}. \tag{11.6}$$

At potential more anodic than 0.75 V occurs the platinum oxide formation:

$$\mathrm{Pt}-(\mathrm{OH})+\mathrm{H_2O}\xrightarrow{-e^-}\mathrm{Pt}-\mathrm{O}+\mathrm{H_3O^+}. \tag{11.7}$$

During the positive potential scan, reactions (11.5), (11.6), and (11.7) take place to the right. Accordingly, in Fig. 11.3, the production of protons causes increasing acid concentration next to the electrode surface, inducing a negative beam deflection. A sharp decrease occurs from 0.05 to 0.50 V where the highest proton production takes place. Then, the signal increases as the diffusion of protons from the surface is the dominant process, and diminishes when the adsorption of hydroxyl ions and oxide formation begin. The change of PBD signal with the potential turns positive (deflection away the electrode surface) during the reverse potential scan, where protons are consumed. The curve describes the opposite behavior than in the positive sweep.

On the other hand, while the CV shows a similar feature, the CVD is quite different in 1 M H_2SO_4 (Fig. 11.4).

An analysis of the PBD data obtained in sulfuric acid (Fig. 11.4) can be made in a similar way. The CV shows the typical peaks of hydrogen (strongly and weakly adsorbed) adsorption/desorption (Fig. 11.4a). During the potential scan in the range 0.05–0.125 V, the probe beam deflects toward the electrode surface indicating hydrogen desorption (Fig. 11.4b). Afterward, a positive change of PBD with the potential occurs between 0.125 and 0.30 V_{RHE}, indicating a deflection away from the electrode surface (at the same potential than the first H_{ad} desorption peak in the CV). These results can be interpreted assuming that the H_{ad} desorption is not the sole reaction that takes place in this potential range, but the adsorption/desorption of sulfate species (HSO_4^-/SO_4^{2-}). It is noticeable that in perchloric acid, where anions do not adsorb, the change in the sign is observed at 0.25 V_{RHE}. The onset for anion adsorption can be considered at 0.01 V, and $(HSO_4^-)_{ad}$ is the predominant species on the surface at low potentials (maximum adsorption at ca. 0.40 V_{RHE}). Conversion to adsorbed SO_4^{2-} (maximum adsorption around 0.70 V_{RHE}) occurs as the potential becomes more positive [10]. Therefore, it is concluded that the positive deflection between 0.125 and 0.30 V_{RHE} in Fig. 11.4b is related mainly with the adsorption of sulfate species. In the reverse potential scan, the PBD curve continuously increases for $E < 0.27$ V_{RHE}, but a change in the slope is apparent at 0.125 V_{RHE}, the same potential for the change in the positive-going sweep.

In the double layer region, a charged solid is in contact with the liquid phase, consisting of molecules of solvent, ions, and dipolar species, which become organized near the solid surface under the orienting force of the static electric field [9]. In the positive-going potential run, the deflection increases between 0.33 and 0.55 V indicating that adsorption of sulfate species prevails. After that, in the 0.55–0.80 V range, the metal surface is more positively charged, and the conversion of adsorbed bisulfate to adsorbed sulfate occurs, generating protons at the surface (11.7). Moreover, the electron donor character of water enhances, and reaction (11.6) takes place, also producing protons which are responsible for the decrease in the deflection signal. The explanations for the shape of the PBD in the negative scan direction in this potential range are similar than before but assuming the consumption of protons and the adsorption of bisulfate. The absence of these features in perchloric media (Fig. 11.3) confirms that they have to be related to the presence of adsorbed anions.

11.6 Electroactive Thin Films

The PBD signal depends on amount of ions exchanged by the surface species. In a monolayer, the maximum coverage of redox groups is of about 10^{-9} mol cm^{-2}. On the other hand, the signal will increase if multilayers of redox groups are used as

Fig. 11.4 Cyclic voltammogram (**a**) and cyclic voltadeflectogam (**b**) of an MP-Pt in 1 M H_2SO_4. Scan rate = 0.01 V s^{-1}

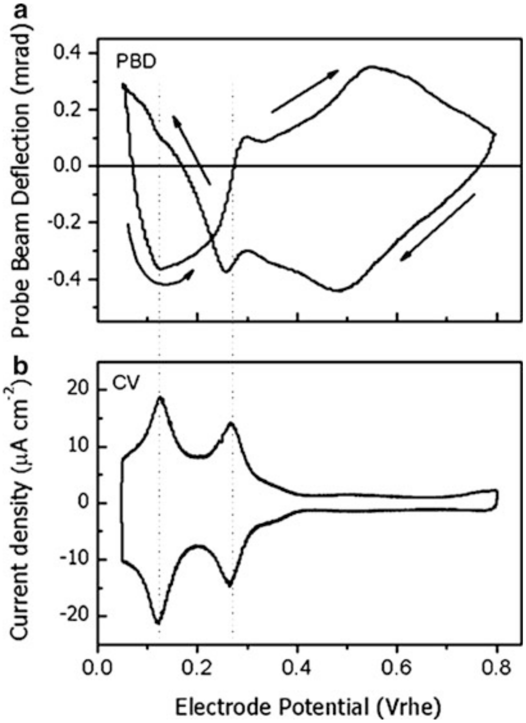

electrodes. Like current, also related to a flux, the deflection will measure the contribution of the entire electrode in the region sampled by the probe beam. Therefore, thin films will show strong PBD signals, and this is the main area of application of PBD techniques. It has to be borne in mind that thick films will show an ion exchange controlled by the ion flux in the solution and ion flux inside the film. Qualitative interpretation of ion exchange is still possible. However, if the experiment is designed for the thin film to obey the condition of discontinuous process, the data can be quantitatively analyzed. In the case of electroactive films, such condition imply the use of thin film where all the material inside is transformed in a time period much smaller than the duration of the PBD measurement.

11.6.1 Electrochromic Oxides

The coloration/bleaching process in electrochromic oxides involves oxidation/reduction of the oxide film. Therefore, an insertion/expulsion of ions is necessary to maintain charge electroneutrality inside the oxide layer. PBD could then be used to study the ion exchange coupled to coloration.

11.6.1.1 Tungsten Oxide (WO_3)

Thin films of WO_3 were produced by electrochemical oxidation of tungsten in acid media. The electrochemical response during oxidation (bleaching) is coupled with a positive deflection (ion expulsion) [11]. The flux could be explained by the reaction occurring during bleaching:

$$WO_3 + xH^+ \xrightarrow{+xe^-} WO_3H_x. \tag{11.8}$$

11.6.1.2 Anodic Iridium Oxide Films

Iridium oxide thin films (IrOx) were prepared as anodic iridium oxide films (AIROF) by electrochemical oxidation of iridium plates in acid media [12]. In the same media (1 M $HClO_4$), the oxidation (coloration) is accompanied by negative deflection, indicating proton expulsion, like in WO_3. On the other hand, in basic media (1 M NaOH), the coloration (oxidation) is accompanied by ion insertion (Fig. 11.5), suggesting that the ion flux corresponds to OH^- insertion:

Region 0 < pH < 3

$$\mathrm{Ir(OH)}_n \xrightarrow{-xe^-} \mathrm{IrO}_x(\mathrm{OH})_{n-x} + \mathrm{H}^+. \tag{11.9}$$

Region 4 < pH < 12

$$\mathrm{Ir(OH)}_n + x\mathrm{OH}^- \xrightarrow{-xe^-} \mathrm{Ir(OH)}_{n-x}. \tag{11.10}$$

The chronodeflectometric measurements of AIROF could be fitted as a discontinuous process. Using the relationship between the beam-electrode distance and the time of the maximum (see Chap. 2), a diffusion coefficient of 1.7×10^{-5} cm^2 s^{-1} is measured in basic media and of 3.8×10^{-5} cm^2 s^{-1} in acid. The values agree closely with those calculated for the binary electrolytes (NaOH and $HClO_4$, respectively) [13]. If a supporting electrolyte is added, diffusion coefficients of 5.8×10^{-5} cm^2 s^{-1} and 9.3×10^{-5} cm^2 s^{-1} in basic and acid media (respectively) are measured. These values of diffusion coefficients agree well with those previously reported for OH^- and H^+, respectively [10].

It seems that the supporting electrolyte ions dominate migration due to its significant excess compared with the ions involved in the surface reaction. Therefore, the PBD data become dominated by the ions moving by diffusion. As it was discussed before, using pulse deflectometry, it is possible to compare the voltammetric and deflectometric responses without diffusional delay.

The DPVD(E) peaks (Fig. 11.6) qualitatively track those on the CV (Fig. 11.5a). However, the relative intensity of the peaks is different in DPVD and CV, suggesting a different ion transference number for each peak. The apparent switching point for the kind of ion exchanged is between pH 3 and 4. Since the

Fig. 11.5 (**a**) Cyclic voltamperogram and (**b**) cyclic voltadeflectogram of a anodic iridium oxide film (AIROF) in 1 M NaOH. ($v = 50$ mV s^{-1})

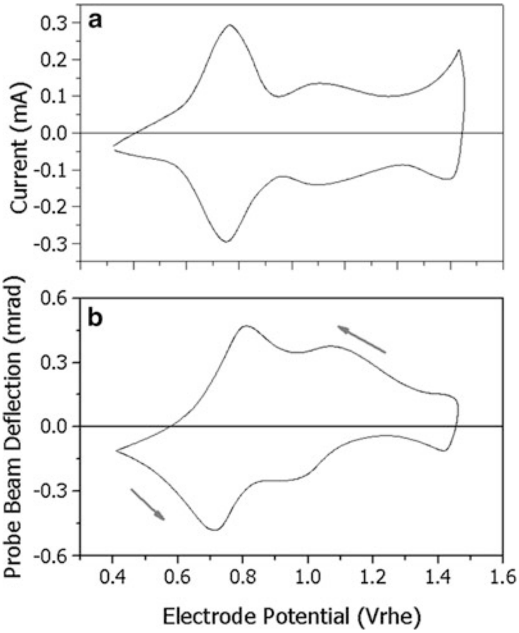

Fig. 11.6 Differential pulse voltadeflectometry (dPVD (E)) of AIROF in 1 M NaOH

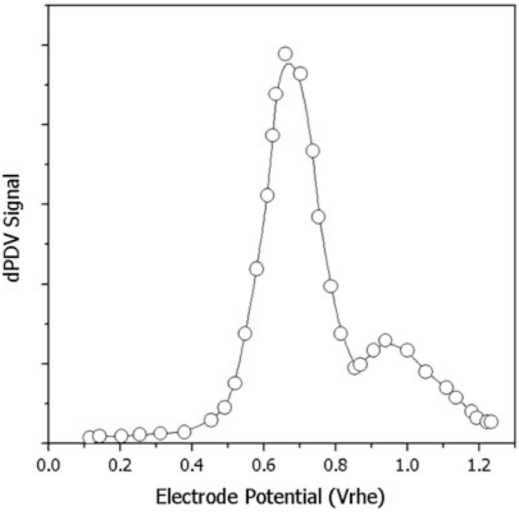

measurements between pH 3 and 11 are made using buffer solutions, the exact value is less certain. However, the fact that the ion exchange changes at a pH different than 7 implies that a surface property (e.g., pK_a of the oxide) is measured and not the trivial predominance of the ion in higher concentration. Plichon and coworkers study the ion exchange on iridium oxide in anhydrous propylene carbonate [14].

11.6.1.3 Cobalt Oxide

Cobalt oxide/hydroxide thin films were deposited by potentiodynamic oxidation of Co^{II} ions in pH 4 media [15]. Since the Co^{III} oxide is insoluble, it is possible to grow a thin film by cycling the electrode in a Co^{+2} solution of the appropriate pH [15]. The ion exchange of cobalt oxides was studied by PBD in basic media and found to be mainly OH^-. The chronodeflectometric response (Fig. 11.7) could be simulated with the theoretical profile of a discontinuous process. The square root of the time for the maxima depends on the beam-electrode distance (Chap. 10), and the binary diffusion coefficient for KOH was obtained, confirming that OH^- is exchanged.

11.6.1.4 Other Oxides

Using current chronodeflectometry, the contribution of OH^- to the ion exchange of nickel oxide films [16] was found to be dominant but with a contribution of co-ions (cations). By combination of PBD with EQCM, the role of ions and solvent was demonstrated [17]. Recently, NiOx films for supercapacitor applications have been studied by different techniques, including PBD [18]. The technique has also been used to study the ion exchange of thermally prepared ruthenium oxide [19].

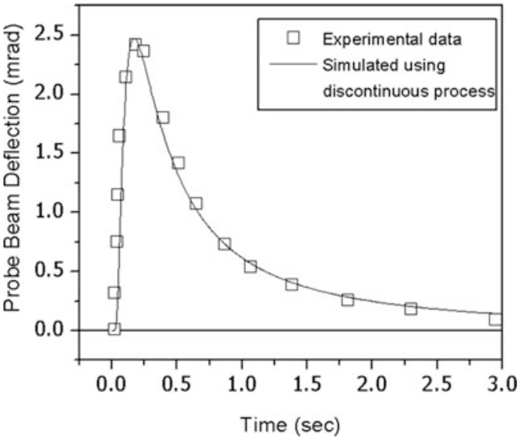

Fig. 11.7 Chronodeflectogram of a cobalt oxide film deposited onto a glassy carbon substrate. Solution = 0.1 M KOH. *Full line* is experimental data, and *gray line* was simulated with $D_o = 1.7 \times 10^{-5}$ cm^2 s^{-1} and $x = 75$ μm

11.6.2 Inorganic Complex Films

PBD techniques have also been utilized to study the redox coupled ion exchange in mixed salts [ferric ferrocyanide (Prussian blue)] [20], cupric ferrocyanide [21], indium ferrocyanide [22, 23], and lutetium diphtalocyanine [24]. In all cases, the ion exchange was found to be dominated by transport of cations, but some contribution of anion transport to the charge compensation was detected.

11.6.3 Electroactive Polymer Films

This is the area where most extensive use has been made of PBD techniques. A pioneering study of the ionic exchange related to redox processes in several polymers (poly(4-vinylpiridine-Ru(bpi)$_2$Cl), polyaniline and poly(1-hydroxyphenazine)) was presented by Haas [25] and coworkers [26]. The ion exchange in polythiophene was then studied [27]. After those initial studies, several more electroactive polymer films have been studied. The results, clearly the main application of PBD techniques, will be described below.

11.6.3.1 Redox Polymers

Poly(1-hydroxyphenazine)

A quite complex redox polymer, poly(1-hydroxyphenazine) (pOHPh), could be produced by electrochemical oxidation of 1-hydroxyphenazine [28]. The ion exchange of the polymer, in acid media, was studied by a combination of PBD (Fig. 11.8) and EQCM [29].

Both PBD and EQCM results suggest a two-step mechanism, with a coupled protonation, similar to polyaniline:

$$(\mathrm{pOHPh})\mathrm{H_2}(\mathrm{A^-H^+})_x \overset{+x\mathrm{H^+}+x\mathrm{A^-}}{\underset{-x\mathrm{H^+}-x\mathrm{A^-}}{\rightleftarrows}} (\mathrm{pOHPh})\mathrm{H_2} \xrightarrow{-\mathrm{e^-}+\mathrm{A^-}} (\mathrm{pOHPh})\mathrm{H_2}^+(\mathrm{A^-}), \quad (11.11)$$

$$(\mathrm{pOHPh})\mathrm{H_2}^+(\mathrm{A^-}) \xrightarrow{-\mathrm{e^-}-\mathrm{H^+}-\mathrm{HA}} \mathrm{pOHPh}. \quad (11.12)$$

The reaction is clearly described in Scheme 11.1.

Chronodeflectometric measurements allow detecting kinetic effects during the ion exchange. A detailed analysis of the EQCM data shows that the mass exchanged does not scale up with the anion mass. Therefore, it was proposed

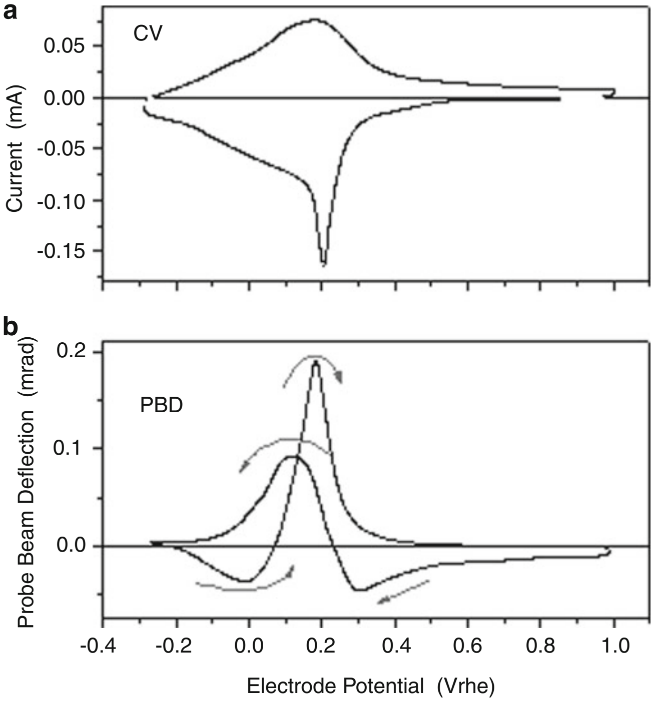

Fig. 11.8 Probe beam deflection (PBD) study of poly(1-hydroxyphenazine) films. (**a**) Current and (**b**) deflection (PBD). $v = 50$ mV s^{-1}. Solution: 1 M $HClO_4$

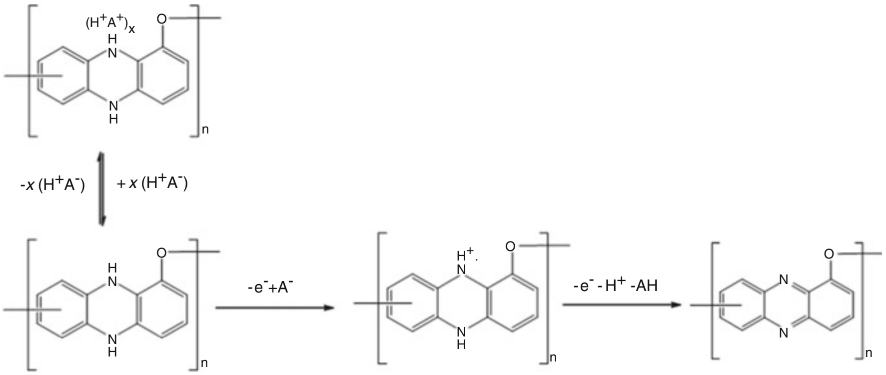

Scheme 11.1 Mechanism of redox coupled ion exchange in poly(1-hydroxyphenazine) thin films

that a counterflux of solvent accounts for the lost mass. Since PBD does not detect solvent, the PBD evidence of anion exchange allows to make the assumption that cation exchange is negligible.

Poly(vinylferrocene)

This system, which has been extensively studied by other techniques (EQCM, radiotracers, etc. [30]), was also investigated by PBD [31]. Thin films, deposited from a solution of the polymer in toluene, were studied in aqueous and nonaqueous media. In nonaqueous media ($LiClO_4$/ACN), only negative deflection accompanies oxidation. The ion exchange mechanism is the expected:

$$\mathrm{PVF} \xrightarrow{-e^- + ClO_4^-} \mathrm{PVF}^+\left(ClO_4^-\right). \tag{11.13}$$

A similar behavior is observed in aqueous media when some acids ($C_6H_5SO_3H$) are used as electrolyte (Fig. 11.9). Using the method proposed by Vieil [32], the current–potential data (Fig. 11.9a) were convoluted, assuming a single anion exchange. The calculated PBD gives excellent agreement with the experimental PBD data (Fig. 11.9b), suggesting that only anions are exchanged. However, in other aqueous media (e.g., $HClO_4$), a more complex mechanism is observed. On oxidation, a negative deflection (ion expulsion) prepeak is followed by a broad positive (ion insertion) deflection peak.

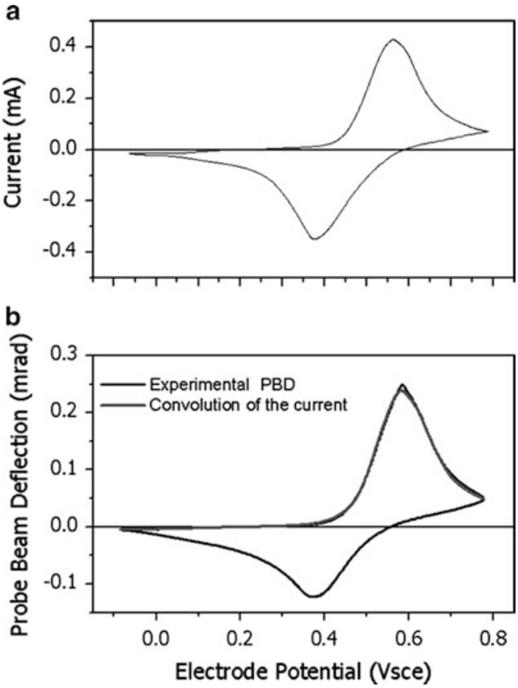

Fig. 11.9 Cyclic voltamperogram (**a**) and voltadeflectogram (**b**) of a poly(vinylferrocene) film on GC in 0.1 M $CH_3C_6H_4SO_3H/H_2O$. $v = 50$ mV s^{-1}. The points in (**b**) were calculated using the convolution technique, with $x_o = 58$ μm and $D_o = 2.8 \times 10^{-5}$ cm^2 s^{-1}

Therefore, the ion exchange mechanism seems to involve two steps:

$$\mathrm{PVF(H+)(A^-)} \xrightarrow{-x\mathrm{e}^-} \left(\mathrm{PVF}^{x+}\right)(\mathrm{A}^-)^x + x\mathrm{H}^+, \tag{11.14}$$

$$\left(\mathrm{PVF}^{x+}\right)(\mathrm{A}^-)_x + (1-x)\mathrm{A}^- \xrightarrow{-(1-x)\mathrm{e}^-} \mathrm{PVF}^+\mathrm{A}^-. \tag{11.15}$$

Moreover, if the same polymer is studied in HBF_4, only negative deflection (ion expulsion) is found during oxidation (Fig. 11.10). The results obtained in several different electrolytes are summarized in Table 11.1.

In Table 11.1, the values for the interaction coefficient between redox centers (ϕ) are also reported, obtained from the width of the voltammetric peak (FWHM). It can be seen that negative values of ϕ (repulsive interaction) correspond to anions exchange, while positive values of ϕ (attractive interaction) correspond to cation exchange. It seems that electrolyte is incorporated during the initial wetting of the polymer in the aqueous media. Then, the kind of ion exchanged is not related with the ion availability in the solution but with the interaction of anions with the positive charge inside the polymer. Therefore, the interaction between positive charges, shielded by the anions, is related with the kind of ion exchanged. PBD was also combined with electroacoustic EQCM to investigate redox coupled ion exchange in polyvinylferrocene (PVF) [33]. It was found that the effect of the anions on the polymer internal interactions also influences the viscoelasticity of the polymer films. It is also known that the first oxidation cycle (after waiting a certain

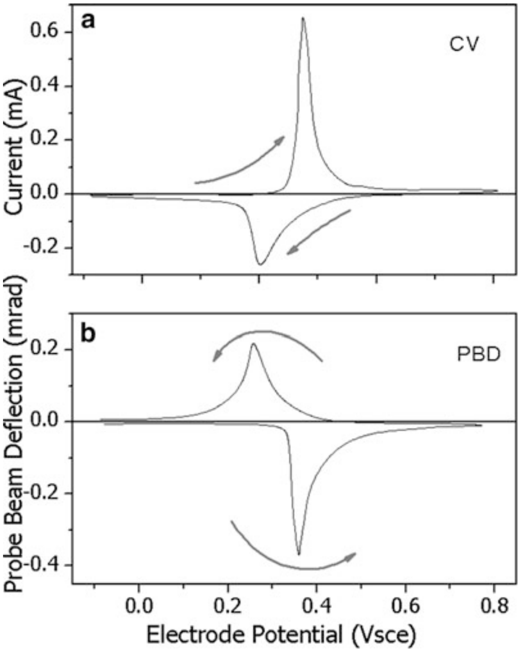

Fig. 11.10 Cyclic voltagram (**a**) and cyclic voltadeflectogram (**b**) of a poly(vinylferrocene) film, deposited on GC, in 0.1 M HBF_4/H_2O. Scan rate = 50 mV s^{-1}

Table 11.1 Effect of solution electrolyte on the ion exchange mechanism and redox center interactions

Counterion	Species exchanged	FWHM (V)	Interaction coefficient (ϕ/M^{-1})
$CH_3C_6H_4SO_3^-$	Anion	0.160	−0.25
ClO_4^-	Anion + Cation	0.150	−0.21
$CF_3SO_3^-$	Anion + Cation	0.100	−0.026
BF_4^-	Cation	0.080	0.046
PF_6^-	Cation	0.075	0.064

time in the reduced state) of PVF shows a voltammogram different from the ones observed during continuous cycling. The first cycle shows lower peak current and a more anodic peak potential than the following ones. This phenomenon has been called secondary "break-in" effect [34] or history effect [35]. The effect was tested using PBD. The deflection signal tracks the current (with opposite sign), and lower PBD signals are associated with lower currents. The potential of the PBD peak also shifts in the same direction as the current peak. Similar results were observed for all the acids studied, even when anions were the dominant ions exchanged.

Ladder Redox Polymers

PBD was used to study ion exchange of electroactive ladder polymers. Oyama et al. polymerize *o*-phenylenediamine to produce a ladder polymer with phenazine units [36]. Thin films of poly(*o*-phenylenediamine) were deposited by electropolymerization. The study of ion exchange using PBD [12] shows that only cations (protons) are exchanged during oxidation/reduction in acid media. The CVD results were confirmed by measurements of the diffusion coefficient of the exchanged ion (proton) using chronodeflectometry. It seems that the oxidation involves two one-electron redox steps with the same ion exchange.

Barbero et al. electropolymerize *o*-aminophenol to form an electroactive polymer with ladder structure of phenoxazine units [37]. The redox coupled ion exchange of poly(*o*-aminophenol) was studied using PBD [38]. The response is shown in Fig. 11.11. As it can be seen, the poly(*o*-aminophenol) film exchanges protons during the first oxidation step and anions during the second oxidation step. To ascertain the process, the PBD response was simulated using convolution of a two electrons/two ions surface process.

11.6.3.2 Conductive Polymers

Polypyrrole

Polypyrrole is an extensively studied conductive polymer. Since it remains electroactive at neutral pH, unlike polyaniline, it is ideally suited to be applied in biological environments [39]. PBD measurements allow to find a clear effect of the

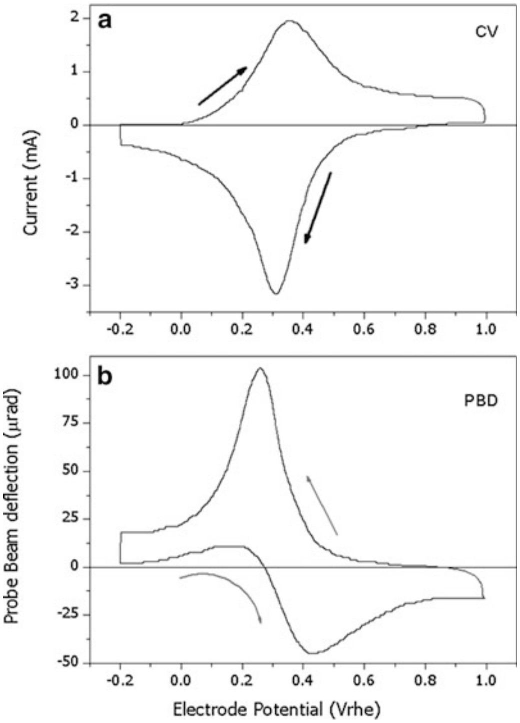

Fig. 11.11 Cyclic voltammogram (**a**) and voltadeflectogram (**b**) of a poly(*o*-aminophenol) film deposited onto GC. Solution = 1 M $HClO_4$. Scan rate = 50 mV s^{-1}. Beam-electrode distance = 65 μm

size of the anion on the ion exchange of polypyrrole (PPy) [40]. In presence of small anions (Cl^-), polymer oxidation is linked to positive deflection (ion insertion), according to the reaction

$$PPy^0 \xrightarrow{-e^- + Cl^-} (PPy^+)(Cl^-). \qquad (11.16)$$

If the solution only contains big anions, like toluenesulfonate, a negative deflection was found, according to the mechanism

$$PPy^0(TsO^-)(Na^+) \xrightarrow{-e^- - Na^+} (PPy^+)(TsO^-). \qquad (11.17)$$

A similar case occurs when dodecylsulfate is used as counterion. Further studies using PBD confirm the trend and identify the role of the co-ions (cations) in the exchange [41–43]. In phosphate buffer solutions, PPy prepared with dihydroxybenzene disulfonate anions also exchanges cations [44]. The controlled release of an anticancer drug (5-fluorouracil) from PPy films was also demonstrated using PBD [45]. Novak et al. [46] used PBD to study the ion exchange of PPy in different nonaqueous media. It was found that the kind of ion (cation or anion) exchanged depends on the solvent. While anions are mainly exchanged in ACN, cations are exchanged in PC.

11.6.3.3 Polythiophene

PBD was used to early used to study the formation of radical cations in poly(3-methylthiophene) [25]. While dominant anion exchange was observed, evidence of some contribution of cations was found. The technique was also used to study the deposition of poly(3-methylthiophene) [47] and poly(alkylterthiophenes) [48]. Correia et al. [49] investigated the electropolymerization of 3-methyltiophene using PBD and multiflux convolution data processing.

11.6.3.4 Polynaphthols

The electropolymerization of 1-naphthol in nonaqueous media produces an electroactive polymer with fused naphthalene and furane rings [50]. The ion exchange of the polymer, studied by PBD, reveals a strong effect of the cation size on the exchange. While anions are exchanged in presence of tetrabutylammonium perchlorate, cations are mainly exchanged in presence of $LiClO_4$. In the latter system, using CVD and chronodeflectometry, a clear kinetic effect is detected. At high scan rates (short times), anions are exchanged, while at slow scan rates (long times) cations are exchanged [51]. The same effect was detected by chronodeflectometry. During the oxidation pulse, a main negative peak (cation exchange) is preceded by a sharp positive peak (anion exchange) at short times. The results were confirmed by combination with in situ infrared spectroscopy (MIRFTIRS). The combined technique (PBD with MIRFTIRS) was also used to study ion exchange in poly(5-amino-1-naphthol) [52] and poly(5-amino-1,4-naphthoquinone) [53]. In the former case, a clear effect of the solvent on the ion exchange was observed. While protons are exchanged in aqueous solution, anions are exchanged in nonaqueous media (ACN) irrespective of the acid concentration in the electrolyte.

11.6.3.5 Polyaniline (PANI)

Polyaniline is one of the most widely studied conducting polymers. The ion exchange has been studied by a plethora of different techniques, including EQCM, ring-disk voltammetry, UV–vis spectroelectrochemistry, and radiotracer (see Chap. 14).

However, PBD studies were the first to provide direct in situ evidence of simultaneous proton-anion exchange in PANI [54]. The CVD and CV responses of a PANI film, in 1 M HCl, are shown in Fig. 11.12. During the first voltammetric oxidation peak, a negative deflection prepeak (proton expulsion) is observed first, followed by a positive deflection peak (anion insertion). In the potential range of the

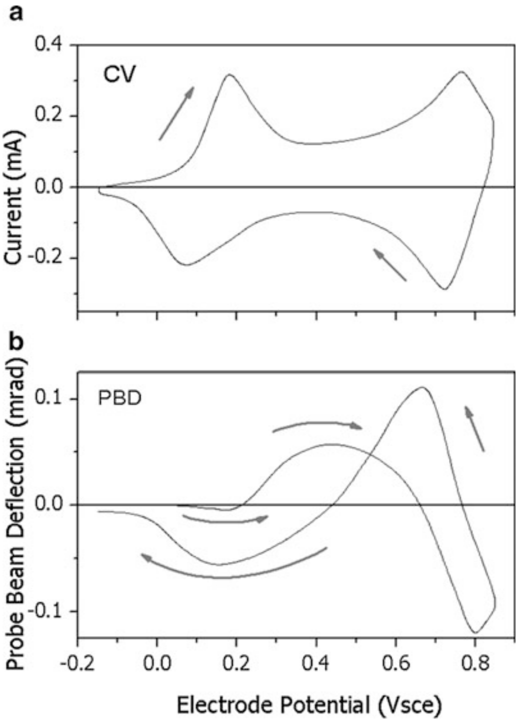

Fig. 11.12 Cyclic voltamperogram (**a**) and voltadeflectogram (**b**) of a polyaniline (PANI) film on GC in 1 M $HClO_4/H_2O$. $v = 50\ \mathrm{mV\ s^{-1}}$

second peak, a negative deflection peak (ion expulsion) is observed. In the reduction scan, the behavior is the opposite [55]. A possible scheme to explain the ion exchange is depicted in Scheme 11.2.

In acid media (e.g., pH = 1) the reduced state of PANI (leucoemeraldine) is partially protonated. The oxidation to emeraldine is accompanied initially by proton expulsion. When all the available protons are expelled, anions are inserted to maintain charge electroneutrality inside the film. If the proton concentration in the solution is increased, an increasing percentage of leucoemeraldine is protonated, and the negative deflection signal increases, while the positive signal decreases. The ratio

$$f_{\mathrm{PBD}} = \frac{\theta(-)}{(\theta(-) + \theta(+))} \tag{11.18}$$

is directly related to the amount of reduced PANI protonated. The plots of f_{PBD} as a function of proton concentration show profiles similar to titration curves. The inflection point of the curve (equivalent to a pK_a) depends on the nature of the acid used because the process implies the formation of a solid salt ($\mathrm{LE(H^+A^-)_x}$) and the stability of the salt depends of the anion properties.

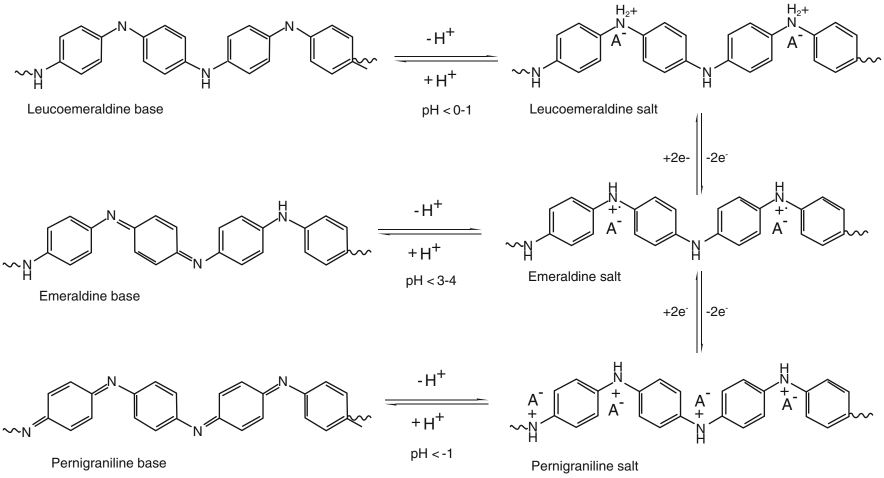

Scheme 11.2 Mechanism of redox coupled ion exchange in polyaniline

During the second oxidation process, the emeraldine salt state is converted into pernigraniline base or salt, depending on the pH. At pH 1, pernigraniline is deprotonated, and the oxidation process is accompanied by deprotonation with loss of protons and anions. This mechanism accounts for the observed ion expulsion. The addition of salt affects the ion exchange mechanism because it decreases the Donnan potential between the film and the solution [56].

In nonaqueous media, the polymer exchanges anions during both redox processes [57]. The ion exchange has been studied in other media using PBD [58, 59]. In all cases, PBD shows that protons are exchanged during the first oxidation process of PANI in acid media.

On the other hand, in a highly cited paper, Orata and Butry [60] were not able to detect a proton signal by electrochemical quartz crystal microbalance (EQCM). It was argued that protons are exchanged unsolvated by the film, and the low mass (1 g mol^{-1}) makes them difficult to be detected. Based on the PBD data, the experiments were looked at in specific conditions (high concentrations of acid) by EQCM, being able to detect the protons [61]. The results suggest that proton exchange is accompanied by a counterflux of solvent (water), effectively canceling the mass change at medium acid concentration (1 M).

If the polymer is prepared in presence of a polyelectrolyte, like poly(vinylsulfonate), the ion exchange is altered [62]. The polyelectrolyte, retained inside the polymer, compensates the positive charge on oxidation. Therefore, a dominant ion exchange of cations is observed. However, both the protonation equilibria of PANI and the polyelectrolyte have to be taken into account to explain the observed ion fluxes. Interestingly, the presence of the polyelectrolyte seems not to affect the exchange in nonaqueous solvents (PC, ACN) which remains dominated by anion exchange. A similar effect on the ion exchange mechanism is induced by retention of redox heteropolyacids (e.g., phosphotungstic acid), inside the polyaniline film [63].

11.6.3.6 Sulfonated Polyaniline

Another way to alter the ion exchange mechanism involves adding negative charges covalently linked to the polymer backbone. The incorporation of sulfonate groups, to produce sulfonated polyaniline, could be effected by electrophilic sulfonation of PANI [64], copolymerization of aniline with aminosulfonic acids [65], or nucleophilic addition [66]. In all cases, the ion exchange is altered. In aqueous media, both redox steps present negative deflection on oxidation. This suggests that both redox processes involve proton expulsion, being the negative charge compensated by the covalently linked anions. It is interesting to note that EQCM data show decreasing frequency (increasing mass) during oxidation. These results could indicate that anions are inserted during oxidation, in contrast to the PBD results. However, a more detailed study using different anions and cations shows that mass increase is independent on the mass of the anion and depends on a 10% on the mass of the cation present in the electrolyte. This effect suggests that anions are not involved, and only a 10% of cations (other than protons) are exchanged at $pH = 1$. The observed mass increase is likely to be due to a counterflux of solvent (water) occurring when the protons are expelled on oxidation [67]. PBD also reveals proton exchange during both redox processes in the copolymer of aniline with aminosulfonic acid. The results were confirmed using EQCM. In nonaqueous media, both redox processes in sulfonated polyaniline (SPAN) show a dominant cation flux. This is surprising since the sulfonating degree (50%) is lower than the 100% necessary to compensate for all the positive charge. It seems apparent that solution counterions (ClO_4^-) form ion pairs with sulfonate and lithium, being retained upon polymer reduction. The mechanism was confirmed by EQCM.

11.6.3.7 Poly(*N*-alkylanilines)

While incorporation of anionic groups should alter the ion exchange mechanism during the first oxidation process, alkylation of the amine nitrogen should block the deprotonation altering the second redox process. Indeed, poly(*N*-methylaniline), a polymer where each amino nitrogen is blocked, shows a CVD with a positive deflection during the second oxidation process, indicating that anions are inserted during the second oxidation process (11.20) when two anions and a proton are expelled in PANI [68] (see Scheme 11.2). The proposed mechanism

$$\mathrm{PNMANI} \xrightarrow{-e^- + A^-} \mathrm{PNMANI}^+(A^-) \tag{11.19}$$

$$\mathrm{PNMANI}^+(A^-) \xrightarrow{-e^- + A^-} \mathrm{PNMANI}^{++}(A^-)_2 \tag{11.20}$$

was confirmed by EQCM. The same effect is observed in poly(*N*-ethylaniline) (PNETANI). An interesting point is that unlike polyaniline, the voltammetric response of PNMANI and PNETANI is strongly affected by the anion present in the electrolyte [69], much alike PVF. However, in these polymers, the ion exchange mechanism is not affected by the anion present in the solution. It seems that the changes of the voltammetric response are related with the hydration energy of the anions and not with the interaction between positive charges, as it seems to be the case in PVF.

11.6.3.8 Other Polyanilines

Hillman and coworkers have studied the redox coupled ion exchange in poly (*o*-toluidine) (POT). Using the convolution method, they could separate the flux of anions and cations in the ion exchange. The study of POT using simultaneous measurement of PBD and EQCM [70] allows to detect hysteresis effects and to separate the solvent fluxes from ion exchange [71]. Besides, the temporal resolution of ion and solvent exchange was achieved in POT/$HClO_4$ films [72]. Thin films of an aniline copolymer poly(aniline-co-(2-aminobenzoic acid)), deposited from ammonia solution onto GC, show a voltammetric response similar to polyaniline [73]. Probe beam deflection measurements show mainly proton expulsion on oxidation up to pH 4 while PANI films exchange mainly anions at pH > 1 [74]. It seems that $–COO^-$ groups are present at low pH and compensate, like $–SO_3^-$ groups in sulfonated polyaniline, the charge in the emeraldine salt state. This is surprising since carboxylic acid groups has a pK_as in the range 3–4 (e.g., pK_a of benzoic acid 4.19 [75]). However, the electronic effect of the amino group could affect the pK_a since the *o*-aminobenzoic acid has a pK_a of 2.05 [76]. PBD was also used to ascertain the alteration of the ion exchange mechanism produced by modification reactions on polyaniline like nucleophilic addition of sulfite, electrophilic addition of SO_3, and the coupling of diazonium salts [77]. In all the cases, the incorporation of $–SO_3^-$ groups to the polyaniline chain favors cation exchange due to Donnan exclusion effect [78]. Yanez-Heras et al. studied the ion exchange of very thin layers of substituted polyanilines deposited onto thin layers of polyaniline using EQCM, PBD, and XPS [79]. Polyanilines functionalized with anionic groups retain electroactivity at neutral pH, unlike polyaniline or thicker layers of the same polymers.

11.6.4 Other Electroactive Polymers

PBD has also been used to study ion exchange in other conductive polymers, such as poly(phenylene) [80, 81].

Pham and coworkers electropolymerize juglone (5-hydroxynaphthoquinone) to form a conductive polymer which can be modified with oligonucleotides to determine DNA [82]. To understand the mechanism of detection, the ion exchange of polyjuglone should be ascertained. In Fig. 11.13, the current and deflection measured during electrochemical oxidation/reduction of a polyjuglone film on

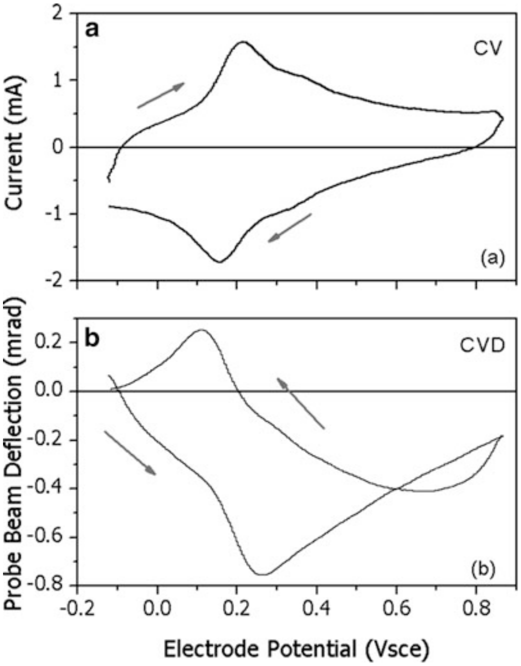

Fig. 11.13 Cyclic voltammogram (**a**) and voltadeflectogram (**b**) of a polyjuglone film (deposited on GC) in $HClO_4$ 1 M. Scan rate = 15 mV s^{-1}

GC are shown. As it can be seen, the positive current due to polyjuglone oxidation (Fig. 11.13a), a negative PBD, is detected (Fig. 11.13b). This result indicates that protons are expelled upon oxidation, as expected for the oxidation of hydroquinone (QH_2) to quinone (Q) groups.

11.7 Nanostructured Systems

11.7.1 Determination of the Potential of Zero Charge of Porous Carbon

As it was described before, the double layer charging of metal electrodes has been qualitatively studied using cyclic voltadeflectometry. A more quantitative evaluation of ion adsorption/desorption by cyclic voltadeflectometry is difficult due to the small signals involved. A way to overcome that involves the use of electrodes with high ratio of electrochemical active area to geometric area (high roughness). A simple way to obtain high roughness involves nanostructuring of the electrode [83]. An interesting kind of nanostructured systems is the high surface area carbon electrodes, commonly used in supercapacitors [84]. Using PBD could be possible to study the double layer charging/discharging processes in those materials.

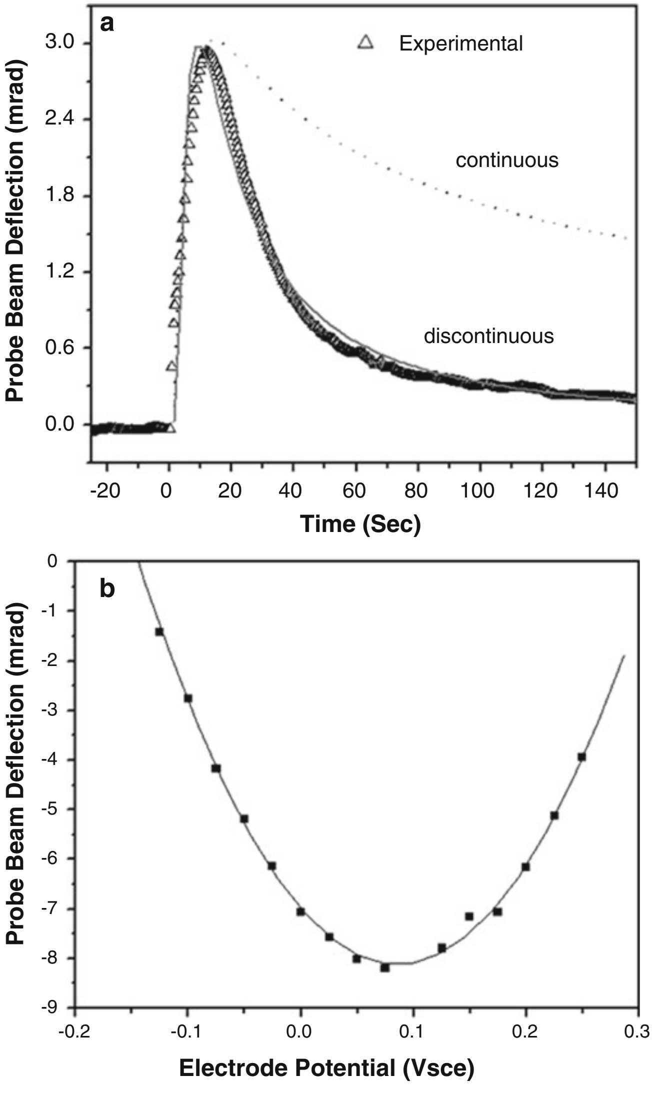

Fig. 11.14 (**a**) Chronodeflectometry of high surface area carbon (aerogel) electrodes in 0.1 M NaF/H_2O solution. $x = 350$ μm. Experimental data (*open triangles*) and simulation with Eq. (10.24) (*full line*). (**b**) Normal pulse voltadeflectometry of the same system

In Fig. 11.14a, the PBD signal obtained during charging the double layer of a carbon aerogel in NaF is shown. As it can be seen, the experimental profile could be fitted by the equation of a discontinuous process. Even that the electrochemical process takes time, by measuring at a distance far away from the minimum (300 μm), it is possible to shift the time of the maxima to bigger values (>10 s). In that way, the assumption of a negligible time span is fulfilled.

Since the system could be fitted with the chronodeflectometric profile, the normal pulse voltadeflectometry technique could be used to measure the relationship between the surface concentration of ions and the electrode potential. The *NPVD(E)* plot for an aerogel electrode in NaF solution is shown in Fig. 11.14b. A parabolic shape could be seen, with a minimum at the potential of minimum charge of the material [85]. This value agrees closely with the minima of the low frequency capacitance, measured by AC impedance spectroscopy, as expected for a simple double layer model. A similar agreement between PBD and capacitance data is observed in a nonaqueous electrolyte ($LiClO_4$/ACN). It is noteworthy that this is a direct measurement of the potential of minimum charge of a solid material, which could only be inferred by other methods.

11.7.2 Determination of pzc of Nanostructured Pt

Typical chronodeflectometric responses, obtained using Pt nanoparticles (NPtC) in 1 M H_2SO_4 [86], are shown in Fig. 11.15. As it can be seen, the sign of the CD signal changes when the potential is stepped around 0.2 V_{RHE}. A similar behavior is observed when CD measurements were performed at MP-Pt electrodes. The

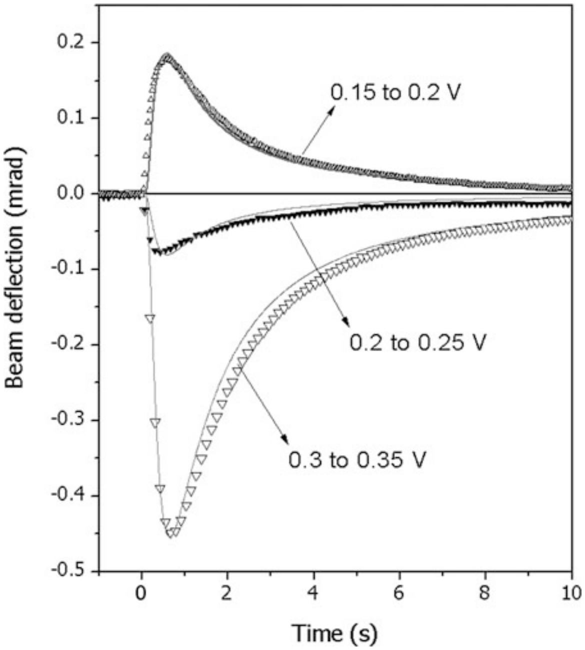

Fig. 11.15 Chronodeflectometric profiles measured while stepping the electrode potential between the values described in the figures. Electrolyte = 1 M H_2SO_4. NPtC electrode. The *gray lines* show the profiles simulated using Eq. (10.24) and the appropriate parameters

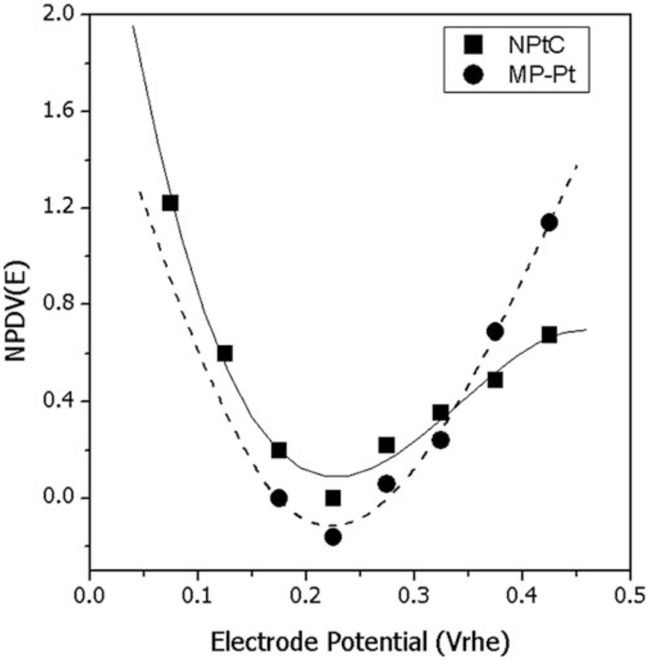

Fig. 11.16 Dependence of NPDV(E), calculated from CD profiles as depicted in Fig. 11.15, for MP-Pt (*circles*, *dashed line*) and NPtC (*squares*, *full line*). All points were measured in 1 M H_2SO_4

chronodeflectometric profiles were simulated using Eq. (10.24) (Chap. 10). The general parameters used in the simulation are $D = 2.6 \times 10^{-5}$ cm^2 s^{-1} (sulfuric acid binary electrolyte [87]) and dn/dC = 0.011 (Table 10.1). The concentration of active sites (C_s) used was $C_s = 1.62 \times 10^{-3}$ mol cm^{-2} and $x = 96$ µm. The good fitting indicates that the double layer charging occurs in a negligible time compared with the CD measurement.

The integral variation between an initial potential and different final potentials is estimated (Fig. 11.16). In that way, the PBD signal will be proportional to the amount of ion exchanged from the initial potential to the final potential. If the potentials are stepped inside the double layer region, the ions exchanged will correspond to the changes in the ion population inside the double layer. At potentials more negative than the potential of zero charge (*pzc*), the amount of cations will decrease when the potential is stepped in the positive direction, while at potentials positive to the pzc, the amount of anions will increase for the same potential step. At the *pzc*, the curve should show a minimum [88]. As it can be seen, while they have some differences, the profiles obtained in both electrodes reveal a minimum value of ca. 0.22 ± 0.05 V_{RHE}. This value corresponds to the potential of zero charge of Pt in the media, and it agrees reasonably with the value reported in the literature, for flat polycrystalline electrodes, of 0.20 V_{RHE} [89].

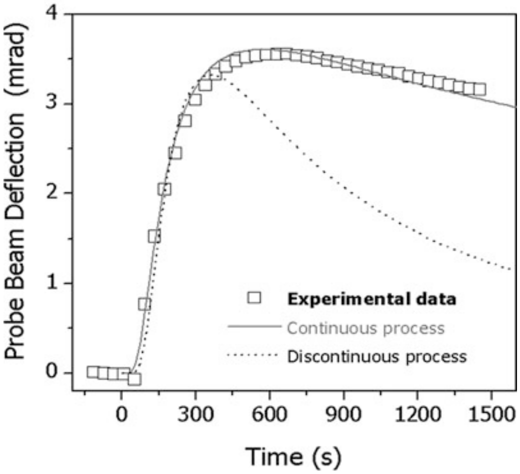

Fig. 11.17 Chronodeflectometry of high monolithic porous carbon electrodes in 1 M H_2SO_4. Beam-electrode distance = 300 μm

11.7.3 Double Layer Charging of Monolithic Nanoporous Carbon

Using the measurement setup developed with carbon aerogels, the chronodeflectometric response of mesoporous carbon monoliths was evaluated. These materials are obtained by template-controlled pore formation in resorcinol–formaldehyde resins [90].

A similar behavior is observed in the case of carbon aerogels. However, instead of a discontinuous process, a continuous process of ion insertion to the carbon materials is observed (Fig. 11.17).

It seems that charge insertion in the porous electrode double layer, related to ion adsorption, is controlled by ion diffusion inside the pores. This result is confirmed by a Cottrell analysis of the chronoamperometric data (see below). As it can be seen, diffusion control of the ion transport is observed. It has to be taken into account that mesogels are monolithic materials with thickness in excess of 500 μm. On the contrary, the carbon aerogels used previously are supported by fibers, and the effective thickness of the porous layer is less than 20 μm.

11.7.4 Hierarchical Porous Carbon Structures

The comparative study of carbon aerogels and mesoporous monolithic carbon using PBD suggests that in the latter, the pore length is large and the ions take a long time (>1,500 s) to enter the monolith. However, the materials have different origin, and other properties could be responsible of the different behavior. To overcome that

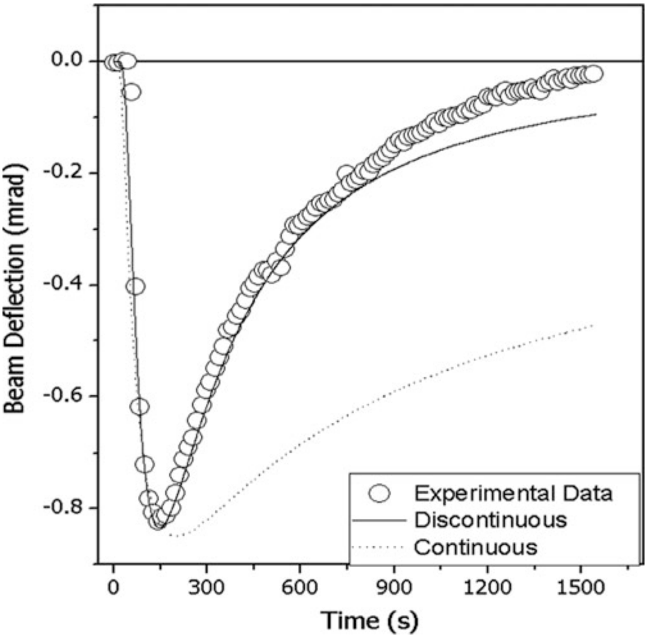

Fig. 11.18 Chronodeflectometric response of a composite mesoporous carbon in aqueous media (0.5 M KNO_3). The potential of the electrode is switched between 0.3 and 0.25 V_{SCE}

limitation, a carbon material bearing mesopores, and macropores should be made. This has been made by impregnation of a cellulosic fiber cloth with RF resin and carbonization of the ensemble [91]. The chronodeflectometric response of the carbon material (Fig. 11.18) shows data in agreement with the simulation for a discontinuous process while it differs clearly from the simulation of a continuous process. Therefore, in less than 100 s, the electrode double layer is charged.

The charging/discharging process of the monolithic porous carbon is controlled by the diffusion of ions inside the carbon. Therefore, it should obey Cottrell equation [92]. A comparison of the Cottrell plots (extracted from the chronoamperometric measurements) of a monolithic and a hierarchical porous carbon shows that the plot obtained in monolithic carbon obeys the equation up to 1,000 s, while the one measured in hierarchical carbon departs after ca. 400 s. The mass transport model proposed is confirmed, and a way to fabricate electrodes for fast supercapacitors is devised.

11.7.5 CO Oxidation on Nanostructured Pt Electrodes

To produce noble metal electrodes with large surface areas, there are two ways (1) fabricate metal monoliths with large porosity and (2) synthesize metal nanoparticles supported on conductive solids. CO adsorption on platinum family metal electrodes is a subject of great importance for the application of such materials in fuel cell electrodes.

11.7.5.1 CVD of CO_{ads} Oxidation Using Mesoporous or Nanoparticulated Pt

PBD has been applied to study the oxidation of adsorbed CO in saturated CO perchloric acid solution at a polycrystalline Pt electrode. Gas production (by oxidation of CO to CO_2) should involve a positive beam deflection as $dn/dC < 0$ for gases and $dn/dC < 0$. However, an unexpected negative value of *PBD* was observed during oxidation of CO_{ad} to CO_2 [93]. We investigated the electrochemical system using a mesoporous Pt electrode (Fig. 11.19). The large electrochemical roughness of the electrode assures a good signal/noise ratio. The reaction for the electrooxidation of adsorbed CO can be written as

$$\mathrm{Pt-CO+Pt-(OH)+H_2O \xrightarrow{-e^-} CO_2+H_3O^+ + 2Pt.} \tag{11.21}$$

In the reaction, only CO_2 and H_3O^+ could be detected by PBD since surface species (e.g., Pt-OH) does not change the refractive index of the solution, and the

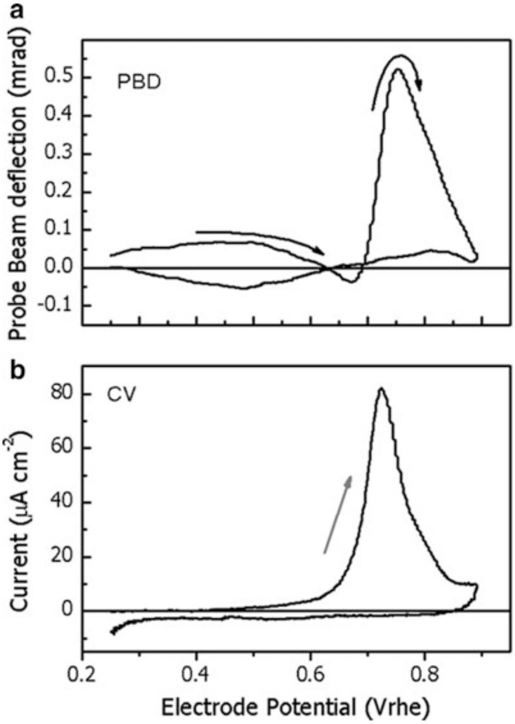

Fig. 11.19 Cyclic voltammogram (**a**) and voltadeflectogram (**b**) for CO_{ads} oxidation in 1 M H_2SO_4 at MP-Pt. $v = 15\ \mathrm{mV\ s^{-1}}$

large value of water self-diffusion coefficient makes the corresponding profiles negligible at the experimental values of beam-electrode distances. Fig. 11.19b shows the corresponding signal for the probe beam deflection during CO stripping. In the positive potential scan, at $E > 0.50\ \mathrm{V_{RHE}}$, the deflection decreases, indicating that reaction (6) takes place. Subsequently, a sharp change in the deflection occurs at $0.67\ \mathrm{V_{RHE}}$, increasing PBD up to a maximum at $0.75\ \mathrm{V_{RHE}}$ for MP-Pt.

In this potential region, all reactions coexist, but the production of CO_2 in the last one seems to determine the net sign of the PBD. This could be due to the fact that $\mathrm{d}n/\mathrm{d}C$ for CO_2 is negative and larger (Table 10.1) than $\mathrm{d}n/\mathrm{d}C$ for H_3O^+. Note that the peak potential in PBD is shifted due to the time delay between the surface reaction and the detection at the laser at several (50–100 μm) away.

11.7.5.2 Dynamic Effects in CO_{ads} Oxidation on Mesoporous Pt Electrodes

Previous studies on the electrochemical oxidation of CO adsorbed on MP-Pt electrodes using chronoamperometry have shown that the oxidation follows a profile typical of a nucleation and growth process [94].

The characteristic curve describes broad current maxima after the initial current spike has decayed. Such feature is clearly seen during the oxidation of CO previously adsorbed on MP-Pt (Fig. 11.20). Since PBD is a technique nearly as fast as electrochemistry, in contrast with other techniques like in situ FTIR, such dynamic effects can be easily studied. As it is displayed in Fig. 11.20a, the nucleation step, denoted by a sharp current spike, is correlated with a small negative deflection peak (Fig. 11.20b). The broad current feature is related to a broad positive deflection peak. It has been proposed that the negative deflection is related with the proton expulsion due to Pt oxide formation while the positive deflection peak corresponds to CO_2 formation (solute concentration increases with negative $\mathrm{d}n/\mathrm{d}C$) due to CO_{ad} oxidation. Therefore, it is likely that the fast oxide formation occurs with nucleation in specific catalytic sites while the CO_{ad} oxidation happens through reaction (11.21), reducing the oxide. Its electrochemical regeneration is responsible for the slow "growth" process. The results give direct evidence in support to the early proposition by McCallum and Pletcher [95] that CO oxidation rate is determined by the rate of nucleation and growth of oxide islands in the CO monolayer at a polycrystalline platinum electrode.

The small prepeak could also be due to a time delay between different fluxes, as it has been shown before in other systems [96, 97]. To clarify this point, the chronodeflectometric signal in Fig. 11.19 was simulated (Fig. 11.21) taking into account the contributions due to CO_2 and H_3O^+, which are produced during CO_{ad} oxidation in reaction (11.21). For this simulation, CD profiles plot are calculated as the addition of two PBD signals, where each PBD profile obeys Eq. (10.24), with the parameters of each mobile species. As CO_2 is uncharged, no migration effects have to be considered, and the electrolyte remains binary. The diffusion coefficient of proton used is that of the binary electrolyte ($2.6 \times 10^{-5}\ \mathrm{cm^2\ s^{-1}}$) [87], while the

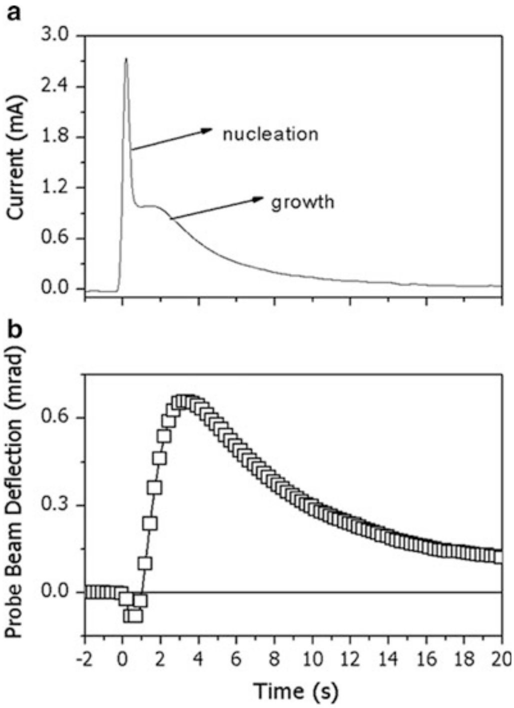

Fig. 11.20 Chronoamperometric (**a**) and chronodeflectometric (**b**) profiles of an MP-Pt electrode with fully covered with adsorbed CO. The potential is stepped from the equilibrium adsorption potential of CO (0.25 V_{RHE}) to the oxidation to 0.80 V_{RHE} where all CO is oxidized to CO_2. Electrolyte: 1 M H_2SO_4

diffusion coefficient of CO_2 is 2.2×10^{-5} cm^2 s^{-1} [98]. The beam-electrode distance is 176 μm, the d*n*/d*C* of H_3O^+/HSO_4^- is 0.011, and of CO_2 is 0.014 (Table 10.1). A good fitting of the whole curve is obtained assuming a multiflux (see Chap. 10). Therefore, the fluxes observed are only slightly dominated by the CO_2 flux, and the CD technique is able to separate the contribution. It is noteworthy that the plot contains features which only can be explained by multiflux. First of all, the prepeak (see insert in Fig. 11.21) can only be explained by a multiflux. Additionally, if the beam-electrode distance is calculated from the maxima in the PBD signal using Eq. (10.24), a value of 226 μm is obtained, which is away from the true value of 176 μm. Finally, the magnitude is almost half the one expected for a flux of only one species. Therefore, the CD profile contains data which unambiguously lead to the reaction mechanism.

It is clear that CD measurements reveal a more clear picture of the actual dynamics of the ion exchange processes than CVD.

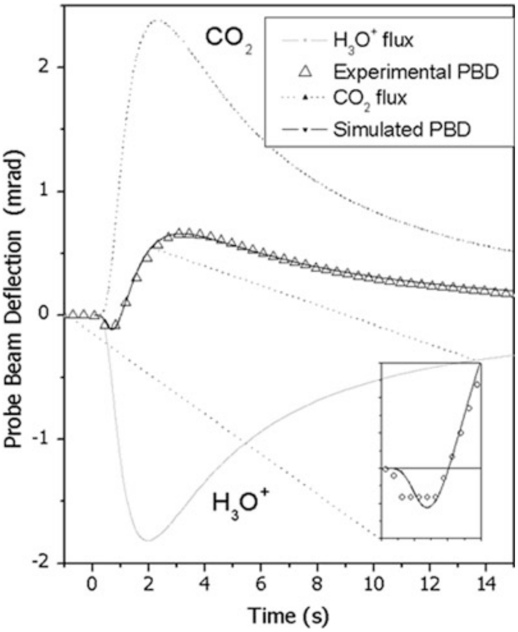

Fig. 11.21 Comparison of the experimental (*open triangles*) chronodeflectometric profiles depicted in Fig. 11.20, together with the simulation of fluxes due to H^+ and CO_2. The *gray full line* corresponds to the contribution of H_3O^+, while the *black dotted line* corresponds to the contribution of CO_2. The *full black line* describes the overall flux. In the *inset*, the region of the prepeak is expanded

11.7.6 Layer-by-Layer Self-Assembled Monolayers

Another nanostructured system studied by PBD is the layer-by-layer (LBL) self-assembled multilayers containing redox species. Such multilayers are built by sequential adsorption of oppositely charged polyelectrolytes onto a solid surface [99]. In the case of redox active multilayers [100], the charge of the constituent polyelectrolytes can be altered by oxidation–reduction of redox centers after film buildup. This may result in changes of ion or salt population within the multilayer (*extrinsic* charge compensation) [101]. To maintain the electroneutrality inside the film, anion or cation ingress or release from the film or a combination of both ion fluxes should occur. However, the fraction of redox charge compensated by either ion cannot be determined in electrochemical experiments alone since only the total charge exchanged with the electrolyte can be monitored.

Chronodeflectometry was therefore used to evaluate the ion exchange of a $(PAH–Os)_x(PSS)_y$ multilayer (Fig. 11.22). The solid lines in Fig. 11.22 correspond to the best fit of the sum of two ion pulses (anion and proton) shifted in time (dotted and gray lines). The time difference between processes could be due to the different diffusion coefficient for the ions, inside the film, or other kinetic constraints. In Fig. 11.22, it could also be seen that the simulation fits well the

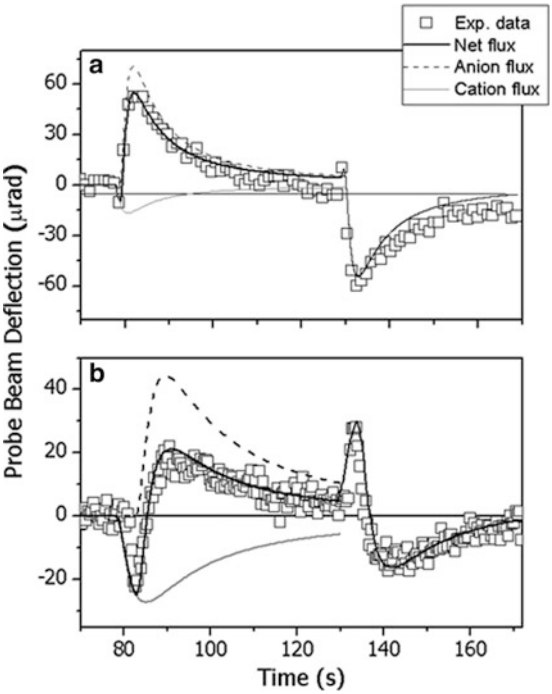

Fig. 11.22 Chronodeflectometric data taken during the oxidation/reduction of PAH–Os(II) in 0.01 M HCl: experimental data (*square*), best fit for individual anion and cation fluxes (*dashed line*) and total ion flux (*full line*). (**a**) $(PAH–Os)_{15}(PSS)_{14}$ (positive outer layer) and (**b**) $(PAH–Os)_{15}(PSS)_{15}$ (negative outer layer). The potential is stepped between 0.15 and 0.60 V_{SCE}

profile of both oxidation and reduction pulses. The PBD profiles strongly depend on whether the multilayer is capped by PAH–Os (positive) or PSS (negative). It seems that the films capped by negative layers show a bigger relative contribution of cation exchange. These results could be due to an adsorption of opposite charges ions on the film surface or internal effects. The results show clearly that PBD could render valuable information on the ion exchange of self-assembled multilayers containing redox centers. It is noteworthy that there are few techniques to monitor ion exchange which are fast enough to detect this kind of kinetic effects.

References

1. Rudnicki JD, McLarnon FR, Cairns EJ (1991) In situ characterization of electrode processes by photothermal deflection spectroscopy. In: Varma R, Selman JR (eds) Techniques for characterization of electrodes and electrochemical processes. Plenum, New York
2. Kertész V, Inzelt G, Barbero C, Kötz R, Haas O (1995) Probe beam deflection studies of electrochemical oscillations during galvanostatic oxidation of formic acid at a platinum electrode. J Electroanal Chem 392:91–95. doi:10.1016/0022-0728(95)04085-3

3. Kötz R, Barbero C, Haas O (1993) Probe beam deflection for the analysis of ion fluxes at the solid/liquid interface. Ber Bunsenges Physik Chemie 97:427–430. doi:10.1002/bbpc.19930970332
4. Barbero C, Silber JJ, Sereno L (1988) Studies of surface-modified glassy carbon electrodes obtained by electrochemical treatment: its effect on Ru(bpy)2 + 3 adsorption and the electron transfer rates of the Fe2+/Fe3+ couple. J Electroanal Chem 248:321–340. doi:10.1016/0022-0728(88)85093-9
5. Sullivan MG, Schnyder B, Bärtsch M, Alliata D, Barbero C, Imhof R, Kötz R (2000) Electrochemically modified glassy carbon for capacitor electrodes characterization of thick anodic layers by cyclic voltammetry, differential electrochemical mass spectrometry, spectroscopic ellipsometry, X-ray photoelectron spectroscopy, FTIR, and AFM. J Electrochem Soc 147:2636–2643. doi:10.1149/1.1393582
6. Levi MD, Levi E, Gofer Y, Aurbach D, Vieil E, Serose J (1999) Dilute graphite − sulfates intercalation stages studied by simultaneous application of cyclic voltammetry, probe-beam deflection, in situ resistometry, and X-ray diffraction techniques. J Phys Chem B 103:1499–1508. doi:10.1021/jp9832443
7. Liu CW, Cheng SJ, Cheng GJ, Sun DY (1996) Probe beam deflection combined with cyclic voltammetry studies of C60-modified electrode film. J Electrochem Soc 143:3787–3880. doi:10.1149/1.1837310
8. Bidoia ED, McLarnon FR, Cairns EJ (2000) Investigation of anion adsorption on platinum electrodes in aqueous media by probe beam deflection. J Electroanal Chem 482:75–80. doi:10.1016/S0022-0728(00)00003-6
9. Garcia G, Bruno MM, Planes GA, Rodriguez JL, Barbero CA, Pastor E (2008) Phys Chem Chem Phys 10:6677–6685. doi:10.1039/B806938G
10. Iwasita T, Nart FC (1990) Bulk effects in external reflection IR spectroscopy: the interpretation of adsorption data for ionic species. J Electroanal Chem 295:215–224. doi:10.1016/0022-0728(90)85017-Y
11. Koetz R, Barbero C, Haas O (1990) Probe beam deflection investigation of the charge storage reaction in anodic iridium and tungsten oxide films. J Electroanal Chem 296:37–49. doi:10.1016/0022-0728(90)87231-8
12. Plichon V, Petit MA (1994) Mirage detection for electrochemical materials characterization. Application of iridium oxide films. J de Physique 4(C7):429–432
13. Barbero C, Miras MC, Koetz R, Haas O (1993) Probe beam deflection: a useful tool for the study of ion transport in polymers. Solid State Ionics 60:167–172. doi:10.1016/0167-2738(93)90292-B
14. Petit MA, Plichon V (1994) Electrochemical study of iridium oxide layers in anhydrous propylene carbonate by cyclic voltammetry and ‘mirage effect’ analysis. J Electroanal Chem 379:165–172. doi:10.1016/0022-0728(94)87135-3
15. Barbero C, Planes GA, Miras MC (2001) Redox coupled ion exchange in cobalt oxide films. Electrochem Commun 3:113–116. doi:10.1016/S1388-2481(01)00107-2
16. Rosolen JM, Decker F, Fracastoro-Decker M, Gorenstein A, Torresi RM, Cordoba de Torresi SI (1993) A mirage effect analysis of the electrochemical processes in nickel hydroxide electrodes. J Electroanal Chem 354:273–279. doi:10.1016/0022-0728(93)80339-J
17. French HM, Henderson MJ, Hillman AR, Vieil E (2001) Ion and solvent transfer discrimination at a nickel hydroxide film exposed to LiOH by combined electrochemical quartz crystal microbalance (EQCM) and probe beam deflection (PBD) techniques. J Electroanal Chem 500:192–207. doi:10.1016/S0022-0728(00)00373-9
18. Nam K-W, Kim K-B (2002) A study of the preparation of NiOx electrode via electrochemical route for supercapacitor applications and their charge storage mechanism. J Electrochem Soc 149:A346–A354. doi:10.1149/1.1449951
19. Barbu A, Plichon V (1997) Voltammetry of thermally prepared ruthenium oxide films and flux detection at the electrolyte interface. Electrochim Acta 42:489–492. doi:10.1016/S0013-4686(96)00240-X

20. Plichon V, Besbes S (1990) Mirage detection of counter-ion flux between Prussian Blue films and electrolyte solutions. J Electroanal Chem 284:141–153. doi:10.1016/0022-0728(90)87068-U
21. Liu CW, Wang Y, Zhu GY, Dong SJ (1997) Study of cupric hexacyanoferrate-modified platinum electrodes using probe beam deflection and electrochemical quartz crystal microbalance techniques. Electrochim Acta 42:1795–1800. doi:10.1016/S0013-4686(96)00379-9
22. Csahók E, Vieil E, Inzelt G (1999) Optical beam deflection study of indium-hexacyanoferrate films. Synth Met 103:2687–2688. doi:10.1016/S0379-6779(98)01321-6
23. Csahok E, Vieil E, Inzelt G (1998) Probe beam deflection study of the transport of ions during the redox reaction of indium-hexacyanoferrate films. J Electroanal Chem 457:251–255. doi:10.1016/S0022-0728(98)00290-3
24. Plichon V, Even E, Benier G (1991) Detection by the mirage effect of the flux of counter-ions between lutetium diphthalocyanine films and the electrolyte solution. J Electroanal Chem 305:195–204. doi:10.1016/0022-0728(91)85518-T
25. Haas O (1989) Probe beam deflection spectroscopy as a tool for mechanistic investigations of modified electrodes. Faraday Discuss Chem Soc 88:123–131. doi:10.1039/DC9898800123
26. Haas O, Rudnicki J, McLarnon FR, Cairns EJ (1991) Mechanistic investigations of redox polymer-coated electrodes using probe-beam deflection and cyclic voltammetry. J Chem Soc Faraday Trans 87:939–945. doi:10.1039/FT9918700939
27. Merle A, Maurin MJP (1989) In situ investigation of the doping and doping of poly methylthiophene by electromirage effect. J Chem Phys 86:173–179
28. Barbero C, Miras MC, Kötz R, Haas O (1999) Study of the structure and redox behaviour of poly (1-hydroxyphenazine). Synth Met 101:23. doi:10.1016/S0379-6779(98)00978-3
29. Miras MC, Barbero C, Koetz R, Haas O, Schmidt VM (1992) Quartz crystal microbalance and probe beam deflection studies of poly(1-hydroxyphenazine) modified electrodes. J Electroanal Chem 338:279–297. doi:10.1016/0022-0728(92)80429-8
30. Smyrl WH, Lien M (1991) Electrical and electrochemical properties of electronically conducting polymers. In: Scrosati B (ed) Applications of conducting polymers. Prentice Hall, New York
31. Barbero C, Calvo EJ, Miras MC, Koetz R, Haas O (2002) A probe beam deflection study of ion exchange at poly(vinylferrocene) films in aqueous and nonaqueous electrolytes. Langmuir 18:2756–2764. doi:10.1021/la010999j
32. Vieil E (1994) Mass transfer and convolution. Part 1. Theory. J Electroanal Chem 364:9–15. doi:10.1016/0022-0728(93)02925-8
33. Barbero C, Calvo EJ, Etchenique R, Morales GM, Otero M (2000) An EQCM electroacoustic study of poly(vinylferrocene) modified electrodes in different aqueous electrolytes. Electrochim Acta 45:3895–3906. doi:10.1016/S0013-4686(00)00452-7
34. Hillman AR, Hughes NA, Bruckenstein SJ (1992) Solvation phenomena in polyvinylferrocene films: effect of history and redox state. J Electrochem Soc 139:74–77. doi:10.1149/1.2069204
35. Inzelt G, Bacskai J (1992) Electrochemical quartz crystal microbalance study of the swelling of poly(vinylferrocene) films. Electrochim Acta 37:647–654. doi:10.1016/0013-4686(92)80067-V
36. Chiba K, Ohsaka T, Ohnuki Y, Oyama N (1987) Electrochemical preparation of a ladder polymer containing phenazine rings. J Electroanal Chem 219:117–124. doi:10.1016/0022-0728(87)85034-9
37. Barbero C, Silber JJ, Sereno L (1989) Formation of a novel electroactive film by electropolymerization of ortho-aminophenol: study of its chemical structure and formation mechanism. Electropolymerization of analogous compounds. J Electroanal Chem 263:333–352. doi:10.1016/0022-0728(89)85103-4
38. Salavagione HJ, Arias-Pardilla J, Pérez JM, Vázquez JL, Morallón E, Miras MC, Barbero C (2005) Study of redox mechanism of poly(o-Aminophenol) using in situ techniques: evidence

of two redox processes. J Electroanal Chem 576:139–145. doi:10.1016/J.JELECHEM.2004.10.013

39. Ateh DD, Navsaria HA, Vadgama P (2006) Polypyrrole-based conducting polymers and interactions with biological tissues. J R Soc Interface 22:741–752. doi:10.1098/rsif.2006.0141
40. Schmidt VM, Barbero C, Koetz R (1993) The ion exchange in polypyrrole in aqueous electrolytes. A probe beam deflection study of the effect of fixed negative charges. J Electroanal Chem 352:301–307. doi:10.1016/0022-0728(93)80272-J
41. Lopez C, Mendes Viegas MF, Bidan G, Vieil E (1994) Comparison of ion exchange properties of polypyrrole with and without immobilized dopants by optical beam deflection. Synth Met 63:73–78. doi:10.1016/0379-6779(94)90252-6
42. Matencio T, De Paoli MA, Peres RCD, Torresi RM, Cordoba de Torresi SI (1995) Ionic exchanges in dodecylbenzenesulfonate doped polypyrrole Part 1. Optical beam deflection studies. Synth Met 71:59–64. doi:10.1016/0379-6779(94)02320-X
43. Bidan G, Lopez C, Mendes-Viegas F, Vieil E, Gadelle A (1995) Incorporation of sulphonated cyclodextrins into polypyrrole: an approach for the electro-controlled delivering of neutral drugs. Biosens Bioelectron 10:219–229. doi:10.1016/0956-5663(95)96808-C
44. Petit MA, Plichon V, Colin C (2000) A CV/PBD coupled study of ionic exchanges at poly (pyrrole) films in phosphate buffered solutions. Electrochim Acta 45:1953–1961. doi:10.1016/S0013-4686(99)00419-3
45. Huang H, Liu C, Liu B, Cheng G, Dong S (1998) Probe beam deflection study on electrochemically controlled release of 5-fluorouracil. Electrochim Acta 43:999–1004. doi:10.1016/S0013-4686(97)00280-6
46. Novak P, Koetz R, Haas O (1993) The ion exchange mechanism of polypyrrole in propylene carbonate and dimethylsulfite based electrolyte. J Electrochem Soc 140:37–40. doi:10.1149/1.2056105
47. Abrantes LN, Correia JP (1999) On the initiation and growth of polymer films onto electrode surfaces. Electrochim Acta 44:1901–1910. doi:10.1016/S0013-4686(98)00299-0 DOI:dx.doi.org
48. Dini D, Decker F, Zotti G (1999) Study of polyalkylterthiophenes deposition. Synth Met 101:22. doi:10.1016/S0379-6779(98)00819-4
49. Correia JP, Vieil E, Abrantes LM (2004) Electropolymerization of 3-methylthiophene studied by multiflux convolution. J Electroanal Chem 573:299–306. doi:10.1016/j.jelechem.2004.06.036
50. Pham MC, Moslih J, Lacaze PC (1990) New conducting films by electrochemical oxidation of 1-naphthol: in-situ MIRFTIRS study of the electropolymerization mechanism. J Electroanal Chem 278:415–423. doi:10.1016/0022-0728(90)85154-W
51. Pham MC, Moslih J, Barbero C, Haas O (1991) Influence of the cation size on the charge compensation process in poly(1-naphthol) coated electrodes: multiple internal reflection FTIR spectroscopy (MIRFTIRS) and probe beam deflection (PBD) study. J Electroanal Chem 316:143–149. doi:10.1016/0022-0728(91)87042-3
52. Barbero C, Haas O, Mostefai M, Pham MC (1995) Ion exchange in poly(5-amino-1-naphthol) probe beam deflection and multiple internal reflection Fourier transform infrared spectroscopic studies. J Electrochem Soc 142:1829–1834. doi:10.1149/1.2044201
53. Piro B, Bazzaoui EA, Pham MC, Novak P, Haas O (1999) Multiple internal reflection FTIR spectroscopic (MIRFTIRS) study of the redox process of poly(5-amino-1,4-naphthoquinone) film in aqueous and organic media. Electrochim Acta 44:1953–1961. doi:10.1016/S0013-4686(98)00304-1
54. Barbero C, Miras MC, Haas O, Kötz R (1991) Direct in situ evidence for proton/anion exchange in polyaniline films by means of probe beam deflection. J Electrochem Soc 138:669–672. doi:10.1149/1.2085655

55. Barbero C, Miras MC, Haas O, Kötz R (1993) Comparative study of the ion exchange and electrochemical properties of sulfonated polyaniline (SPAN) and polyaniline (PANI). Synth Met 55–57:1539–1544. doi:10.1016/0379-6779(93)90281-Z
56. Barbero C, Koetz R, Kalaji M, Nyholm L, Peter LM (1993) Ion exchange and memory effects in polyaniline. Synth Met 55–57:1545–1551. doi:10.1016/0379-6779(93)90282-2
57. Barbero C, Miras MC, Kötz R (1997) Sulphonated polyaniline (SPAN) films as cation insertion electrodes battery applications Part II: Exchange of mobile species in aqueous and non-aqueous solutions. J Electroanal Chem 437:191–198. doi:10.1016/S0022-0728(97)00357-4
58. Matencio T, Vieil E (1991) Optical beam deflection study of ionic movements during the charge transfer of polyaniline and poly(alkylanilines) in NH4F:HF medium. Synth Metals 44:349–356. doi:10.1016/0379-6779(91)91822-R DOI:dx.doi.org
59. Koziel K, Lapkowski M, Vieil E (1997) Microgravimetric and laser beam deflection studies of redox reactions in polyaniline at various concentrations of doping anions. Synth Met 84:91–92. doi:10.1016/S0379-6779(96)03851-9
60. Orata D, Buttry DA (1987) Determination of ion populations and solvent content as functions of redox state and pH in polyaniline. J Am Chem Soc 109:3574–3581. doi:10.1021/ja00246a013
61. Miras MC, Barbero C, Kötz R, Haas O (1994) Electrochemical quartz crystal microbalance investigation of the ion exchange mechanism in the first oxidation step of polyaniline in HClO4. J Electroanal Chem 369:193–197. doi:10.1016/0022-0728(94)87098-5
62. Barbero C, Miras MC, Koetz R, Haas O (1997) Electrochemical and ion exchange properties of polyaniline-poly(vinylsulfonate) composites in aqueous and nonaqueous media. J Electrochem Soc 144:4170–4174. doi:10.1149/1.1838161
63. Jones VW, Kalaji M, Walker G, Barbero C, Kötz R (1994) Influence of immobilising anions on the redox switching of polyaniline. J Chem Soc Faraday Trans 90:2061–2064. doi:10.1039/FT9949002061
64. Barbero C, Miras MC, Schnyder B, Haas O, Kötz R (1994) Sulfonated polyaniline films as cation insertion electrodes for battery applications. Part 1. Structural and electrochemical characterization. J Mater Chem 4:1775–1783. doi:10.1039/JM9940401775
65. Barbero C, Koetz R (1994) Electrochemical formation of a self-doped conductive polymer in absence of a supporting electrolyte. The copolymerization of o-aminobenzenesulfonic acid and aniline. Adv Mater 6:577–580. doi:10.1002/adma.19940060711
66. Salavagione H, Morales GM, Miras MC, Barbero C (1999) Synthesis of a self-doped polyaniline by nucleophilic addition. Acta Polym 50:40–44. doi:10.1002/(SICI)1521-4044(19990101)50:1
67. Mello Q, Torresi RM, Cordoba de Torresi SI, Ticianelli EA (2000) Ellipsometric, electrogravimetric, and spectroelectrochemical studies of the redox process of sulfonated polyaniline. Langmuir 16:7835–7841. doi:10.1021/la000391v
68. Barbero C, Miras MC, Koetz R, Haas O (1991) Alteration of the ion exchange mechanism of an electroactive polymer by manipulation of the active site: probe beam deflection and quartz crystal microbalance study of poly(aniline) and poly(N-methylaniline). J Electroanal Chem 310:437–443
69. Planes GA, Miras MC, Barbero C (2002) Strong effect of counterions nature on the electrochemistry of poly(N-methylaniline). Polym Int 51:429–433. doi:10.1002/pi.830
70. Henderson MJ, Hillman AR, Vieil E, Lopez C (1998) Combined electrochemical quartz crystal microbalance (EQCM) and probe beam deflection (PBD): validation of the technique by a study of silver ion mass transport. J Electroanal Chem 458:241–247. doi:10.1016/S0022-0728(98)00358-1
71. Henderson MJ, Hillman AR, Vieil E (1999) Ion and solvent transfer discrimination at a poly(o-toluidine) film exposed to $HClO_4$ by combined electrochemical quartz crystal microbalance (EQCM) and probe beam deflection (PBD). J Phys Chem B 103:8899–8907. doi:10.1021/jp9910845

72. Henderson MJ, Hillman AR, Vieil E (2000) Chronoamperometric resolution of ion and solvent transfers at a poly(o-toluidine) modified electrode by combined electrochemical quartz crystal microbalance (EQCM) and probe beam deflection (PBD). Electrochim Acta 45:3885–3894. doi:10.1016/S0013-4686(00)00453-9
73. Salavagione HJ, Acevedo DF, Miras MC, Motheo AJ, Barbero CA (2004) Comparative study of 2-amino and 3-aminobenzoic acid copolymerization with aniline synthesis and copolymer properties. J Polym Sci A Polym Chem 42:5587–5599. doi:10.1002/pola.20409
74. Salavagione HJ, Acevedo DF, Miras MC, Barbero C (2003) Redox coupled ion exchange in copolymers of aniline with aminobenzoic acids. Port Electrochim Acta 21:245–254
75. Hollingsworth CA, Seybold PG, Hadad CM (2002) Structure and pKa of benzoic acid. Int J Quantum Chem 90:1396–1403. doi:10.1002/qua.10362
76. Purich DL, Allison RD (1999) Handbook of biochemical kinetics. Academic, New York
77. Barbero C, Salavagione HJ, Acevedo DF, Grumelli DE, Garay F, Planes GA, Morales GM, Miras MC (2004) Novel synthetic methods to produce functionalized conducting polymers I. Polyanilines. Electrochim Acta 49:3671–3686. doi:10.1016/j.electacta.2003.11.035
78. Mafé S, Manzanares JA, Reiss H (1993) Donnan phenomena in membranes with charge due to ion adsorption. Effects of the interaction between adsorbed charged groups. J Chem Phys 98:2325–2332. doi:10.1063/1.464214
79. Yánez-Heras J, Planes GA, Williams F, Barbero CA, Battaglini F (2010) Sequential electrochemical polymerization of aniline and their derivatives showing electrochemical activity at neutral pH. Electroanalysis 22:2801–2808. doi:10.1002/elan.201000325
80. Vieil E, Meerholz K, Matencio T, Heinze J (1994) Mass transfer and convolution: Part II. In situ optical beam deflection study of ionic exchanges between polyphenylene films and a 1:1 electrolyte. J Electroanal Chem 368:183–191. doi:10.1016/0022-0728(93)03110-B
81. El Rhazi M, Lopez C, Deslouis C, Musiani MM, Tribollet B, Vieil E (1996) Ionic transport in poly(N-ethylcarbazole) films, investigated by quartz crystal microbalance and mirage effect techniques. Synth Met 78:59–66. doi:10.1016/0379-6779(95)03568-0
82. Piro B, Haccoun J, Pham MC, Tran LD, Rubin A, Perrot H, Gabrielli C (2005) Study of the DNA hybridization transduction behavior of a quinone-containing electroactive polymer by cyclic voltammetry and electrochemical impedance spectroscopy. J Electroanal Chem 577:155–165. doi:10.1016/j.jelechem.2004.12.002
83. Bruno MM, Cotella NG, Miras MC, Barbero CA (2010) A novel way to maintain resorcinol-formaldehyde porosity during drying: stabilization of the sol-gel nanostructure using a cationic polyelectrolyte. Colloids Surf A Physicochem Eng Asp 362:28–32. doi:10.1016/j.colsurfa.2010.03.032
84. Conway BE (1999) Electrochemical supercapacitors. Scientific fundamentals and technological applications. Kluwer Academic, New York
85. Planes GA, Miras MC, Barbero C (2002) Double layer properties of carbon aerogel electrodes measured by probe beam deflection and AC impedance techniques. In: Advanced batteries and supercapacitors, PV-2001. The Electrochemical Society, Pennigton
86. García G, Bruno MM, Planes GA, Rodriguez JL, Barbero CA, Pastor E (2008) Probe beam deflection studies of nanostructured catalyst materials for fuel cells. Phys Chem Chem Phys 10:6677–6685. doi:10.1039/B806938G
87. Nzikou JM, Baklouti M, Vincent LM, Lapicque F (1997) Improvement in the measurement of diffusion coefficients in a restricted diffusion cell: case of binary electrolytes. Chem Eng Process 36:161–165. doi:10.1016/S0255-2701(96)04180-3
88. Planes GA, Miras MC, Barbero CA (2005) Double layer properties of carbon aerogel electrodes measured by probe beam deflection and AC impedance techniques. Chem Commun 2146–2148. doi:10.1039/B419448A
89. Chen QS, Solla-Gullón J, Sun SG, Feliu JM (2010) The potential of zero total charge of Pt nanoparticles and polycrystalline electrodes with different surface structure: the role of anion adsorption in fundamental electrocatalysis. Electrochim Acta 55:7982–7994. doi:10.1016/j.electacta.2010.03.050

90. Bruno MM, Cotella NG, Miras MC, Koch T, Seidler S, Barbero C (2010) Characterization of monolithic porous carbon prepared from resorcinol/formaldehyde gels with cationic surfactant. Colloids Surf A Physicochem Eng Asp 358:13–20. doi:10.1016/j.colsurfa.2010.01.017
91. Bruno MM, Cotella NG, Miras MC, Barbero CA (2005) Porous carbon–carbon composite replicated from a natural fibre. Chem Commun 5896–5898. doi:10.1039/B511771B
92. Southampton Electrochemistry Group (2001) Instrumental methods in electrochemistry. Woodhead, Chichester
93. Shi P, Fromondi J, Shi Q, Wang Z, Scherson DA (2007) Simultaneous in situ reflectance and probe beam deflection measurements at solid electrode − aqueous electrolyte interfaces. Anal Chem 79:202–207. doi:10.1021/ac061452i
94. Jiang J, Kucernak A (2002) Electrooxidation of small organic molecules on mesoporous precious metal catalysts I: CO and methanol on platinum. J Electroanal Chem 533:153–165. doi:10.1016/S0022-0728(02)01083-5
95. McCallum C, Pletcher D (1976) An investigation of the mechanism of the oxidation of carbon monoxide adsorbed onto a smooth Pt electrode in aqueous acid. J Electroanal Chem 70:277–290. doi:10.1016/S0022-0728(76)80196-9
96. Grumelli DE, Wolosiuk A, Forzani E, Planes GA, Barbero C, Calvo EJ (2003) Probe beam deflection study of ion exchange in self-assembled redox polyelectrolyte thin films. Chem Commun 3014–3015. doi:10.1039/B308449C
97. Grumelli DE, Forzani ES, Morales GM, Miras MC, Barbero CA, Calvo EJ (2004) Microgravimetric study of electrochemically controlled nucleophilic addition of sulfite to polyaniline. Langmuir 20:2349–2355. doi:10.1021/la0354990
98. Tamimi A, Rinker ER, Sandall OR (1994) Diffusion coefficients for hydrogen sulfide, carbon dioxide, and nitrous oxide in water over the temperature range 293–368 K. J Chem Eng Data 330–332. doi:10.1021/je00014a031
99. Decher G (1997) Fuzzy nanoassemblies: toward layered polymeric multicomposites. Science 277:1232–1237. doi:10.1126/science.277.5330.1232
100. Laurent D, Schlenoff JB (1997) Multilayer assemblies of redox polyelectrolytes. Langmuir 13:1552–1557. doi:10.1021/la960959t
101. Schlenoff JB, Ly H, Li M (1998) Charge and mass balance in polyelectrolyte multilayers. J Am Chem Soc 120:7626–7634. doi:10.1021/ja980350+

Chapter 12
Application of Probe Beam Deflection to Solution Electrochemical Systems

12.1 Introduction

The interpretation of probe beam deflection (PBD) data obtained in electrochemical systems containing soluble redox species (eq. 12.1) is difficult since the concentration of both O_{sol} and R_{sol} changes during the experiment.

$$O_{sol} + ne^- \rightarrow R_{sol} \tag{12.1}$$

Therefore, it is not possible to relate the overall refractive index change, measured by PBD, with the concentration gradients. Additionally, the charge of the redox species involved in the reaction is altered and the charge has to be compensated by transport of ions of the supporting electrolyte. Therefore, the concentration of two more mobile species could be changed, with a related refractive index change. The problems in data interpretation have made the application of PBD to solution electrochemical systems much limited.

12.2 Ferricyanide $\left[\mathrm{Fe(CN)_6}\right]^{3-}$ Reduction

As it has been discussed before, the study of redox systems in solutions is difficult due to inherent complexity of the concentration profiles. However, soluble redox systems have been used to test the techniques. The chronodeflectometry presents a positive peak with a small prepeak. The response seems to be due to the sum of the ferrocyanide and ferricyanide PBD profiles [1]. Being the dn/dC higher for ferrocyanide than for ferricyanide (Table 10.1), the first dominates the overall PBD signal. The prepeak is caused by the difference of diffusion coefficients for $\left[\mathrm{Fe(CN)_6}\right]^{3-}$ ($D = 9.4\ 10^{-6}\ \mathrm{cm^2\ s^{-1}}$) and $\left[\mathrm{Fe(CN)_6}\right]^{4-}$ ($D = 7.4\ 10^{-6}\ \mathrm{cm^2\ s^{-1}}$). The minor contributor to the PBD signal is faster and dominates at

G.G. Láng and C.A. Barbero, *Laser Techniques for the Study of Electrode Processes*,
Monographs in Electrochemistry, DOI 10.1007/978-3-642-27651-4_12,

short times. The cyclodeflectometric signal observed during oxidation of ferrocyanide shows a positive peak with a potential shift (due to the time delay) with respect to the peak in voltamperometry [2]. Garay and Barbero use the system to test the effect of supporting electrolyte on PBD data and to validate a finite difference simulation of chonodeflectometry [3] and cyclic voltadeflectometry [4].

Figure 12.1 shows the current (Fig. 12.1a) and probe deflection signal (Fig. 12.1b) response measured during ferricyanide electrochemical reduction. The PBD signal is negative during reduction, like the current. This seems reasonable since the concentration of ferrocyanide increases at the electrode surface, rendering a negative deflection. However, unlike the case of surface-confined couples (Chap. 11), in this case, the ferricyanide concentration decreases at the same time [4]. If the d*n*/d*C* of ferricyanide and ferrocyanide would be the same, the PBD signal will be null. Therefore, the PBD signal is negative because the effect of ferrocyanide concentration gradient dominates refractive index gradient due to its larger d*n*/d*C*.

12.3 Ferric Ion (Fe^{3+}) Reduction

To test the assumption that PBD signal of soluble couples depends strongly on the relative values (of O_{sol} and R_{red}) of d*n*/d*C*, a cyclovoltadeflectogram was measured with Fe^{3+}/Fe^{2+}.

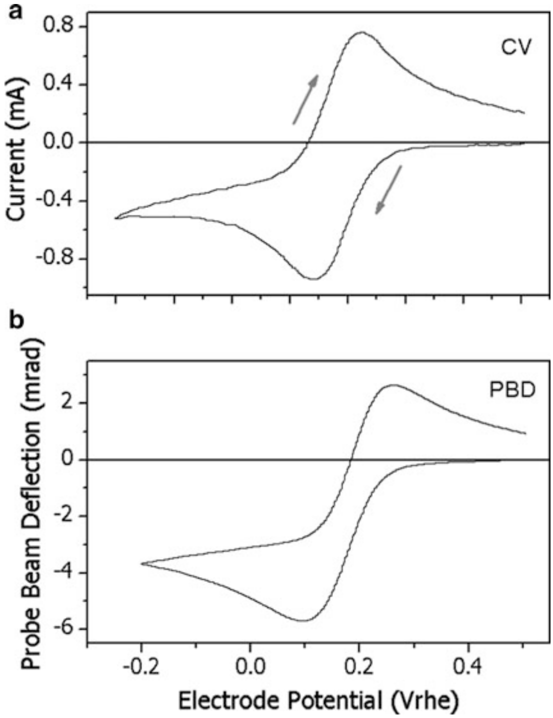

Fig. 12.1 Cyclic voltammogram (**a**) and cyclic voltadeflectograms (**b**) obtained with a gold film planar electrode in a solution of $K_3Fe(CN)_6$ (1.3 mM in KCl 0.1 M), $E_{ini} = E_2 = 0.5$ V, $E_1 = -0.2$ V, scan rate = 6 mVs^{-1}. The CVD profile was measured at a beam-electrode distance of 68 μm

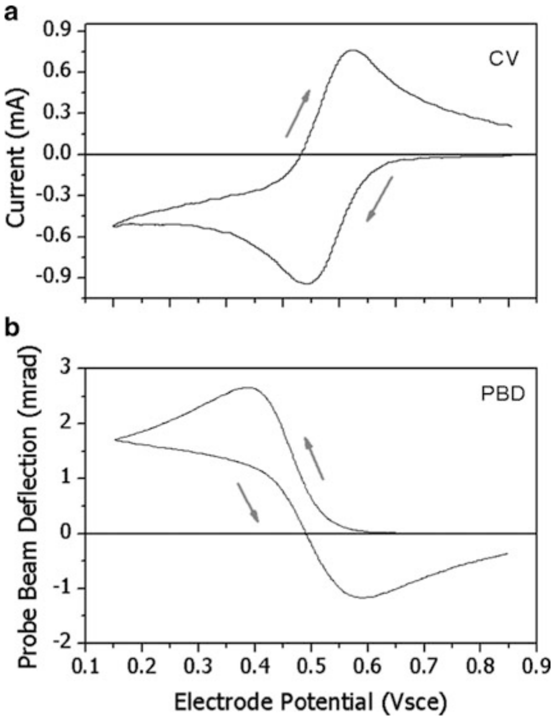

Fig. 12.2 Cyclic voltammogram (**a**) and voltadeflectogram (**b**) obtained with gold film electrode in a solution of Fe $(NO_3)_3$ (0.7 mM in HCl 0.1 M). $E_{\mathrm{ini}} = 0.85\ \mathrm{V_{RHE}}$, $E_2 = 0.15\ \mathrm{V_{RHE}}$. Scan rate = 3 mV s^{-1}. Beam-electrode distance, 85 μm

The redox couple has a $\mathrm{d}n/\mathrm{d}C_\mathrm{O}$ ($FeCl_3 = 0.04114$) > $\mathrm{d}n/\mathrm{d}C_\mathrm{R}$ ($FeCl_2 = 0.03125$) (Table 10.1). Figure 12.2 shows the cyclic voltammogram (Fig. 12.2a) and voltadeflectogram (Fig. 12.2b) measured during the electrochemical reduction of Fe^3 on a gold electrode. As seen in the figure, a negative current (reduction) corresponds to a positive deflection due to the fact that the decrease of Fe^3 concentration dominates the refractive index gradient.

12.4 Oxygen Reduction

A more interesting system is the reduction of oxygen. The reduction of oxygen on Au in basic media (0.1 M KOH) was studied by PBD [5]. In the voltammetric curve, two waves are observed corresponding to

$$O_2 + H_2O \xrightarrow{+2e^-} HO_2{}^- + OH^-, \tag{12.2}$$

$$HO_2{}^- + H_2O \xrightarrow{+2e^-} 3OH^-. \tag{12.3}$$

The deflection would depend on the concentration gradients of O_2, HO_2^-, and OH^-. In the experimental data, a single wave at ca. +0.4 V_{RHE} is observed. Taking into account the d*n*/d*C* values [$KOH = 0.0097$, $H_2O_2 = 0.0014$, and $O_2 = -0.014$ (Table 10.1)], it is apparent that the latter will dominate the signal. Then only O_2 reduction is observed. As it can be seen, the study of soluble species is of complex interpretation.

12.5 Oxidation of Small Organic Molecules

While oscillatory phenomena are quite complex in their own, PBD could be used to evaluate the role of solution species in the oscillations. One case of electrochemical oscillatory phenomena is the galvanostatic oxidation of organic molecules [6]. The system was studied using PBD [7]. A clear correlation of the potential oscillations with deflection oscillations was observed, suggesting a role of solution species in the oscillations. To clarify the issue, the oxidation of formic acid is studied using PBD. During the oxidation ($E > 0.45\ V_{SCE}$), a positive deflection is observed. Such flux could be assigned to CO_2 generation (CO_2, as a gas, has a negative d*n*/d*C*). It seems that the electrode initially becomes poisoned, then the potential increases, and the poison is oxidized, allowing the potential to decrease. During the oxidation of the poison, CO_2 is not produced, as the PBD decreases.

12.6 Metal Deposition and Corrosion

Cairns and coworkers studied the oxidation of Cu in basic media using PBD and photothermal deflection spectroscopy (PDS) [8, 9]. Eriksson studied the concentration profiles during Cu and Ag deposition [10, 11]. PBD has also been used to study electroless deposition of nickel [12]. Brolo and Sharma studied the dissolution of Ag in a chloride-containing solution [13]. Quantitative analysis using convolution allows elucidating the corrosion mechanism. A similar study using bromide solution shows the formation of AgBr anodic film [14].

12.7 Silicon Corrosion

Decker and coworkers studied the electrochemical dissolution and passivation of Si in alkaline media [15]. The PBD technique was combined with the measurement of the bending of the electrode (beam bending method, BBM), discussed in Part 1 of this monograph. The PBD technique permits a monitoring of dissolution and passivation (oxide formation) processes. It also provides an estimate of the oxide etch times during the open circuit (no electrochemical control) corrosion process.

Then, the same group studies the dissolution of Si in HF solution [16]. In this case, the current oscillates due to the passivation of the surface followed by dissolution of the passive oxide layer. The PBD signal follows closely the current signal, indicating that both formation of oxide (production of protons) and its dissolution (consumption of protons) are related to the oscillations.

12.8 Thiophene Polymerization

Vieil and coworkers studied the 3-methylthiophene oxidation and polymerization using PBD [17]. To separate the contribution of the different species, they data process the experimental data using diffusional convolution. [18]

References

1. Rudnicki JD, McLarnon FR, Cairns EJ (1991) In situ characterization of electrode processes by photothermal deflection spectroscopy. In: Varma R, Selman JR (eds) Techniques for characterization of electrodes and electrochemical processes. Plenum, New York, 1991
2. Barbero C, Miras MC, Kötz R (1992) Electrochemical mass transport studied by probe beam deflection: potential step experiments. Electrochim Acta 37:429–43. doi:10.1016/0013-4686(92)87032-U
3. Garay F, Barbero CA (2006) Charge neutralization process of mobile species at any distance from the electrode/solution interface. 1. Theory and simulation of concentration and concentration gradients developed during potentiostatic conditions. Anal Chem 78:6733–9. doi:10.1021/ac0603678
4. Garay F, Iglesias RI, Barbero CA (2008) Charge neutralization process of mobile species developed during potentiodynamic conditions. Part 2: Simulation and fit of probe beam deflection experiments. J Electroanal Chem 624:211–7. doi:10.1016/j.jelechem.2008.09.009
5. Kötz R, Barbero C, Haas O (1993) Probe beam deflection for the analysis of ion fluxes at the solid/liquid interface. Ber Bunsenges Phys Chem 97:427–30. doi:10.1002/bbpc.19930970332
6. Inzelt G, Kertesz V, Lang G (1993) Simultaneous oscillations of the surface mass and potential in the course of the galvanostatic oxidation of 2-propanol. J Phys Chem 97:6104–6. doi:10.1021/j100125a002
7. Kertész V, Inzelt G, Barbero C, Kötz R, Haas O (1995) Probe beam deflection studies of electrochemical oscillations during galvanostatic oxidation of formic acid at a platinum electrode. J Electroanal Chem 392:91–5. doi:10.1016/0022-0728(95)04085-3
8. Russo RE, McLarnon FR, Spear JD, Cairns EJ (1987) Probe beam deflection for in situ measurements of concentration and spectroscopic behavior during copper oxidation and reduction. J Electrochem Soc 134:2783–7. doi:10.1149/1.2100287
9. Brisard GM, Rudnicki JD, McLarnon FR, Cairns EJ (1995) Application of probe beam deflection to study the electrooxidation of copper in alkaline media. Electrochim Acta 40:859–65. doi:10.1016/0013-4686(94)00360-D
10. Eriksson R (1996) A study of the PBD-technique using the copper refining cell as a model system. Electrochim Acta 41:871–87. doi:10.1016/0013-4686(95)00384-3
11. Eriksson R (1995) Experimental determinations of concentration fields in the copper and silver refining systems using probe-beam deflection. Electrochim Acta 40:725–73. doi:10.1016/0013-4686(94)00334-W

12. Abrantes LM, Oliveira MC, Vieil E (1996) A probe beam deflection study of the hypophosphite oxidation on a nickel electrode. Electrochim Acta 41:1515–24. doi:10.1016/0013-4686(95)00403-3
13. Brolo AG, Sharma SD (2003) Using probe beam deflection (PBD) to investigate the electrochemical oxidation of silver in perchlorate media in the presence and absence of chloride ions. Electrochim Acta 48:1375–84. doi:10.1016/S0013-4686(03)00003-3
14. Brolo AG, Yang Y (2004) Investigating mechanisms of anodic film formation by electrochemical probe beam deflection (EPBD). Electrochim Acta 49:339–47. doi:10.1016/j.electacta.2003.08.016
15. Cattarin S, Pantano E, Decker F (1999) Investigation by electrochemical and deflectometric techniques of silicon dissolution and passivation in alkali. Electrochem Commun 1:483–7. doi:10.1016/S1388-2481(99)00102-2
16. Dini D, Cattarin S, Decker F (1998) Probe beam deflection study of p-Si electrodissolution in acidic fluoride medium in the oscillating regimes. J Electroanal Chem 446:7–11. doi:10.1016/S0022-0728(97)00630-X
17. Correia JP, Vieil E, Abrantes LM (2004) Electropolymerization of 3-methylthiophene studied by multiflux convolution. J Electroanal Chem 573:299–306. doi:10.1016/j.jelechem.2004.06.036
18. Vieil E (1994) Mass transfer and convolution. Part 1. Theory. J Electroanal Chem 364:9–15. doi:10.1016/0022-0728(93)02925-8

Chapter 13
In Situ Electrochemical Photothermal Deflection Techniques

13.1 Basic Principles

The basis of an in situ photothermal deflection spectroscopy (PDS) is the generation of temperature gradients by nonradiative decay of the energy of the light absorbed on the species under study. In electrochemical systems, the species could be the electrode surface, a film over it, or a substance in solution which changes during the electrochemical experiment. Additionally, in the case of semiconductors, the light could penetrate some distance under the surface of the interface electrode/solution. On the other hand, if part of the light absorbed is reemitted (e.g., fluorescence process), this amount of light will not be present in the photothermal signal. In that way, the fluorescence quantum yield of the material can be calculated. Indeed, photothermal beam deflection spectroscopy can be used to measure in absolute way the extinction coefficient (α) of solids transparent to the probe beam (e.g., inorganic [1, 2] and organic semiconductors [3]). Therefore, it is useful in photoelectrochemistry [4]. Figure 13.1 shows a scheme of the geometry of the PBDS measurement. The setup is called transversal since pump and probe beam are set in 90° angle. The pump beam travels through the measurement fluid and illuminates the sample, which can be situated over a substrate. The energy of the absorbed light is converted into heat. Heat is transported from the illuminated region to the other parts of the experimental system. Part of the heat originates a temperature gradient in the electrolyte solution, in front of the electrode. A probe beam travels parallel to the electrode surface and suffers a deviation θ due to the refractive index gradient, associated with the temperature gradient. The interaction zone between the pump and probe beam has a length L, defined by the size of the pump beam. The heat associated with light absorption can flow to the fluid or to the sample substrate. To increase the signal/noise ratio, the substrate should have low conductivity. This is quite difficult in electrochemistry because electrical conductivity is usually accompanied by thermal conductivity. On the other hand, if thin films of conductive materials are used, most of the heat will transfer to the solution.

G.G. Láng and C.A. Barbero, *Laser Techniques for the Study of Electrode Processes*,
Monographs in Electrochemistry, DOI 10.1007/978-3-642-27651-4_13,

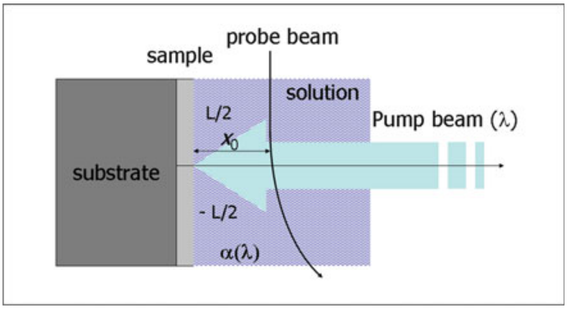

Fig. 13.1 Geometry of the photothermal deflection spectroscopy experiment

The sample is set onto a substrate and receives a pump beam of wavelength λ. The probe beam enters the solution at a beam-electrode distance (x) and is deflected by the thermal gradient. The sample, of width L, has an extinction coefficient [$\alpha(\lambda)$].

The deflection equation is

$$\theta(x,t) = \left(\frac{L}{n}\frac{\mathrm{d}n}{\mathrm{d}T}\right)\left(\frac{\partial T(x,t)}{\partial x}\right). \tag{13.1}$$

The refractive index gradient is related to the temperature gradient.

The photothermal experiment can be analyzed using the heat transport theory. The power dissipated as heat will be

$$P(t) = I(t)(1-\eta)\varepsilon(\lambda)C_{\mathrm{abs}}, \tag{13.2}$$

where $I(t)$ is the intensity of the incident light, η is the quantum yield of emission, $\varepsilon(\lambda)$ is the absorptivity coefficient, and C_{abs} is the concentration of the absorbing species.

Assuming that the heat quantity P is all transferred to the electrolyte ($x > 0$), the heat transfer will obey the equation:

$$\frac{\partial^2 T}{\partial x^2} = \frac{1}{\kappa_{\mathrm{f}}}\frac{\mathrm{d}T}{\mathrm{d}t}, \tag{13.3}$$

where κ_{f} is the thermal diffusion coefficient in the fluid [5].

The boundary conditions are

$$T(x,0) = T_{\mathrm{f}} \quad \text{for all } x \tag{13.4}$$

and

$$\lim_{x\to\infty} T(x,t) = T_{\mathrm{f}} \quad \text{for all } t, \tag{13.5}$$

where T_{f} is the temperature in the bulk of the fluid.

The other boundary condition implies that all the heat flow into the fluid:

$$\kappa_{\mathrm{f}} \left.\frac{\mathrm{d}T}{\mathrm{d}x}\right|_{x=0} = \pm \frac{P(t)}{\rho_{\mathrm{f}} C p_{\mathrm{f}}}, \tag{13.6}$$

where κ_{f}, ρ_{f}, and Cp_{f} are the thermal diffusivity, density, and heat capacity of the fluid.

The light can be modulated in different ways. The most common are continuous (applying a light intensity step at $t = 0$), periodic modulation (mechanically chopping or electronically modulating the pump beam), and short pulse (flash or pulsed laser light). In the following, we describe the equations that define the profile of deflection signal as a function of time (continuous or pulsed excitation). In that way, we can discuss the effect of experimental parameters on the signal. Then, we made the same discussion for periodic excitation, where the signal depends on the excitation frequency.

13.2 Photothermal Deflection Techniques

13.2.1 Continuous Excitation

In the case that a pump beam illuminates the electrode continuously, it is assumed that $I(t) = 0$ for $t < 0$ and $I(t) =$ constant for $t > 0$. Applying this boundary condition in Eqs. (13.3)–(13.7), we obtain

$$T(x,t) = \left(\frac{P_0}{\kappa_{\mathrm{f}} \rho_{\mathrm{f}} C p_{\mathrm{f}}}\right) \left[2\sqrt{\frac{\kappa_{\mathrm{f}} t}{\pi}} \mathrm{e}^{x^2/\kappa_{\mathrm{f}} t} - x \operatorname{erfc}\left(\frac{x}{\sqrt{4\kappa_{\mathrm{f}} t}}\right)\right]. \tag{13.7}$$

Differentiation with respect to x gives the temperature gradient; combining with Eq. (13.1) renders the deflection profile:

$$\theta(x,t) = \left(\frac{L}{n} \frac{\mathrm{d}n}{\mathrm{d}T}\right) \left(\frac{P_0}{\kappa_{\mathrm{f}} \rho_{\mathrm{f}} C p_{\mathrm{f}}}\right) \left[\operatorname{erfc}\left(\frac{x}{\sqrt{4\kappa_{\mathrm{f}} t}}\right)\right]. \tag{13.8}$$

The profiles are shown in Fig. 13.2. As it can be seen, the intensity of the deflection increases when the beam is closer to the electrode.

13.2.2 Pulsed Excitation

Pulsed excitation is easily achieved either by using a flash lamp or a pulsed laser. Nowadays, it is also possible to modulate the light intensity by electrically

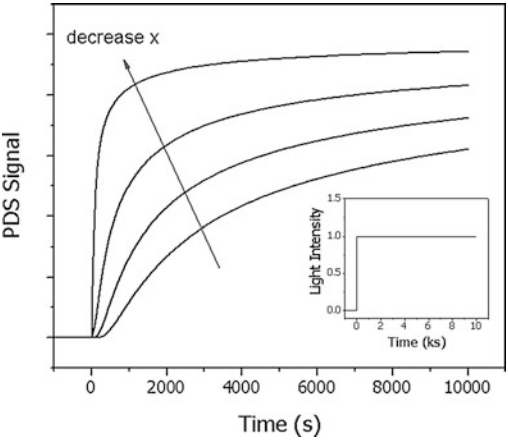

Fig. 13.2 Photothermal deflection signal recorded during continuous irradiation of a surface. The *insert* shows the shape of the light intensity perturbation

modulating a light-emitting diode (LED) light source. Since those sources are nearly as monochromatic as lasers and high intensities can be easily obtained, they can be used with profit as PBDS pump beams. In this case, all light absorption occurs during a short time lapse (τ) which is much smaller than the time required for the thermal gradient to reach the probe beam. Therefore, it can be assumed that all the heat (P_0) is produced at $t = 0$. The temperature-time profile will be

$$T(x,t) = T_\mathrm{f} + \left(\frac{P_0}{\rho_\mathrm{f} C p_\mathrm{f}}\right) \frac{\mathrm{e}^{-x^2/4\kappa_\mathrm{f} t}}{\sqrt{\pi \kappa_\mathrm{f} t}}, \tag{13.9}$$

where P_0 is energy of the pump beam. Differentiating Eq. (13.9) against x and combining with Eq. (13.1), we obtain the deflection profile:

$$\theta(x,t) = \left(\frac{L}{n}\frac{\mathrm{d}n}{\mathrm{d}T}\right)\left(\frac{P_0}{\rho_\mathrm{f} C p_\mathrm{f}}\right) \frac{x}{2\kappa_\mathrm{f} t} \frac{\mathrm{e}^{-x^2/4\kappa_\mathrm{f} t}}{\sqrt{\pi \kappa_\mathrm{f} t}}. \tag{13.10}$$

If P_0 remains constant, between pulses, it is possible to average the signal obtained during successive pulses, improving the signal/noise ratio. The deflection signal will show maxima (Fig. 13.3).

The deflection signal maximum occurs at a time (t_max) which depends on the beam-electrode distance (x):

$$t_\mathrm{max} = \frac{(x - x_0)^2}{6\kappa_\mathrm{f}}. \tag{13.11}$$

Measuring the deflection signal after light pulse and changing in a known way the beam to electrode distance, it is possible to calculate the thermal diffusivity of the fluid (κ_f) and the initial beam to electrode distance (x_0).

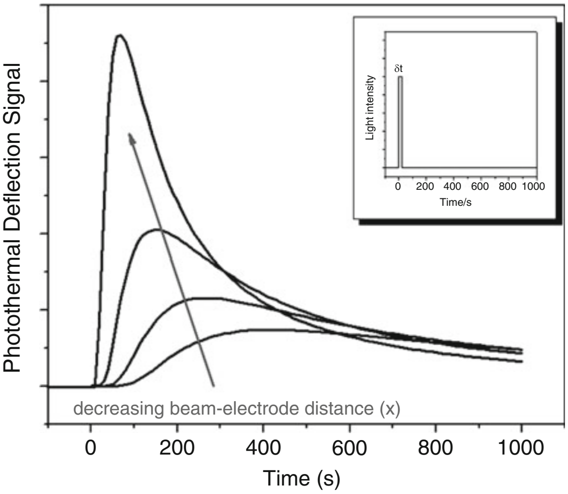

Fig. 13.3 Photothermal deflection signal as a function of time, after a light pulse is applied to the electrode surface. The *insert* shows the time profile of the light intensity perturbation

13.2.3 Sinusoidal Periodic Perturbation

If a periodic perturbation is applied, by modulation of the pump beam intensity, the thermal gradient will show as a signal at acoustic frequencies ($\omega > 20$ Hz) being the basis for photoacoustic spectroscopy. Solving the heat transfer equations (13.2)–(13.4) for the case of a periodic excitation of frequency (ω).

$$P(t) = P_0[1 + \sin(\omega t)]. \tag{13.12}$$

After an initial transient equilibration time, the temperature will obey the equation:

$$T(x,t) = T_\mathrm{f} + \left(\frac{P_0}{\rho_\mathrm{f} C p_\mathrm{f} \sqrt{\kappa_\mathrm{f}\omega}}\right) \mathrm{e}^{\left(-x\sqrt{\omega/2\kappa_\mathrm{f}}\right)} \sin\left(\omega t - x\sqrt{\frac{\omega}{2\kappa_\mathrm{f}}} - \frac{\pi}{4}\right). \tag{13.13}$$

Differentiating against x and combining with Eq. (13.1) gives the deflection profile:

$$\theta(x,t) = \left(\frac{L}{n}\frac{\mathrm{d}n}{\mathrm{d}T}\right) \left(\frac{P_0}{\rho_\mathrm{f} C p_\mathrm{f} \sqrt{\kappa_\mathrm{f}\omega}}\right) \omega \mathrm{e}^{\left(-x\sqrt{\omega/2\kappa_\mathrm{f}}\right)} \sin\left(\omega t - x\sqrt{\frac{\omega}{2\kappa_\mathrm{f}}} - \frac{\pi}{4}\right). \tag{13.14}$$

Equation (13.14) has been experimentally verified [6]. It allows calculating the effect of measurement parameters on the signal. The amplitude of the signal is proportional to P_0, giving a way to measure the absorption of light by the sample.

The logarithm of amplitude or phase will be proportional to the beam-electrode distance (x) with a slope m:

$$m = -\sqrt{\frac{\omega}{2\kappa_{\mathrm{f}}}}. \tag{13.15}$$

In that way, the diffusivity of the fluid (κ_{f}) can be measured.

13.3 Probe Beam Deflection Spectroscopy

13.3.1 General Principles

In this technique, the heat dissipated (P_0) is measured as function of the wavelength of the light in the pump beam. It is assumed that the properties of the fluid and the base substrate are constant during the measurement. The thermal properties of the material do not depend on the wavelength; therefore, P_0 is proportional to the light absorption. If the pump beam is normal to the surface, the optical pathlength does not depend on the wavelength. Sometimes, the pump beam is shined obliquely to the surface to increase the optical pathlength. In that case, a certain dependence of the pathlength with the angle exists. There are several possible systems: thermally thick sample, thermally thin sample, etc. The temperature profile for each case has been analytically expressed and could be quite complex [7]. Besides, the PDS signal could be measured from the front or rear side of the electrode. In electrochemistry, it is simpler to measure from the front side, as no special cell needs to be designed. The electrode is supposed to absorb or reflect all incident light, and the sample is considered to be thermally thin [8].

The parameter to measure is the deflection amplitude, which depends on the perturbation signal. For a sinusoidal periodic perturbation:

$$|\theta(\lambda)| = -\left(\frac{\mathrm{d}n}{\mathrm{d}T}\,\frac{\mathrm{e}^{-(1/\sqrt{2\kappa_{\mathrm{f}}})}}{n\rho_{\mathrm{f}}Cp_{\mathrm{f}}\sqrt{\kappa_{\mathrm{f}}}}\right)\left(\mathrm{e}^{\left(-x\sqrt{\frac{\omega}{2\kappa_{\mathrm{f}}}}\right)}\sqrt{\omega}\right)(LI_0)([1-\eta]\varepsilon(\lambda)C_{\mathrm{abs}}). \tag{13.16}$$

The first term in Eq. (13.16) contains the fluid parameters, thermal diffusivity (κ_{f}), change of refractive index with temperature ($\mathrm{d}n/\mathrm{d}T$), density (ρ_{f}), and calorific capacity (Cp_{f}). The second term contains the parameters which can be adjusted experimentally: beam-electrode distance (x) and perturbation frequency (ω). The third term contains the incident light intensity (I_0) and the optical pathlength (L). The latter parameter will depend on the thickness of the film deposited on the electrode or, if the film is thicker than the attenuation length, could be considered a constant. The last term contains the materials parameter: optical absorptivity [$\varepsilon(\lambda)$], quantum yield for emission (η), and the concentration of absorbing entities (C_{abs}).

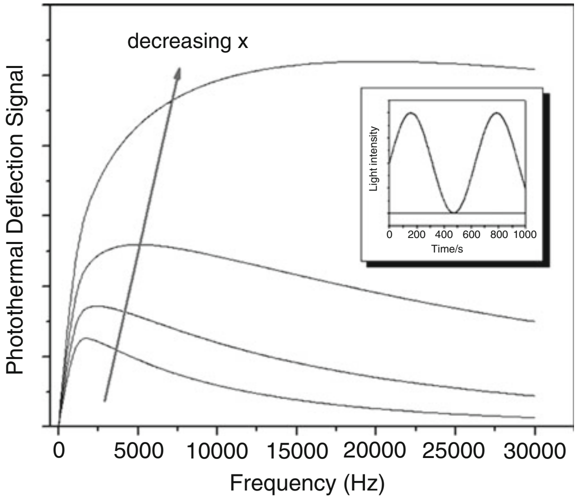

Fig. 13.4 Plot of the PDS signal as a function frequency for different beam-electrode distances. The *insert* shows the profile of the light intensity perturbation

To increase the signal/noise ratio, some parameters can be optimized. The frequency has a complex effect on Eq. (13.7). As it can be seen in Fig. 13.4, where the normalized θ signal is plotted as a function of frequency, there is an optimum frequency for the measurement. The optimum value depends on the beam-electrode distance (x). The beam-electrode distance can be diminished down to the radius of the probe beam (usually 30 μm).

It can be seen that the signal drops abruptly at low frequencies. This is due to the fact that the PDS signal is proportional to the thermal gradient which decreases with increasing time. On the other hand, at very high frequencies, the signal also decreases since the probe beam is not able to probe most of the thermal gradient.

13.3.2 Square Wave Periodic Perturbation

The sinusoidal perturbation can only be achieved if the light intensity is electrically modulated. This can only be achieved experimentally by electrical modulation of the light source in the case of lasers or LEDs. An alternative is to mechanically chopping a continuous pump beam. From Eq. (13.10), Eq. (13.17) can be obtained:

$$|\theta(\lambda)| = \left(\frac{\mathrm{d}n}{\mathrm{d}T}\frac{1}{n\rho_\mathrm{f}Cp_\mathrm{f}2{\kappa_\mathrm{f}}^{3/2}}\right)\left[\operatorname{erfc}\left(\frac{x}{\sqrt{4\kappa_\mathrm{f}/F_\mathrm{c}}}\right)\right](LI_0)[(1-\eta)\varepsilon(\lambda)C_\mathrm{abs}], \tag{13.17}$$

where F_c is the frequency of the pulses and I_0 is the light intensity.

In that way, it is possible to measure changes in the optical properties of the materials [$\varepsilon(\lambda)$], the concentration of chromophores (C_abs), or on the relationship between absorption [$\varepsilon(\lambda)$] and radiative emission $n(\eta)$.

A simplified form of Eq. (13.16) or Eq. (13.17) is

$$|\theta(\lambda)| = K_{\text{fluid}} K_{\text{exp}} (I_0(\lambda)[1 - \eta]\varepsilon(\lambda)C_{\text{abs}}), \tag{13.18}$$

where K_{fluid} contains all the constant of the fluid and K_{exp} all the parameters of the experimental setup. Therefore, the amplitude is proportional to the optical properties of the material. K_{fluid} and K_{exp} depend on the solution and experimental parameters. To maximize the signal, it is convenient to work at low frequencies (see Fig. 13.6), with the beam as close as possible (small x), high light intensity (I_0), and large pathlength (L). However, if L is increased, the beam-electrode distance has to be increased to maintain the beam parallel to the electrode (see Fig. 13.2). If a lamp is used as light source, its image is usually larger than the width of the probe beam. Therefore, lasers are preferable as light sources. The availability of tunable laser light will be useful to make spectroscopic measurements.

The parameters in $K_{\text{fluid}} = (\mathrm{d}n/\mathrm{d}T)(1/n\rho_{\text{f}}Cp_{\text{f}}2\kappa_{\text{f}}{}^{3/2})$ are defined for the solvent used in the experiment (see Table 13.1). While in general application of PDS [11] it is possible to select the fluid with the best thermal properties to obtain large signal/noise ratio, in electrochemistry, the solvent is defined by the electrolytic media. Therefore, it should have a large enough dielectric constant to dissolve the electrolyte and have low enough electrical resistance. Carbon tetrachloride (which is the fluid of choice in PDS due to its high K_{fluid}) is not a suitable solvent for electrochemistry. On the other hand, water has a K_{fluid} one order of magnitude lower than the other solvent due to the structured nature of water. Therefore, it should be replaced with other electrochemical solvents such as alcohols or acetonitrile. Indeed, it has been shown that replacing water by alcohol improves significantly the signal/noise ratio [12].

An advantage of PDS, like other photothermal and photoacoustic techniques, is that the detector sensitivity does not depend on the wavelength. Therefore, as far as a radiation source is available, the PDS signal could be recorded. This behavior contrasts with conventional photodetectors, like photomultipliers, which could not be used in the near-infrared range [13].

Table 13.1 Photothermal parameters of common solvents [9, 10]

Solvent	ρ_{f} (10^3 g cm^{-3})	Cp_{f} (J g^{-1} K^{-1})	n	κ (10^7 m^2 s^{-1})	dn/dT (10^4 K^{-1})	K_{fluid} (10^9)
Water	1.00	4.19	1.3325	1.36	0.87	0.15
Ethanol	0.79	2.45	1.3611	0.90	3.7	2.60
Methanol	1.17	2.50	1.3288	1.00	3.9	1.59
Acetonitrile	0.78	2.14	1.4409	1.70	4.6	1.36
CCl_4	1.59	0.85	1.4664	0.82	5.8	6.23
CH_2Cl_2	1.43	1.26	1.3348	0.83	5.4	4.69
Nitrobenzene	1.20	1.50	1.5530	0.80	4.6	3.64

13.4 Photothermal Monitoring of Concentration Gradients

In the previous discussion, it has been assumed that only the solid absorbs light and the solution is transparent to the pump and probe beams. However, if some species which are produced or consumed during the electrochemical experiment absorbs light, it would be possible to detect the changes in concentration of those species. Such determination, as it will be discussed below, is of great interest to understand electrochemical phenomena. It is possible to use a reflective electrode, which does not absorb the pump beam. Therefore, the thermal gradients will originate only on the solution species. If low-frequency (or even continuous) illumination is used, the signal will be proportional to all the substance produced or consumed. In that way, the technique would not show advantage to monitoring the colored species by UV-visible spectrophotometry. On the other hand, if the pump beam is modulated at a high enough frequency, the thermal gradient will only come from the region close to the probe beam. It has to be borne in mind that thermal diffusivities (κ_f) are in the order of 10^{-7} m^2 s^{-1} (see Table 13.1) while mass diffusivities (diffusion coefficient in a diffusion-controlled system) are in the order of 10^{-10} $m^2 s^{-1}$ [14]. Therefore, the effect of thermal gradient on the refractive index could be measured without interference by the concentration gradient. Pawliszyn et al. [15, 16] used the procedure to monitor the reduction of benzoquinone in DMSO. They were able to record the spectrum of the products. Then, Pawliszyn developed a theoretical framework of the technique which was experimentally tested [17].

The advantage of this method over the measurement of refractive index gradients due to concentration gradients is that it is possible to monitor only one chemical species in the presence of others which do not absorb the pump beam. The technique is more feasible now using high-intensity and monochromatic lasers or LEDs as pump beams which can be electrically modulated at high frequency. In principle, a collinear PBDS where a laser pump beam illuminates a region coincident with the probe beam, as it has been widely used in photochemistry, is possible. However, up to now, the technique has not been developed further.

13.5 Experimental Setup

The experiment requires a pump beam, which is absorbed by the electrode and creates a thermal gradient in front of it, and a probe beam which measures the deflection signal due to the refractive index gradient related with the thermal gradient.

In Fig. 13.5, the scheme of a typical PBDS setup is shown.

The electrochemical potential of the working electrode (W) is controlled by the potentiostat with respect to the reference (R) while passing a current between the

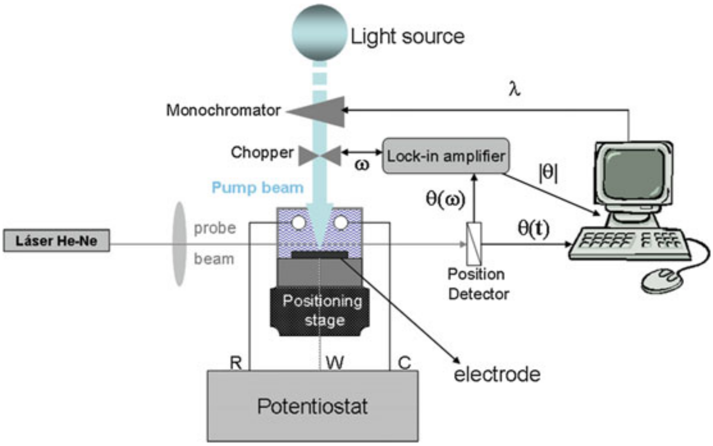

Fig. 13.5 Experimental setup for photothermal deflection experiment

working and counter electrode (C). The pump beam is chopped to produce light pulses, if necessary. Using a lock-in amplifier, it is possible to measure the deflection signal at the frequency of the chopper (F_c) to obtain the signal amplitude ($|\theta/$). Alternatively, the deflection signal [$\theta(t)$] is directly measured by an AD/DA converter at the PC. The light source could be a polychromatic lamp, a laser, or a LED. In the former case, the light has to be monochromatized to measure the absorption of light from defined regions of the wavelength range. A slit will define the wavelength bandwidth. Since only a small portion of the lamp output will illuminate the electrode, high-intensity lamps (>500 W) have to be used. The advent of affordable lasers and cheap LEDs makes them the source of choice for monochromatic measurements. While continuous pumping is of simple setup, it suffers from the interference of background thermal noise. On the other hand, periodic light perturbation (by chopping of a continuous pump beam or electrical modulation of the source) allows to synchronously detecting small signals using a lock-in amplifier. In this case, the frequency of the modulation has to be maintained low (see Figs. 13.4 and 13.5). The region sampled by the probe beam has to coincide with the region illuminated by the pump beam, requiring a precise focusing with a planar lens. Using an oscilloscope, it is possible to monitor the deflection signal and adjust the focus and the beam-electrode distance to get the maximum signal. The beam-electrode distance is adjusted using a positioning stage which also allows tilting the cell with respect to the probe beam, assuring that the probe beam is parallel to the electrode surface. The usual probe beam is a He–Ne gas laser, which has a wavelength where most solutions are transparent. Affordable He–Ne lasers have good pointing stability (<20 μrads) and show Gaussian beam shape which optical behavior is well known. The deflection signal is measured using a differential position detector (PSD) which is sensitive to the changes of light spot position, related directly with the deflection. The most common PSD is a bicell device with two photodiodes. The light spot is set to illuminate both photodiodes for a zero signal. After deflection of the signal, the illumination is unbalanced and a positive or negative signal is measured. To overcome for intensity variations in the laser, the output of the PSD is processed according to Eq. (13.19).

$$\text{Signal} = \left(\frac{\text{Cell}_1 - \text{Cell}_2}{\text{Cell}_1 + \text{Cell}_2}\right). \tag{13.19}$$

Usually, this is done by an analog amplifier, but it is possible to perform the calculation by a computer after analog to digital conversion. Other ways to measure deflection involve using a graded photodetector. In this case, the response is linear with the deflection. A simple system uses a knife edge which blocks half of the light beam in the null position. The displacement of the spot shows as a change in light intensity. To overcome light intensity variations, a second photodiode is illuminated with a fraction of the light beam diverted by a beam splitter. The ratio of both signals is directly related with the deflection.

To measure the absolute absorption spectrum of the electrode [*absorbance*(λ)], it is necessary to use lamps as light sources which are passed through a monochromator. The light source has an emission spectrum where the emitted light intensity I_0 depends on λ. Upon measurement of the PDS spectra of an electrode material, the PDS signal will show a convolution of the emission spectra of the source and the material spectrum. In optical spectroscopies based on transmitted light, it is possible to measure in absence of sample [$I(\lambda) = I_0(\lambda)$, i.e., a*bsorbance*($\lambda$) $= 0$] and record the spectra of sample and detector to subtract from the measured spectra as background. In the case of PDS, the background spectra should be measured in the condition of *absorbance*(λ) $= 1$. Such measurement requires a blackbody sample replacing the electrode. Alternatively, the light intensity spectrum [$I_0(\lambda)$] could be measured by a calibrated photodiode.

On the other hand, if only the variations of the optical spectrum due to electrochemical changes are required, the difference spectrum could be calculated. Since the spectrum of the source does not depend on the electrochemical potential, the result will show the changes in absorption spectra.

13.6 Photothermal Deflection: Experimental Results

PDS has been extensively used to measure optical properties of solution species or solid-state materials. However, it has been seldom used to monitor soluble species or thin films in an electrochemical environment.

13.6.1 In Situ PDS of Soluble Species

Royce et al. studied the photocorrosion of ZnSe by PDS [18, 19]. Mendoza-Alvarez et al. studied the optical properties of CdTe and its photocorrosion [1]. Pawlyszin used PDS to monitor the oxidation of hydroquinone, with spatial resolution [16].

Cairns and coworkers study the dissolution of Cu by a combination of PBD and PDS. They were able to detect the solution species produced during Cu oxide dissolution [20]. Rudnicki et al. studied the electrochemical oxidation of uranium oxide [21]. The use of PDS to measure optical absorption of soluble species allows localizing the species with respect to the electrode but requires data processing to know if the species is located between the probe beam and the electrode surface or at a distance to the electrode larger than the probe beam-electrode distance.

13.6.2 In Situ PDS of Surface Films

As discussed before, there are two modes to measure the in situ spectra: relative to a blackbody reference, rendering absolute spectra, or as a difference between states, rendering a differential spectrum. Examples of each mode will be presented.

13.6.2.1 Electrochromism of Tungsten Oxide (WO_3)

In Fig. 13.6 are shown the spectra of a tungsten oxide (WO_3) film at different applied potentials.

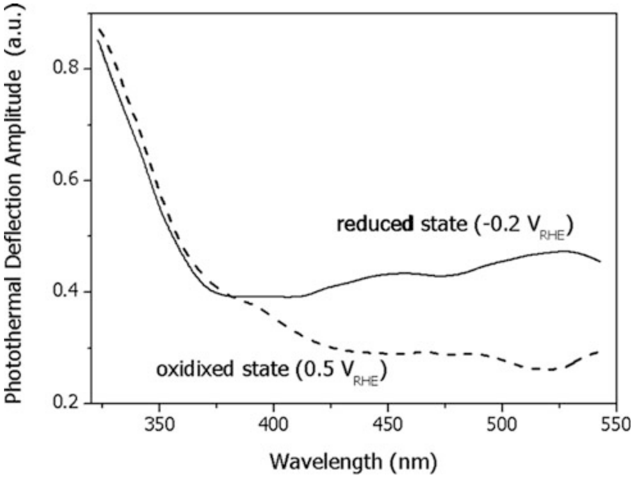

Fig. 13.6 In situ absolute photothermal deflection spectra of a WO_3/W/glass in 1 M H_2SO_4. Reduced (*full line*) and oxidized (*dashed line*). Chopping frequency = 11 Hz. Illumination: Xe lamp of 250 W

The film was produced by voltammetric cycling of a thin W film, evaporated onto a glass between −0.25 V and 1.3 V_{SCE} in 1 M H_2SO_4. The reference blackbody was a thin film of Vulcan XC-72 carbon microparticles, attached onto an epoxy layer, deposited onto the same glass support of the W films, where the metal was removed by chemical attack. In that way, by displacing the glass support, it is possible to expose the reference or the WO_3 film to the pump and probe beam. The spectra were measured by chopping the light of a Xe lamp at 11 Hz and measuring the signal amplitude synchronously with a lock-in amplifier. The light was monochromatized with a diffraction grating setup and a slit with a resolution of 20 nm. The spectra show a clear electrochromism, with higher absorption, in the visible range, at the reduced state (−0.2 V_{RHE}) than at the oxidized state (0.5 V_{RHE}). Both spectra show absorption at ca. 380 nm, corresponding to the forbidden band of amorphous WO_3 [22]. The spectrum taken in the reduced state shows an additional band at ca. 450 nm, corresponding to the absorption band of doped tungsten oxide, produced by the reaction [23]

$$WO_3 \xrightarrow{+xe^- + xH^+ + zH_2O} WO_3H_x(H_2O)_z. \tag{13.20}$$

The spectra obtained are in agreement with those measured by transmission spectroscopy [24].

13.6.2.2 Electrochromism of Anodic Iridium Oxide Film

A film of anodic iridium oxide (AIROF) was formed by cyclic voltammetry between −0.25 and 1.2 V_{SCE} in 1 M H_2SO_4 [25]. In Fig. 13.7, the differential PDS spectrum of AIROF/Ir/glass electrode in 1 M $HClO_4$ is shown. The spectrum was taken at 1.25 V_{SCE} (oxidized state), while the one at 0.25 V_{SCE} (reduced state) is taken as reference.

A band at ca. 610 nm is observed, with a shoulder at 450 nm. The band at 610 nm has been observed in transmission [26] and modulated reflectance measurements [27]. The bands are superimposed onto a baseline which increases absorption upon oxidation. The electrochromism in AIROF has its ground on the shift of the Fermi level of the oxide from the valence band (reduced film) into the t_{2g} band for the oxidized material [28]. Since the t_{2g} is partially filled, optical transitions in the visible or near-infrared range are allowed.

13.6.2.3 Electrochromism of Polyaniline (PANI)

Conductive polymers suffer a change in optical absorption when their oxidation state is altered [29]. This effect has been used to build electrochromic devices [30] and have been measured by ex situ PDS [31, 32]. Here, we describe its application to in situ measurement of optical absorption changes.

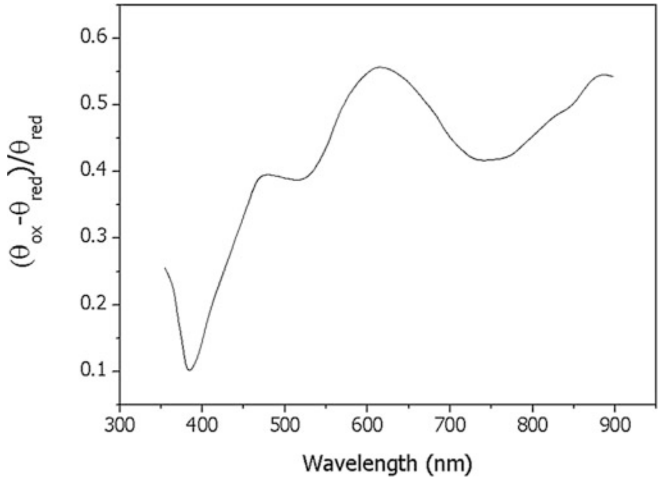

Fig. 13.7 Differential photothermal deflection spectrum of an AIROF/Ir/glass electrode. The spectrum was taken at 1.25 V_{SCE} (oxidized state), while the one at 0.25 V_{SCE} (reduced state) is taken as reference. Solution: 1 M $HClO_4$. Chopping frequency = 31 Hz. Xe lamp of 250 W

In Fig. 13.8 are shown the differential spectra of a PANI film, electrochemically deposited onto a thin (200 nm) gold film supported on a glass slide.

The film was produced by cycling (between −0.25 and 0.8 V_{SCE}) at 50 mVs^{-1} in a 0.1-M aniline solution in 1 M $HClO_4$. The raw PDS spectrum at −0.2 V_{SCE} (reduced state) is used as reference.

The main feature observed (Fig. 13.8) is a broad band at ca. 830 nm (1.5 eV) which is assigned to the delocalized polarons in the polyaniline (emeraldine state) chain [33]. At more anodic potentials, both the concentration of oxidized rings and the delocalization increase. The intensity of the optical absorption follows a Nernstian law (Fig. 13.9a). The energy of the transition increases, with a hypsochromic shift of the band (Fig. 13.9b). As it was discussed before, the whole wavelength range [including the near-infrared range ($\lambda > 800$ nm)] can be measured without changing detectors.

13.6.3 Voltammetric Absorptiometry

When the PDS signal is measured at a single wavelength during a voltammetric scan, there is no need for a reference spectrum, and the optical absorption is directly measured as function of the applied potential. The method does not give direct spectroscopical information but allows monitoring the electrochromism of thin solid films. The data analysis involves the measurement of optical absorption [$PDS_\lambda(E)$] to be compared with the measurement of electron flux [$i(E)$] and/or charge [$Q(E)$]. Since the PDS signal is measured during the scan, kinetic effects can

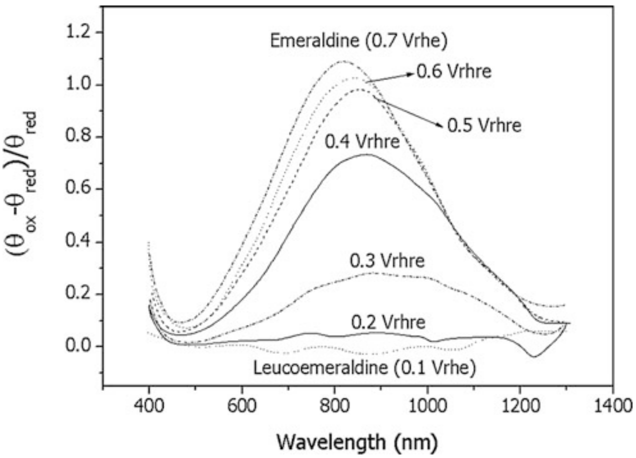

Fig. 13.8 Differential photothermal deflection spectra of a PANI/Au/glass system in 1 M $HClO_4$. Chopping frequency = 11 Hz. Reference spectrum taken at 0.0 V_{RHE}

Fig. 13.9 Dependence of PANI optical absorption with potential (calculated from the spectra depicted in Fig. 13.8). (**a**) Maximum value of the PDS signal (band at ca. 810 nm) as a function of the electrode potential. (**b**) Wavelength of the maxima (λ_{max}) as a function of the electrode potential

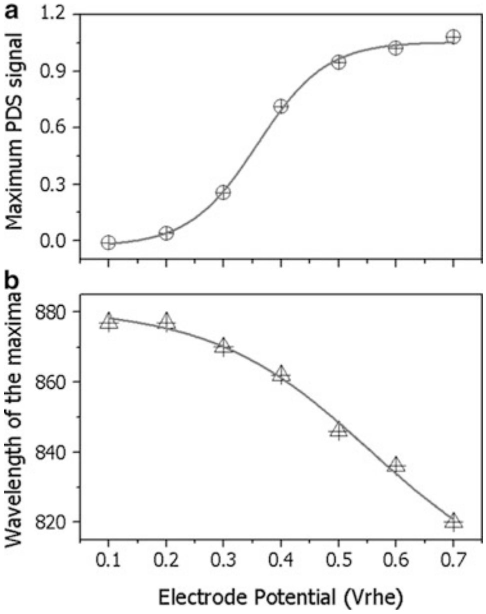

be also measured. Since spectral measurements (PDS) require a finite time to scan the wavelength, usually kinetic effects could not be measured. On the other hand, if the electrochemical system has high reproducibility (i.e., the electrochemical response is the same during multiple cycles), it is possible to record the PDS signal during multiple cycles while varying the wavelength between cycles. In that way, the variation of optical spectra during cycling can be calculated.

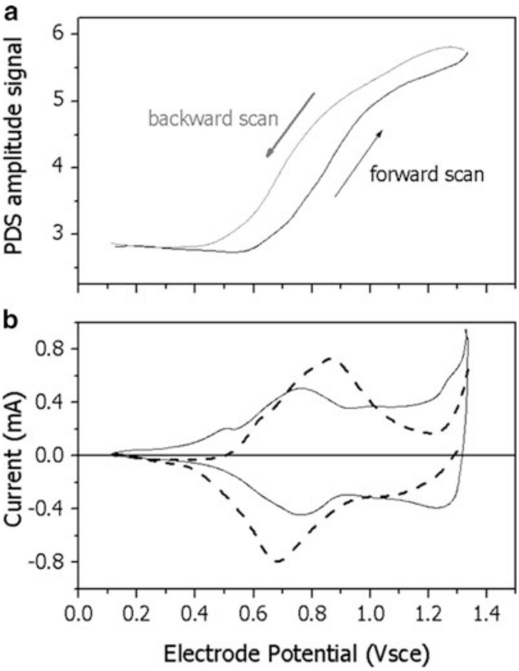

Fig. 13.10 (**a**) Photothermal deflection signal amplitude measure on an AIROF/Ir/glass electrode, during a voltammetric scan. The scan was performed between 0.1 and 1.3 V_{SCE}, at 20 mV s^{-1}, while the light is chopped at 31 Hz. (**b**) Cyclic voltammogram (*full line*) of an AIROF film compared with the derivative of the signal depicted in Fig. 13.9a (*dashed line*)

13.6.3.1 Anodic Iridium Oxide Film

An anodic oxide iridium film was prepared by anodic oxidation (1.2 V_{SCE}, 30 s) in 1 M H_2SO_4. The film was subjected to a cyclic voltammetry scan (20 mV s^{-1}), between 0.1 and 1.3 V_{SCE}, in 1 M $HClO_4$.

The PDS signal, measured at 560 nm, shows a sigmoid profile which is typical of concentration-dependent optical absorption (Fig. 13.10a). A comparison of the current signal (full line, Fig. 13.10b) with the derivative of the PDS signal against potential (dashed line, Fig. 13.10b) reveals that the main redox process is directly related with the coloration.

13.6.3.2 Sulfonated Polyaniline

In the previous example exists a monotonic relationship between the optical absorption and charge. However, in conducting polymers, it is also possible to detect intermediate species. Figure 13.11 shows the PDS signal measured during voltammetric excursions of a sulfonated polyaniline film. Monitoring the PDS signal at two different wavelengths, different potential dependence of the optical absorption can be detected.

The film was prepared by a postfunctionalization method. First, a polyaniline film was deposited by electrochemical oxidation of aniline. Then, the film was

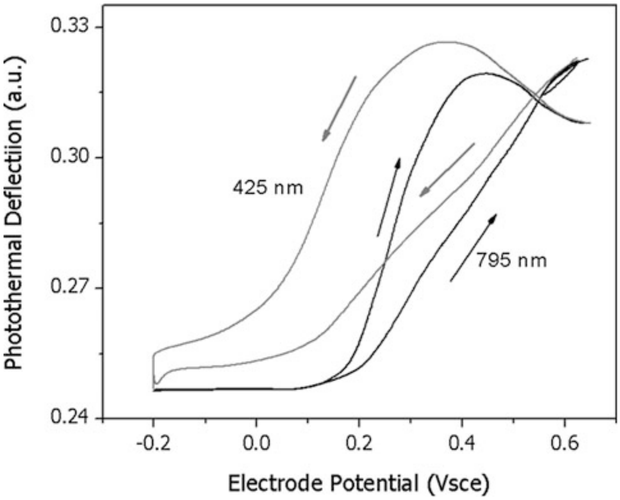

Fig. 13.11 Photothermal deflection signal amplitude measure on a SPAN/Au/glass electrode, during a voltammetric scan. The scan was performed between 0.1 and 1.3 V_{SCE}, at 20 mV s^{-1}, while the light is chopped at 31 Hz

treated with a bisulfite ion, under potential control [34]. The resultant film bears fixed sulfonate groups ($-SO_3^-$). Then, the potential was scanned between while the PDS signal measured at 795 nm shows a monotonically increasing signal, which is directly proportional to the charge; the one at 425 nm shows a maximum at ca. 0.45 V_{SCE} (forward scan) and 0.375 V_{SCE} (backward scan). This result indicates that at 425 nm has its optical absorption an intermediate species which increases concentration up to ca. 0.4 V_{SCE}, to decrease at more anodic potentials. The most likely species is a localized radical cation, which converts to the delocalized polaron at more anodic potentials [35]. On the other hand, at 795 nm, it seems to absorb the delocalized polaron which increases concentration monotonically [36].

13.7 Conclusions

In situ electrochemical photothermal deflection techniques can be used to determine optical properties of both soluble and surface-confined electrochemical systems. They have some advantages over conventional transmission or reflectance spectroscopy such as the capability to measure rough electrodes or the wide wavelength range of measurement with only one detector. However, probably due to the lack of commercial instruments, they have been used sparingly. Like PBD techniques, the application to surface-confined redox systems seems to arise more interest than its application to solution electrochemical systems.

References

1. Mendoza-Alvarez JG, Royce BSH, Sanchez-Sinencio F, Zelaya-Angel O, Menezes C, Triboulet R (1983) Optical properties of CdTe thin films studied by photothermal deflection spectroscopy. Thin Solid Films 102:259–263. doi:10.1016/0040-6090(83)90093-7
2. Li B, Deng Y, Cheng J (1995) Pulsed photothermal deflection spectroscopy with optically dense samples. Appl Spectrosc 49:279–285. doi:as-49-3-279
3. Seager CH, Sinclair M, McBranch D, Heeger AJ, Baker GL (1992) Synth Met 49:91–97. doi:10.1016/0379-6779(92)90077-V
4. Decker F, Fracastoro-Decker M (1988) The mirage effect in photoelectrochemistry. J Electroanal Chem 243:187–191. doi:10.1016/0022-0728(88)85038-1
5. Bird RB, Stewart WE, Lightfoot EN (2001) Transport phenomena. Wiley, New York
6. Fracastoro-Decker M, Decker F (1989) The mirage effect under controlled current conditions. J Electroanal Chem 266:215–225. doi:10.1016/0022-0728(89)85069-7
7. Brilmyer GH, Bard AJ (1980) Application of photothermal spectroscopy to in-situ studies of films on metals and electrodes. Anal Chem 52:685–691. doi:10.1021/ac50054a023
8. Harada M, Obata S, Kitamori T, Sawada T (1993) Anal Chem 65:2181–2183. doi:10.1021/ac00063a046
9. Braslavsky S, Heihoff K (1991) Photothernal methods. In: Scaiano JC (ed) CRC handbook of organic photochemistry. CRC, Boca Raton, FL
10. CRC (1978) CRC handbook of chemistry and physics, 68th edn. CRC, New York
11. Bialkowski SE (1996) Photothermal spectroscopy methods for chemical analysis. Wiley, New York
12. Barbero C, Kőtz R, Haas O (1999) Differential photothermal deflection spectroscopy (dpds). A technique to study electrochromism of synthetic metals. Synth Met 101:170. doi:10.1016/S0379-6779(98)00766-8 DOI:dx.doi.org
13. Bruining H (1954) Physics and applications of secondary electron emission. McGraw-Hill, New York
14. Robinson RA, Stokes RH (2002) Electrolyte solution. Courier Dover Publications, Londres
15. Pawliszyn J, Weber MF, Dignam MJ, Venter RD, Moon Park S (1986) Observation of concentration gradients by the laser beam deflection sensor. Anal Chem 58:236–239. doi:10.1021/ac00292a058
16. Pawliszyn J, Weber MF, Dignam MJ, Moon Park S (1986) Selective observation of concentration gradients by the laser beam deflection sensor applied to in situ electrochemical studies. A novel approach. Anal Chem 58:239–242. doi:10.1021/ac00292a059
17. Pawliszyn J (1988) Spectroelectrochemical sensor based on Schlieren optics. Anal Chem 60:1751–1758. doi:10.1021/ac00168a022
18. Royce BSH, Sánchez-Sinencio F, Goldstein R, Muratore R, Williams R, Yim WM (1982) Studies of photocorrosion at the ZnSe-electrolyte interface by photothermal deflection spectroscopy. J Electrochem Soc 129:2393–2395. doi:10.1149/1.2123551
19. Royce BSH, Voss D, Bocarsly A (1983) Mirage effect of electrochemical processes. J de Physique 44:325–329
20. Russo RE, McLarnon FR, Spear JD, Cairns EJ (1987) Probe beam deflection for in situ measurements of concentration and spectroscopic behavior during copper oxidation and reduction. J Electrochem Soc 134:2783–2787. doi:10.1149/1.2100287
21. Rudnicki JD, Russo RE, Shoesmith DW (1994) Photothermal deflection spectroscopy investigations of uranium dioxide oxidation. J Electroanal Chem 372:63–74. doi:10.1016/0022-0728(94)03301-3
22. Deb SK (1973) Optical and photoelectric properties and color centers in thin films of tungsten (VI) oxide. Philos Mag 27(4):801–822
23. Malpas RE, Bard AJ (1980) In situ monitoring of electrochromic systems by piezoelectric detector photoacoustic spectroscopy of electrodes. Anal Chem 52(1):109–112. doi:10.1021/ac50051a026

24. Leftheriotis G, Yianoulis P (2008) Development of electrodeposited WO_3 films with modified surface morphology and improved electrochromic properties. Solid State Ionics 179:2192–2197. doi:10.1016/j.ssi.2008.07.018
25. Kotz R, Barbero C, Haas O (1990) Probe beam deflection investigation of the charge storage reaction in anodic iridium and tungsten oxide films. J Electroanal Chem 296:37–49. doi:10.1016/0022-0728(90)87231-8
26. Kang KS, Shay JL (1983) Blue sputtered iridium oxide films (blue SIROF's). J Electrochem Soc 130:766–769. doi:10.1149/1.2119800
27. Gutiérrez C, Sánchez M, Peña JI, Martínez C, Martínez MA (1987) Potential-modulated reflectance study of the oxidation state of iridium in anodic iridium oxide films. J Electrochem Soc 134:2119–2125. doi:10.1149/1.2100835
28. Koetz ER, Neff H (1985) Anodic iridium oxide films: an UPS study of emersed electrodes. Surf Sci 160:517–530. doi:10.1016/0039-6028(85)90791-5
29. Hyodo K (1994) Electrochromism of conducting polymers. Electrochim Acta 39:265–272. doi:10.1016/0013-4686(94)80062-6
30. Monk P, Mortimer R, Rosseinsky D (2007) Electrochromism and electrochromic devices. Cambridge University Press, Cambridge
31. Weinberger BR, Roxlo CB, Etemad S, Baker GL, Orenstein J (1984) Optical absorption in polyacetylene: a direct measurement using photothermal deflection spectroscopy. Phys Rev Lett 53:86–89. doi:10.1103/PhysRevLett.53.86
32. Tzolov M, Koch VP, Bruetting W, Schwoerer M (2000) Optical characterization of chemically doped thin films of poly(p-phenylene vinylene). Synth Met 109:85–89. doi:10.1016/S0379-6779(99)00207-6
33. Huang WS, MacDiarmid AG (1993) Optical properties of polyaniline. Polymer 34:1833–1845. doi:10.1016/0032-3861(93)90424-9
34. Grumelli DE, Forzani ES, Morales GM, Miras MC, Barbero CA, Calvo EJ (2004) Microgravimetric study of electrochemically controlled nucleophilic addition of sulfite to polyaniline. Langmuir 20:2349–2355. doi:10.1021/la0354990
35. Stilwell DE, Park SM (1989) Electrochemistry of conductive polymers. J Electrochem Soc 136:427–433. doi:10.1149/1.2096649
36. Barbero C, Miras MC, Schnyder B, Haas O, Kötz R (1994) Sulfonated polyaniline films as cation insertion electrodes for battery applications. Part 1.—Structural and electrochemical characterization. J Mater Chem 4:1775–1783. doi:10.1039/JM9940401775

Chapter 14
Comparison of Probe Beam Deflection Techniques with Other Methods to Monitor Fluxes of Mobile Species

14.1 Introduction

Probe beam deflection (PBD) techniques are able to detect fluxes of mobile species (ions, neutral compounds) during electrochemical experiments. Other experimental techniques have been applied to the same goal. Those techniques have been used to study similar systems than PBD and, sometimes, have been used together with PBD in the same work.

Since concentration measurement is the main goal of instrumental analytical techniques, most of them can be used to monitor fluxes as far as local concentrations can be evaluated.

14.2 Electrochemical Techniques

Solution electrochemical systems involve changes of concentration of electroactive soluble species away from the electrode surface. Therefore, electrochemical methods applied to second electrode (detector) could be used to measure the concentration gradients induced by a first electrode (source). Any pair of electrodes could be used. However, if both electrodes are of similar size, they will influence each other. Therefore, small electrodes (ultramicroelectrodes) have been used as detectors (e.g., scanning electrochemical microscopy), or a forced flux of solution is set up between both electrodes (rotating ring-disk electrochemistry). Besides solution electrochemical systems, redox-active species which redox state is not changed at the source electrode (e.g., protons) but are consumed or produced at the source electrode, can also be determined. A variant of electrochemical detection involves using potentiometry to measure the concentration. In this case, not only the flux of redox-active species can be determined but any species measurable by ion-specific electrodes.

G.G. Láng and C.A. Barbero, *Laser Techniques for the Study of Electrode Processes*, Monographs in Electrochemistry, DOI 10.1007/978-3-642-27651-4_14,

14.2.1 Ring-Disk Voltammetry

A rotating disk electrode (RDE) is a hydrodynamic working electrode used in an electrochemical system to control the mass transport [1]. The electrode rotates during experiments, inducing a flux of analyte to the electrode which is determined by the rotation speed. The electrode includes a conductive disk embedded in an inert nonconductive material that can be attached to an electric motor, or similar controlled speed device, that could have fine control of the electrode's rotation rate. The electric motor could be analogue with optical feedback or a fast stepping motor, driven by a high-frequency pulse train. As the electrode turns, some of the solution is dragged by the spinning disk, and the resulting centrifugal force expels the solution away from the center of the electrode. New solution flows from the bulk to the electrode, perpendicular to the electrode. The result is a laminar flow of solution toward and across the electrode surface. The rate of the solution flow can be controlled by the disk's angular velocity. In that way, conditions in which the steady-state current is controlled by the solution flow can be achieved. The mass transport rate is larger than the one given by diffusion and does not change in time. If the rotating piece is made of a center disk and an outer ring, with a small gap (0.1–0.5 mm) of insulating material between them, the system constitutes a rotating ring-disk electrode (RRDE) [2]. Soluble species produced or consumed in the disk will reach the ring and could be detected there. In that way, a source (disk) and detector (ring) electrode is set up. The time delay between production/consumption and detection is determined by the width of the gap and the electrode rotation speed. The potential of disk and risk electrode can be controlled independently using a bipotentiostat. The current measured in the ring electrode is used to measure the flux of redox-active species produced/consumed at the ring electrode. The RRDE takes advantage of the laminar flow created during rotation. As the system is rotated, the solution in contact with the disk electrode is driven to the side of the electrode and crosses the ring electrode and goes back into the bulk of the solution. Since the flow in the solution is laminar, the solution transport between disk and the ring occurs in a very controlled manner. The resulting currents are dependent on the electrodes' potentials, their areas, and the width of the gap, as well as the rotation rate [3]. There are other experimental schemes, like a solution jet impinging on a wall electrode, which can be used for the same purpose [4].

RRDE has been used to detect extensively to study the mechanism of oxygen reduction [5–8], a key factor in fuel cell operation. It has been also used to study a variety of electrocatalytic systems [9, 10]. It can also be used to monitor nonelectrochemical redox reactions like those occurring on redox enzymes [6]. The underpotential deposition of Cu was studied by RRDE [11], and PBD [12], giving complementary information. The diffusion coefficient of an electroactive species can be measured by chronodeflectometry without prior knowledge of electrode surface area or the number of electrons exchanged (see Chap. 2) [13]. Using chronoamperometry at RRDE systems, it is possible to determine independently the diffusion coefficient and the number of electrons exchanged [14]. The system has been used to study thin electroactive films. Specifically, it has been used to study the polymerization, redox-coupled ion exchange, and degradation of conductive polymers [15, 16]. The system was then studied using PBD techniques [17], giving complementary information. The time delay between the current detected signal measured in the disk and ring electrode is related the mass transport across the ring-disk surface. In cyclic voltammetric experiments, the time delay is observed as an apparent potential shift in the current-potential plot. The behavior is similar to the shift observed in cyclic voltadeflectometry due to the distance between the probe beam and the electrode surface. Cyclic deflectometry data has been data processed by deconvolution to allow direct comparison of current and deflection data [18, 19]. A similar procedure has been used to process the ring current and be able to directly compare with the disk current [20]. It has to be borne in mind that the transfer function used is different since mass transport occurs by diffusion in PBD and by hydrodynamic controlled convection in RRDE.

14.2.2 Scanning Electrochemical Microscopy

This technique involves the scanning of an ultramicroelectrode (diameter below ca. 100 μm) in front of the working electrode surface. It has been extensively reviewed [21–26]. In a similar fashion than RRDE, the macro working electrode acts as source which produces/consumes soluble redox species, and the scanning ultramicroelectrode is the probe which measures the fluxes [27]. Besides its ability to probe the redox species in solution, an ultramicroelectrode gives additional properties. On one side, its small size allows the concentration gradients in the source electrode to develop undisturbed. Additionally, the high perimeter-to-area ratio of ultramicroelectrodes creates a spherical diffusion layer in front of the probe [28]. When the probe is close to the source, the diffusion layer is blocked and the mass transport changes. In that way, the probe-source distance can be controlled and/or evaluated [29]. In fact, to simply monitor the fluxes on flat electrodes, the imaging capabilities of the instrument are not required. Indeed, Engstrom et al. use a microelectrode to measure concentration gradients inside the diffusion layer without scanning [30, 31]. The electrochemical oxygen reduction was also studied by SECM [32]. SECM was used to study the ion exchange occurring during oxidation/reduction of electroactive films [33, 34]. The study of polypyrrole ion exchange gives similar results PBD measurements [35] but requires the use of redox-active anions (ferrocyanide, bromide) to be able to detect changes in concentration with the ultramicroelectrode [36]. The ion exchange in polyaniline, a subject thoroughly studied by PBD [37], was investigated using SECM [38], supporting the same ion exchange mechanism.

Besides typical soluble redox ions, the fluxes of other analytes have been determined using amperometric SECM, such as gaseous oxygen [39] and protons [40]. Additionally, it is possible to scan potentiometric electrodes in front of a source electrode [41, 42]. This measurement method should allow to detect almost any ion [41] using the ultramicroelectrode form of ion-selective electrodes as detector [43]. However, it should be borne in mind that the measurement involves quantifying a potential difference (down to tens of millivolts) between a ultramicroelectrode and a reference electrode inside an electrochemical cell where a potential gradient is established between the working (source) electrode and the counter electrode. The approximation of the detector electrode implies moving it inside the potential gradient. Therefore, it could be difficult to ascertain the origin of the potential measured.

In the case of ion transfer trough membranes or liquid-liquid interfaces, it is possible to use a nanopipette to measure the ion conductance [44–46]. The subject should be ideally suited to apply PBD techniques, but it has not been investigated so far.

SECM measures concentration in the solution in a direct way, like PBD, but it has the specificity which PBD lacks. On the other hand, the specificity of SECM requires knowing the ion to be determined prior to the evaluation, while PBD can be applied without such prior knowledge. Therefore, both techniques should be complementary.

An ion-sensitive sensor placed close to the working electrode will be able to detect the changes of ion concentration during the electrochemical experiment [47]. A drawback is the effect of the size of the detector in front of the electrode. A solution involves the use of microelectrodes as sensors (see Sect 14.2.2).

14.3 Electrochemical Quartz Crystal Microbalance

Quartz crystal microbalance (QCM) and related methods [48] are based on the measurement of characteristic resonance of piezoelectric systems [49]. In QCM, a quartz thin crystal is set between two metal electrodes, and a sinusoidal perturbation potential is applied between the electrodes, producing a mechanical oscillation due to the piezoelectric effect. The system will show a characteristic resonance frequency which can be detected by an electronic resonance circuit or measured by a high-frequency impedance analyzer. The frequency depends on parameters of the system, including mass. If one of the metal electrodes is used as working electrode of an electrochemical system, the mass of the electrode during electrochemical processes can be measured. The technique is called electrochemical quartz crystal microbalance (EQCM). The actual behavior is more complex because the presence of the fluid (electrolyte solution) dampens the mechanical oscillation of the crystal. For an ideal system (smooth electrode with a thin rigid film), the frequency change obeys the Sauerbrey [50] equation:

$$\Delta f = -\frac{2f_0^2}{A\sqrt{\rho_q \mu_q}}\Delta m, \tag{14.1}$$

where f_0 is the resonant frequency (Hz), Δf is the frequency change (Hz), Δm is the mass change (g), A is the active crystal area (area between electrodes, cm^2), ρ_q is the density of quartz ($\rho_q = 2.648$ g/cm^3), and μ_q is the shear modulus of quartz for AT-cut crystal ($\mu_q = 2.947 \times 10^{11}$ g/cm s^2). The equation was derived for crystals in gases, but it has demonstrated its validity in fluids [51, 52].

Additionally, if the mass of attached films has to be measured, those films should be rigid or additional damping occurs. Initially, EQCM was used to measure the deposition of metals [53, 54], and the effect of temperature and viscosity of the solution was evaluated [55]. Then, different electrochemical phenomena were studied, including anion adsorption [56–59], neutrals adsorption [60–63], and underpotential deposition [64, 65]. Then, the technique was used to monitor the exchange of ions and other mobile species occurring during electrochemical oxidation/reduction of thin electroactive films [66]. Among them, electroactive oxides [67], solid metal complexes [68], redox polymers [69], and conductive polymers [70, 71]. Its high sensitivity allows to measure ion exchange by self-assembled monolayers [72]. Additionally, the electrochemistry of novel porous carbon materials has been also studied using EQCM [73, 74].

CO adsorption and oxidation on Pt surfaces, an important subject in fuel cell operation, has been studied using EQCM [75]. As discussed in Chap. 3, the same process in Pt nanostructured electrodes has been studied using PBD [76]. It seems that PBD produces information on the dynamics of CO oxidation, due to its intrinsic fast response, while EQCM gives more quantitative information.

The method determines the amount of mass which become bonded to the electrode. Therefore, the measurement of movement of mobile species is indirect. Additionally, the method measures the movement of all mobile species at the same time. An important factor is the solvent movement which could make the interpretation of the mass changes difficult. As discussed in Chap. 11, the technique has been used together with PBD measurements as independent measurements [77] or as an in situ combined technique [78]. Since PBD measures the ion fluxes outside the electrode and EQCM measures the changes of ion concentration inside the electrode, the combination gives unique insight on the electrochemical processes. Additionally, PBD is nearly insensitive to solvent transfer, and its response does not depend on the mass of the ion exchanged. Therefore, PBD allows clarifying the information provided by EQCM. As an example, early studies of ion exchange coupled to redox processes in polyaniline (PANI) were unable to detect the expulsion of protons during oxidation in acid media [79]. It was assumed that the low mass of proton (1 g/mol) makes it difficult to be detected by EQCM. However, the successful detection of proton expulsion during PANI oxidation by PBD, prompts to investigate again the system by EQCM [80, 81]. Proton expulsion was clearly detected, and it was found that protons move as hydronium ions (H_3O^+) with a more detectable mass (19 g/mol). It seems that the expulsion of hydronium ions is accompanied by solvent influx (mass gain) which compensates the mass loss due to hydronium ion expulsion. Such effect of solvent exchange on the EQCM response was quantitatively ascertained in an electroactive polymer (poly(1-hydroxyphenazine)) [82].

In the case of sulfonated polyaniline, PBD measurements clearly indicate that positive charge formation during polymer electrochemical oxidation is mainly compensated by proton expulsion. However, EQCM shows mass gain during oxidation, suggesting anion insertion is used for charge compensation [83]. A more detailed EQCM study shows that the mass gain does not scale up with the anion mass, suggesting that protons are expelled during SPAN oxidation, but water influx shows up as mass gain [84–86].

The technique was able to detect ion flux oscillations occurring during oxidation of formic acid [87]. The ion flux oscillations were then confirmed independently by PBD [88]. When adsorption of ions or neutral mobile species on the electrode is involved in solution electrochemical processes, EQCM could also provide insight into the mechanism [89].

EQCM has been applied extensively to the study of ion exchange between electrode and the solution. However, it has some drawbacks such as the unknown amount of solvent exchanged along the ions. Additionally, it has been recognized in the last years that Sauerbrey equation is only obeyed when thin rigid films with low roughness are attached to the EQCM electrode surface [90]. In other situations, the electrode shows significant damping, and the measured frequency is not linear with the mass change. While it is possible to evaluate the viscoelastic parameters of the electrode using electroacoustic measurements, both the measurement and the interpretation of the data become more complex [91].

14.4 Spectroelectrochemistry

Spectroelectrochemistry is the application of spectroscopic techniques to in situ monitoring electrochemical processes [92]. The techniques could be applied to monitor changes at the electrode surface or absorption changes in the solution. Usually, the conditions of reflectance spectroscopy are set to increase the sensitivity to surface species. Indeed, p-polarized light is used since the dipole moment is perpendicular to the surface and the selection rule only allows absorption of surface species [93]. Therefore, special measurement setup is used to monitor solution species by spectroelectrochemistry.

14.4.1 UV–Visible Spectroscopy with Indicator Dyes

When measuring the absorbance [94–96], or fluorescence [97], of indicator dyes, it is possible to evaluate (e.g., proton) concentration of ions in the solution. In a grid electrode, the absorption will occur in the region between wires, allowing early detection of ion fluxes.

Besides processes where ions are exchanged, electrode reactions where ions are involved, such as oxygen reduction, could be also detected [98]. Indeed, the detection of protons by fluorescence has been used in the high-throughput screening of electrocatalysts for methanol oxidation [99]. Using a confocal microscope and fluorescent pH indicators, it has been also possible to map the diffusion layer of a flat electrode [100]. Usually, the absorbance of the whole cell is measured. However, spatial resolution measurements have been performed [101]. If a laser is used as light source and the beam travels parallel to the electrode surface, a combination of absorption and refraction, like in PBD, will occur. McCreery and coworkers imaged the diffusion layer when a colored product is formed, using a laser which suffers diffraction and absorption [102–106]. Only species absorbing at the wavelength of the available lasers can be monitored.

14.4.2 In Situ FTIR Spectroscopy

While external reflectance in situ FTIR could in principle be used to monitor ion fluxes in solution, the high infrared absorption of common electrochemical solvents makes difficult the measurement. Usually, the fact that p-polarized light has higher sensitivity to surface species than s-polarized light is used to obtain spectra only of adsorbed species [107, 108], losing information of concentration gradients in solution [93]. Therefore, it has been seldom used to study electrochemical process in solution [109–111]. However, the technique provides plenty of information on the processes occurring at the surface [112].

On the other hand, using attenuated total reflectance (ATR), it is possible to measure from the back of the electrode. The spectra will contain information about the changes of absorption in the solution because ATR samples a region of several micrometers [113, 114]. It has been used to study concentration gradients in electrochemical systems [115–121]. The signal could be increased by surface enhancement (SEIRAS) [122]. The technique was used to monitor the oscillatory phenomena occurring when small organic molecules are electrochemically oxidized on Pt [123], a subject previously studied by PBD [88]. The results of each technique are complementary, given the different information they provide.

It could also be applied to surface-confined electrochemical systems, where it will monitor the changes of ion content in the film and solution [124]. The interpretation could be complex because the ion gain by the film is a loss at the solution. Using ions with a defined IR signature, it is possible to separate the contribution of each species to the spectra [125]. It has been used to study the ion exchange in polyaniline [126–128]. The results obtained agree with the ones obtained by PBD [129], inasmuch that only cations can be detected by FTIR-ATR while PBD detects anion and cation fluxes.

The technique was combined with PBD to study the ion exchange in poly(1-naphtol) [130], poly(5-amino-1-naphtol) [131], and poly(5-amino-1,4-naphtoquinone) [132]. The PBD data allows to interpret the observed FTIR spectral changes unambiguously.

14.4.3 *In Situ Raman Spectroscopy*

Raman spectroscopy uses a visible or near-infrared light to measure vibrational states of molecules and materials. Therefore, it does not suffer of the high absorption by solvent. On the other hand, the small scattering cross section of Raman absorbers makes difficult to detect small changes of concentration in solution. While it has been used to measure ion transport in membranes [133–136], its use in electrochemical system have been scarce. On the other hand, using confocal Raman microscopy is possible to map the concentration gradients in front of an electrode [137].

14.5 Radiotracer Detection

A way to detect ion movement in an electrochemical system involves the use of radioactive isotopes [138]. Using a small concentration of the mobile species which contain a radioactive isotope, it is possible to detect the nuclear emission (α, β, or γ rays) occurring during the decay. The method has been used to study ion adsorption [139], and organic molecules [140], on metal electrodes. It has also be used to study ion exchange during oxidation/reduction of electroactive films, such as solid metal complex [141], redox [142], and conductive polymers [143, 144]. The detected ion fluxes in solid metal complexes were also studied by PBD techniques [145]. Indeed, the radiotracer detects the exchange of co-ions (ions with positive charge) during the oxidation/reduction of polyvinylferrocene [146]. The phenomena were then confirmed by PBD [147] and EQCM [148]. It has been used in combination with EQCM [149].

In a similar way, the ion exchange of a solid metal complex (indium hexacyanoferrate) was studied using radiotracers, and the transport of anions was detected [150]. Using PBD, with convolution data processing, it was possible to assess the amount of anion contribution to charge compensation [145]. The specific adsorption of ions on metal electrodes, under potential control, was studied using radiotracers [151]. The same phenomenon has been studied using PBD techniques [152, 153], giving less quantitative data but easier choice of anions.

The technique was used to study ion exchange in polyaniline [144] and polypyrrole [154]. The results agree with those obtained by PBD [35, 129]. It is noteworthy that radiotracer technique, like PBD, can monitor fluxes of anions and cations.

14.6 Surface Plasmon Resonance

Surface plasmons are surface electromagnetic waves that propagate in a direction parallel to the metal/dielectric (or metal/vacuum) interface. Since the wave is on the boundary of the metal and the external medium (e.g., air or water), these oscillations are very sensitive to any change of this boundary, such as the adsorption of molecules to the metal surface or the refractive index of the solution in contact with the metal. Using light to excite surface plasmon waves, in the Kretschmann configuration, a thin metal film is evaporated onto the glass block. The polarized laser light illuminates the glass block, and an evanescent wave penetrates through the metal film. The plasmons are excited at the outer side of the film, sensing the refractive index of the solution and the presence of adsorbed species. The simplest configuration of surface plasmon resonance (SPR) uses the thin metal film as electrode, allowing monitoring of the changes in refractive index related to electrochemical reactions of solution species [155]. An alternative setup uses a glass fiber, covered by metal at the tip, placed close to the electrode surface as SPR sensor, allowing sensing of the refractive index gradient in front of the electrode [156–158], like PBD. It is noteworthy that the technique is not specific, like PBD, and detects the concentration gradients of all species present, including that of the supporting electrolyte. Therefore, the mass transport model has to include all the species involved. For example, as discussed in Chaps. 2 and 4, if ferrocyanide $[Fe(CN)_6]^{4-}$ ion is oxidized to ferricyanide $[Fe(CN)_6]^{3-}$, the SPR signal will depend of the dn/dC of both ions and not only of the oxidized species. Additionally, the contributions of the supporting electrolyte have to be considered. As in PBD, the use of surface-confined systems with binary electrolytes would allow straightforward interpretation. Fortunately, the entire theoretical framework devised for PBD [159] could be used to evaluate the SPR signal. Indeed, a digital simulation method to calculate the refractive index gradients, like those measured by SPR, under potentiostatic [160] and potentiodynamic conditions [161] has been described.

The SPR has been used to monitor the doping/dedoping of polyaniline [162], obtaining results in agreement with PBD because the measurable quantity is essentially the same. A similar situation was observed when the copolymers of aniline and 2-aminobenzoic acid were investigated by SPR [163]. It is found that the ion exchange mechanism is affected by the presence of the −COOH groups, as observed using PBD [164].

14.7 Interferometry

Optical interferometry is based on the detection of refractive index gradients, related to concentration or thermal gradients, through the observation of an interferometric pattern produced in front of the electrode surface [165]. It has relatively low sensitivity, slow response, and both complex experimental setup and analysis [166, 167]. Therefore, it was used mainly to study metal electrodeposition in electroplating cells and similar systems [168, 169]. The results are equivalent to those obtained by Eriksson [170], using PBD, but the latter technique shows faster response [171].

Kragt et al. used an interferometric microscope to measure concentration gradients in front of an electrode [172]. A similar experimental scheme was used by Plichon and coworkers [173] and applied to study the ion exchange in ruthenium oxide films, producing similar results than PBD. The microscope has imaging capabilities (ca. 5-μm resolution), while imaging ability is not available in PBD techniques.

14.8 Conclusions

There are several methods, direct and indirect, to measure flux of mobile species (ions, neutrals, solvent) during potential experiments. Some of them have been used extensively, such as EQCM and scanning electrochemical microscopy. The former is indirect and has been combined with success with PBD to study various electrochemical systems. Scanning electrochemical microscopy measures the same concentration gradients in solution but determines specific mobile species. Surface plasmon resonance, measured from the back of the electrode or with a fiber optical probe in front of the electrode, measures essentially the same information than PBD. This is a disadvantage for exploratory studies but an advantage in deeper studies of fluxes. PBD detects all the ions and neutrals, with low specificity. A combination of specific and unspecific techniques could be advantageous to elucidate different electrochemical phenomena.

References

1. Schmidt TJ, Gasteiger HA, Stab GD, Urban PM, Kolb FM, Behm RJ (1998) Characterization of high-surface-area electrocatalysts using a rotating disk electrode configuration. J Electrochem Soc 145:2354–2358. doi:10.1149/1.1838642
2. Prater KB, Bard AJ (1970) Rotating ring-disk electrodes. J Electrochem Soc 117:1517–1520. doi:10.1149/1.2407362
3. Harvey SLR, Parker KH, O'Hare D (2007) Theoretical evaluation of the collection efficiency at ring-disc microelectrodes. J Electroanal Chem 610:122–130. doi:10.1016/j.jelechem.2007.07.006
4. Toda K, Oguni S, Takamatsu Y, Sanemasa I (1999) A wall-jet ring disk electrode fabricated within a thin-layered micromachined cell. J Electroanal Chem 479:57–63. doi:10.1016/S0022-0728(99)00430-1
5. Schmidt TJ, Paulus UA, Gasteiger HA, Behm RJ (2001) The oxygen reduction reaction on a Pt/carbon fuel cell catalyst in the presence of chloride anions. J Electroanal Chem 508:41–47. doi:10.1016/S0022-0728(01)00499-5 DOI:dx.doi.org
6. Coutanceau C, Croissant MJ, Napporn T, Lamy C (2000) Electrocatalytic reduction of dioxygen at platinum particles dispersed in a polyaniline film. Electrochim Acta 46:579–588. doi:10.1016/S0013-4686(00)00641-1
7. Maruyama J, Inaba M, Ogumi Z (1998) Rotating ring-disk electrode study on the cathodic oxygen reduction at Nafion(R)-coated gold electrodes. J Electroanal Chem 458:175–182. doi:10.1016/S0022-0728(98)00362-3

8. Strbac S, Anastasijevic NA, Adzic RR (1994) Oxygen reduction on Au(111) and vicinal Au (332) faces: a rotating disc and disc-ring study. Electrochim Acta 39:983–990. doi:10.1016/0013-4686(94)85116-6
9. Zhang J, Pietro WJ, Lever ABP (1996) Rotating ring-disk electrode analysis of CO_2 reduction electrocatalyzed by a cobalt tetramethylpyridoporphyrazine on the disk and detected as CO on a platinum ring. J Electroanal Chem 403:93–100. doi:10.1016/0022-0728(95)04270-9
10. Gu Y, Zhang Y, Zhang F, Wei J, Wang C, Du Y, Ye W (2010) Investigation of photoelectrocatalytic activity of Cu2O nanoparticles for p-nitrophenol using rotating ring-disk electrode and application for electrocatalytic determination. Electrochim Acta 56:953–958. doi:10.1016/j.electacta.2010.09.051
11. Santos MC, Mascaro LH, Machado SAS (1998) Voltammetric and rotating ring-disk studies of underpotential deposition of Ag and Cu on polycrystalline Au electrodes in aqueous H_2SO_4. Electrochim Acta 43:2263–2272. doi:10.1016/S0013-4686(97)10171-2
12. Kötz R, Barbero C, Haas O (1993) Probe beam deflection for the analysis of ion fluxes at the solid/liquid interface. Ber Bunsenges Phys Chem 97:427–430. doi:10.1002/bbpc.19930970332
13. Barbero C, Miras MC, Kötz R (1992) Electrochemical mass transport studied by probe beam deflection: potential step experiments. Electrochim Acta 37:429–443. doi:10.1016/0013-4686(92)87032-U
14. Menshykau D, O’Mahony AM, Cortina-Puig M, del Campo FJ, Munoz FX, Compton RG (2010) Chronoamperometry on ring, ring-recessed and disk electrodes, and their arrays. The sensitive measurement of diffusion coefficients independent of a knowledge of concentration or number of electrons transferred. J Electroanal Chem 647:20–28. doi:10.1016/j.jelechem.2010.05.018
15. Kobayashi T, Yoneyama H, Tamura H (1984) Oxidative degradation pathway of polyaniline film electrodes. J Electroanal Chem 177:293–297. doi:10.1016/0022-0728(84)80230-2
16. Mu Shaolin M, Sun Donghao S (1991) The investigation of the electrochemical polymerization of aniline and o-methylaniline by means of the rotating ring-disk electrode. Synth Met 43:3085–3088. doi:10.1016/0379-6779(91)91244-5
17. Henderson MJ, Hillman AR, Vieil E (1998) A combined electrochemical quartz crystal microbalance (EQCM) and probe beam deflection (PBD) study of a poly(o-toluidine) modified electrode in perchloric acid solution. J Electroanal Chem 454:1–8. doi:10.1016/S0022-0728(98)00245-9
18. Vieil E (1994) Mass transfer and convolution. Part 1. Theory. J Electroanal Chem 364:9–15. doi:10.1016/0022-0728(93)02925-8
19. Vieil E, Meerholz K, Matencio T, Heinze J (1994) Mass transfer and convolution: Part II. In situ optical beam deflection study of ionic exchanges between polyphenylene films and a 1:1 electrolyte. J Electroanal Chem 368:183-191. doi: 10.1016/0022-0728(93)03110-B
20. Stockgen U, Heusler KE (1999) A mathematical method to eliminate the transfer time from disc to ring at a rotating ring-disc electrode. Electrochim Acta 44:2765–2770. doi:10.1016/S0013-4686(98)00398-3
21. Bard AJ, Denault G, Lee C, Mandler D, Wipf DO (1990) Scanning electrochemical microscopy: a new technique for the characterization and modification of surfaces. Acc Chem Res 23:357–363. doi:10.1021/ar00179a002
22. Troise Frank MH, Denuault G (1994) J Electroanal Chem 379:399–406. doi: 10.1016/0022-0728(94)87163-9
23. Bard AJ, Fu Fan RRF, Kwak J, Lev O (1989) Scanning electrochemical microscopy. Introduction and principles. Anal Chem 61:132–138. doi:10.1021/ac00177a011
24. Engstrom RC, Pharr CM (1989) Scanning electrochemical microscopy. Anal Chem 61:1099A–1104A. doi:10.1021/ac00194a002
25. Bard AJ, Fan FRF, Mirkin MV (1994) Scanning electrochemical microscopy. In: Bard AJ (ed) Electroanalytical chemistry. Marcel Dekker, New York

26. Bard AJ, Fan RFR, Mirkin M (1995) Scanning electrochemical microscopy. In: Rubenstein I (ed) Physical electrochemistry: principles, methods, and applications. Marcel Dekker, New York
27. Bard AJ, Denuault G, Friesner RA, Dornblaser BC, Tuckerman LS (1991) Scanning electrochemical microscopy: theory and application of the transient (chronoamperometric) SECM response. Anal Chem 63:1282–1288. doi:10.1021/ac00013a019
28. Fleischmann M, Rolinson DR, Pons S (1988) Ultramicroelectrodes. Datatech Systems, New York
29. Martin RD, Unwin PR (1998) Theory and experiment for the substrate generation/tip collection mode of the scanning electrochemical microscope: application as an approach for measuring the diffusion coefficient ratio of a redox couple. Anal Chem 70:276–284. doi:10.1021/ac970681p
30. Engstrom RC, Weber M, Wunder DJ, Burgess R, Winquist S (1986) Measurements within the diffusion layer using a microelectrode probe. Anal Chem 58:844–848. doi:10.1021/ac00295a044
31. Engstrom RC, Meany T, Tople R, Wightman RM (1987) Spatiotemporal description of the diffusion layer with a microelectode probe. Anal Chem 59:2005–2010. doi:10.1021/ac00142a024
32. Sánchez-Sánchez CM, Rodríguez-López J, Bard AJ (2008) scanning electrochemical microscopy. 60. Quantitative calibration of the secm substrate generation/tip collection mode and its use for the study of the oxygen reduction mechanism. Anal Chem 80:3254–3260. doi: 10.1021/ac702453n
33. Syritski V, Gyurcsanyi RE, Opik A, Toth K (2005) Synthesis and characterization of inherently conducting polymers by using scanning electrochemical microscopy and electrochemical quartz crystal microbalance. Synth Met 152:133–136. doi:10.1016/j.synthmet.2005.07.097
34. Kwak J, Anson FC (1992) Monitoring the ejection and incorporation of ferricyanide [Fe(CN) 63-] and ferrocyanide [Fe(CN)64-] counterions at protonated poly(4-vinylpyridine) coatings on electrodes with the scanning electrochemical microscope. Anal Chem 64:250–256. doi:10.1021/ac00027a003
35. Schmidt VM, Barbero C, Koetz R (1993) The ion exchange in polypyrrole in aqueous electrolytes. A probe beam deflection study of the effect of fixed negative charges. J Electroanal Chem 352:301–307. doi:10.1016/0022-0728(93)80272-J
36. Arca M, Mirkin MV, Bard AJ (1995) Polymer films on electrodes. 26. Study of ion transport and electron transfer at polypyrrole films by scanning electrochemical microscopy. J Phys Chem 99:5040–5050. doi:10.1021/j100014a026
37. Barbero CA (2005) Ion exchange at the electrode/electrolyte interface studied by probe beam deflection techniques. Phys Chem Chem Phys 7:1885–1899. doi:10.1039/b419382b
38. Troise Frank MH, Denuault G (1994) Relationship between proton concentration and electronic charge as a function of ionic-strength during the oxidation of polyaniline. J Electroanal Chem 379:399–406. doi:10.1016/0022-0728(94)87163-9
39. Carano M, Holt KB, Bard AJ (2003) Scanning electrochemical microscopy. 49. Gas-phase scanning electrochemical microscopy measurements with a clark oxygen ultramicroelectrode. Anal Chem 75:5071–5079. doi: 10.1021/ac034546q
40. Nugues S, Denuault G (1996) Scanning electrochemical microscopy: amperometric probing of diffusional ion fluxes through porous membranes and human dentine. J Electroanal Chem 408:125–140. doi:10.1016/0022-0728(96)04523-8
41. Etienne M, Schulte A, Mann S, Jordan G, Dietzel ID, Schuhmann W (2004) Constant-distance mode scanning potentiometry. 1. Visualization of calcium carbonate dissolution in aqueous solution. Anal Chem 76:3682–3688. doi:10.1021/ac0349227
42. Amatore C, Szunerits S, Thouin L (2000) Mapping concentration profiles within the diffusion layer of an electrode: Part II. Potentiometric measurements with an ultramicroelectrode. Electrochem Commun 2:248–253. doi:10.1016/S1388-2481(00)00016-3

43. Horrocks BR, Mirkin MV, Pierce DT, Bard AJ, Nagy G, Toth K (1993) Scanning electrochemical microscopy. 19. Ion-selective potentiometric microscopy. Anal Chem 65:1213–1224. doi:10.1021/ac00057a019
44. Comstock DJ, Elam JW, Pellin MJ, Hersam MC (2010) Integrated ultramicroelectrode – nanopipet probe for concurrent scanning electrochemical microscopy and scanning ion conductance microscopy. Anal Chem 82:1270–1276. doi:10.1021/ac902224q
45. Chen C-C, Derylo MA, Baker LA (2009) Measurement of ion currents through porous membranes with scanning ion conductance microscopy. Anal Chem 81:4742–4751. doi:10.1021/ac900065p
46. Tsionsky M, Bard AJ, Mirkin MV (1996) Scanning electrochemical microscopy. 34. Potential dependence of the electron-transfer rate and film formation at the liquid/liquid interface. J Phys Chem 100:17881–17888. doi:10.1021/jp9612700
47. Shimazu K, Murakoshi K, Kita H (1990) Quantitative and in-situ measurements of proton transport at polyaniline film electrodes. J Electroanal Chem 277:347–353. doi:10.1016/0022-0728(90)85114-K
48. Martin MI, McHale NG, Melzak KA, Gizeli E (2004) Pulse mode shear horizontal-surface acoustic wave (SH-SAW) system for liquid based sensing applications. Biosens Bioelectron 19:627–632. doi:10.1016/S0956-5663(03)00257-4
49. Abruña HD (ed) (1991) Electrochemical interfaces: modern techniques for in-situ interface characterization. VCH, Deerfield
50. Sauerbrey G (1959) Verwendung von Schwingquarzen zur Wägung dünner Schichten und zur Mikrowägung. Z Phys 155:206–209. doi:10.1007/BF01337937
51. Schumacher R (1990) The quartz microbalance: a novel approach to the in-situ investigation of interfacial phenomena at the solid/liquid junction. Angew Chem Int Ed Engl 29:329–343. doi:10.1002/anie.199003293
52. Buttry DA, Ward MD (1992) Measurement of interfacial processes at electrode surfaces with the electrochemical quartz crystal microbalance. Chem Rev 92:1335–1379. doi:10.1021/cr00014a006
53. Oliveira RTS, Santos MC, Bulhões LOS, Pereira EC (2004) Rh electrodeposition on Pt in acidic medium: a study using cyclic voltammetry and an electrochemical quartz crystal microbalance. J Electroanal Chem 569:233–240. doi:10.1016/j.jelechem.2004.03.006
54. Inzelt G (1993) Oscillations of the EQCM frequency response in the course of open-circuit copper dissolution in aqueous solutions of H2SO4 and CuSO4. J Electroanal Chem 348:465–471. doi:10.1016/0022-0728(93)80153-9
55. Bruckenstein S, Shay M (1985) Experimental aspects of use of the quartz crystal microbalance in solution. Electrochim Acta 30:1295–1300. doi:10.1016/0013-4686(85)85005-2 DOI: dx.doi.org
56. Jusys Z, Bruckenstein S (2000) Electrochemical quartz crystal microbalance study of perchlorate and perrhenate anion adsorption on polycrystalline gold electrode. Electrochem Commun 2:412–416. doi:10.1016/S1388-2481(00)00044-8
57. Uchida H, Ikeda N, Watanabe M (1997) Electrochemical quartz crystal microbalance study of copper adatoms on gold electrodes Part II. Further discussion on the specific adsorption of anions from solutions of perchloric and sulfuric acid. J Electroanal Chem 424:5–12. doi:10.1016/S0022-0728(96)04924-8
58. Lei H-W, Uchida H, Watanabe M (1996) Electrochemical quartz crystal microbalance study of adsorption of iodide on highly ordered Au(111). J Electroanal Chem 413:131–136. doi:10.1016/0022-0728(96)04675-X
59. Deakin MR, Li TT, Melroy OR (1988) A study of the electrosorption of bromide and iodide ions on gold using the quartz crystal microbalance. J Electroanal Chem 243:343–351. doi:10.1016/0022-0728(88)80039-1
60. Shu ZX, Bruckenstein S (1991) Iodine adsorption studies at platinum. J Electroanal Chem 31:263–277. doi:10.1016/0022-0728(91)85019-L

61. Bruckenstein S, Shay M (1985) An in situ weighing study of the mechanism for the formation of the adsorbed oxygen monolayer at a gold electrode. J Electroanal Chem 188:131–136. doi:10.1016/S0022-0728(85)80057-7
62. Shimazu K, Kita H (1992) In situ measurements of water adsorption on a platinum electrode by an electrochemical quartz crystal microbalance. J Electroanal Chem 341:361–367. doi:10.1016/0022-0728(92)80494-O
63. Lori JA, Hanawa T (2001) Characterization of adsorption of glycine on gold and titanium electrodes using electrochemical quartz crystal microbalance. Corros Sci 43:2111–2120. doi:10.1016/S0010-938X(01)00003-8
64. Hepel M, Kanige K, Bruckenstein S (1989) In situ underpotential deposition study of lead on silver using the electrochemical quartz crystal microbalance: direct evidence for lead(II) adsorption before spontaneous charge transfer. J Electroanal Chem 266:409–421. doi:10.1016/0022-0728(89)85085-5
65. Chatenet M, Soldo-Olivier Y, Chainet E, Faure R (2007) Electrochemical quartz crystal microbalance determination of nickel formal partial charge number during nickel-underpotential deposition on platinum in sulphate media. Electrochem Commun 9:1463–1468. doi:10.1016/j.elecom.2007.02.001
66. Bruckenstein S, Wilde CP, Shay M, Hillman AR, Loveday DC (1989) Observation of kinetic effects during interfacial transfer at redox polymer films using the quartz crystal microbalance. J Electroanal Chem 258:457–462. doi:10.1016/0022-0728(89)85128-9
67. Bohnke O, Vuillemin B, Gabrielli C, Keddam M, Perrot H, Takenouti H, Torresi R (1995) An electrochemical quartz crystal microbalance study of lithium insertion into thin films of tungsten trioxide I. Modeling of the ionic insertion mechanism. Electrochim Acta 40:2755–2764. doi:10.1016/0013-4686(95)00254-C
68. Kim K, Jureviciute I, Bruckenstein S (2001) Electrochemical quartz crystal microbalance studies of anion and pH effects on water fluxes accompanying redox switching of Prussian blue. Electrochim Acta 46:4133–4140. doi:10.1016/S0013-4686(01)00707-1
69. Hillman AR, Loveday DC, Bruckenstein S (1989) Thermodynamic changes in ion and solvent populations accompanying redox switching in polyvinylferrocene films. J Electroanal Chem 274:157–166. doi:10.1016/0022-0728(89)87037-8
70. Peres RCD, De Paoli M-A, Torresi RM (1992) The role of ion exchange in the redox processes of polypyrrole/dodecyl sulfate films as studied by electrogravimetry using a quartz crystal microbalance. Synth Met 48:259–270. doi:10.1016/0379-6779(92)90229-C
71. Lim JY, Paik W-K, Yeo I-H (1995) A study of ion transports and growth of conducting polypyrrole with electrochemical quartz crystal microbalance. Synth Met 69:451–454. doi:10.1016/0379-6779(94)02526-5
72. Shimazu K, Yagi I, Sato Y, Uosaki K (1994) Electrochemical quartz crystal microbalance studies of self-assembled monolayers of 11-ferrocenyl-1-undecanethiol: structure-dependent ion-pairing and solvent uptake. J Electroanal Chem 372:117–124. doi:10.1016/0022-0728(94)03296-3 DOI:dx.doi.org
73. Barisci JN, Wallace GG, Baughman RH (2000) Electrochemical quartz crystal microbalance studies of single-wall carbon nanotubes in aqueous and non-aqueous solutions. Electrochim Acta 46:509–517. doi:10.1016/S0013-4686(00)00634-4
74. Morallón E, Arias-Pardilla J, Calo JM, Cazorla-Amorós D (2009) Arsenic species interactions with a porous carbon electrode as determined with an electrochemical quartz crystal microbalance. Electrochim Acta 54:3996–4004. doi:10.1016/j.electacta.2009.02.023
75. Visscher W, Gootzen JFE, Cox AP, van Veen JAR (1997) Electrochemical quartz crystal microbalance measurements of CO adsorption and oxidation on Pt in various electrolytes. Electrochim Acta 43:533–547. doi:10.1016/S0013-4686(97)00092-3
76. Garcia G, Bruno MM, Planes GA, Rodriguez JL, Barbero CA, Pastor E (2008) Phys Chem Chem Phys 10:6677–6685. doi:10.1039/B806938G
77. Liu C, Wang Y, Zhu G, Dong S (1997) Study of cupric hexacyanoferrate-modified platinum electrodes using probe beam deflection and electrochemical quartz crystal microbalance

techniques. Electrochim Acta 42:1795–1800. doi:10.1016/S0013-4686(96)00379-9 DOI:dx.doi.org

78. French HM, Henderson MJ, Hillman AR, Vieil E (2001) Ion and solvent transfer discrimination at a nickel hydroxide film exposed to LiOH by combined electrochemical quartz crystal microbalance (EQCM) and probe beam deflection (PBD) techniques. J Electroanal Chem 500:192–207. doi:10.1016/S0022-0728(00)00373-9
79. Orata D, Buttry DA (1987) Determination of ion populations and solvent content as functions of redox state and pH in polyaniline. J Am Chem Soc 109:3574–3581. doi:10.1021/ja00246a013
80. Miras MC, Barbero C, Koetz R, Haas O (1994) Electrochemical quartz crystal microbalance investigation of the ion exchange mechanism in the first oxidation step of polyaniline in HClO4. J Electroanal Chem 369:193–197. doi:10.1016/0022-0728(94)87098-5
81. Torresi RM, Cordoba de Torresi SI, Gabrielli C, Keddam M, Takenouti H (1993) Quartz crystal microbalance characterization of electrochemical doping of polyaniline films. Synth Met 61:291–296. doi:10.1016/0379-6779(93)91275-7
82. Miras MC, Barbero C, Koetz R, Haas O, Schmidt VM (1992) Quartz crystal microbalance and probe beam deflection studies of poly(1-hydroxyphenazine) modified electrodes. J Electroanal Chem 338:279–297. doi:10.1016/0022-0728(92)80429-8
83. Barbero C, Miras MC, Haas O, Kötz R (1993) Comparative study of the ion exchange and electrochemical properties of sulfonated polyaniline (SPAN) and polyaniline (PANI). Synth Met 55–57:1539–1544. doi:10.1016/0379-6779(93)90281-Z
84. Barbero C, Miras MC, Kötz R (1997) Sulphonated polyaniline (SPAN) films as cation insertion electrodes battery applications Part II: Exchange of mobile species in aqueous and non-aqueous solutions. J Electroanal Chem 437:191–198. doi:10.1016/S0022-0728(97)00357-4
85. Mello Q, Torresi RM, Cordoba de Torresi SI, Ticianelli EA (2000) Ellipsometric, electrogravimetric, and spectroelectrochemical studies of the redox process of sulfonated polyaniline. Langmuir 16:7835–7841. doi:10.1021/la000391v
86. Grumelli DE, Forzani ES, Morales GM, Miras MC, Barbero CA, Calvo EJ (2004) Microgravimetric study of electrochemically controlled nucleophilic addition of sulfite to polyaniline. Langmuir 20:2349–2355. doi:10.1021/la0354990
87. Inzelt G, Kertesz V (1997) Effect of poly(aniline) pseudocapacitance on potential and EQCM frequency oscillations arising in the course of galvanostatic oxidation of formic acid on platinum. Electrochim Acta 42:229–235. doi:10.1016/0013-4686(96)00148-X
88. Kertesz V, Inzelt G, Barbero C, Koetz R, Haas O (1995) Probe beam deflection studies of electrochemical oscillations during galvanostatic oxidation of formic acid at a platinum electrode. J Electroanal Chem 392:91–95. doi:10.1016/0022-0728(95)04085-3
89. Omura J, Yano H, Watanabe M, Uchida H (2011) Electrochemical quartz crystal microbalance analysis of the oxygen reduction reaction on Pt-based electrodes. Part 1: Effect of adsorbed anions on the oxygen reduction activities of Pt in HF, HClO4, and H_2SO_4 solutions. Langmuir 27:6464–6470. doi: 10.1021/la200694a
90. Ivanchenko MI, Kobayashi H, Kulik EA, Dobrova NB (1995) Studies on polymer solutions, gels and grafted layers using the quartz crystal microbalance technique. Anal Chim Acta 314:23–31. doi:10.1016/0003-2670(95)00262-X
91. Barbero C, Calvo EJ, Etchenique R, Morales GM, Otero M (2000) An EQCM electroacoustic study of poly(vinylferrocene) modified electrodes in different aqueous electrolytes. Electrochim Acta 45:3895–3906. doi:10.1016/S0013-4686(00)00452-7
92. Gale RJ (1988) Spectroelectrochemistry: theory and practice. Plenum, New York
93. Planes GA, Moran E, Rodriguez JL, Barbero C, Pastor E (2003) Electrochemical behavior of benzaldehyde on polycrystalline platinum. An in situ FTIR and DEMS study. Langmuir 19:8899–8906. doi:10.1021/la034627h

94. Rajeshwahr K, Lezna RO, de Tacconi NR (1992) Light in an electrochemical tunnel? Solving analytical problems in electrochemistry via spectroscopy. Anal Chem 64:429A–441A. doi:10.1021/ac00031a001
95. Lapkowski M, Genies EM (1990) Spectroelectrochemical studies of proton exchange processes in the electrochemical reactions of polyaniline using pH indicators. J Electroanal Chem 284:127–140. doi:10.1016/0022-0728(90)87067-T
96. Nath A, Kanungo M, Contractor AQ (2003) In situ measurement of pH in the interior of conducting polymer microtubules. J Electroanal Chem 557:119–125. doi:10.1016/S0022-0728(03)00354-1 DOI:dx.doi.org
97. Engstrom RC, Ghaffari S, Qu H (1992) Fluorescence imaging of electrode-solution interfacial processes. Anal Chem 64:2525–2529. doi:10.1021/ac00045a012
98. Vitt JE, Engstrom RC (1997) Imaging of oxygen evolution and oxide formation using quinine fluorescence. Anal Chem 69:1070–1076. doi:10.1021/ac960816b
99. Reddington E, Sapienza A, Gurau B, Viswanathan R, Sarangapani S, Smotkin ES, Mallouk TE (1998) Combinatorial electrochemistry: a highly parallel, optical screening method for discovery of better electrocatalyst. Science 280:1735–1737. doi:10.1126/science.280.5370.1735
100. Cannan S, Macklam ID, Unwin PR (2002) Three-dimensional imaging of proton gradients at microelectrode surfaces using confocal laser scanning microscopy. Electrochem Commun 4:886–892. doi:10.1016/S1388-2481(02)00482-4 DOI:dx.doi.org
101. Posdorfer J, Olbrich-Stock M, Schindler RN (1994) Spatially resolved UV–VIS absorption measurements in planar, cylindrical and spherical diffusion layers. Kinetic investigations of a heterogeneous electron transfer reaction Electrochim Acta 39:2005–2013. doi:10.1016/0013-4686(94)85081-X
102. McCreery RL (1988) Electronic and vibrational spectroscopy of electrode surfaces. Prog Anal Spectrosc 11:141–178
103. Jan CC, McCreery RL, Gamble T (1985) Diffusion layer imaging: spatial resolution of electrochemical concentration profiles. Anal Chem 57:1763–1765. doi:10.1021/ac00285a059
104. Rossi P, McCurdy CW, McCreery RL (1981) Diffractive spectroelectrochemistry. Use of diffracted light for monitoring electrogenerated chromophores. J Am Chem Soc 103:2524–2529. doi:10.1021/ja00400a006
105. Jan CC, McCreery RL (1986) High-resolution spatially resolved visible absorption spectrometry of the electrochemical diffusion layer. Anal Chem 58:2771–2777. doi:10.1021/ac00126a041
106. Jan CC, Lavine BK, McCreery RL (1985) High-sensitivity spectroelectrochemistry based on electrochemical modulation of an absorbing analyte. Anal Chem 57:752–758. doi:10.1021/ac00280a040
107. Korzeniewski C (2002) Infrared spectroelectrochemistry. In: Griffiths PM, Chalmers JM (eds) Handbook of vibrational spectroscopy. Wiley, New York
108. Korzeniewski C (1999) Vibrational coupling effects on infrared spectra of adsorbates on electrodes. In: Wieckowski A (ed) Interfacial electrochemistry. Marcel Dekker, New York
109. Garcia G, Rodriguez JL, Lacconi GI, Pastor E (2006) Adsorption and oxidation pathways of thiourea at polycrystalline platinum electrodes. J Electroanal Chem 588:169–178. doi:10.1016/j.jelechem.2005.12.012
110. Planes GA, Rodríguez JL, Miras MC, García G, Pastor E, Barbero C (2010) Spectroscopic evidence for intermediate species formed during aniline polymerization and polyaniline degradation. Phys Chem Chem Phys 12:10584–10593. doi:10.1039/C002920C
111. Martinez Y, Hernandez R, Kalaji M, Marquez OM, Marquez J (2004) SNIFTIRS studies of the electrochemical oxidation of 1,3-dimethoxybenzene on platinum in acetonitrile/tetrabutilammonium electrolytes. J Electroanal Chem 563:145–152. doi:10.1016/j.jelechem.2003.09.001

112. Salimon J, Hernandez-Romero RM, Kalaji M (2002) The dynamics of the conversion of linear to bridge bonded CO on Cu. J Electroanal Chem 538–539:99–108. doi:10.1016/S0022-0728(02)01052-5
113. Urban MW (1996) Attenuated total reflectance spectroscopy of polymers: theory and practice. American Chemical Society, Washington
114. Fringeli UP (1999) ATR and reflectance IR spectroscopy, applications. In: Lindon J (ed) Encyclopedia of spectroscopy and spectrometry. Academic, Oxford. ISBN: 10.1016/B978-0-12-374413-5.00104-4
115. Ping Z, Nauer GE (1996) In situ FTIR-ATR spectroscopic investigations on the polymerization process and the redox behavior of poly(thienylpyrrole) thin film electrodes in aqueous and non-aqueous solutions. Part 1. Characterization of the polymerization process in acetonitrile containing different supporting salts. J Electroanal Chem 416:157–166. doi:10.1016/S0022-0728(96)04723-7
116. Zippel E, Kellner R, Krebs M, Breiter W (1992) ATR-IR studies of CO adsorption from solutions. J Electroanal Chem 330:521–527. doi:10.1016/0022-0728(92)80328-2
117. Heinen M, Chen YX, Jusys Z, Behm RJ (2007) CO adsorption kinetics and adlayer build-up studied by combined ATR-FTIR spectroscopy and on-line DEMS under continuous flow conditions. Electrochim Acta 53:1279–1289. doi:10.1016/j.electacta.2007.05.020
118. Webster RD (2003) In situ electrochemical-ATR-FTIR spectroscopic studies on solution phase 2,4,6-tri-substituted phenoxyl radicals. Electrochem Commun 5:6–11. doi:10.1016/S1388-2481(02)00517-9
119. Hatta A, Sasaki Y, Suutaka W (1986) Polarization modulation infrared spectroscopic measurements of thiocyanate and cyanide at the silver electrode/aqueous electrolyte interface by means of Kretschmann's ATR prism configuration. J Electroanal Chem 215:93–102. doi:10.1016/0022-0728(86)87007-3
120. Chen S, Peng HM, Webster RD (2010) Infrared and UV-vis spectra of phenoxonium cations produced during the oxidation of phenols with structures similar to vitamin E. Electrochim Acta 55:8863–8869. doi:10.1016/j.electacta.2010.07.096
121. Zhu Y, Uchida H, Yajima T, Watanabe M (2001) Attenuated total reflection – Fourier transform infrared study of methanol oxidation on sputtered Pt film electrode. Langmuir 17:146–154. doi:10.1021/la000457m
122. Shao MH, Warren J, Marinkovic NS, Faguy PW, Adzic RR (2005) In situ ATR-SEIRAS study of electrooxidation of dimethyl ether on a Pt electrode in acid solutions. Electrochem Commun 7:459–465. doi:10.1016/j.elecom.2005.02.024
123. Boscheto E, Batista BC, Lima RB, Varela H (2010) A surface-enhanced infrared absorption spectroscopic (SEIRAS) study of the oscillatory electro-oxidation of methanol on platinum. J Electroanal Chem 642:17–21. doi:10.1016/j.jelechem.2010.01.026
124. Ping Z, Nauer GE (1997) In situ FTIR-ATR spectroscopic investigations on the redox behavior of poly(thienylpyrrole) thin film electrodes in non-aqueous solutions. Synth Met 84:843–844. doi:10.1016/S0379-6779(96)04175-6
125. Ping Z, Neugebauer H, Neckel A (1996) FTIR ATR spectroelectrochemical investigations of polyaniline with perrhenate as a new doping system. Electrochim Acta 41:767–772. doi:10.1016/0013-4686(95)00365-7
126. Kuzmany H, Sariciftci HS, Neugebauer H, Neckel A (1988) Evidence for two separate doping mechanisms in the polyaniline system. Phys Rev Lett 60:212–215. doi:10.1103/PhysRevLett.60.212
127. Ping Z, Neugebauer H, Neckel A (1995) The determination of the anion content in polyaniline as a function of the pH value and the electrode potential: an in situ FTIR spectroscopic study. Synth Met 69:161–162. doi:10.1016/0379-6779(94)02403-0
128. Kvarnstrom C, Neugebauer H, Ivaska A, Sariciftci NS (2000) Vibrational signatures of electrochemical p- and n-doping of poly(3,4-ethylenedioxythiophene) films: an in situ attenuated total reflection Fourier transform infrared (ATR-FTIR) study. J Mol Struct 521:271–277. doi:10.1016/S0022-2860(99)00442-1

129. Barbero C, Miras MC, Haas O, Kötz R (1991) Direct in situ evidence for proton/anion exchange in polyaniline films by means of probe beam deflection. J Electrochem Soc 138:669–672. doi:10.1149/1.2085655
130. Pham M-C, Moslih J, Barbero C, Haas O (1991) Influence of the cation size on the charge compensation process in poly(1-naphthol) coated electrodes: multiple internal reflection FTIR spectroscopy (MIRFTIRS) and probe beam deflection (PBD) study. J Electroanal Chem 316:143–154. doi:10.1016/0022-0728(91)87042-3 DOI:dx.doi.org
131. Barbero C, Haas O, Mostefai M, Pham MC (1995) Ion exchange in poly(5-amino-1-naphthol) probe beam deflection and multiple internal reflection Fourier transform infrared spectroscopic studies. J Electrochem Soc 142:1829–1834. doi:10.1149/1.2044201
132. Piro B, Bazzaoui EA, Pham MC, Novak P, Haas O (1999) Multiple internal reflection FTIR spectroscopic (MIRFTIRS) study of the redox process of poly(5-amino-1,4-naphthoquinone) film in aqueous and organic media. Electrochim Acta 44:1953–1961. doi:10.1016/S0013-4686(98)00304-1
133. Tugas I, Lambert JM, Maillols J, Bribes JL, Pourcelly G, Gavach C (1993) Identification of the ionic species in anion exchange membranes equilibrated with sulphuric acid solutions by means of Raman spectroscopy and radiotracers. J Membr Sci 78:25–33. doi:10.1016/0376-7388(93)85244-Q
134. Thibault C, Huguet P, Sistat P, Pourcelly G (2002) Confocal Raman micro-spectroscopy and electrochemical investigation of anion transport through ion-exchange membranes. Desalination 149:429–433. doi:10.1016/S0011-9164(02)00770-1
135. Lopez-Garcia U, Antano-Lopez R, Orozco G, Chapman T, Castaneda F (2009) Characterization of electrodialysis membranes by electrochemical impedance spectroscopy at low polarization and by Raman spectroscopy. Sep Purif Technol 68:375–381. doi:10.1016/j.seppur.2009.06.012
136. Deabate S, Fatnassi R, Sistat P, Huguet P (2008) In situ confocal-Raman measurement of water and methanol concentration profiles in Nafion(R) membrane under cross-transport conditions. J Power Sources 176:39–45. doi:10.1016/j.jpowsour.2007.10.044
137. Amatore C, Bonhomme F, Bruneel J-L, Servant L, Thouin L (2000) Mapping concentration profiles within the diffusion layer of an electrode: Part I. Confocal resonance Raman microscopy. Electrochem Commun 2:235–239. doi:10.1016/S1388-2481(00)00015-1
138. Horanyi G (2004) Studies of electrified solid/liquid interfaces. In: Horanyi G (ed) Radiotracer studies of interfaces. Elsevier, Amsterdam
139. Horanyi G, Rizmayer EM, Inzelt G (1978) Radiotracer study of the adsorption of phosphoric acid on platinized platinum electrodes in the presence of different ions and oxalic acid. J Electroanal Chem 93:183–194. doi:10.1016/S0022-0728(78)80214-9
140. Lukomska A, Sobkowski J (2005) Adsorption of urea on a polycrystalline silver electrode; comparison of electrochemical and radiometric methods. J Solid State Electrochem 9:277–283. doi:10.1007/s10008-004-0603-0
141. Horanyi G, Inzelt G, Kulesza PJ (1990) Radiotracer study of metal hexacyanometalate films. Sorption of Ca2+ ions into cupric hexacyanoferrate films. Electrochim Acta 35:811–816. doi:10.1016/0013-4686(90)90073-9
142. Inzelt G, Horanyi G, Chambers JQ, Day EW (1987) Combined electrochemical and radiotracer (cyclic voltradiometric) study of the motion of counter-ions in tetracyanoquinodimethane modified electrodes. J Electroanal Chem 218:297–306. doi:10.1016/0022-0728(87)87024-9
143. Inzelt G, Horányi G (1989) Combined electrochemical and radiotracer study on the ionic charge transport coupled to electron transfer and ionic equilibria in electroactive polymer films on electrodes. J Electrochem Soc 136:1747–1752. doi:10.1149/1.2097004
144. Horanyi G, Inzelt G (1988) Anion-involvement in electrochemical transformations of polyaniline. A radiotracer study. Electrochim Acta 33:947–952. doi:10.1016/0013-4686(88)80093-8

145. Csahok E, Vieil E, Inzelt G (1998) Probe beam deflection study of the transport of ions during the redox reaction of indium-hexacyanoferrate films. J Electroanal Chem 457:251–255. doi:10.1016/S0022-0728(98)00290-3
146. Inzelt G, Horanyi G, Chambers JQ (1987) Radiotracer study of the sorption of counter- and co-ions in tetracyanoquinodimethane and poly(vinyl ferrocene) modified electrodes. Electrochim Acta 32:757–763. doi:10.1016/0013-4686(87)85106-X
147. Barbero C, Calvo EJ, Miras MC, Koetz R, Haas O (2002) A probe beam deflection study of ion exchange at poly(vinylferrocene) films in aqueous and nonaqueous electrolytes. Langmuir 18:2756–2764. doi:10.1021/la010999j
148. Jureviciute I, Bruckenstein S, Hillman AR (2006) Cation participation during the redox switching of poly(vinylferrocene) films in aqueous 0.05 M perchlorate solutions. Part 1: Cyclic voltammetry and the EQCM. Electrochim Acta 51:2351–2357. doi:10.1016/j.electacta.2005.02.155
149. Wasberg M, Bacskai J, Inzelt G, Horanyi G (1996) The harmony of EQCM and radiotracer sorption results obtained in the course of voltammetric study of a rhodized electrode. J Electroanal Chem 418:195–198. doi:10.1016/S0022-0728(96)04854-1
150. Malik MA, Horanyi G, Kulesza PJ, Inzelt G, Kertesz V, Schmidt R, Czirok E (1998) Microgravimetric monitoring of transport of cations during redox reactions of indium(III) hexacyanoferrate(III, II): radiotracer evidence for the flux of anions in the film. J Electroanal Chem 452:57–62. doi:10.1016/S0022-0728(98)00095-3
151. Horanyi G, Wasberg M (1996) Comparative radiotracer study of the adsorption of Cl-, HSO4- and H2PO4- anions on rhodized electrodes. J Electroanal Chem 404:291–298. doi:10.1016/0022-0728(95)04353-5
152. Bidoia ED, McLarnon FR, Cairns EJ (2000) Investigation of anion adsorption on platinum electrodes in aqueous media by probe beam deflection. J Electroanal Chem 482:75–80. doi:10.1016/S0022-0728(00)00003-6
153. García G, Bruno MM, Planes GA, Rodriguez JL, Barbero CA, Pastor E (2008) Probe beam deflection studies of nanostructured catalyst materials for fuel cells. Phys Chem Chem Phys 10:6677–6685. doi:10.1039/B806938G
154. Inzelt G, Horanyi G (1987) Combined electrochemical and radiotracer study of anion sorption from aqueous solutions into polypyrrole films. J Electroanal Chem 230:257–265. doi:10.1016/0022-0728(87)80147-X
155. Dong H, Cao X, Li CM, Hu W (2008) An in situ electrochemical surface plasmon resonance immunosensor with polypyrrole propylic acid film: comparison between SPR and electrochemical responses from polymer formation to protein immunosensing. Biosens Bioelectron 23:1055–1062. doi:10.1016/j.bios.2007.10.026
156. Wang S, Huang X, Shan X, Foley KJ, Tao N (2010) Electrochemical surface plasmon resonance: basic formalism and experimental validation. Anal Chem 82:935–941. doi:10.1021/ac902178f
157. Andersson O, Ulrich C, Björefors F, Liedberg B (2008) Imaging SPR for detection of local electrochemical processes on patterned surfaces. Sens Actuators B Chem 134:545–550. doi:10.1016/j.snb.2008.05.042
158. Iwasaki Y, Horiuchi T, Morita M, Niwa O (1999) Electrochemical reaction of Fe(CN) 3−/4 − 6 on gold electrodes analyzed by surface plasmon resonance. Surf Sci 427–428:195–198. doi:10.1016/S0039-6028(99)00264-2 DOI:dx.doi.org
159. Rudnicki JD, McLarnon FR, Cairns EJ (1991) In situ characterization of electrode processes by photothermal deflection spectroscopy. In: Varma R, Selman JR (eds) Techniques for characterization of electrodes and electrochemical processes. Plenum, New York
160. Garay F, Barbero CA (2006) Charge neutralization process of mobile species at any distance from the electrode/solution interface. 1. Theory and simulation of concentration and concentration gradients developed during potentiostatic conditions. Anal Chem 78:6733–6739. doi:10.1021/ac0603678

161. Garay F, Barbero CA (2008) Charge neutralization process of mobile species developed during potentiodynamic conditions. Part 1: Theory. J Electroanal Chem 624:218–227. doi:10.1016/j.jelechem.2008.09.010
162. Baba A, Tian S, Stefani F, Xia C, WangZ ARC, Johannsmann D, Knoll W (2004) Electropolymerization and doping/dedoping properties of polyaniline thin films as studied by electrochemical-surface plasmon spectroscopy and by the quartz crystal microbalance. J Electroanal Chem 562:95–103. doi:10.1016/j.jelechem.2003.08.012
163. Wang Y, Knoll W (2006) In situ electrochemical and surface plasmon resonance (SPR) studies of aniline-carboxylated aniline copolymers. Anal Chim Acta 558:150–157. doi:10.1016/j.aca.2005.11.006
164. Salavagione HJ, Acevedo DF, Miras MC, Barbero C (2003) Redox coupled ion exchange in copolymers of aniline with aminobenzoic acids. Port Electrochim Acta 21:245–254
165. McLarnon FR, Muller RH, Tobias CW (1976) Interferometric study of transient diffusion layers. Electrochim Acta 21:101–105. doi:10.1016/0013-4686(76)85045-1
166. Forgacs C, Leibovitz J, O'Brien RN, Spiegler KS (1975) Interferometric study of concentration profiles in solutions near membrane surfaces. Electrochim Acta 20:555–563. doi:10.1016/0013-4686(75)80006-5
167. O'Brien RN, Michalik W, Visaisouk S (1986) A laser interferometric study of chlorine evolution from concentrated NaCl solutions. Electrochim Acta 31:1675–1677. doi:10.1016/0013-4686(86)87093-1
168. Mueller RH (1973) Optical techniques in electrochemistry. In: Advances in electrochemistry and electrochemical engineering. Wiley, New York
169. Shaposhnik VA, Vasil'eva VI, Praslov DB (1995) Concentration fields of solutions under electrodialysis with ion-exchange membranes. J Membr Sci 101:23–30. doi:10.1016/0376-7388(94)00270-9
170. Eriksson R (1996) A study of the PBD-technique using the copper refining cell as a model system. Electrochim Acta 41:871–887. doi:10.1016/0013-4686(95)00384-3
171. Eriksson R (1995) Experimental determinations of concentration fields in the copper and silver refining systems using probe-beam deflection. Electrochim Acta 40:725–773. doi:10.1016/0013-4686(94)00334-W
172. Kragt HJ, Smith CP, White HS (1990) Refractive index mapping of concentration profiles. J Electroanal Chem 378:403–407. doi:10.1016/0022-0728(90)85152-U
173. Fantini J, Fournier D, Boccara AC, Plichon V (1997) Microflux detection at the solid-liquid interface with an interferometric microscope. Electrochim Acta 42:937–944. doi:10.1016/S0013-4686(96)00259-9

About the Author

Cesar A. Barbero

Cesar A. Barbero (born 1961) has been professor at National Rio Cuarto University (UNRC), in Rio Cuarto, Argentina, since 1995 and is presently full professor and head of the Advanced Materials Program at UNRC. He obtained his B.Sc. in chemistry in 1984 and his Ph.D. in chemistry in 1988 at the same institution. He worked as post-doctoral associate and senior scientist for the Paul Scherrer Institut (Switzerland) from 1988 to 1994. He is a member of the Ph.D. evaluation board of the Ph.D. in chemistry program at UNRC.

Prof. Dr. Barbero is a permanent research fellow of the Argentinian Research National Council (CONICET) since 1995, being presently a principal researcher, the second highest category. He has served as member of the chemistry commission and chairman of the chemistry fellowship commission. He is presently cochairman of the project evaluation commission, chemistry chapter, of the Argentinian Agency for Science and Technology Promotion (ANPCyT). He is also a member of the National Nanotechnology Foundation (Argentina) executive board.

He received the Tajima Prize of the International Society of Electrochemistry (ISE) in 1996, the Rafael Labriola Prize of the Argentinian Chemistry Society (AQA) in 2004, and the Maria Cristina Giordano Prize of the Argentinian Society for Physical Chemistry Research (AAIFQ) in 2007. He is an IUPAC fellow since 2000. In 2007, he received the John Simon Guggenheim Fellowship (USA). He has been invited professor at the universities of Paris VII (France), Alicante (Spain), La Laguna (Spain), Wales at Bangor (UK), and Buenos Aires (Argentina).

He has carried out research in various fields of electrochemistry including modified electrodes, conducting polymers, electroanalysis, in situ characterization techniques, batteries, supercapacitors, and fuel cells. He has also performed research in chemistry of materials: porous carbons and metals, carbon nanotubes, graphene,

G.G. Láng and C.A. Barbero, *Laser Techniques for the Study of Electrode Processes*,
Monographs in Electrochemistry, DOI 10.1007/978-3-642-27651-4,

smart hydrogels, and conducting polymer nanoparticles. He has additionally pioneered the use of combinatorial chemistry to synthesize conducting polymers and the development of lithographic methods to structure polymer surfaces and thin films.

He has published as author or coauthor over 110 research papers (at least a 30 dealing with PBD) and three book chapters, which have received more than 1,400 citations. He has developed technological applications of his research, being awarded four patents and two national innovation prizes.

Győző G. Láng

Győző G. Láng (born 1960) has been a full professor at Eötvös Loránd University, in Budapest, Hungary, since 2006 and is the head of the Department of Analytical Chemistry and is the vice director for education of the Institute of Chemistry. He attained his diploma in chemistry in 1985 and his PhD in 1991 at the Eötvös Loránd University. He received his D.Sc. in 2004 from the Hungarian Academy of Sciences. Dr. Láng is the president of the Electrochemical Committee of the Hungarian Academy of Sciences (since 2005). He has been the regional representative for Hungary of the International Society of Electrochemistry (2005–2010). He is a member of the editorial board of the Journal of Electrochemical Science and Engineering.

He worked as visiting researcher and Alexander for Humboldt research fellow during 1993–1994 at TU Clausthal, Germany (in the group of Prof. K.E. Heusler), and as visiting researcher and JSPS fellow in 1998 and 1999 at the Hokkaido University in Sapporo, Japan (in the group of Prof. Masahiro Seo).

He received the Tajima Prize of the International Society of Electrochemistry (ISE) in 1997, the Bolyai Fellowship in 1999, and the Széchenyi Fellowship in 2002.

He has carried out research in various fields of physical chemistry including electrochemical thermodynamics, mechanical properties of liquid/liquid and solid/liquid interfaces, quantum chemistry of organic molecules, electrochemistry and corrosion of metals and amorphous alloys, environmental aspects of electrochemistry, the reduction of perchlorates, modified electrodes, and conducting polymers. He also has been active in the development of instruments, instrumental methods, and measuring techniques.

He has published as author or coauthor over 100 papers and 10 books and book chapters, which have received more than 1,000 citations.

About the Editor

Fritz Scholz

Fritz Scholz is professor at the University of Greifswald, Germany. Following studies of chemistry at Humboldt University, Berlin, he obtained a Dr. rer. nat. and a Dr. sc. nat. (habilitation) from that university. In 1987 and 1989, he worked with Alan Bond in Australia. His main interest is in electrochemistry and electroanalysis. He has published more than 280 scientific papers, and he is editor and coauthor of the book *Electroanalytical Methods* (Springer, 2002, 2005, 2010, and Russian Edition: BINOM, 2006), coauthor of the book *Electrochemistry of Immobilized Particles and Droplets* (Springer 2005), coeditor of the *Electrochemical Dictionary* (Springer, 2008), and coeditor of volumes 7a and 7b of the *Encyclopedia of Electrochemistry* (Wiley-VCH 2006). In 1997, he has founded the *Journal of Solid State Electrochemistry* (Springer) and serves as editor-in-chief since that time. He is the editor of the series *Monographs in Electrochemistry* (Springer), in which modern topics of electrochemistry are presented. Scholz introduced the technique “voltammetry of immobilized microparticles” for studying the electrochemistry of solid compounds and materials, he introduced three-phase electrodes to determine the Gibbs energies of ion transfer between immiscible liquids, and currently, he is studying the interaction of free oxygen radicals with metal surfaces, as well as the interaction of liposomes with the surface of mercury electrodes, in order to assess membrane properties.

G.G. Láng and C.A. Barbero, *Laser Techniques for the Study of Electrode Processes*,
Monographs in Electrochemistry, DOI 10.1007/978-3-642-27651-4,

Index

G.G. Láng and C.A. Barbero, *Laser Techniques for the Study of Electrode Processes*, Monographs in Electrochemistry, DOI 10.1007/978-3-642-27651-4,